A Miniaturised Focussed Ultrasound Transducer for Soft Tissue Ablation

Jack Edward Stevenson

SUBMITTED IN FULFILMENT OF THE REQUIREMENTS FOR THE DEGREE OF
DOCTOR OF PHILOSOPHY

JAMES WATT SCHOOL OF ENGINEERING

COLLEGE OF SCIENCE AND ENGINEERING

OCTOBER 2024

In memory of Jack Leitch

Abstract

Focussed ultrasound surgery (FUS) in literature has been developed in the direction of large extra-corporeal transducers. With the rise of surgical robotics in recent years, a new niche is emerging in which miniaturised ultrasonic transducers for laparoscopic surgery will be required. Laparoscopic surgery can be advantageous to FUS transducer miniaturisation due to the robotic control being able to move the transducer into a position closer to the target tissue for treatment.

A new FUS transducer for soft tissue ablation is proposed, with a miniaturised configuration that can be readily integrated with a surgical robot. The FUS transducer consists of a single piezoceramic disc with a microballoon filled epoxy backing layer to approximate an air backing, and an acoustic Fresnel lens. The transducer was first developed as a virtual prototype in finite element analysis (FEA) that characterised the device's acoustic field output with respect to different piezoelectric and acoustic lens materials.

The transducer housing and Fresnel lens were made from photopolymer resins in a mask stereolithography (mSLA) printer. Fifteen miniature FUS transducers were fabricated and tested, incorporating five different piezoceramic materials: a soft PZT, a specialised composition for high intensity focused ultrasound, a low acoustic impedance porous PZT, and a lead free piezoceramic. The devices were electrically matched to a high power amplifier and characterised at high power in an experimental high power impedance analysis.

A new technique was proposed to steer the focal region of the single element transducer by varying the driving signal frequency. This achieved a 64% positional change of the focus with a 1 MHz frequency change. Through finite element simulations and experimental characterisations of the acoustic field, it was shown that the porous piezoceramic, with lower piezoelectric and coupling coefficients, achieved the highest focal zone intensity and efficiency.

Contents

List of Tables

List of Figures

Acknowledgements

I would like to extend my heartfelt gratitude to my supervisor, Professor Margaret Lucas. Each meeting with her was a valuable learning experience and her guidance has taught me to be a meticulous and thorough researcher. Her support and mentorship have been instrumental in my academic and professional development. I also thank my secondary supervisor, Professor Sandy Cochran, for his support and expertise.

I express my thanks to my friends at C-MIU who supported me from the very beginning. Special thanks to Dr. Xuan Li, Dr. Rebecca Cleary, Dr. Colin Souza, Dr. Alexandru Moldovan, Dr. Nicola Fenu, Dr. Nathan Giles-Donovan, Dr. Hannah Thomson, Dr. Ben Jacobson, Hilde Metzger and Paul Daly. I have learnt a lot from them and have aspired to attain the same level of knowledge and expertise that they demonstrate daily. Countless problems were solved on the backs of notepads or during spontaneous lab meetings. Their support and our conversations (along with plenty of joking around) provided the motivation I needed to complete this work. I am truly grateful.

Thank you to my close friend Charlie Stables; their creativity and balanced views always inspire me to reframe the problem, many times conversations sparked ideas that evolved into solutions. However, even better was the much needed breaks from research to focus on music. I would also like to thank Sean Bommer and Dan Geddes for their friendship and support since our times at undergraduate level.

I must give thanks to my family for the continual support I received during this long journey, my dad Paul, my mum Elaine, my sisters Lauren and Katie and my grandparents Jack and Elizabeth Leitch.

A special thanks to my partner Elise Burns who helped me through even the worst days and always provides me with support and understanding.

Each of them helped me through these past four years and I could not have achieved this without them.

"Together we can conquer the world"

- Jack Leitch

Declaration

I declare that, except where explicit reference is made to the contribution of others, that this dissertation is the result of my own work and has not been submitted for any other degree at the University of Glasgow or any other institution

Jack Stevenson

Abbreviations

- 2-D - 2 dimensional
- 3-D - 3 dimensional
- ABS - Acrylonitrile butadiene styrene
- AM - Additive manufacturing
- CAD - Computer aided design
- cc - Cubic centimeters (= mL)
- CNC - Computer numerical control
- DFT - Discrete Fourier transform
- DI - De-ionised (water, Type II clean)
- DMLS - Direct metal laser sintering
- EDX - Energy dispersive X-ray spectroscopy
- EPD - Elastic - piezoelectric - dielectric (matrix)
- FEA - Finite element analysis
- FDM - Fused deposition modelling
- FEP - Fluorinatedethylenepropylene
- FFT - Fast Fourier transform
- FUS - Focussed ultrasound surgery
- HIFU - High intensity focussed ultrasound
- IIR - Infinite impulse response (digital filter)
- IMU - Inertial measurement unit
- IR - Infrared
- LCD - Liquid crystal display
- LDV - Laser Doppler vibrometer
- MRI - Magnetic resonance imaging
- mSLA - Mask stereolithography
- NDT - Non-destructive testing

- NH - Needle hydrophone
- OD - Outer diameter (dimension)
- PDE - Partial differential equation
- PETG - Polyethylene terephthalate glycol
- PLA - Polylactic acid
- PNP - Peak negative pressure
- PTFE - Polytetrafluoroethylene
- RO - Reverse osmosis (water, Type III clean)
- SEM - Scanning electron microscope
- SLA - Stereolithography
- UV - Ultraviolet
- XRD - X-Ray diffraction

Chapter 1

Introduction

The study and utilisation of sound was first seen in the development of polyphony in the ninth century [1]. Music was predominantly used as a method of religious worship in the form of Plain chants or Gregorian monk chants where a congregation sung in unison. It is speculated that the overtones produced when the unison melody reverberated around large halls were observed and imitated. The first overtone is the octave above the tone being sung, double the fundamental frequency. The second overtone is the perfect fifth, then the major third, and perfect fourth. The interaction of these overtones with the fundamental frequency is pleasing to the ear and also aligns mathematically. The octave oscillates with the fundamental in a frequency ratio of 2:1. The other intervals have a frequency ratio of 3:2 (fifth), 5:4 (third) and 4:3 (fourth). The imitation of these "harmonic consonances" led to the creation of early polyphony (harmony) known as Organum. Early percussive instruments led to the first stringed instruments such as the lute, which vibrated a thin string in tension coupled to a resonance chamber. Early wind instruments amplified an oscillation in pressure created by the musicians' lips (brass) or by forcing air over a sharp edge leading to standing waves caused by Bernoulli's principle (pipe). This in turn evolved into the complex music that we consume today.

One of the first uses of acoustics in a scientific context was an observation made by Leonardo da Vinci [2] in 1490, "If you cause your ship to stop, and place the head of a long tube in the water and place the other outer extremity to your ear, you will hear ships at a great distance from you". In 1826 the speed of sound in water was recorded in Lake Geneva by simultaneously ringing a bell underwater while flashing a light above the surface. The two signals were observed on a boat 13 km away and the time delay

for the sound was recorded [3]. Later in the 19th century, Lord Rayleigh provided a comprehensive mathematical description of pressure waves in his work “The Theory of Sound” [4]. Therefore, sound waves were classified as mechanical pressure waves that periodically oscillate. The molecules of the propagation media physically bump into one another, which causes the wave to progress through space. The particles themselves only oscillate around an equilibrium position, whereas the wave itself propagates through the medium. At the point where the particles are in higher density, the pressure is higher (compression) than when the particles are farthest apart (rarefaction).

1.1 History and background in piezoelectric devices

In 1880 Pierre and Jacques Curie discovered the piezoelectric effect where an electric potential was produced when mechanical pressure was exerted on a quartz crystal [5]. Soon after, Gabriel Lippmann theoretically proved that the reciprocal therefore must be true [6]. This inverse piezoelectric effect was quickly validated by the Curies by applying a voltage to the same quartz crystals and achieving mechanical stress. This technology was crucial in the exploration of sound generation in detection at higher frequencies.

1.1.1 Ultrasound

The presence of sound above what can be heard by human hearing was uncovered in a series of experiments by the Italian biologist Lazzaro Spallanzani. Unsurprisingly, the study of bats and owls led Spallanzani to examine how each animal navigated under low-light conditions. By damaging the bats eyes and ears, it was observed that the main dependence on successful navigation at night was the bats hearing [7]. This led to the conclusion that high frequency inaudible sound was being generated by the bats and they located obstacles based on the ultrasonic echo.

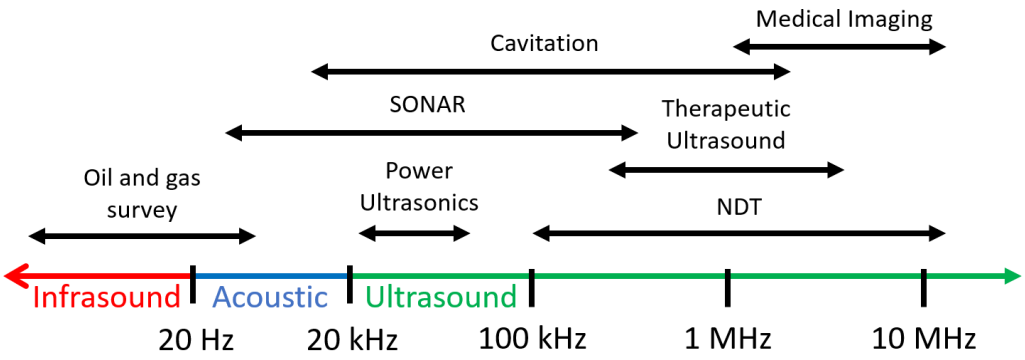

Figure 1.1: Pressure wave dependant technologies grouped by frequency range and shown with respect to human hearing range (acoustic region)

Research into the use of sonic devices for sound navigation and ranging (Sonar) accelerated in the early 20th century. Primarily driven by the first world war and the titanic disaster, an echo ranging device based on a magnetic coil transducer detected icebergs more than two miles away (but was unable to resolve direction) [8]. After the invention of the diode, high power and frequency amplifiers allowed the further development of piezoelectric transducers for sonar applications. In 1941, Paul Langevin patented a piezoelectric transducer which consisted of a quartz crystal glued between two steel plates with a resonance frequency of 150 kHz [9]. This transducer was named a 'hydrophone'.

The first sinking of a submarine that was detected by sonar was during the first world war, 1916. However, the technology took until the mid 1930s to be widespread on ocean liners. The second world war saw a technology race that emphasised the importance of sonar and radar. German Uboats used arrays of Rochelle crystal hydrophones (piezoelectric) to passively monitor and track targets.

After WWII, the discovery of a more powerful piezoelectric material was made when von Hippel permanently polarised barium titanate samples in 1944 [10]. Barium titanate falls into the sub-section of piezoelectricity, ferroelectricity. The greater piezoelectric characteristics exhibited by this class of crystals were further developed with the discovery of lead zirconate titanate (PZT) in 1954 [11]. Figure 1.1 shows the industries that emerged from the advent of piezoelectric devices, grouped by frequencies of interest.

1.1.2 Medical ultrasound

The use of ultrasound in medicine began with therapeutic studies rather than diagnostic applications. In the context of ultrasound, therapeutic doses are high in intensity and cause permanent and irreversible tissue changes. Diagnostic ultrasound does not permanently change the tissue and is much lower intensity. In 1927, Robert Wood and Alfred Loomis investigated a piezoelectric oscillator operated between 100-700 kHz [12]. The piezoelectric used was a quartz disc that required a 2 kW source from an old furnace to drive the disc with up to 60 kV of voltage. This device was powerful enough to cause cavitation and was used to emulsify oil and water. Frogs, fish and rodents were exposed to the ultrasound bath and effects studied with predictable outcomes. The authors also touched the apparatus and noted the various burns and injuries they sustained. However, there was no increase in temperature of the oscillator and connected wave guides. This marked the first observation of ultrasound's effect on tissue and remarks on its potential applications.

By the 1940s, the use of ultrasound was claimed as a treatment for many conditions (this continues today), accompanied by a lack of evidence to support the claims. At this time, the use of ultrasound as a diagnostic tool was discovered based on previous nondestructive testing (NDT) work in metals [13]. Although the evidence was weak, it led to a study in 1949 by George D. Ludwig using a repurposed pulse echo NDT detector to measure animal tissue [14]. In Germany, similar work performed as low-frequency ultrasound (47 kHz) was used to make rudimentary volumetric measurements of the heart [15].

Ludwig's work further outlined that the velocity of sound in animal soft tissues had a mean value of 1540 m/s [16]. The same paper from 1950 concluded that the optimal frequency range of ultrasound in soft tissue diagnostic applications was between 1-2.5 MHz. This work evolved into a collaboration with Siemens (Erlangen, Germany) and Massachusetts Institute of Technology (MIT) to map the brain with ultrasound. The study verified similar claims from the literature however suffered from severe noise [17]. Experiments of an empty skull in water showed similar noise and the aberrations were

deduced to be caused by the skull itself. This study was shut down in 1954 with the conclusion that ultrasound could not be used for clinically relevant data on the brain structure. Subsequently, the research of ultrasound for brain scanning diminished until better piezoelectric materials became available.

Research in the mid 1950s was increasing and diversifying all over the world. The most well-known use of ultrasound was being developed at the University of Glasgow under Prof. Ian Donald. In 1957 a prototype of an obstetric B-mode contact scanner was built, which would evolve into the Diasonograph. A-mode measurements were made with a single-element pulse-echo tester, but these provide only limited information about the tissue. A B-mode scanner, on the other hand combines an array of piezoelectric elements to produce a 2-D image of the tissue in the ultrasound beam. When the acoustic impedance changes between different types of tissue, this changes the strength of the return signal to the probe and a map of the tissue features is captured [18].

1.1.3 Focussed ultrasound surgery (FUS)

The first use of focussed ultrasound was in 1935, reported in a paper by Gruetzmacher [19]. A vibrating quartz plate was placed behind a lens made of polystyrene. A rudimentary radiation force was studied and a gain of 150 times was achieved at the focal point compared to an unfocussed source. The focussed ultrasound source was improved by Lynn et al. in 1942 by including a backing layer of air [20]. The frequency of operation was 835 kHz and the device was used to ensonify paraffin wax. The melting point was 58 °C, which was easily achieved by the focussed source.

The stages of wax melting with respect to pulse amplitude and duration are shown in Fig. 1.2. In this early literature, the precision that could be achieved with FUS was becoming apparent. To conclude this study, the brains of cats and dogs were subjected to *in vivo* ultrasound. All animals showed tissue damage in the near field (the scalp) and various cerebral effects were observed, believed to be caused by the generation of heat at the focus.

Paraffin Melting Defects Produced by Focused Ultrasound

Paraffin block.....	1	2	3	4	5	6
T-200 plate, *volts*.....	0.290	600	1600	1730	1730	1730
T-200 plate, *amp*.....	0.030	0.060	0.115	0.130	0.130	0.130
R.F. output, *amp*.....	0.100	0.200	0.520	0.700	0.700	0.700
Total exposure time, *sec.*	30	30	30	30	15	10
Time from 0 to power indicated, *sec*.....	5	5	5	5	5	1
Diagram of longitudinal section of melting defect.....	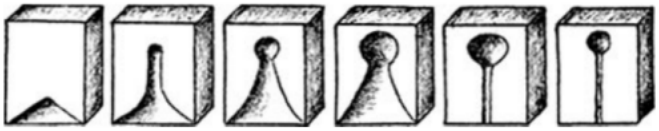					

Figure 1.2: The melting defects caused in paraffin wax due to an 835 kHz focussed ultrasound source, re-presented from [20]

Fry et al. conducted a study on the use of focussed ultrasound for neurological applications in various articles from 1950 to 1954 [21, 22, 23, 24]. The large pressure amplitudes generated led to the early use of the phrase high intensity focussed ultrasound (HIFU). In these studies, irreversible change to nerve and brain tissue without damaging surrounding tissue was revolutionary. The transducer developed an intensity at the focus of 60-80 W/cm^2 at a frequency of 1 MHz.

By the 1960s a HIFU device was used to study the treatment of Parkinson's disease [25]. The intensity of this treatment was estimated to be 1 W/cm^2 and multiple driving frequencies were tested, from 1 - 4 MHz. These devices, all consisted of a planar disc of piezoelectric material and an acoustic lens. Although tremors and associated symptoms of Parkinson's were treated in 48 patients, the technique was not pursued. This was likely due to the dangers of the craniotomy that was necessary before the application of ultrasound and the development of drugs to treat symptoms more safely [26].

Focussed ultrasound as a therapy was plagued with dosimetry and real-time measurement problems and was not easily adopted in the clinical setting. Later, techniques such as magnetic resonance imaging (MRI), which validate the treatment in real time, became more accurate. These then served as a reason for diagnostic ultrasound imaging techniques

to become more reliable for real time monitoring. There followed an explosion in research in focussed ultrasound surgery (FUS), initiated by G. ter Haar in 1995 [27]. FUS devices were studied for use in the ablation of tumours in soft tissues including the liver [28], kindey [29], bladder [30] and prostate [31, 32].

For non-ultrasound procedures for tissue ablation the region of tissue that is ablated from the procedure is difficult to control. The ablation region is based on a $1/r^2$ distribution of energy from the source. Heat can be generated by high frequency oscillating electric fields, around the radio frequency band. Called radio frequency ablation (RFA), the cells immediately surrounding the electrode are ablated quickly, with heat spreading from the point source [33]. RFA can be guided by exciting the electric field between multiple electrodes instead of grounding the patient but the guidance lacks precision. However, cryoablation [34] and chemical ablation [35] are techniques that cannot be guided.

The principle of FUS ablation and comparison of the ablation site with that produced by RFA is shown in Fig. 1.3. FUS has a well-defined region of cell death via coagulative necrosis. This region can be as small as six cells wide between ablated tissue and unaffected tissue. A comparable ablation region from an RFA procedure has indistinct borders that have a steady gradient from dead to live cells.

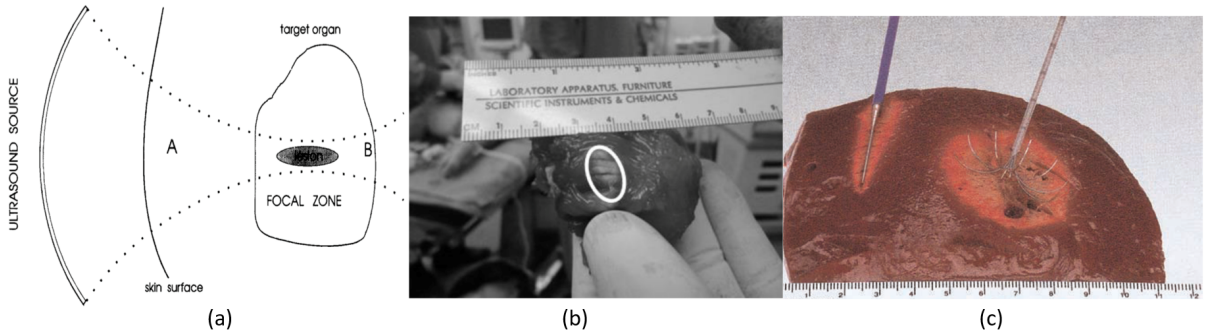

Figure 1.3: (a) Schematic of a FUS device for ablating soft tissue [27], (b) an ablated region of soft tissue [36] and (c) a comparable RFA ablation site showing both one (left) and multiple electrodes (right) [33]

To extend focussed ultrasound to a variety of therapeutic applications and improve the size and effect on tissue, research focussed on quantifying the dose of energy that the tissue absorbed. To ablate tissue with hyperthermia, the only factor that affects cell death is heat. A mathematical relationship was proposed that was based on experimental results

of cell death in heated tissue, Eq. 1.1 [26, 37]. The integral is shown in Eqn. 1.1. The result of increasing the tissue temperature by 1 °C is a halving of the time it takes to ablate the tissue. The thermal dose required for cell death is the equivalent of 240 minutes at 43 °C or 1 second at 56 °C.

$$CEM_{43}(r,z) = \int_0^{t_f} R^{T(r,z,s)+T_0-43} ds, \qquad R = \begin{cases} 4, & \text{if } T \leq 43\,^{\circ}\text{C} \\ 2, & \text{if } T > 43\,^{\circ}\text{C} \end{cases} \tag{1.1}$$

where CEM_{43} is the cumulative equivalent minutes at 43 °C, t_f is the total time the tissue is exposed to the temperature, T is the instantaneous temperature and T_0 is the raised equilibrium temperature. In this model, the CEM varies with respect to a focus in 2D space consisting of radius (r) and depth (z). The temperature is therefore dependent on the radius (r), depth (z) and time (s) [38]. A FUS device can raise the temperature in tissue to above this threshold if it has a spatial peak intensity of ~1 kW/cm^2 [39].

The current literature spans a wide range of applications where the output signal of the FUS device is regulated to apply hyperthermia. In other applications the signal is controlled to shorten the pulse length in time while increasing the pressure amplitude considerably. This changes the mechanism of cell death by exciting cavitation in the tissue that leads to mechanical destruction of cells. Cavitation can also allow for targeted drug delivery via collapsing microbubbles or even temporary disruption of barriers such as the blood brain barrier in the body.

The other main categories of therapeutic ultrasound are shown in Fig. 1.4. The applications are generally dependant on frequency, attenuation and power. For applications requiring large displacement, a lower frequency is required, which allows for a more powerful device. However, therapies that are dependent on the absorption of energy by the target tissue are more dependent on the frequency-dependent attenuation of ultrasound. For

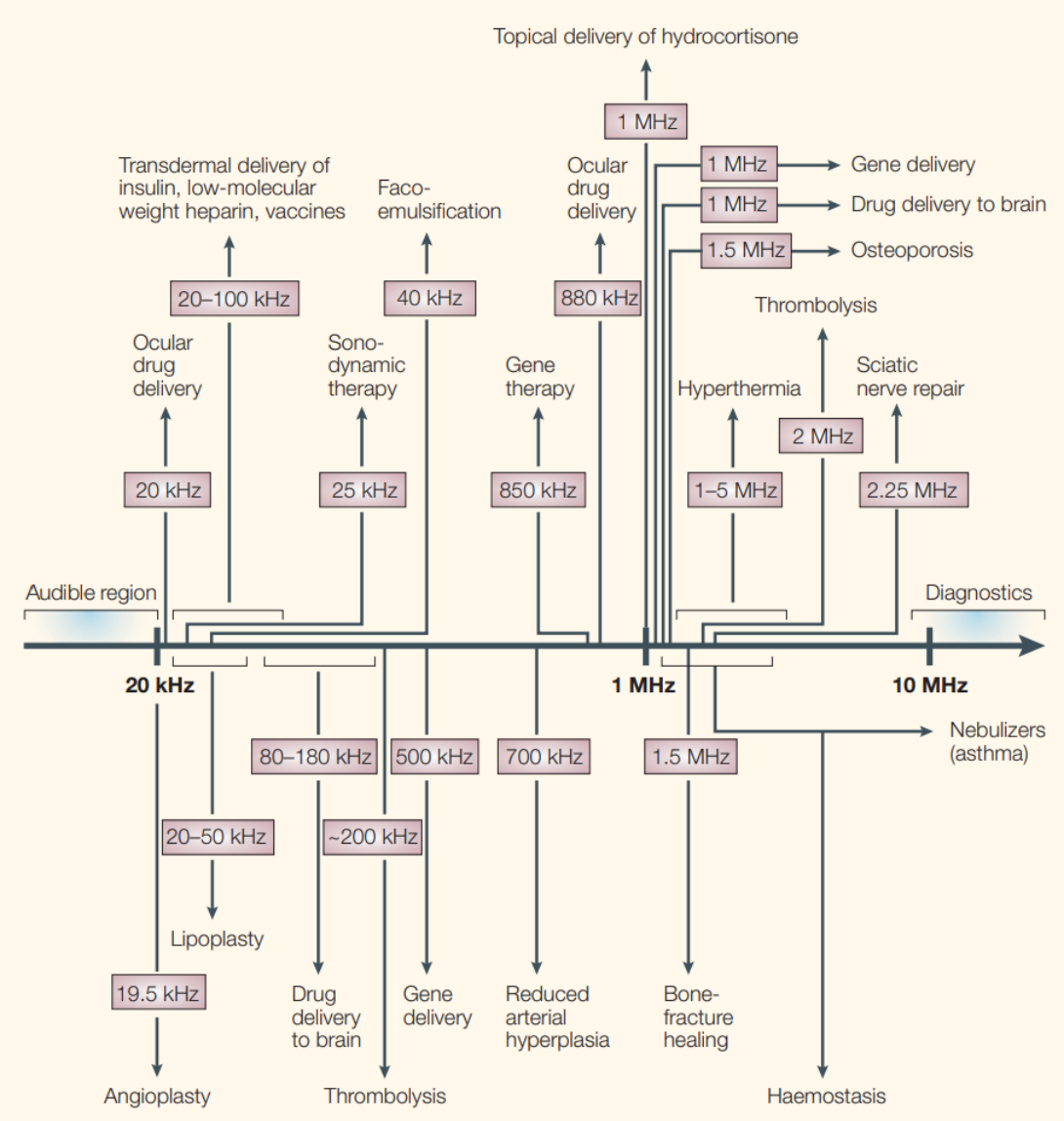

Figure 1.4: An overview of therapeutic ultrasound [40]

FUS devices delivering hyperthermia, a balance is found at a driving frequency between 1-5 MHz where attenuation is high enough such that sufficient energy can be deposited at the focus. Attenuation increases above this frequency range to a level which limits how far into tissue the beam can propagate.

Therapeutic ultrasound showed clear improvements over mechanical or electrical techniques such as RFA. The non-invasive nature of ultrasound shows promise to change procedures that can require surgery to an outpatient visit [41]. This benefits the patient with reduced recovery times because the patient does not have typical wound healing associated with surgery. However, benefits are also clear for the healthcare industry. Decreasing patient recovery time will relieve pressure on the NHS by increasing patient throughput.

1.2 Focussed ultrasound transducer design

There are three main routes to designing a focussed ultrasound source. In the early literature, an acoustic lens was easier to implement as a result of the difficulties in manufacturing a curved active element. With modern piezoelectric ceramics the active element can be formed into a curved source which will naturally come to a focus when driven. With advances and miniaturisation of driving electronics, arrays of elements can be time delayed from one another in order to focus the energy at a point in the near field. Each of these device types has its drawbacks and attributes that lend themselves to miniaturisation.

1.2.1 Bowl transducer

The most simple FUS transducer from a device design perspective is the bowl transducer. The active element (usually a piezoelectric ceramic such as PZT) is pressed into a bowl shape before sintering. Many examples of bowl FUS devices can be found in the literature [27] and many have matured to become commercial systems such as the HifuPlex (Sonic Concepts, WA, USA) [42]. These devices aim to preserve the noninvasive nature of FUS transducers by remaining large in dimensions and serving as an extracorporeal device (staying outside the body). Often a hole will be cut in the bowl to allow an US imaging probe to record the treatment. This cuts down on the price of the procedure as the alternative to US imaging is MRI guided procedures. The devices discussed by ter Haar [27] had resonance frequencies ranging from 1 MHz to 4 MHz which have a focal

length of 320 mm to 25 mm and intensities from 10,000 W/cm^2 to 1680 W/cm^2, respectively. Higher frequency devices cannot focus deep into tissue and the high attenuation also leads to lower intensities being required. However, the low-frequency devices have large focal length and can achieve higher power. In a study of prostate ablation, a threshold for ablation was found at intensities of 1000 W/cm^2 [31] for 1 second. Longer exposure times of four seconds led to intraprostatic lesions at 720 W/cm^2. This device operated at 2.25 MHz with a focal length of 35 mm.

Bowl transducers work well in creating lesions of cell death. However, tumours are often much larger than the dimensions of the focal zone. In this case, multiple focal zones must overlap to completely ablate a region much larger than the size of an individual lesion. One route to achieve this is to mechanically move the piezoceramic bowl in at least one axis. This is shown in Fig. 1.5 where the transducer has been cut into a rectangle to aid rectal ablation. The device has an integrated linear stage that enables overlap of the ablation sites, the device with a latex membrane filled with degassed water that fills the area surrounding the transducer face is shown in Fig. 1.5 (b). The latex membrane conforms to the soft tissue while the water acts as a coupling medium for the ultrasound.

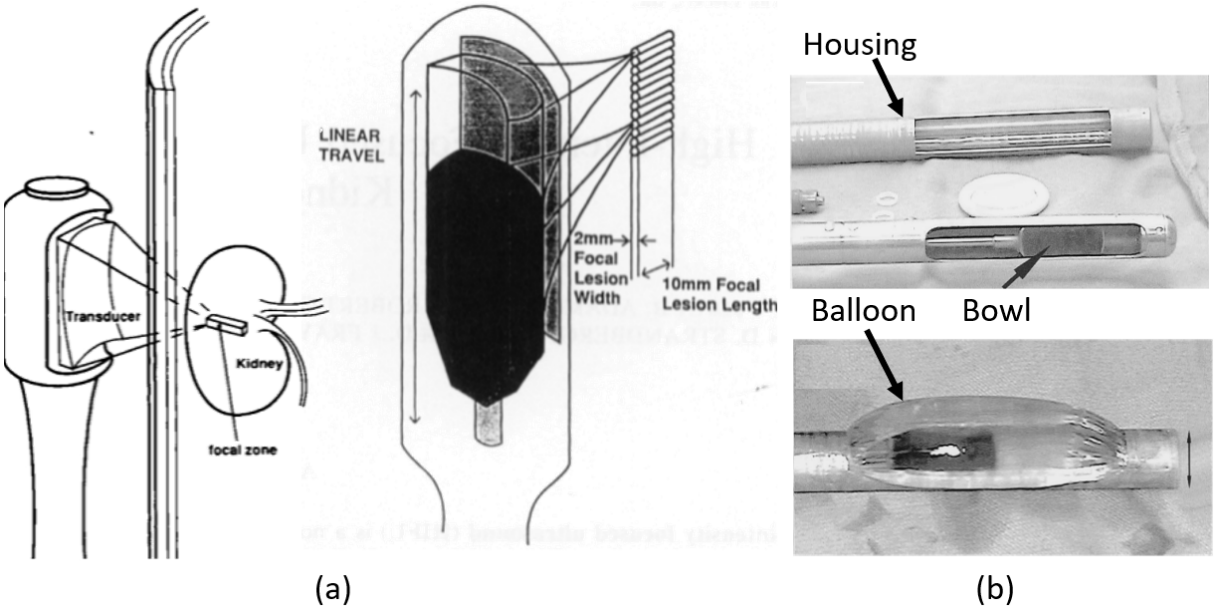

Figure 1.5: (a) A bowl transducer with integrated linear stage [43] and (b) a bowl transducer with integrated linear stage and coupling balloon. [44]

Therefore, design space for the miniaturisation of bowl transducers is limited. The bowl shape must be pressed into the ceramic element itself so the focal zone and other characteristics cannot be altered past this point. It is also difficult to overlap the ablation zones because either a linear stage must be integrated into the device itself or the entire transducer must be moved in the 2-D plane that follows the surface of the tissue, with no scope to change the focal length.

1.2.2 Multi-element array

A technology that excels in flexibility is the multi-element array. It is possible to electrically steer the focus of the beam by having multiple active elements that are all individually driven.

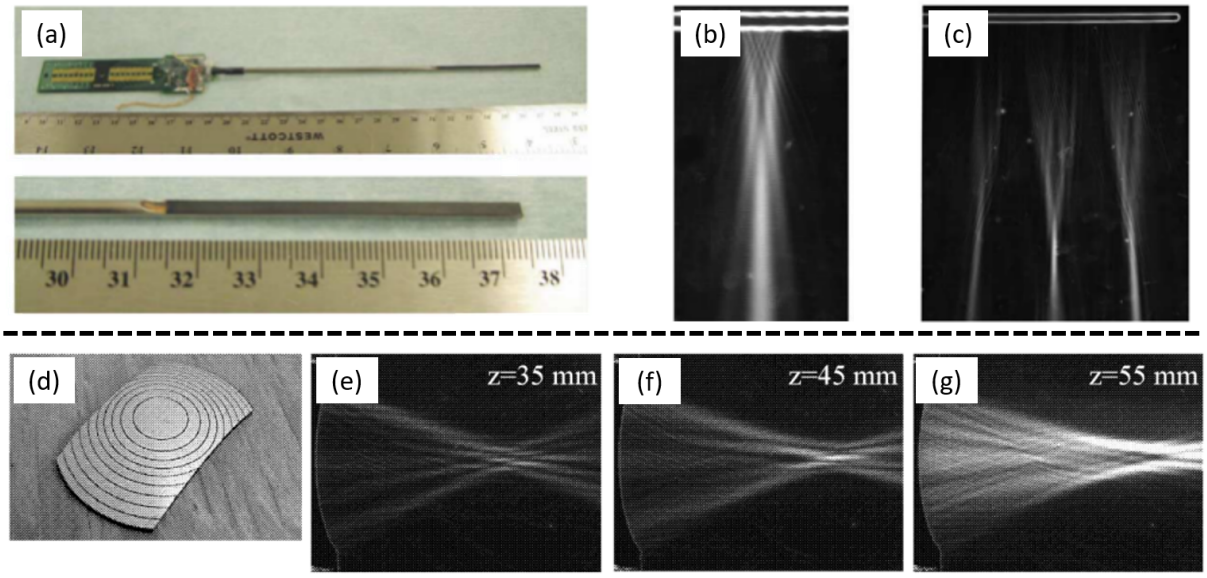

Figure 1.6: (a) A linear phased array, (b) Schlieren images of the unfocussed acoustic field of four elements, (c) field of 32 elements electronically steered into three focal zones [45]. (d) An annular phased array and (e) - (g) beam plots of the acoustic field output at various focal lengths [46].

Figure 1.6 (a) shows a linear array that has been sized to puncture interstitial tissue and have a focal length of 60 mm. The acoustic field plots of the device are shown in Fig. 1.6 (b) with the unfocussed beam pattern above. The 64 elements in this array make electrical beam steering possible by delaying the signal such that the wave fronts all arrive at the target focal zone in phase. For this device, the elements have been steered to three distinct

focal zones at a focal length of 60 mm. The frequency of this device is 3 MHz allowing the focal zones to be small in the azimuth dimension shown in the figure (49 mm total). However, the elevation dimension of the device is only 3.3 mm leading to a larger spread of energy in that axis.

To steer the focal zone deeper into the target tissue, an annular array can be used. The annular array shown in Fig. 1.6 (c) operates at 2 MHz. Phase delays between the circular elements were used to vary the focal length from 35 to 55 mm.

The adaptability of the array is a strong reason to produce miniature devices for robotic integration with this technology. The inherent need to overlap ablation sites can be achieved in a controlled and algorithmic way through electric steering. However, the drawback comes with build complexity, cost and, most crucially, the complex driving system and electronics. As each element requires an individual amplified channel, the cable that would run the length of any robotic arm would be too large to integrate effectively.

1.2.3 Acoustic lens

A device that requires only one element to function can be achieved by employing an acoustic lens to focus ultrasound from a planar source. A bulk lens can be further miniaturised by compressing the profile of the lens to a pattern that repeats every wavelength as seen in Fig. 1.7.

The planar profile of the lens can then be approximated by steps. The steps are called phases, so that a binary lens (two steps) has a phase number of two. The diffraction efficiency of the lens is proportional to the phase number. An increased phase number more accurately approximates the smooth surface of the original bulk lens. In the context of additive manufacturing, the discretisation of the lens face enables the 3D printer resolution to be taken into account in the lens design process. A phase number can be selected which corresponds to the minimum feature size the printer can achieve. This design can be integrated with other innovative lens techniques, such as using a segmented lens to increase the volume of the focal zone, shown in Fig. 1.8.

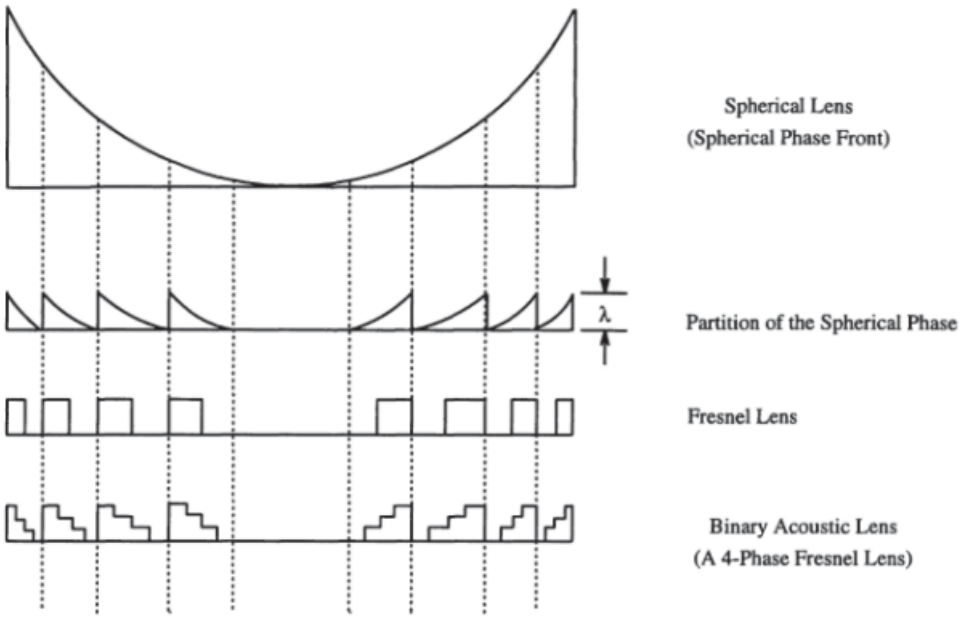

Figure 1.7: The evolution of a typical bulk lens into a four level Fresnel lens. The lens is repeated with respect to the wavelength of sound propagating through it, which is approximated by discrete steps [47]

This lens design, Fig. 1.8 (c), can be integrated into a Fresnel lens to tailor the acoustic field to each procedure. This concept can be taken further by integrating holographic techniques to correct for the phase aberrations that plagued the early literature reports of brain treatments.

Figure 1.9 shows a 3D printed lens for transcranial focussed ultrasound therapy that can correct for phase aberrations in a skull that has been scanned before the procedure. The wave velocity has been modelled and the inverse problem solved to produce a focal zone within the skull.

1.2.4 Transducer design for robotic surgery

It is clear from the literature, that there is a gap in FUS technology, where a miniaturised bespoke FUS device based on pre-procedure patient scans would greatly increase the effectiveness of many ablation procedures. With robotic actuation, the focal region could be precisely steered throughout the procedure or fully automated. With a variable focal length, the device would be capable of ablating a 3D volume. Combined with laparoscopic

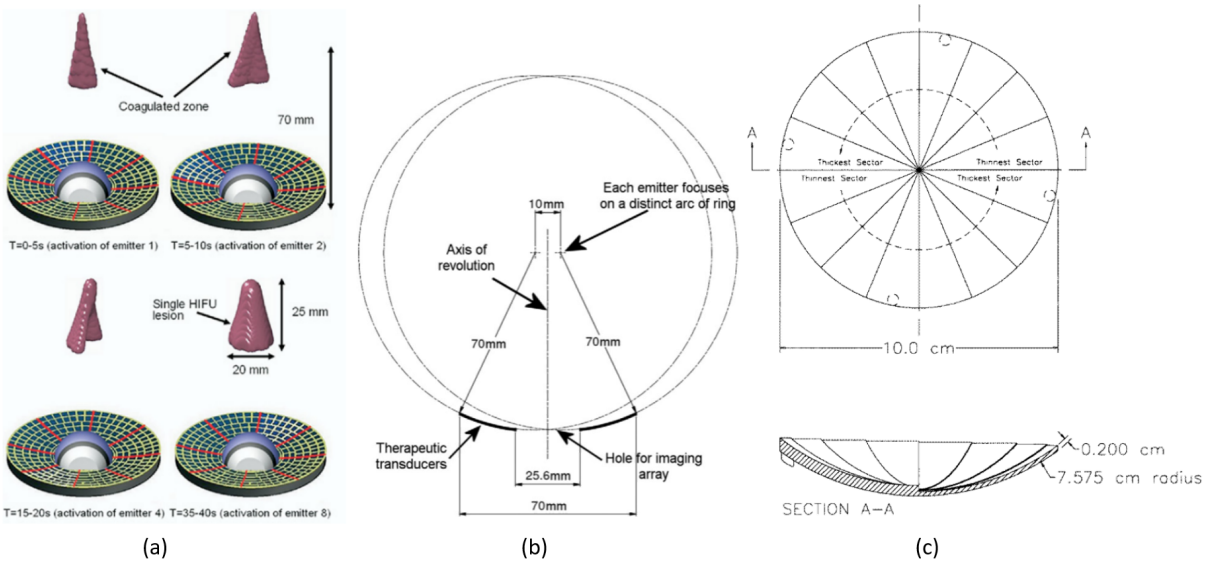

Figure 1.8: (a) Schematic of a segmented bowl transducer, (b) the cross-section showing offset focal zones [48] and (c) a lens design to achieve the same effect [49]

surgery, patient recovery time would be reduced. With a versatile platform bespoke to each procedure, there would also be the option of an extracorporeal application such as peripheral nerve ablation. Also, all procedures could be conducted in an outpatient basis, significantly reducing costs to healthcare providers.

1.3 Piezoelectric materials

The key component in any new ultrasonic technology is the driving material. Piezoelectric materials generate electricity when subject to strain (hence in Greek, piezein, means 'to squeeze'). This is known as the direct piezoelectric effect. The indirect piezoelectric effect is the inverse phenomenon, when strain within the material is generated by application of an electric field. Piezoelectric materials achieve this due to their unique crystal structure. Of the 31 crystal classes piezoelectric crystals are a subsetFig. 1.10. Within this subset lies pyroelectric crystal classes that generate electricity when subject to heat. Finally, within this subset, there is a class of ferroelectric materials. Although quartz (one of the first piezoelectric crystals) is a non-pyroelectric material, modern piezoelectric materials such as $PbZr/TiO_3$ (PZT) and $BaTiO_3$ are ferroelectric [51].

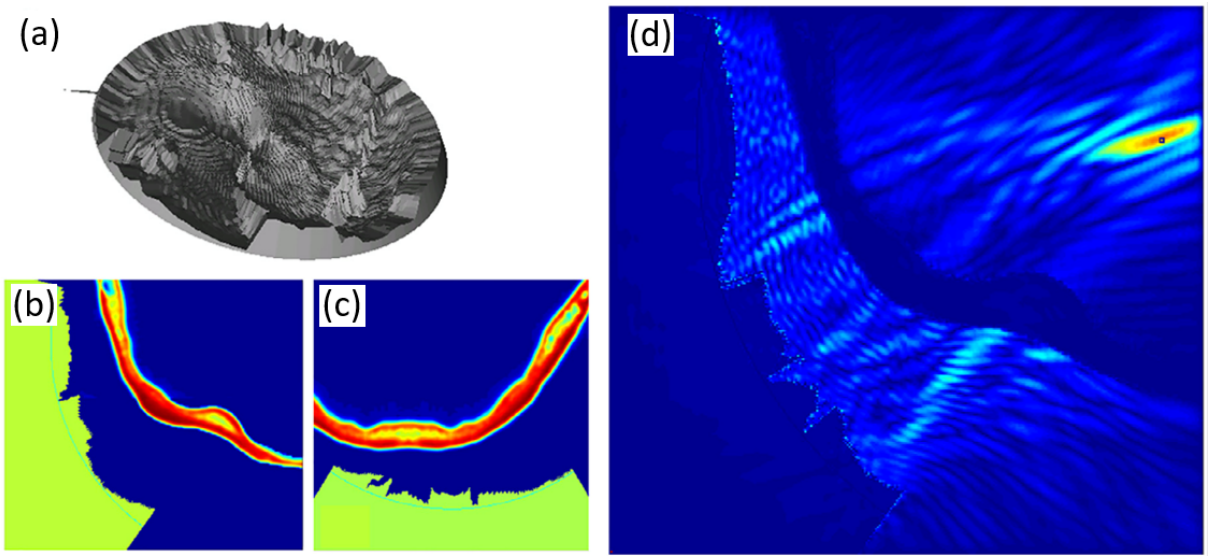

Figure 1.9: (a) 3D printed lens for transcranial focussed ultrasound. (b) Sagittal and (c) Transverse sections of the model where the green structure is the acoustic lens and the blue to red indicate low to high skull wave velocity profile. (d) The acoustic field coming to a focus within the skull [50]

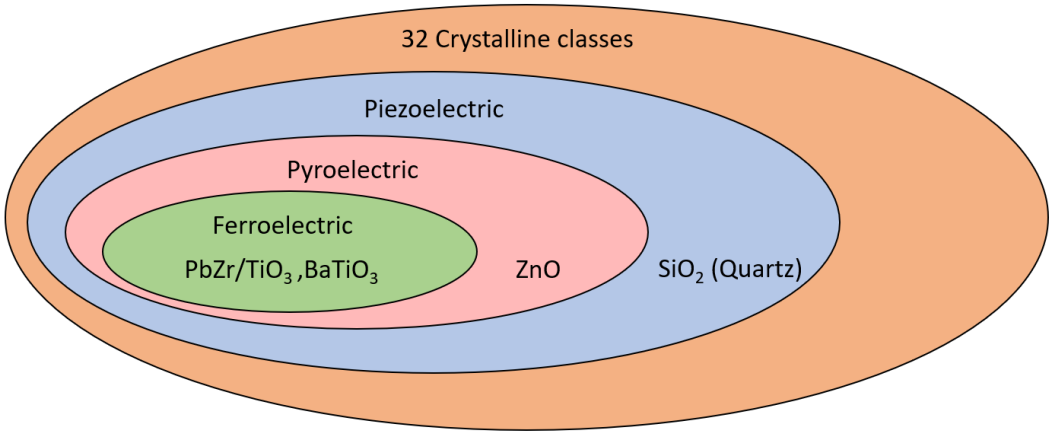

Figure 1.10: The relevant subsets of the 32 crystalline classes [52]

1.3.1 The Piezoelectric effect

To understand why piezoelectric crystals react in such a way to strain, the crystal structure itself must be considered. Figure 1.11 shows the crystal unit cell of PZT. Above a certain temperature, called the Curie temperature (T_c) the unit cell is centrosymmetric and does not exhibit piezoelectric properties due to the absence of a dipole moment. However, below the Curie temperature it undergoes a phase change to a noncentrosymmetric tetragonal structure that does have an electric dipole. This built-in electric dipole may be reversed or switched in certain allowed directions by application of a large electric field.

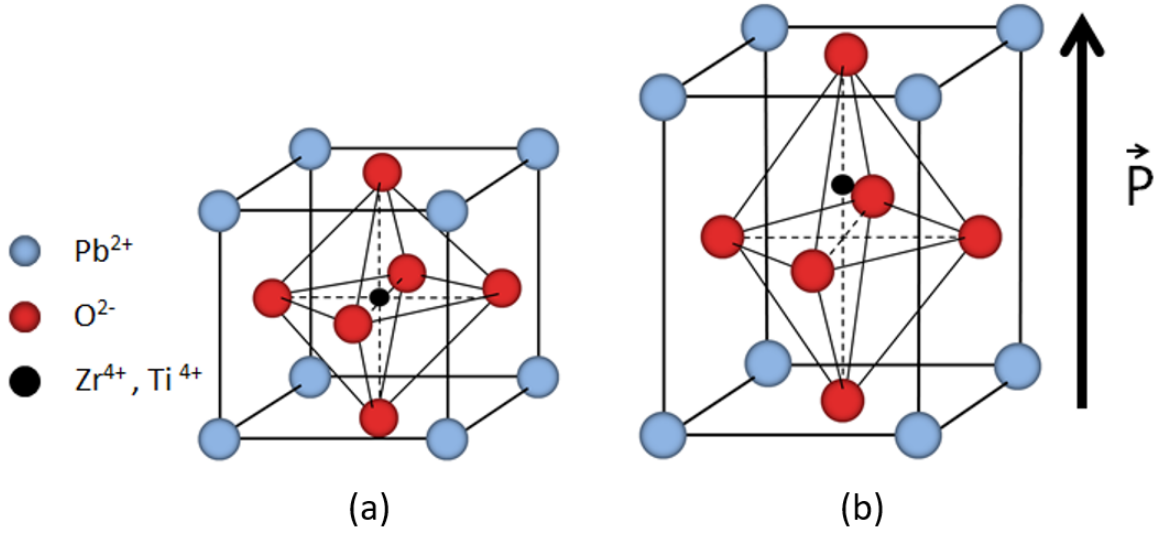

Figure 1.11: (a) The unit cell of PZT where the temperature is greater than the curie temperature (T_c) and (b) the tetragonal structure of PZT when $T < T_c$ where $\overrightarrow{P}$ is the poling vector

Polarisation is explained in Fig. 1.12. Within a single crystal of PZT there are domains of unit cells that have their dipoles aligned at 90° or 180° from each other. This results in a net zero dipole and the material does not exhibit piezoelectric behaviour, Fig. 1.12 (a). When a large electric field is applied to the crystal, the dipoles realign to the electric field and the material as a whole becomes piezoelectric, Fig. 1.12 (b). When the crystal is cooled with this applied electric field the domains come to rest in a new position closer to the field lines and the material itself now has an electric dipole, Fig. 1.12 (c) [53]. The domains relax after poling to a direction that is not the ideal poling direction and can be observed in Fig. 1.12 (d). As the electric field, E, returns to zero at the top right of the hysteresis loop, the polarisation, P, relaxes to a residual polarisation value, P_r. PZT is made as a ceramic formed of many crystals; once the powder has been fired the ceramic body exhibits no piezoelectricity before the poling process. This is because both the domain structures are randomly orientated within the crystallites, and the crystals in the structure are also randomly orientated.

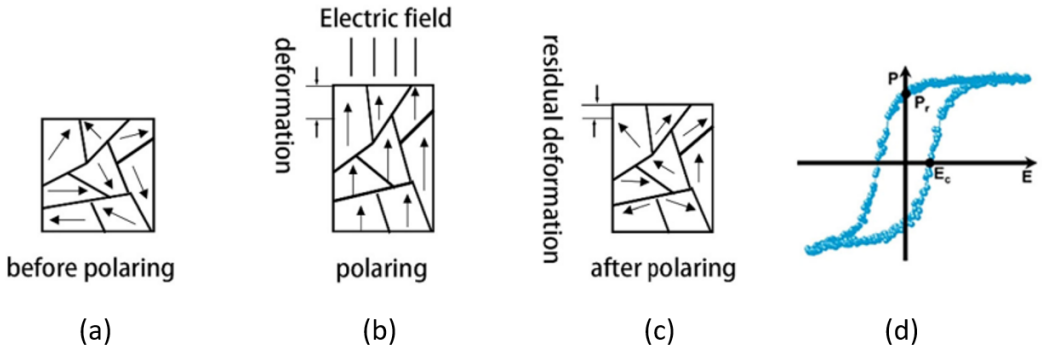

Figure 1.12: (a) The polarisation of each domain in a ferroelectric ceramic before poling, (b) during poling and (c) after poling. (d) Applied electric field, E, against polarisation, P [52]

The point of zero polarisation in Fig. 1.12 (d), E_c is known as the coercive field. If the coercive field is higher than 1 kV/mm the PZT is called hard. If E_c is less than 100 V/mm, it is called soft. This greatly influences the behaviour of the material for transducer designers. A hard PZT has low losses, a high mechanical quality factor, Q_m, but low coupling, k. However, a soft PZT will have the opposite characteristics. In other words, for high-driving systems that require high Q, a hard PZT is more suitable. Whereas a soft PZT is more suited to low-power situations that require high displacement per volt [54].

The mathematical representation of piezoelectric materials comes in the form of equations coupling the mechanical system to the electrical one. The mechanical conditions are related to stress, T, and strain, S, while electrical conditions are related to the electric field, E, and the dielectric displacement, D. Equations 1.2 show that the strain produced in the material will be equal to the stress multiplied by the elastic compliance of the material, s. The dielectric displacement of the material is also related to the applied electric field multiplied by the electrical permittivity, ε (the materials resistance to form an electric field).

$$\begin{aligned} S &= sT \\ D &= \varepsilon E \end{aligned} \tag{1.2}$$

Due to the boundary conditions and mode shapes that are possible with the piezoelectric material in a device, usually a disc, plate or bar, the representations of the piezoelectric (first equation in each pair) and inverse piezoelectric (second equation) effect are presented in Eqs. 1.3 - 1.6. Where Eq. 1.3 is a PZT sample operating in the thickness mode and Eq. 1.4 is the longitudinal mode where the electric field is applied transversely [55, 56, 57, 58].

$$\begin{aligned} T_i &= c_{ij}^E S_j - e_{mi} E_m \\ D_m &= e_{mi} S_i + \varepsilon_{mk}^S E_k \end{aligned} \tag{1.3}$$

$$\begin{aligned} S_i &= s_{ij}^E T_j + d_{mi} E_m \\ D_m &= d_{mi} T_i + \varepsilon_{mk}^T E_k \end{aligned} \tag{1.4}$$

$$\begin{aligned} S_i &= s_{ij}^D T_j + g_{mi} D_m \\ E_m &= -g_{mi} T_i + \beta_{mk}^T D_k \end{aligned} \tag{1.5}$$

$$\begin{aligned} T_i &= c_{ij}^D S_j - h_{mi} D_m \\ E_m &= -h_{mi} S_i + \beta_{mk}^S D_k \end{aligned} \tag{1.6}$$

The dielectric permittivity, ε_{mk} and impermittivity β_{mk} constants are second-order symmetric tensors relating two vectors. The elastic compliance, s_{ij}, and stiffness, c_{ij} are fourth-order symmetric tensors relating two second-order symmetric tensors. The piezoelectric constants are d, g, e and h, and these are third-order tensors which relate second order symmetric tensors (stress and strain) to vectors (dielectric displacement and electric field). This tensor notation can be shortened to matrix notation using the Voigt form. This transforms indices ii to 11, 22 and 33. However, in matrix form, this is shown as m = 1, 2 and 3. The mixed indices ij translate to 23 or 32, 13 or 31, 12 or 21 which corresponds to a matrix form of m = 4, 5 and 6. In this notation 1, 2 and 3 represent the primary axis (x, y, z) while 4, 5 and 6 represent rotation around these axes. For the matrix notation used in Eqs. 1.3 - Eqs. 1.6, i, j = 1 - 6, and m, k = 1 - 3 [59].

Equations 1.3 - 1.6 can be represented in a matrix known as the EPD (Elastic, Piezoelectric, Dielectric) matrix shown in Eq. 1.7.

$$\begin{bmatrix} S_1 \\ S_2 \\ S_3 \\ S_4 \\ S_5 \\ S_6 \\ D_1 \\ D_2 \\ D_3 \end{bmatrix} = \begin{bmatrix} s_{11}^E & s_{12}^E & s_{13}^E & s_{14}^E & s_{15}^E & s_{16}^E & d_{11} & d_{12} & d_{13} \\ s_{21}^E & s_{22}^E & s_{23}^E & s_{24}^E & s_{25}^E & s_{26}^E & d_{21} & d_{22} & d_{23} \\ s_{31}^E & s_{32}^E & s_{33}^E & s_{34}^E & s_{35}^E & s_{36}^E & d_{31} & d_{32} & d_{33} \\ s_{41}^E & s_{42}^E & s_{43}^E & s_{44}^E & s_{45}^E & s_{46}^E & d_{41} & d_{42} & d_{43} \\ s_{51}^E & s_{52}^E & s_{53}^E & s_{54}^E & s_{55}^E & s_{56}^E & d_{51} & d_{52} & d_{53} \\ s_{61}^E & s_{62}^E & s_{63}^E & s_{64}^E & s_{65}^E & s_{66}^E & d_{61} & d_{62} & d_{63} \\ d_{11} & d_{12} & d_{13} & d_{14} & d_{15} & d_{16} & \varepsilon_{11}^T & \varepsilon_{12}^T & \varepsilon_{13}^T \\ d_{21} & d_{22} & d_{23} & d_{24} & d_{25} & d_{26} & \varepsilon_{21}^T & \varepsilon_{22}^T & \varepsilon_{23}^T \\ d_{31} & d_{32} & d_{33} & d_{34} & d_{35} & d_{36} & \varepsilon_{31}^T & \varepsilon_{32}^T & \varepsilon_{33}^T \end{bmatrix} \begin{bmatrix} T_1 \\ T_2 \\ T_3 \\ T_4 \\ T_5 \\ T_6 \\ E_1 \\ E_2 \\ E_3 \end{bmatrix} \tag{1.7}$$

This EPD matrix is simplified by accounting for the symmetry in the crystal. PZT has a crystal symmetry of 6mm which reduces many of the coefficients to zero as seen in Fig. 1.13. This symmetry represents a hexagonal crystal structure with a primitive cell. This leads to a 6 fold rotational symmetry (denoted by 6) while also including two mirror symmetries (denoted by m).

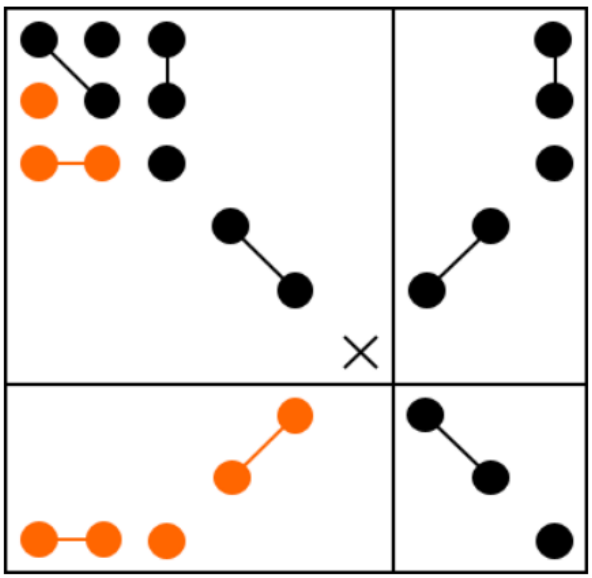

Figure 1.13: The simplification of the EPD matrix based on a 6mm crystal symmetry (PZT). Black dots represent non-zero, independent values, linked dots have equal values and orange denotes values defined by symmetry (e.g. $s_{12} = s_{21}$). The cross represents $2(s_{11} - s_{12})$. All blank coefficients equal zero.

1.3.2 Impedance spectroscopy

A key method of characterising a piezoelectric material is to measure the electrical impedance of specific sample configuration. This can determine the phase of the voltage and current in the AC circuit via the impedance phase. The impedance, Z, has a real component, resistance R and an imaginary component, X, as shown in Eq. 1.8.

$$\begin{aligned} |Z| &= \sqrt{R^2 + X^2} \\ \theta &= arctan\frac{X}{R} \end{aligned} \tag{1.8}$$

A typical electrical impedance measurement of a piezoelectric element is shown in Fig. 1.14. The resonance frequency (or electrical resonance), f_r, exhibits at the minimum impedance for each mode. The antiresonance frequency (or mechanical resonance), f_a, is at the maximum impedance and is always higher in frequency than the resonance. The phase crosses zero degrees at both frequencies. The phase starts at -90° meaning that the current leads the voltage trace, at this point the circuit is acting capacitive. However, above the resonance frequency, the phase goes to +90° and the circuit is now inductive. This is crucial when considering matching the electrical impedance of a device containing piezoelectric material to a source of fixed impedance.

Figures of merit such as the effective electromechanical coupling coefficient, k_{eff}, and the mechanical quality factor, Q_m, can be calculated from the electrical impedance. The former is a description of the efficiency in which the piezoelectric element converts electrical energy to mechanical energy and is a unitless coefficient that lies between zero and one, calculated from Eq. 1.9.

$$k_{eff}^2 = \frac{f_a^2 - f_r^2}{f_a^2} \tag{1.9}$$

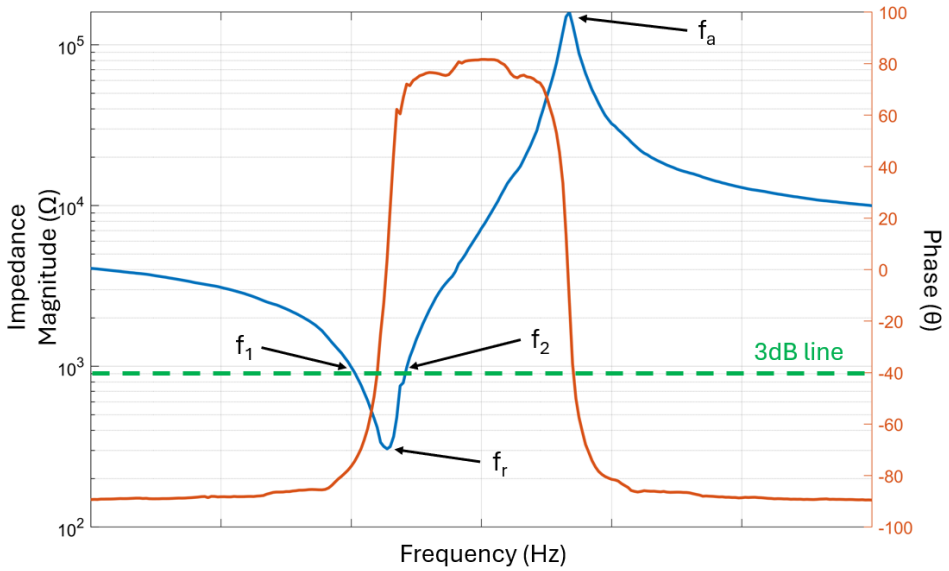

Figure 1.14: A typical electrical impedance measurement with the impedance magnitude (blue) and phase (orange).

The mechanical quality factor can be estimated by using the 3 dB method. The two frequencies 3 dB higher in impedance magnitude either side of f_r are used in Eq. 1.10, with the two frequencies f_1 and f_2 shown in Fig. 1.14.

$$Q_m = \frac{f_r}{(f_1 - f_2)} \tag{1.10}$$

Impedance spectroscopy and the calculation of the figures of merit are fundamental to ultrasonic device design and to the miniaturisation of FUS devices.

1.4 Additive manufacturing

The miniaturisation of FUS devices relies on additive manufacturing of an acoustic lens and housing. Additive manufacturing techniques were first explored in the 1980s as a way of producing rapid prototypes from computer-aided design (CAD) models. Traditional manufacturing techniques involve removing material from a bulk block to resolve the end topology (subtractive manufacturing) or producing a mould to press powders or curable

liquids to produce a final part. However, additive manufacturing uses a supply of material and builds the part in 3D, often one layer at a time. This enables prototypes to be rapidly converted from the proof-of-concept 3D CAD design to a physical part quickly. Due to having access to the inner structure of the part during the printing procedure, additive manufacturing can achieve designs that are simply not possible from subtractive manufacturing.

The variety of additive manufacturing techniques is shown in Fig. 1.15. Each method is specialised to the materials being manufactured.

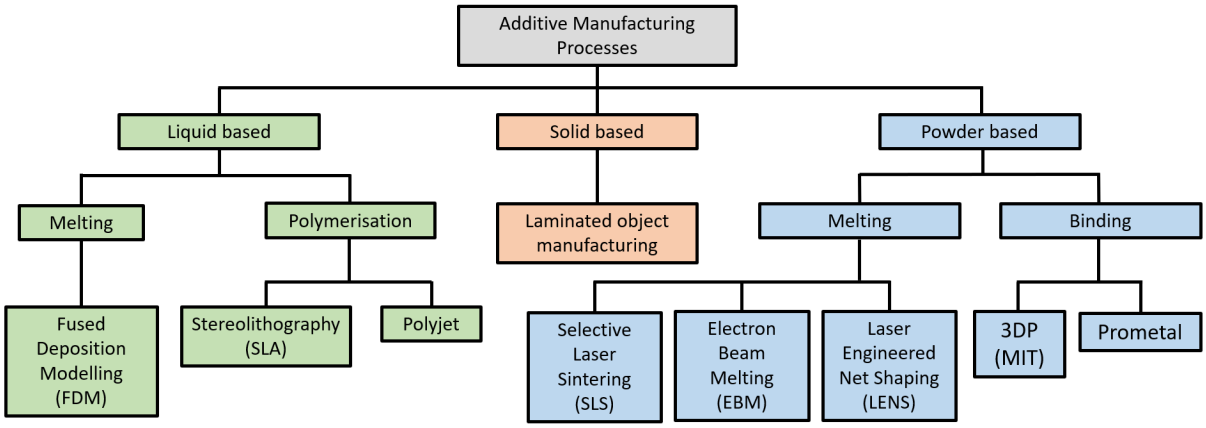

Figure 1.15: An overview of additive manufacturing techniques (adapted from [60])

For acoustic propagation into soft tissue, a homogeneous and low acoustic impedance (close to water) material is necessary. This removes many techniques from the list. Further to this, the feature sizes on an acoustic lens operating at 1.5 MHz requires resolution of the order of 10's of microns. Ultimately this narrows the applicable technologies to polymerisation and potentially also metal printing such as selective laser sintering. The aim is to provide a cost-effective lens, since metal (SLS) printers are typically 10-100 times the cost of for example stereolithography (SLA).

An SLA printer focusses a laser onto a spot on a print bed that is submerged in ultraviolet (UV) curing resin (photopolymer resin). This cures the resin and it binds to the print bed. The laser is then scanned across the print bed with a mirror based scanning system to build the layer as designed in CAD. The build plate then moves one layer height further from the laser and the next layer of resin is cured onto the top of the previous one. A masked stereolithography, mSLA, printer simplifies this process by replacing the laser as a source of UV radiation with a UV LED Fig. 1.16. As this is not a directional source, the

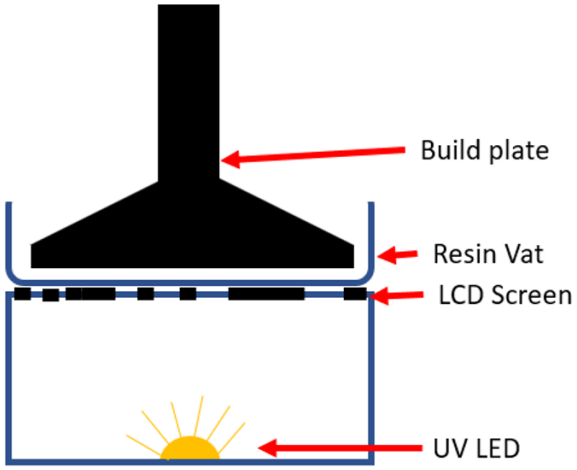

Figure 1.16: A cross view schematic of an mSLA printer

resin vat is shielded from the LED via a liquid crystal display (LCD) screen. The dark pixels do not cure the resin immediately above them, whereas the activated pixels become transparent and cure the resin in the immediate vicinity between the LCD screen and the build plate. The inherent nature of this action also changes the time taken to manufacture a part from being dependent on the total scanning length of the laser to purely dependent on the height of the part (as each layer cures at the same time). The cost of the mSLA printers has decreased drastically in recent years due to the screen technologies used in digital handheld devices (such as phones) becoming much more advanced and cost-effective. This makes mSLA an ideal candidate for manufacturing miniature FUS lenses.

1.5 Contribution to knowledge

This research aims to investigate a platform for bespoke, miniaturised FUS transducers capable of robotically delivered therapeutic applications. The following highlights the original contributions discussed in this thesis;

- A virtual prototype of a FUS transducer was developed and parametric studies conducted on acoustic lens parameters and feature sizes. This study included six different piezoelectric materials to compare and identify characteristics for acoustic lens devices.
- A novel heat management solution was integrated into the housing of the FUS device.
- A database of photopolymer resin acoustic properties was developed for the further development of acoustic lenses via additive manufacturing. This led to a characterisation of key parameters to optimise for this application.
- A manufacturing method was developed to build a FUS device with an additively manufactured housing and acoustic lens as a versatile and low cost device.
- A force feedback system was integrated into the ultrasonic coupling mechanism at the front of the FUS device. This led to the development of a control loop for autonomous procedures.
- The frequency dependant characteristics of a Fresnel lens have been utilised to develop a novel beam steering technique by sweeping the frequency of the device. This unlocks the beneficial characteristics of an annular array but with the use of only one active element, thus enhancing the integration with robotics by reducing the wiring and complexity of the electronics associated with arrays.

1.6 Publications

Peer-reviewed Journal Papers

- **Stevenson, J.**, and Lucas, M., "A miniature FUS transducer based on an acoustic Fresnel lens for integration with a surgical robot", Submitted to : Ultrasonics, 30/10/2024
- Thanou, M., Moldovan, A. C., Turcanu, M. V., Lines, D., Clutton, R. E., **Stevenson, J.**, Nathke, I., Gachagan, A., Cochran, S., "Ultrasound capsule device enhances intestinal absorption of insulin in pigs", Submitted to : Devices, 27/10/2024

Proceedings

- **Stevenson, J.**, Cochran, S., Lucas, M. (2021) Optimising the Materials of a FUS Transducer Sized for Robotic Delivery. In: 2021 IEEE International Ultrasonics Symposium (IUS), 11-16 Sept 2021, ISBN 978-1-6654-0355-9
  (doi: 10.1109/IUS52206.2021.9593530)
- **Stevenson, J.**, Fenu, N. G., Chilles, J., Cochran, S. (2021) Characterisation of PZTs Non-Linear Behaviour for High-Power Systems. In: 2021 IEEE International Ultrasonics Symposium (IUS), 11-16 Sept 2021, ISBN 978-1-6654-0355-9
  (doi: 10.1109/IUS52206.2021.9593358)
- Devireddy, S., **Stevenson, J.**, Fenu, N. G. , Giles-Donovan, N. and Cochran, S. (2021) High-Power Characterization of d32-Mode Mn:PIN-PMN-PT Piezoelectric Single Crystals at Different Temperatures. In: 2021 IEEE International Ultrasonics Symposium (IUS), 11-16 Sept 2021, ISBN 9781665403559
  (doi: 10.1109/IUS52206.2021.9593597)
- Marahrens, N., Dominic, J., **Stevenson, J.**, McLaughlan, J., Biyani, C. S., Lucas, M., Valdastri, P., (2024) Enabling Autonomous Ultrasound-Guided Tumor Ablation during Robotic Surgery. In: 10th IEEE RAS/EMBS International Conference on Biomedical Robotics and Biomechatronics (BioRob 2024), 1-4th Sept 2024

Conference or Workshop Items

- **Stevenson, J.**, Eadie, R., Cochran, S., Lucas, M., "Modelled piezoelectric material characterisation for use in an acoustic Fresnel lens", In: Piezoelectrics for end users XI, February 2021, Poster
- **Stevenson, J.**, Cochran, S., Lucas, M., "Virtual prototype of a miniaturised FUS transducer", In: Ultrasonic Industry Association, April 2021, Presentation
- Cochran, S., **Stevenson, J.**, "Biomedical Acoustics: Instrumentation and Simulation in Biomedical Acoustics: Rapid Prototyping for Focused Ultrasound Sources"-Session 3pBAa, In: Acoustic in Focus 180th Annual meeting, June 2021, Invited panel discussion
- **Stevenson, J.**, Fenu, N. G., Devireddy, S., Giles-Donovan, N., Cochran, S., "Characterization of Piezoceramics and Piezocrystals for Power Ultrasonics", In: 3rd Scottish Ultrasound Annual Meeting, August 2021, Presentation (Best presentation award recipient)
- **Stevenson, J.**, Cochran, S., Lucas, M., "Optimizing the Materials of a FUS Transducer sized for Robotic Delivery", In: IEEE - International Ultrasonics Symposium, September 2021, Presentation
- **Stevenson, J.**, Cochran, S., Lucas, M., "A miniaturised FUS transducer utilising additive manufacturing", In: Ultrasonic Industry Association, April 2022, Presentation
- **Stevenson, J.**, Cochran, S., Lucas, M., "A miniaturised FUS transducer utilising additive manufacturing", In: IEEE - International Ultrasonics Symposium, November 2022, Presentation
- **Stevenson, J.**, Cochran, S., Lucas, M., "The performance of Lead-free material in a miniaturised HIFU device", In: Ultrasonic Industry Association, April 2023, Presentation
- **Stevenson, J.**, Cochran, S., Lucas, M., "The use of additive manufacturing to miniaturise a HIFU transducer", In: British Society for Strain Measurement, August 2023, Presentation
- **Stevenson, J.**, Cochran, S., Lucas, M., "Design of a bespoke, additively manufactured HIFU transducer characterised at high power", In: Anglo-French Physical Acoustics Conference, January 2024, Presentation

- **Stevenson, J.**, Li, X., "Impedance matching for a range of different power ultrasonic transducers", In: Ultrasonic Industry Association - Virtual collaborations, February 2024, Invited Talk
- **Stevenson, J.**, Marahrens, N., Cochran, S., Valdastri, P., Lucas, M., "Miniaturised FUS Transducer for Automated Robotic Delivery", In: Ultrasonic Industry Association, April 2024, Poster

Chapter 2

Design and model of a FUS transducer based on a Fresnel lens

The study of a miniaturised FUS transducer starts with the development of a virtual prototype. This chapter describes the design process, from the equations of a Fresnel lens to the transducer model in the Finite Element Analysis (FEA) program, OnScale.

2.1 Miniaturised FUS transducer Design

2.1.1 Fresnel Lens Design

The dimensions of the Fresnel lens were first defined by selecting a transducer diameter of 25 mm. This represented a miniaturised device that can be integrated with the endowrist of a surgical robot and was within the size range associated with procedures such as prostate tissue ablation (< 60 mm) [41]. Although not meeting the requirements for delivery via the trocar of a typical laparoscopic procedure (< 10 mm) the selected diameter represents an achievable first step towards a laparoscopic FUS transducer and a proof of concept. A frequency of 1.5 MHz was chosen as this is on the lower end of the FUS range. This keeps acoustic attenuation low, allowing a higher depth of penetration into soft tissue. The final design parameter specified from the literature is a target acoustic intensity at the focal zone of > 1.0 kW/cm^2 [31].

The governing equations of an acoustic Fresnel lens are defined in Eqs. 2.1 and 2.2 [61]. This is shown in Fig. 2.1.

$$r_k = \left[\left(z_0 + k\frac{\lambda}{N}\right)^2 - z_0^2\right]^{0.5} \tag{2.1}$$

where r is the radius of the k-th step from the centre, z_0 is the focal length, λ is the wavelength of the pressure wave being focussed by the lens and N is the phase number. Each step has a corresponding height which is related to the time delay required at each radial location in order to achieve constructive interference at the focus and is given by

$$h_k = \frac{1}{Nf((\frac{1}{v_1}) - (\frac{1}{v_2}))} \tag{2.2}$$

where f is the frequency corresponding to the wavelength in Eq. 2.1, v_1 is the speed of sound in the coupling medium and v_2 is the speed of sound in the lens material.

MATLAB scripts were written to generate Fresnel lens designs with a substrate layer attached to the bottom as seen in Fig. 2.1. This script generates a vector of radius values at which each step starts, and a single value for the height of each step. Then, steps are generated with their defined starting point and a height being a multiple of the phase number. The phase number is then treated as a maximum value and the height repeats.

The substrate material is included for the following reasons:

1. To aid the manufacturing process. The first step in the Fresnel lens is at a height of 0, this would make the lens in Fig. 2.1 three separate structures. By adding the substrate this enables the manipulation of a single structure.
2. To allow the pressure waves generated by the active piezoelectric element to couple to a homogeneous material before being focussed.

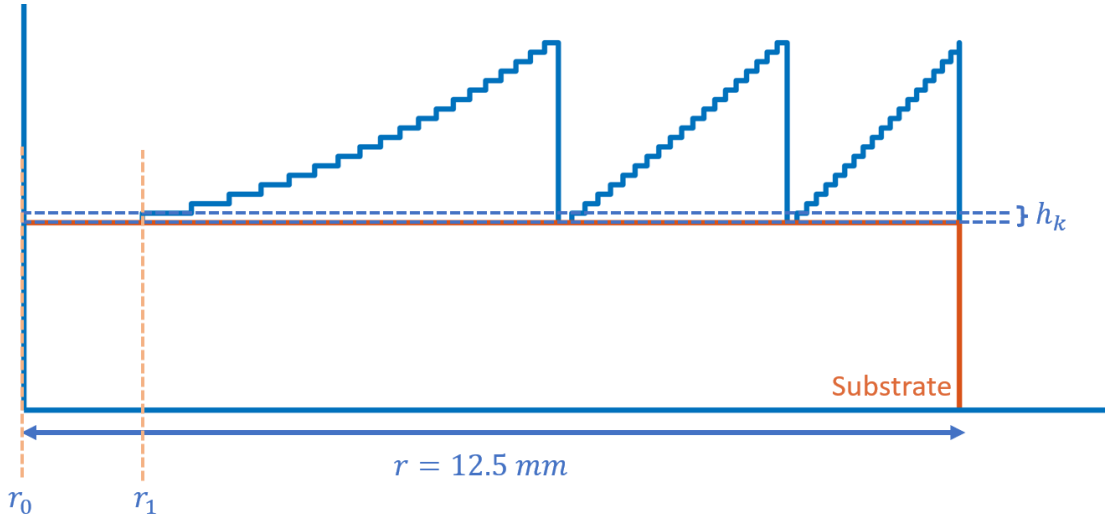

Figure 2.1: Example of a Fresnel lens, phase number 20 with a 1.6mm substrate applied below. The profile is axisymmetric with the axis of symmetry at r_0.

The selection of a scalable vector graphic (.svg) to be the output of the Fresnel lens profile was to coincide with the import option in computer aided design (CAD) software Fusion 360 (Autodesk). However, the .svg dimensions depend upon the MATLAB figure size when generated. With known values such as the radius of the lens and the height of the substrate, a uniform scaling was performed to correct the distorted import. With corrected dimensions, the profile was patched to a 2-D face with infinitesimally small thickness. This 'face' was imported to the FEA software OnScale.

2.1.2 Initial Housing Design

The primary requirement of the transducer housing is to secure the Fresnel lens, piezoelectric element and backing layer without disturbing the path of the acoustic field. The Fresnel lens in this case has a fixed diameter of 25 mm so a securing lip with a diameter of 24.3 mm was included to leave a 0.35 mm tolerance around the lens, as seen in Fig. 2.2. The securing lip protrudes into the acoustic field however is necessary to hold the lens within the housing and a 0.35 mm overhang was found to minimise this disruption while providing adequate support.

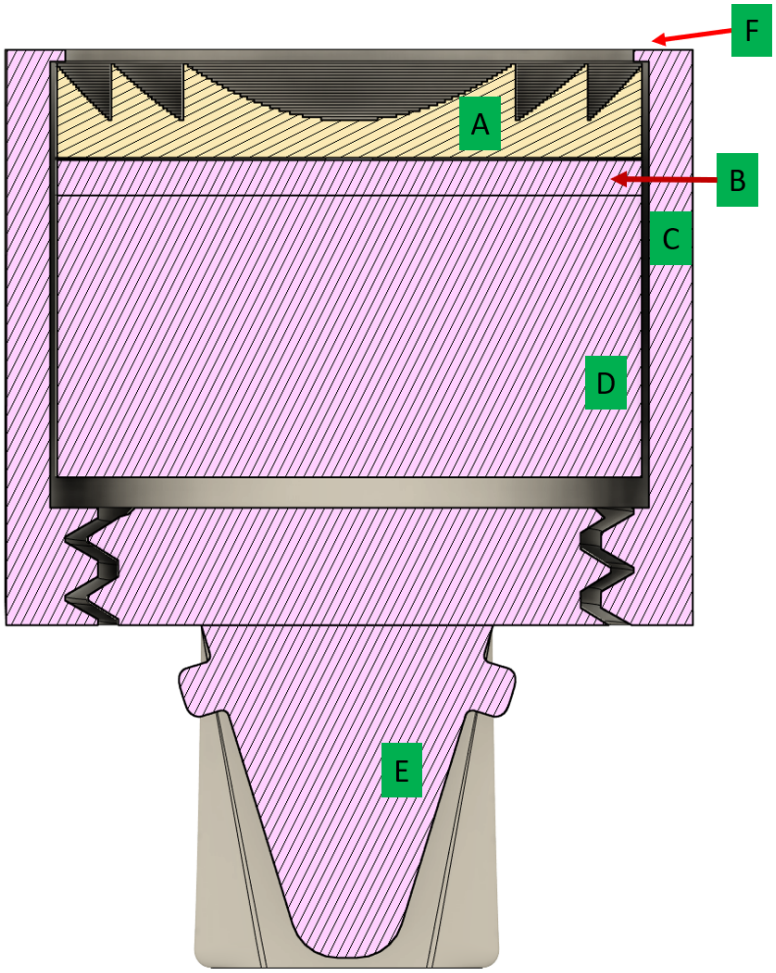

Figure 2.2: Cross section of the FUS transducer design with A) Fresnel lens, exposed directly to the coupling media/water, B) single piezoceramic disc, C) housing, D) backing layer, E) robotic attachment and F) securing lip

As the lens radius was 12.5 mm, the radius of the internal wall of the housing was set to 12.8 mm to ensure a spacing of 0.2 mm to allow epoxy to flow in this void during manufacturing. If centred correctly, this allows for symmetric damping of the piezoelectric disc for more efficient driving. A notch was included in the underside of the Fresnel lens as shown in Fig. 2.3 (b) to accommodate the wires attached to the piezoelectric disc, also ensuring the interface between the lens and piezoceramic disc was as flat as possible. For the positive and ground wires to exit the side of the housing a 2 mm wide and 7.5 mm length hole in the side wall was included. To aid the manufacturing process the housing was split into two semi-cylinders allowing the wires to be threaded through the housing and each half of the housing can be simply secured in place. A pin and hole were included at the interface between the two semi-cylinders and can be seen in Fig. 2.3 (b).

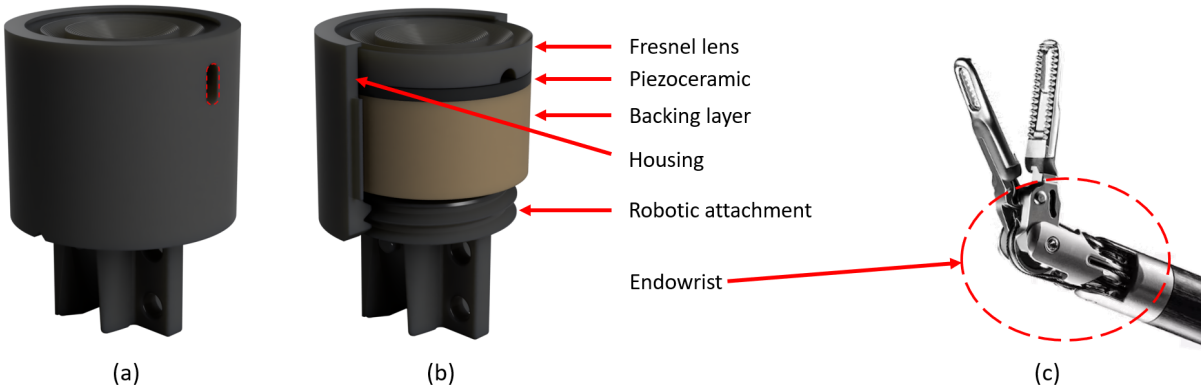

Figure 2.3: Images of (a) complete FUS transducer, (b) housing partially cut to show notch in Fresnel lens and pins for housing alignment seen on the left. (c) The DaVinci surgical robot grasper with endowrist pulley joint highlighted in red.

For acoustic waves generated by the piezoelectric disc to be directed forward towards the target tissue, a highly mismatched impedance backing layer must be included. In this case, a 10 mm depth air based backing layer was used in the form of a 50% volume fraction, micro-balloon loaded epoxy, as depicted in Fig. 2.3 (b). This results in an acoustic impedance much lower than that of the lens at the front of the transducer, leading the energy to propagate forward towards the target tissue for ablation. A more detailed look into the properties and role of the backing layer is discussed in Ch 4.4.3. In the design, a 13 mm void was left for the backing layer to be poured in at the manufacturing stage.

The FUS transducer was designed for integration with the DaVinci surgical robot platform and therefore incorporated a robotic attachment as seen in Fig. 2.3 (b). This was designed as a threaded part that forms a closure for the transducer housing. The bottom end of the attachment consists of an angled holder for the DaVinci Force Bipolar tool (Fig. 2.3 (c)) to attach via two pins. A bracket was also included to allow for an inertial measurement unit (IMU) and infrared (IR) reflectors to be attached, for robotic position tracking and control.

2.1.3 Housing Design - Incorporating cooling

An important requirement of the FUS transducer housing is to handle the heat generated by the piezoelectric disc. A PZ29 disc operating at a tanδ of 0.016 in the operating conditions expected of this transducer will heat by $\sim 20\,^{\circ}\mathrm{C}$ every 5 seconds. This is before the addition of non-linearities that will arise with high power driving and heating that will increase the loss factor significantly. In addition, the ceramic is surrounded by thermally insulating polymers and epoxy, which inhibit the rate at which heat can be transferred out of the device.

This was addressed by incorporating cooling channels seen in Fig. 2.4. The two channel ends at the base of the housing enable two pipes to be connected to each semi-cylinder for coolant to be pumped in and the warmed coolant to drain.

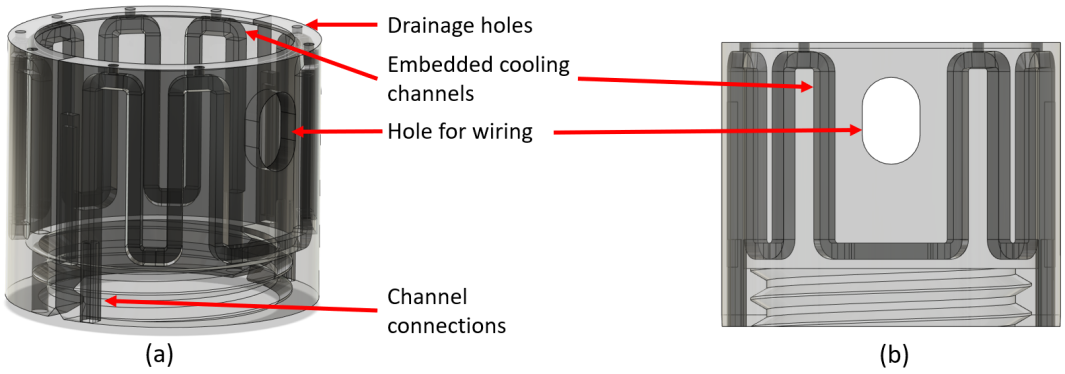

Figure 2.4: Transducer housing with cooling channels embedded. (a) full housing showing cooling channels for front and rear semi-cylinders, (b) front semi-cylinder with wiring hole.

The channels themselves were set to be 1.4 mm square pipes with an S pattern, repeating 5 times in the rear semi-cylinder and 4 times in the front semi-cylinder due to the wiring hole as seen in Fig. 2.4. This resulted in a channel length of $\sim$ 400 mm and volume of $\sim$ 700 mm^3. The channel has a 200 µm wall thickness between it and the inside of the housing. Given a water pump that has a flow rate of 50 L/hr, the heat dissipation in the above design is $\sim$ 1 kW. However, the main limiting factor in the design is the thermally insulating material and geometry of the housing. As the cooling channels are around

the circumference of the piezoelectric disk, heat will not be efficiently transferred away from the centre. As thermal properties are not available for the photopolymer resins, the maximum volume of cooling channels was integrated into the design. The upper limit on channel volume was manufacturing complexities.

2.2 Finite Element Modelling of a FUS transducer

The efficacy of the miniaturised FUS ultrasound transducer is based on its ability to focus acoustic waves and achieve high intensity in the focal region, which can result in tissue ablation. The investigation of the capability of the transducer design was initially carried out by creating finite element analysis models in OnScale.

2.2.1 Introduction to FEA

A computational model of the FUS device is created in FEA where iterations can be carried out in a virtual space. Numerical simulations are generally accurate and idealised due to the driving partial differential equations (PDE's) being the pure solution to a given problem [62], but often complex models become too computationally intensive to be practical. Finite element analysis (FEA) discretises the PDEs into finite elements (or domains) [63]. The entire model is divided into cells whose vertices are these discrete elements, referred to as nodes. In a 2D model these cells are made up of 4 nodes as a quadrilateral and in 3D they are eight vertex hexahedrons as seen in Fig, 2.5.

The FEA program used in this thesis is OnScale (Atlanta, USA) which uses a structured grid where nodes are orthogonal to one another. However, the mesh does not need to be uniform and can have varying density. To determine an appropriate mesh density, the number of elements can be defined with respect to the shortest wavelength of interest in the model. The shortest wavelength (highest frequency) in the material with the lowest sound speed will result in the smallest distance between wave fronts, shown in the following equation;

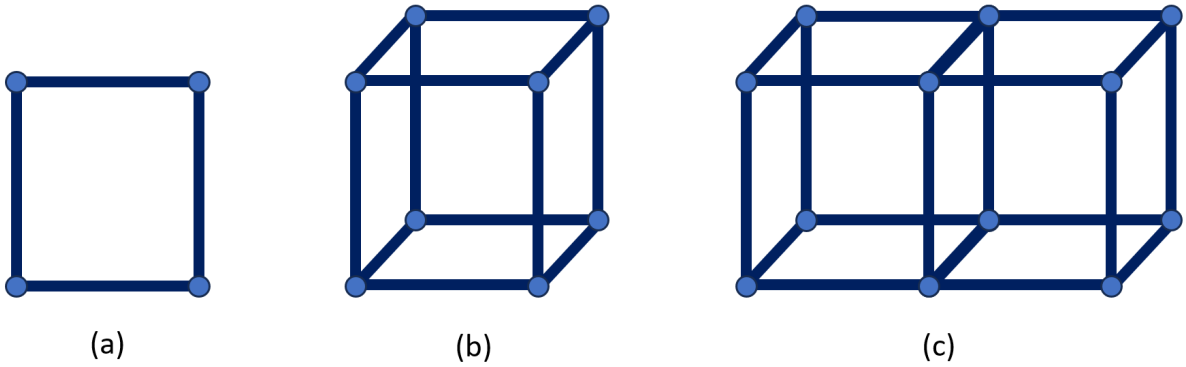

Figure 2.5: Examples of cells within a finite element model where (a) is a 2D cell with four nodes, (b) is a 3D cell with 8 nodes and (c) is two adjacent 3D cells.

$$\Delta x = \frac{\lambda}{n_{FE}} \tag{2.3}$$

where Δx is the spacing between elements, λ is the shortest wavelength, and n_{FE} is the mesh density in elements per wavelength. A recommendation of 15 elements per wavelength is necessary to achieve an accurate resolution in the model [64]. With an increase in mesh density the computational cost increases, hence a convergence study is needed to determine the optimum trade-off between accuracy and computational burden.

Finite element packages can generally be described by two solver types, implicit and explicit. The former computes the solutions to the governing equations at each node and time step based on the solutions of the previous time step. It also considers the effect of each node on all surrounding nodes. Therefore, this is a computationally intensive solver. The explicit solver effectively decouples the nodes from one another and solves the mechanical dynamics of the model over the whole simulated volume. The difference in computational time of these two solvers is extreme for large models, as the solve time scales with the number of nodes in each dimension to the power of 4 for the explicit solver but to the power of 7 for the implicit solver.

By decoupling the nodes in the explicit solver it is important to note that the model may become unstable if the acoustic wave propagating through the nodes reaches an adjacent node before the simulation reaches its next time step. This is known as the Courant-Friedrichs-Lewy condition [65] and is described by Eqn. 2.4.

$$c\frac{\Delta t}{\Delta x} \leq 1 \tag{2.4}$$

where c is the slowest sound speed in the model, Δt is the time step and Δx is the space between nodes. OnScale determines a stable time step which has a minimum value of 80% of the minimum model transit time (or time between nodes). The total simulation time is then user defined and split into an integer number of time steps.

OnScale uses a hybrid approach between the two solvers to exploit the benefits of each. Due to the reduced complexity and being suited to acoustic field solving, the explicit solver is used for most of the transducer and acoustic field model. However, for the piezoelectric material, the implicit solver is used to evaluate the electro-mechanical system of the piezoelectric disc [64].

As the model is finite in size, boundary conditions must be set at the extremities of the model for the simulation to determine how to solve a pressure wave approaching the edge of the simulation volume. There are four common types of boundary conditions;

- Absorbing, applied to outer walls of models where the propagating wave must not be reflected.
- Fixed, where the boundary acts as a rigid barrier reflecting the wave.
- Free, where the elements at the edge of the model are free to deform as determined by the wave propagating. This condition is used to model a highly unmatched acoustic impedance boundary.
- Symmetry, where there is an axis of symmetry. This can be used to create, for example, a quarter model or an axi-symmetric model.

To apply an input signal to the model, a load is created in OnScale. This can be in the form of a pressure, voltage, velocity or force. The piezoelectric disc in reality will be driven via an electrical signal passed through electrodes on the two parallel faces of the disc so this is replicated in FEA. Two electrodes are added to the top and bottom of the disc and a voltage signal (time varying) is applied to one live electrode while the other is des-

ignated ground. The implicit solver calculates the movement of the piezoelectric element determined by its electrical and mechanical properties. To evaluate the electromechanical response of the piezoelectric disc the density, stiffness matrix, piezoelectric constants, poling direction, damping and dielectric constants are required.

The appropriate material properties are assigned to the elements that represent the different parts of the model. As these material definitions are applied, a precedence must be set, where higher precedence materials are selected where nodes of different parts overlap. For example, the Fresnel lens occupies the same space as a block of water, so a higher precedence ensures the lens overrides the water block material properties at the overlapping nodes.

The FEA model calculated the acoustic field pressure at each time step, time history data for charge and voltage across the electrodes and maximum acoustic pressure at each node. The data packs are split into field data or time history data; the former is stored as a 2D coordinate system of the model and the appropriate 3rd measured dimension, while the latter is saved with respect to time from the start of the model to the total time. Both data sets can be logged in a local file format and a separate file for post-processing in MATLAB.

2.2.2 Virtual Prototype Design

The first step to building a virtual prototype in FEA is to identify the experimental set-up to be used to test the FUS device. In this case, the transducer will be submerged in water and the acoustic field measured using a hydrophone. Therefore, the FEA model must include the FUS transducer (piezoelectric disc, Fresnel lens and backing layer) plus a sufficient geometry of water elements to capture the acoustic field to be measured by the hydrophone and contain the focal zone.

For this analysis, there is axisymmetry on the centre line of the transducer and block of water elements, as seen in Fig. 2.6, allowing an axisymmetric FEA model to be adopted.

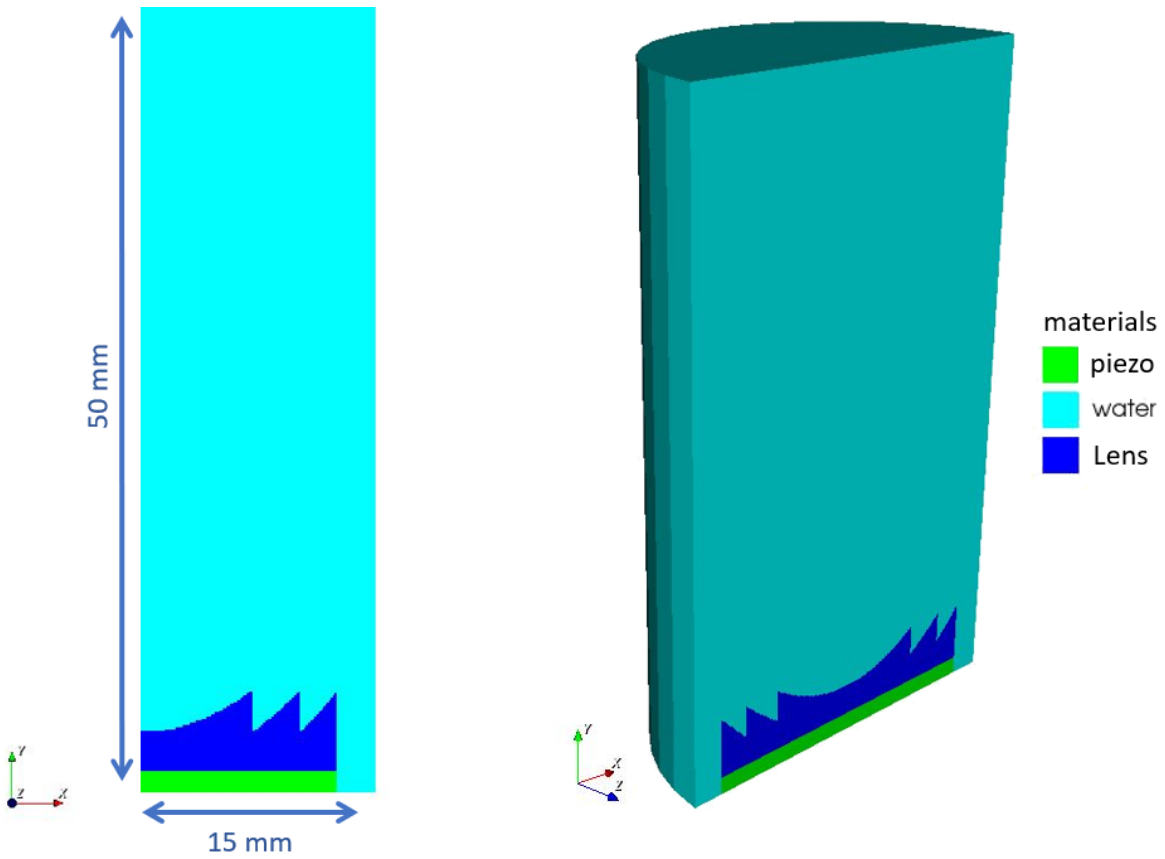

Figure 2.6: Geometry and materials of the axisymmetric FEA model

Dimension	Boundary Condition
x = 0	symmetry
y = 0	free
x = 15 mm	absorbing
y = 50 mm	absorbing

Table 2.1: Boundary conditions used in the FEA model

As described in Table 2.1, the external walls of the block of water elements in the FEA mesh are set to absorbing. The boundary condition y = 0 is free, which is equivalent to having a vacuum coupled to the outermost node and acts as a large impedance mismatch while allowing the piezoceramic to vibrate freely.

The thickness of the piezoceramic disc was determined from an FEA model using the matrix of material properties provided by the manufacturer. Initially, disc thickness was estimated to achieve a thickness resonance of 1.5 MHz to match the centre frequency of the Fresnel lens.

$$N_t = f_r \cdot d_{th} \tag{2.5}$$

Using equation 2.5 with the thickness of the element initially used in the model (d_{th}) and the resonance frequency found in the impedance trace (f_r), a more accurate value of N_t is calculated iteratively to ensure a centre frequency of 1.5 MHz (Fig. 2.7 (c)). In the FEA model axis orientation, the piezoelectric element in Fig 2.6 is poled in the positive y dimension.

To drive the piezoelectric element two electrodes are modelled, the electrically live electrode on the y = 0 boundary of the element and electrical ground on the interface between the piezoceramic element and the Fresnel lens. The live electrode was driven with a sinusoidal 10 cycle burst with an arbitrary amplitude of 50 V, as seen in Fig. 2.7. The total run time of the model was simply chosen to be larger than the flight time in water, 50 μs.

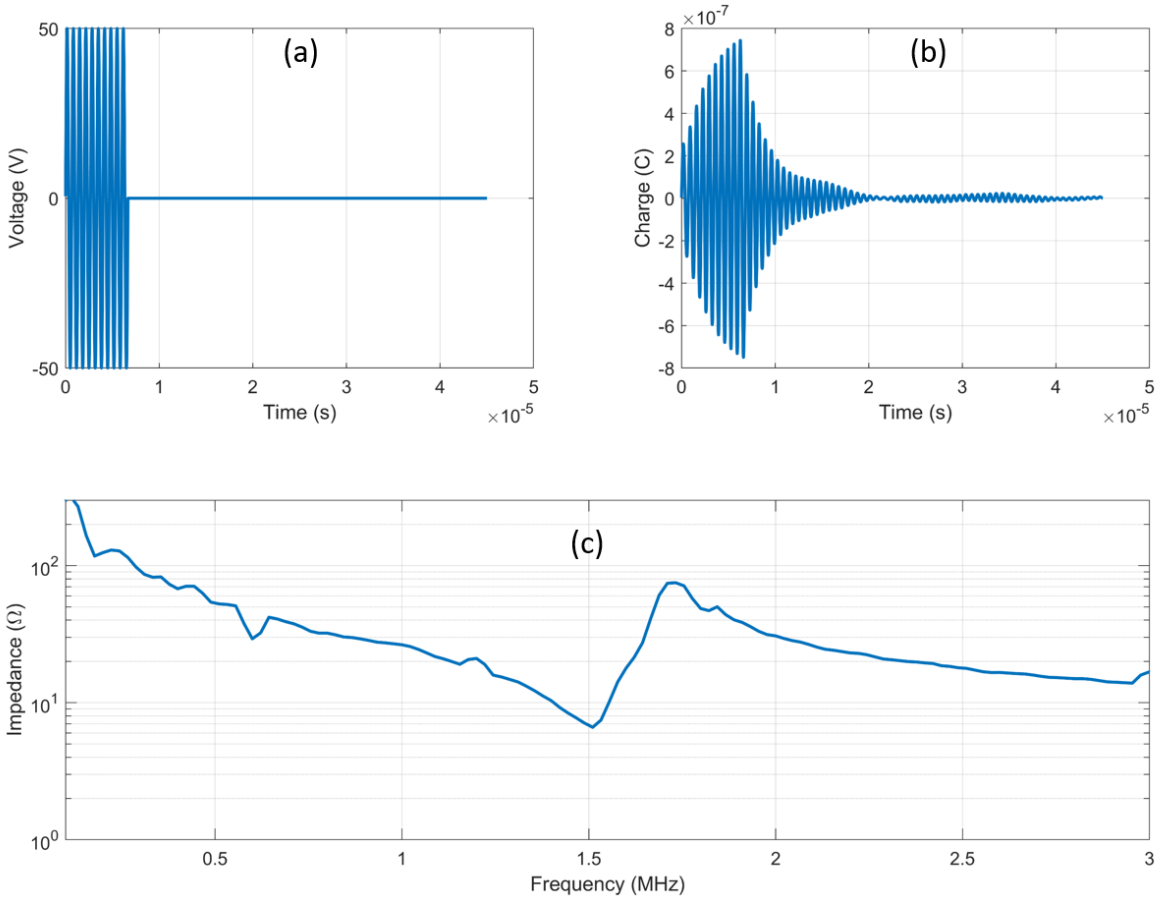

Figure 2.7: (a) The driving voltage signal applied to the live electrode, (b) the charge from the live electrode during driving and (c) the impedance frequency response.

The material properties were assigned to all parts of the FEA model. As will be described in Chapter 3, StrongX was used as the lens material [23]. The piezoelectric disc was selected to be a generic navy type I, PZT4. The water was 25 °C non-linear, selected from the OnScale material library, and included thermal dispersion properties. The Fresnel lens used in initial tests had an arbitrarily chosen substrate height of 2.5 mm, and phase number of 20.

2.2.3 Virtual prototype analysis

Outputs calculated from OnScale were saved in formats such that the data could be post-processed in Onscale or MATLAB.

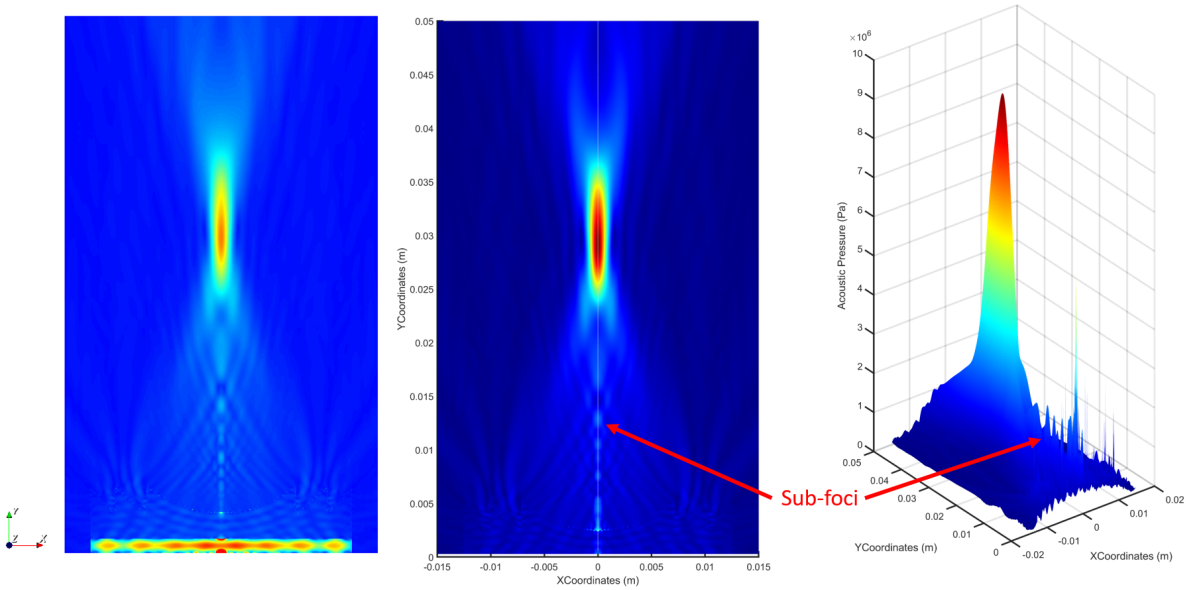

Figure 2.8: Viewing acoustic pressure maximum (APMX) data in (a) OnScale post-processor, (b) the same data in MATLAB and (c) a surf plot of intensity showing the gain at the focus. The location of sub-foci present in the near field are indicated in (b) and (c)

The acoustic pressure data shown in Fig.2.8 (a) is from the OnScale postprocesses. The heatmap at the bottom of the figure is dominated by the pressure in the piezoceramic disc. Due to the limited post-processing capabilities of OnScale, the pressure field using MATLAB is shown in 2.8 (b) with the piezoceramic disc omitted. Fig. 2.8 (c) shows the

location and gain achieved at the focal zone. The noise peaks are spatial peaks caused by abrupt changes in the Fresnel lens structure. The location of the spatial peaks are highlighted in 2.8 (b) and (c). Along the axis of symmetry in the centre of the model there are multiple smaller focal zones (sub-foci) that are characterised in Ch. 2.2.8.

From the data it is possible to calculate the intensity at the focus. By approximating the pressure field to be a Gaussian at the focus, the spatial peak intensity (I_{sp}) is calculated from Eq. 2.6 [66]. Knowing the acoustic power and measuring the 6 dB radial beamwidth, the intensity is calculated as

$$I_{sp} = 1.8 I_{sal} = \frac{1.56W}{A} \tag{2.6}$$

where I_{sal} is the spatial average acoustic intensity of the area enclosed by the full width half maximum pressure. It can be seen that this is proportional to the acoustic power (W) over the square of the 6 dB radial beamwidth (A), which is again measured at the full width half maximum of the peak pressure. During the physical measurement of I_{sal}, the side lobes cannot be isolated from the main focus and are included. When the entire acoustic field is known, such as the case for the output from the model, the peak-to-peak pressure can be used to calculate I_{sp} from Eqn. 2.7 [26];

$$I_{sp} = \frac{p_{pp}^2}{2\rho c} \tag{2.7}$$

where p_{pp} is the peak to peak pressure, ρ is the density of the medium and c is the sound speed. From the acoustic contours shown in Fig. 2.9, the focus parameters are calculated and shown in Table 2.2

Pressure$_{pk-pk}$ (MPa)	Intensity$_{sp}$ (W/cm^2)	Axial dimension (mm)	Radial dimension (mm)
6.68	1508	1.6	11.3

Table 2.2: Focal zone parameters at -6 dB

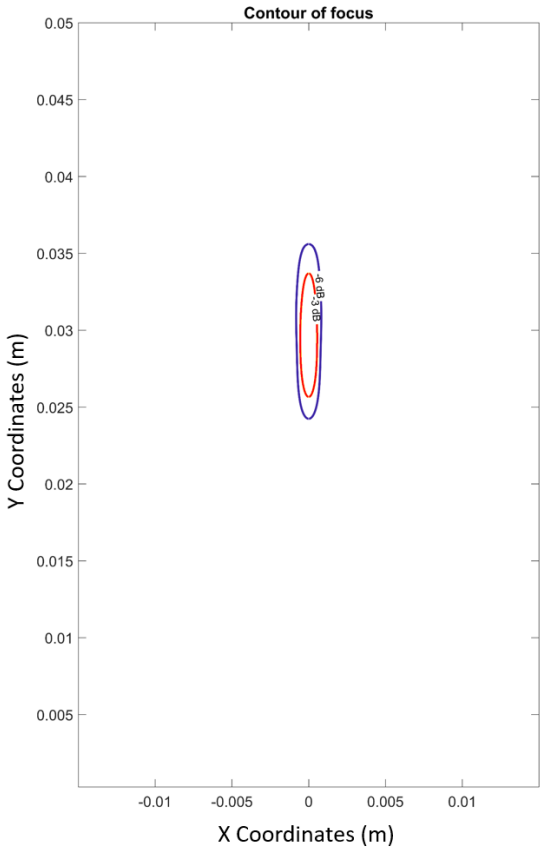

Figure 2.9: The -3dB and -6dB contours of the focus acoustic pressure used to calculate the parameters in Table 2.2

2.2.4 Validation of Focal zone

The length and width of the focal zone can be validated against a purely theoretical value dependent on the wavelength and derived from the wave equation [67]. First, by considering the field of an unfocussed circular transducer, the following intensity can be derived;

$$\left|\widetilde{\phi}(\overrightarrow{r_0},\omega)\right| = \left(\frac{ka^2}{z}\right)^2 \left(\text{jinc}^2\left(\frac{2ax_0}{\lambda z}\right)\right) \tag{2.8}$$

where k is the wavenumber ($k = 2\pi/\lambda$), 2a and z are the diameter and distance from the transducer respectively, λ is the wavelength. The jinc function is defined as;

$$\text{jinc}(X) = \frac{2(J_1(\pi x))}{\pi x} \tag{2.9}$$

where J_1 is a Bessel function of the first kind. As seen in Fig. 2.10 the first zero crossing is found at x = 1.22.

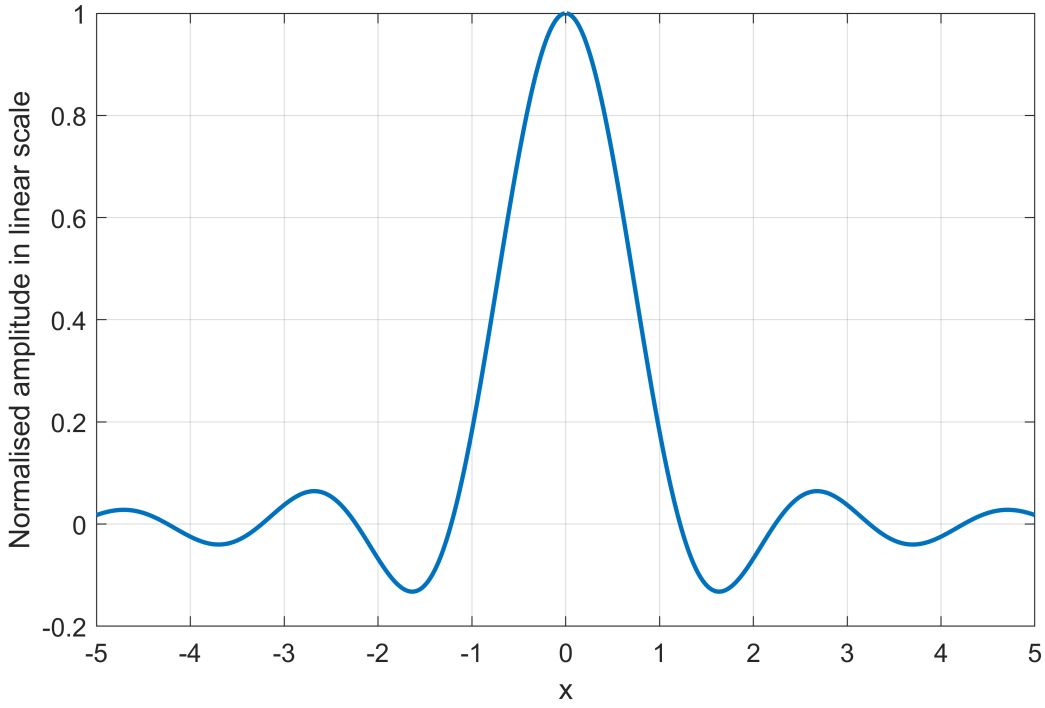

Figure 2.10: jinc(X) plotted for a circular transducer

The following is also true for a circularly focussed transducer for x_0 that represents half of the main beamwidth of the transducer;

$$x_0 = 1.22\frac{\lambda z}{2a} = 1.22\lambda F_N \tag{2.10}$$

where constants follow the same naming convention as above and F_N is the F number of the transducer (F/2 a). The value of x_0 that is specific to the transducer in the model can be used in Eq. 2.11 to determine the focal diameter D_f at the -6 dB point.

$$D_f(xdB) = 1.44\frac{\lambda F}{2a} = k_x \lambda F_N \tag{2.11}$$

k_x is a value obtained from the jinc(X) graph plotted where $X = kax_0/F$. At -6 dB in Fig. 2.11 the beamwidth is 1.41 therefore Eq. 2.11 gives a theoretical axial length of 1.44 mm.

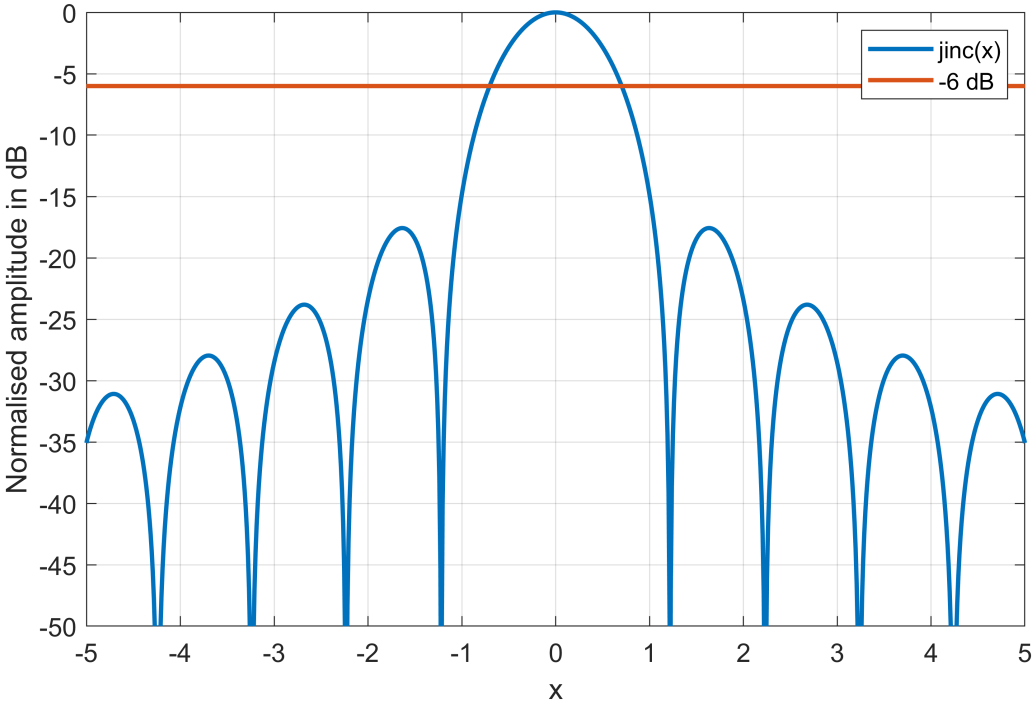

Figure 2.11: jinc(X) (where $X = kax_0/F$) identifying the -6 dB value of k_x.

The radial length of the focus is determined from Eq. 2.12

$$L_f(kdB) = 8a_k \lambda (F_N)^2 \tag{2.12}$$

where a_k is found from $\text{sinc}(a_k/2)$ at $-k$ dB in Fig. 2.12. a_{6dB} was found to be 1.21 and as such Eq. 2.12 gives a theoretical radial length of 9.65 mm.

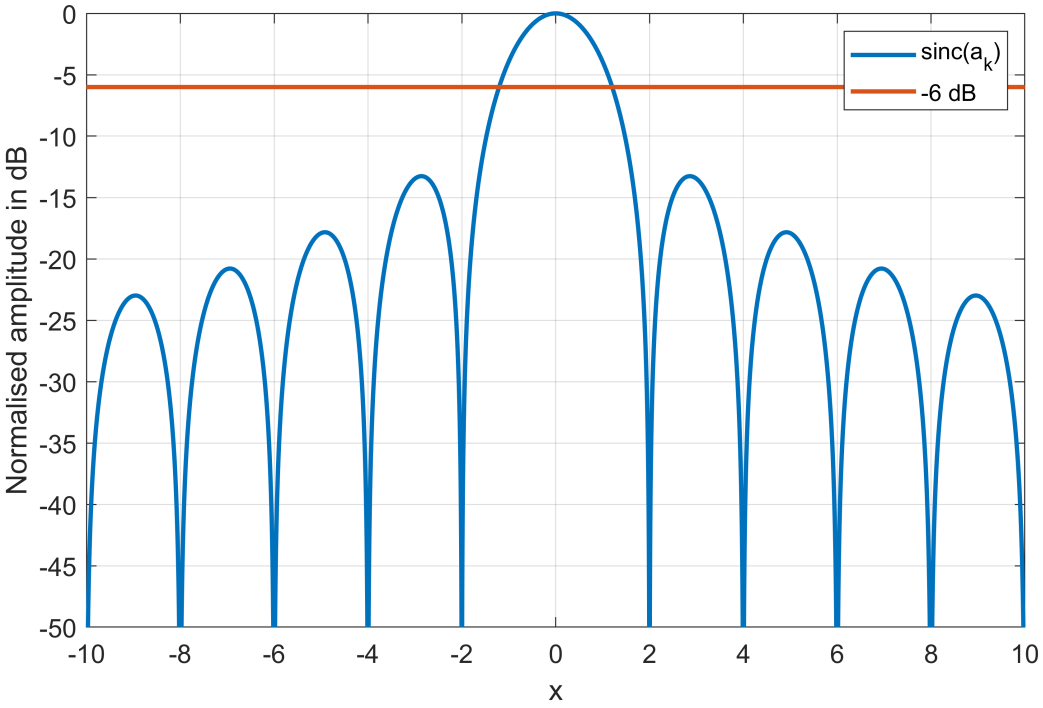

Figure 2.12: sinc(a_k) as a function of x

Dimension	Value (FEA)	Value (Theory)	Difference mm (%)
Axial Length	1.6 mm	1.44 mm	+ 0.16 mm (+10%)
Radial Length	11.5 mm	9.65 mm	+ 1.85 mm (+16%)

Table 2.3: FEA calculated focal spot size of a Fresnel lens compared to spot size from theory of a circularly focussed transducer

Due to the theoretical values being generated from a perfect circularly focussed transducer, the FEA focal spot sizes of the Fresnel lens are larger as shown in Table 2.3. As the Fresnel lens relies on constructive interference to achieve gain at a focal zone, there are reduced efficiencies compared to those of a circular source. The literature on Fresnel lenses quotes this as diffraction efficiency [68, 61], which affects both the intensity and profile of the acoustic field. However, to be within $(13 \pm 3)\%$ of a conventional lens transducer is promising and a justifiable compromise to achieve miniaturisation.

2.2.5 Convergence Study

In an FEA model, it is necessary to demonstrate model accuracy through a mesh convergence study. For the model of the FUS transducer and acoustic field in water, the required mesh density depends on the wavelength in water, which has a speed of sound of 1500 m/s, similar to that of the Fresnel lens material. From the OnScale documentation, a default value is around 15 elements per wavelength [69]. However, the size of the features of the Fresnel lens is on the order of 100 µm, which requires a much smaller element size. As seen in Fig. 2.13, even a density of 30 elements per wavelength is unable to reproduce the features of the Fresnel lens accurately. Fig. 2.14 plots the peak acoustic pressure at the focus for different mesh densities in terms of elements per wavelength. The asymptotic value of pressure allows for the selection of a mesh density trade-off between accuracy and simulation time.

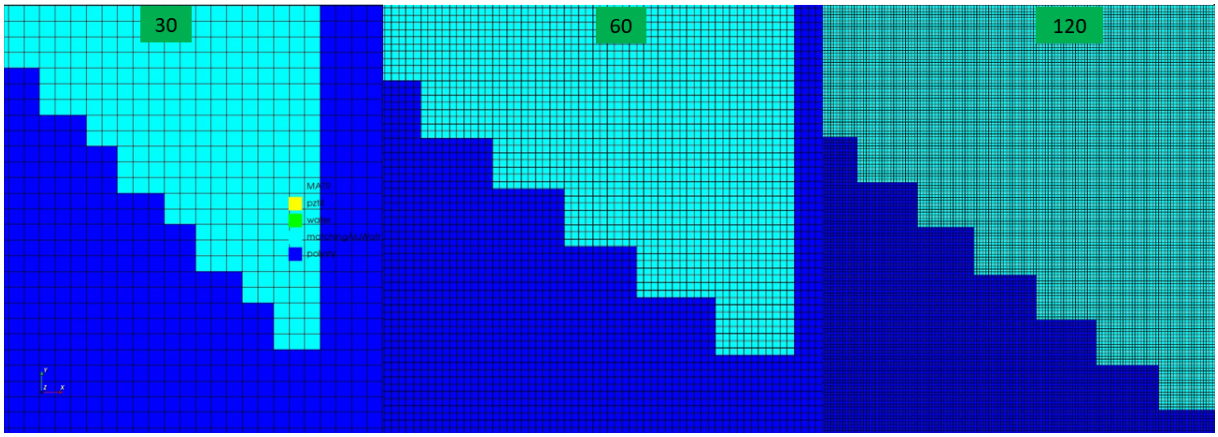

Figure 2.13: Mesh densities of 30, 60 and 120 elements per wavelength related to small feature sizes of the Fresnel lens.

The most effective trade-off in this case is a mesh density of 70 elements per wavelength. At this point, the peak pressure is within 1% of the maximum calculated value; however, the simulation time is 30% that of 100 elements per wavelength.

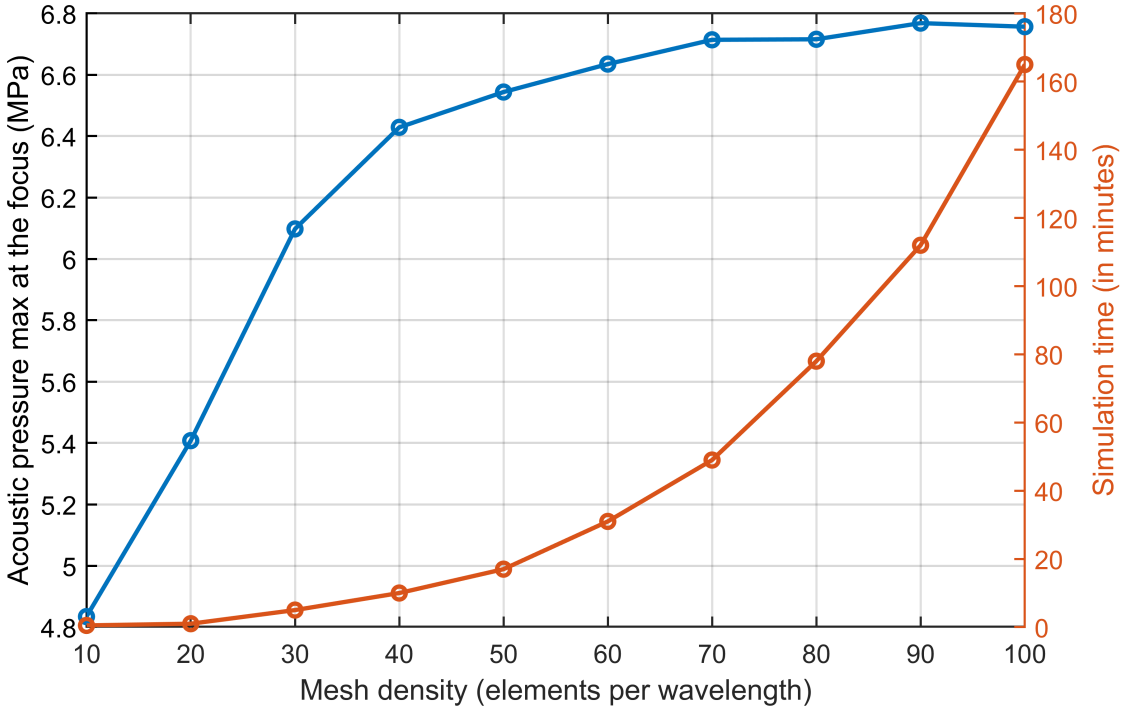

Figure 2.14: The peak acoustic pressure at the focal zone for increasing mesh density.

2.2.6 Substrate Thickness

A substrate is added to the bottom of the Fresnel lens to allow the pressure waves to propagate through a homogeneous material before exiting the lens. As discussed previously, this backing is of paramount importance in the manufacturing process to keep the transducer parts aligned (see Fig. 2.15). The two factors dictating the substrate height are attenuation of the material and the space required by the top electrode wiring. The wire, adhered to the electrode with conductive epoxy, needs a minimum of 1 mm clearance from the lens. To ensure the lens stays as flat as possible to the rest of the electrode, a notch is included, which the wire will use. Attenuation in the lens material results in losses which are proportional to the thickness of the material.

A study was carried out to calculate the acoustic pressure at the focal point as the thickness of the substrate increased. The thickness was varied from 0.1 to 3 mm in increments of 0.1 mm. As seen in Fig. 2.16, the general trend is a decrease in the acoustic pressure at the focus due attenuation in the substrate material. However, the effect of interference of the pressure waves in the lens material can be seen with a maximum of 1.7 mm thickness. The lens material has a sound speed of 2483 m/s, therefore the wavelength in the material

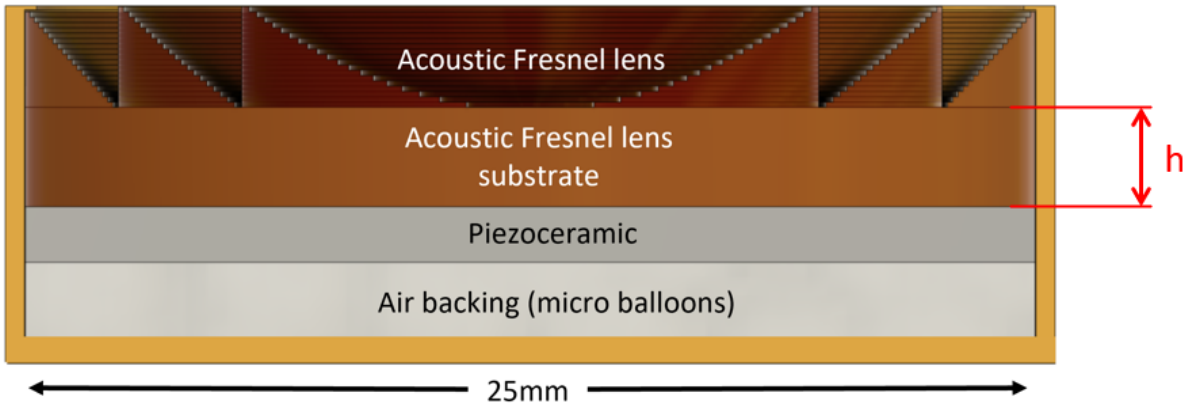

Figure 2.15: Schematic of transducer internal structure with Fresnel lens substrate height denoted as 'h'

at 1.5 MHz is 1.65 mm. Therefore, the presence of standing waves in the substrate gives rise to this local maximum. A substrate height of 1.6 mm was chosen to maximise acoustic pressure at a substrate height of more than 1 mm, as less than this would result in manufacturing problems when routing the wire from the top electrode of the piezoelectric disc.

2.2.7 Phase Number

The phase number, N, of the Fresnel lens is the number of steps used to approximate the shape of a full spherical lens. As N increases, the feature size decreases on the Fresnel lens and tends towards a more accurate representation of the profile needed to focus the waves to the selected point in space. The diffraction efficiency of a Fresnel lens phase number is given in Eq. 2.13 [61];

$$\eta = \left[\frac{\sin(n/N)}{(n/N)}\right]^2 \tag{2.13}$$

where n is the photolithography masking steps required for 2^n phase levels (N). The context for this equation in the literature is the photolithography process, where masks were needed in the manufacturing process to allow structures to be created. As can be seen in Fig. 2.17, a phase number of 8 (achieved by 3 masking steps) results in a 95%

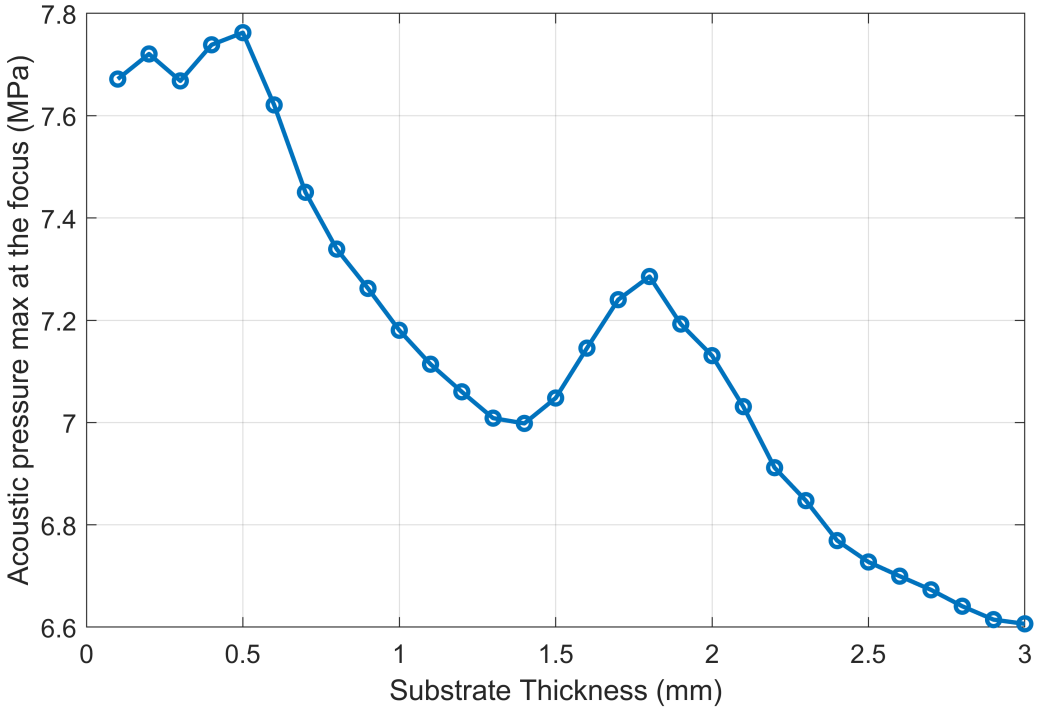

Figure 2.16: Calculated acoustic pressure at the focal zone as the substrate thickness is increased

efficiency. A phase number of 20 achieves a 98.5% diffraction efficiency and results in a minimum feature size of $\sim$ 100 µm that is easily achievable within the resolution of the mSLA printers (Ch. 1.4). Fig. 2.17 shows a decrease in acoustic pressure above a phase number of 10-12, This is likely due to the increasing height of the lens resulting in a reflection of acoustic waves away from the focus. The drop in acoustic pressure at the focus is only 4%; however, future optimisation can be explored in the phase number region of 10-12.

2.2.8 Acoustic Matching Layer

To guarantee the effectiveness of a transducer, an acoustic matching layer is incorporated. When a pressure wave reaches a boundary between two different materials, the transmission and reflection interaction is related to the acoustic impedance of the materials. Acoustic impedance is defined in Eq. 2.14 [70];

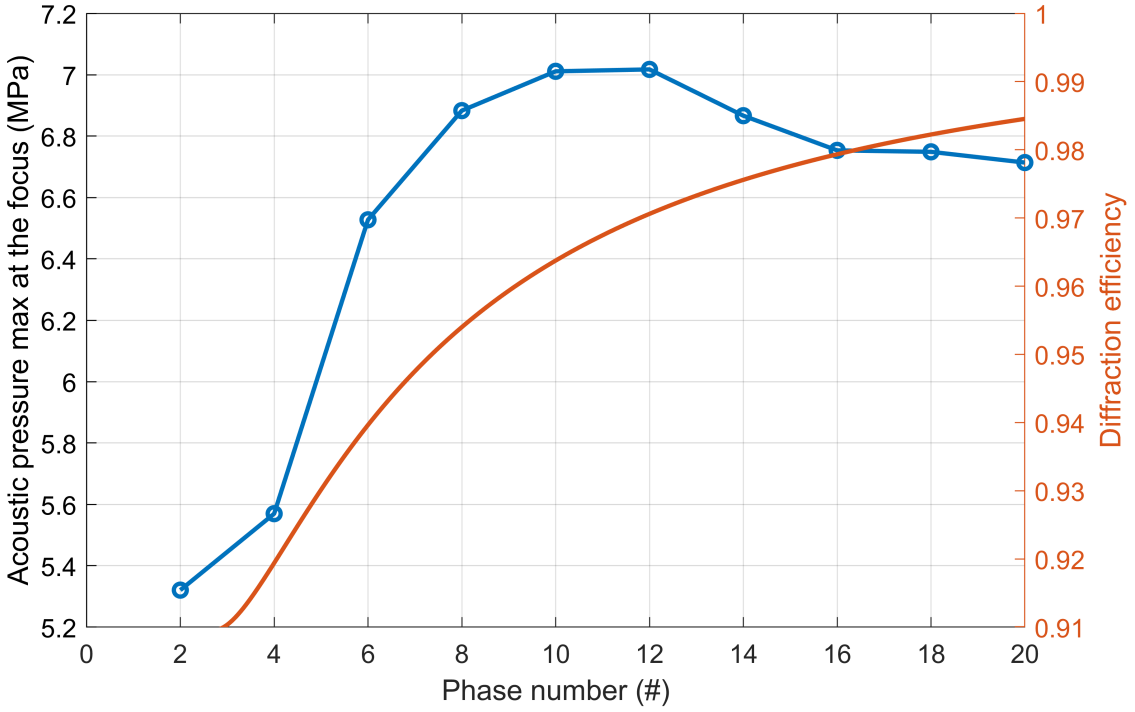

Figure 2.17: Acoustic pressure maximum at the focus with varying phase number, plotted with theoretical diffraction efficiency

$$Z = \rho c \tag{2.14}$$

where ρ is the density and c is the sound speed of the material. As a wave propagates from medium 1 to medium 2 the transmitted and reflected components are calculated in Eq. 2.15 and Eq. 2.16, respectively.

$$T = \frac{A_T}{A_I} = 1 + \frac{Z_2 - Z_1}{Z_2 + Z_1} \tag{2.15}$$

$$R = \frac{A_R}{A_I} = \frac{Z_2 - Z_1}{Z_2 + Z_1} \tag{2.16}$$

where Z is the acoustic impedance in materials 1 and 2, A is the amplitude of the pressure wave, while the subscripts T, R and I denote the transmitted, reflected and incident wave amplitudes, respectively. For the most efficient power transfer between materials with an acoustic impedance mismatch, the optimum impedance of the matching layer to be placed between the materials can be determined with Eq. 2.17

$$Z_M = \sqrt{Z_1 Z_2} \tag{2.17}$$

where Z_M denotes the geometric mean of the acoustic impedance of materials 1 and 2.

For effective matching with minimal layer thickness, a quarter wavelength thickness is used. However, the centre of the bowl in a conventional bulk lens is a difficult space within which to manufacture this matching layer. A solution is to fill the space with matching layer material; however, this is costly and inefficient. This creates another interface in the beam path that causes reflections. A Fresnel lens greatly reduces this height at the front of the transducer, where a matching layer can be incorporated into the space between the lens step features, providing a flat interface for coupling the transducer to the target medium. However, this creates another interface for the pressure wave, which can be represented by Snell's law in Eq. 2.18;

$$\frac{n_2}{n_1} = \frac{\sin(\theta_1)}{\sin(\theta_2)} = \frac{v_1}{v_2} \tag{2.18}$$

where n is the refractive index in materials 1 and 2, θ is the angle (from the normal of the interface) of the pressure wave and v is the velocity of the wave. If there is a difference between the two velocities of the matching layer and propagation medium, there will be a change in θ, which in the case of the Fresnel lens affects the focussing efficiency (the ratio of acoustic energy refracted to the focus and the total energy) and results in a lower intensity at the focal zone. A study was carried out to characterise the influence of the

matching layer on the maximum pressure and location of the focal zone. For this model, the piezoceramic material was selected to be generic Navy Type I, PZT4. The Fresnel lens was made from polystyrene, an acoustic lens material common in the literature for its low attenuation [23].

The speed of sound in the matching layer material was varied around the value for water, the propagation medium. The acoustic impedance of the matching layer was then kept constant by decreasing the density of the material, as seen in Table 2.4. The acoustic impedance of water, $Z = 1.5$ MRayls, for polystyrene, $Z = 2.52$ MRayls, and therefore from Eq. 2.17, the acoustic impedance of the matching layer was calculated as 1.944 MRayls.

Model No.	Bulk wave speed (m/s)	Density (kg/m^3)	Acoustic Impedance (MRayls)
1	1000	1944.2	1.944
2	1050	1851.6	1.944
3	1100	1767.5	1.944
4	1150	1690.6	1.944
5	1200	1620.2	1.944
6	1250	1555.4	1.944
7	1300	1495.6	1.944
8	1350	1440.2	1.944
9	1400	1388.7	1.944
10	1450	1340.8	1.944
11	1500	1296.1	1.944
12	1550	1254.3	1.944
13	1600	1215.1	1.944
14	1650	1178.3	1.944
15	1700	1143.7	1.944
16	1750	1111.0	1.944
17	1800	1080.1	1.944
18	1850	1050.9	1.944
19	1900	1023.3	1.944
20	1950	997.0	1.944
21	2000	972.1	1.944

Table 2.4: The acoustic matching layer parameters used for FEA studies.

The peak pressure of the focal zone and its position are shown in Fig. 2.18 (a). In addition to the focal zone, the Fresnel lens generates a subfocus due to reflections in the lens, an inherent property of utilising a lens to focus waves. Therefore, the maximum pressure and the location of the subfocus are also shown in Fig. 2.18 (b). It can be seen that as the speed of sound increases, the location of the focus moves away from the transducer. This is due to Snell's law where the pressure waves are refracting at the interface between the

matching layer and water, and also the Fresnel lens governing equations, which assume that the pressure wave enters the propagation media with no matching layer. When the sound speed in the matching layer matches that of water, the gradient of the peak pressure with respect to sound speed in Fig. 2.18 (a) decreases, indicating a larger region in sound speed that is a suitable value for a matching layer. The pressure peak at the focus is at a maximum where the sound speeds match. The sound speed is as important as the acoustic impedance when selecting a matching layer material. An interesting observation in Fig. 2.18 (b) is the dependence of the subfocus on the sound speed of the matching layer. As the sound speed increases above 1150 m/s, the pressure at this subfocal point decreases to a third of the pressure in the primary focal zone. The first four points in Fig. 2.18 (b) show that the second highest magnitude focal point is farther from the transducer than the main focus and with a small pressure. The subfocus is generated in the near field only when the sound speed of the matching layer is $\geq$ 1200 m/s. The position of the subfocus remains largely constant at around 20 mm in front of the lens. However, it is important to note that the subfocus is orders of magnitude smaller in size than the primary focus.

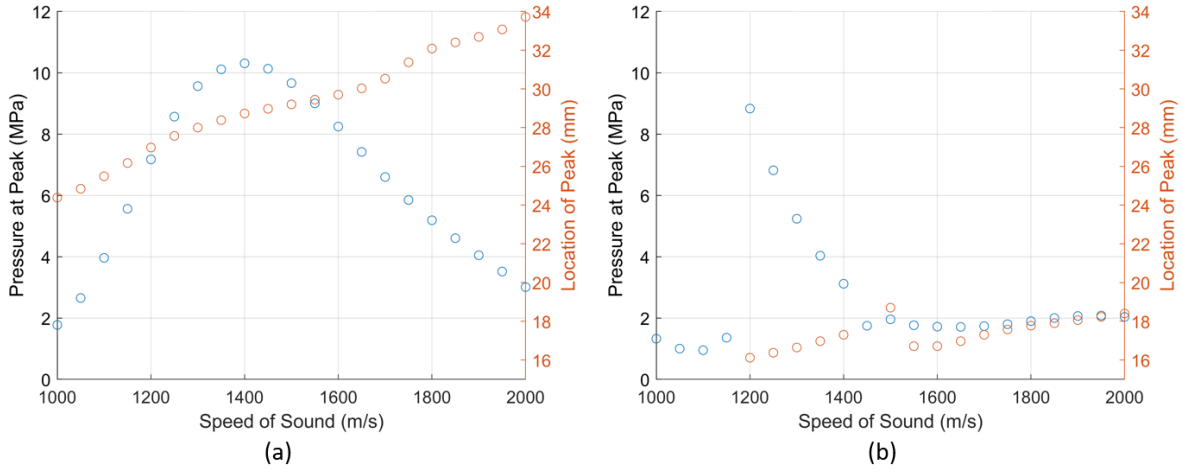

Figure 2.18: Peak acoustic pressure and location of the focus for impedance matching layer materials with different speed of sound. (a) primary focus and (b) subfocus

If the sound speed of the acoustic matching layer is 1450 $\pm$ 50 m/s the lens can effectively generate the acoustic field for constructive interference at the focal zone.

A second study was conducted to investigate the effect of changing the density of the matching layer. The sound speed was constant at 1500 m/s and density increased through the values given in Table 2.4. In this case, the acoustic impedance changes, affecting the energy transfer between the matching layer and the propagation medium. However, as seen

in Fig. 2.19 (a), changes in both location and pressure at the peak are small compared to the effect of sound speed. In conclusion, when selecting a material for the matching layer in a Fresnel lens device, the sound speed is of primary importance. If the sound speed is chosen as 1450 ± 50 m/s, the density can be in the region of 1340 ± 368 kg/m^3.

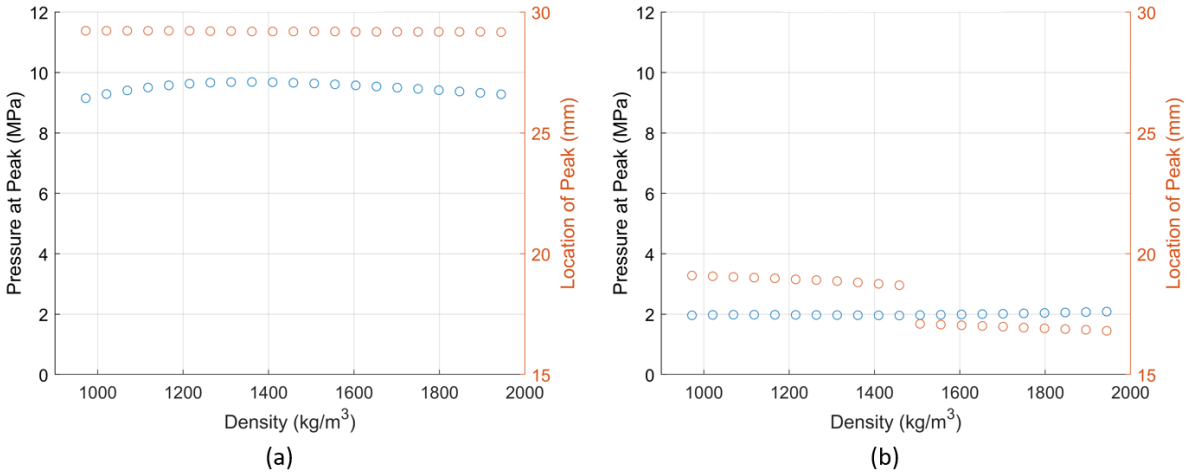

Figure 2.19: Peak acoustic pressure and location of the focus for impedance matching layer materials with different density. (a) primary focus and (b) subfocus

To show the effectiveness of this matching layer on the position of the focus and peak pressure, an identical lens without a matching layer was modelled. The pressure at the focus was calculated to be 9.3 MPa, with a focal position of 28.5 mm. Therefore, the maximum pressure was 4.3% higher with the best matching layer. Eq. 2.15 shows that there is 75% transmitted pressure without a matching layer, therefore the improvement of the matching layer was marginal. The importance of including a matching layer is more prominent when the difference between the acoustic impedance of the lens and the propagating medium is high.

2.3 Comparison of four different piezoceramic disc materials

Four different piezoceramic materials were considered for the FUS transducer. All four materials were supplied by CTS Ferroperm (Kvistgard, Denmark), with material properties supplied [71].

2.3.1 Discs of material

To determine the correct centre frequency for the thickness mode of a disc of each material, a model was used as discussed previously. Time series data for both the voltage and charge on the electrodes were calculated, and hence the impedance was plotted and a value of the thickness constant (N_t) was calculated and adjusted using Eq. 2.5. Table 2.5 shows the calculated thickness mode resonance frequency obtained from a model of a disc.

Material	Initial thickness (mm)	Initial frequency (MHz)	Thickness Constant (Hz · m)	Corrected Thickness (mm)	Change to CTS data sheet N_t
PZ28	1.4	1.4203	1988.42	1.3256	-0.4%
PZ29	1.4	1.3874	1942.36	1.295	-2 %
PZ54	1.4	1.4024	1963.36	1.3089	-2 %
PZ52	1.4	1.3364	1870.96	1.2473	-5 %
PZ36HD	1.4	1.0582	1481.48	0.9876	-1.5%
PZ36LD	1.4	0.8911	1247.44	0.8316	-3.2%

Table 2.5: Evaluation of N_t for the FUS transducer models for four different piezoceramic disc materials

An initial disc thickness of 1.4 mm was used and the resonance frequency of the thickness mode was calculated and used to calculate a more accurate N_t. Using the new N_t, a thickness was calculated, which results in a resonance frequency of 1.5 MHz. The value of N_t did not differ by more than 5% of the value quoted by the manufacturer [71].

2.3.2 Piezoceramic material performance in devices

An FEA model of the transducer was created using a polystyrene lens with a substrate height of 2.5 mm and a phase number of 20. The active piezoceramic material in the model was changed using those in Table 2.5. The maximum pressure was calculated for each transducer along with the -6 dB beam shape of the focal zone. The ceramics are grouped into material families, piezoelectrically Hard, Soft, HIFU type and porous, with hard and soft being terms discussed previously to describe low loss/high T_c and vice versa.

A HIFU type ceramic is a material whose properties lie between hard and soft, with the aim of combining their strengths for use in HIFU such as high d_{33} and T_c while maintaining lower losses. Porous type ceramics retain a porous structure during the sintering process and give the piezoceramic a lower density.

Material family	Material	Axial Length (mm)	Radial Length (mm)	Pressure max (MPa)
Navy Type I	PZT4	1.53	10.71	10.20
Hard	PZ28	1.61	10.85	7.45
Soft	PZ29	1.40	10.61	16.40
HIFU	PZ54	1.45	10.36	16.40
HIFU	PZ52	1.52	10.24	9.42
Porous	PZ36HD	1.48	10.35	11.50
Porous	PZ36LD	1.50	10.69	8.20

Table 2.6: The focal zone characteristics from an FEA model of FUS transducers with different active materials.

Table 2.6 shows the dimensions of the focal zone along with the maximum pressure achieved. Similar dimensions are shown as this is a representation of the lens rather than the piezoelectric material. The axial and radial length did not vary much because the lens was identical in all models. However, the small differences between the transducers are due to the interactions of reflected waves within the lens because of the impedance mismatch between the lens and water. This results from the differences in the piezoelectric and mechanical properties of the six piezoelectric discs.

The peak pressure at the focus can be compared to a baseline of generic PZT4 (from the OnScale material database). The results show that PZ28 is a poor choice due to the hard piezoceramic properties that result in the lowest peak pressure for the same driving conditions. The HIFU type materials look promising for this transducer, with PZ54 delivering the highest pressure, due to its higher d_{33} and k_t than the harder piezoceramics. The porous ceramic high density variation (HD) which has piezoelectric coefficients lower than those of the HIFU type, performs well in spite of this. This indicates a high dependence on the efficient transfer of energy at acoustic impedance boundaries in a HIFU lens design transducer. As the porous ceramic has the lowest overall density, the coupling into the lens is higher. However, the low-density (LD) version does not achieve high acoustic pressure at the focus. In fact, the piezoelectric properties of this material are so low that the benefits of its low density are not realised and the peak pressure is lower. The transducer with the soft piezoceramic material achieved the joint highest peak pressure due to its

high piezoelectric properties. It is important to note that the model does not incorporate the nonlinear phenomenon of piezoelectric softening, which can exhibit at high excitation driving conditions. This, coupled with the high losses associated with soft piezoelectric material properties, can cause transducer overheating under prolonged driving conditions.

For the miniature FUS transducer, materials PZ29 and PZ54 were of interest; PZ29 to determine whether the soft ceramic could withstand high driving conditions and PZ54 as it is likely to perform well, as modelled. Porous ceramic was of interest; however, the material useed in this study was PZ37HD, which has marginally higher piezoelectric coefficients than PZ36HD. A lead-free ceramic, PZ12, was also chosen due to the increasing interest from the medical device industry in this material. to comply with regulations aiming to reduce the use of lead.

Chapter 3

Materials

Understanding and engineering the materials used in an ultrasonic transducer is crucial to its development. For the design of the FUS transducer, the three materials of interest are the lens, the piezoelectric material, and the backing layer. The primary focus is the materials that generate and focus the pressure waves, the piezoelectric disc and lens. This chapter will characterise materials and select those suitable for use in the miniaturised FUS transducer.

3.1 Passive Material Characterisation and Selection

To fit the design philosophy of the transducer in this study, the lens material must be suitable for additive manufacturing. As discussed, 3D printed resin has the general material properties required for transmitting ultrasound. Other techniques such as FDM printing do not achieve the resolution that mSLA printers do, and the nature of FDM printing does not lend itself to fully dense infill prints of 100%. Ensuring a homogeneous material is crucial, as any air pockets will reflect the pressure wave due to the large impedance mismatch. Metals are good lens materials because of their low losses and high sound speeds. However, the acoustic impedance mismatch between metal and water is large, although this can be managed with acoustic matching layers as discussed previously. Hence, the

Fresnel lens design that is being developed can be implemented with metal in the future. One reason why it is not considered here is the cost of a DMLS printer, which is orders of magnitude more expensive than its mSLA counterparts (around $ 250,000 compared to £250).

3.1.1 Photopolymer resins

The materials used in mSLA printers are as important as the printer itself. Different resins were characterised as acoustic lens materials. The resins chosen were from a variety of types, colours, and companies to sample the widest data set possible. Companies producing such resins do not supply mechanical or chemical properties due to commercial sensitivity, and therefore, it is difficult to estimate the properties of interest for ultrasound devices. The resins were obtained from five separate manufacturers, as seen in Table 3.1.

Manufacturer	Manufacturer Location	Colour	Resin type
Elegoo	Shenzhen, China	Grey	ABS-like
		Grey	Standard
		Clear Red	Standard
Any Cubic	Hong Kong	Grey	Standard
		Clear Green	Standard
Nova3D	Shenzhen, China	Clear Blue	Standard
3Dream Labs	Kent, UK	Amber	Low Odour
Liqcreate	Utrecht, NL	Grey	StrongX

Table 3.1: The commercial photopolymer resins acquired for acoustic characterisation

The first three companies in this table make standard cost-effective resins that are advertised for making miniature models the size of chess pieces with high detail. As such, there is no emphasis on mechanical properties. From these standard resins, ABS-like and standard were purchased because of the material properties of the former, as ABS is a popular material for toy model makers to use in FDM printers and are the most common and widespread resins. The only other choice was to select the translucent colours which may have a different chemical makeup compared to the standard types, which are opaque grey. The resin Lodour from 3DreamLabs aims to decrease the odour emitted by resins. The technology behind this was again commercially sensitive. An engineering polymer

was purchased from Liqcreate called StrongX. Resin data sheets are provided that include tensile and flexural strength and modulus along with hardness, T_g (glass transition temperature), and elongation at break. A full curing schedule is suggested, including a post-cure UV process at an elevated temperature of 60 °C for 120 minutes.

3.1.2 Characterisation methods

The material properties required to perform an acoustic model of a lens are the sound speed and attenuation. With both longitudinal and shear wave properties, OnScale can calculate an accurate representation of a pressure wave propagating through the material. To measure these parameters experimentally, the pulse-echo technique was used, the aim of which is to excite a pressure wave into a sample with a nondestructive test (NDT) transducer and record the waves returning after reflecting off the back surface of the sample. This is depicted in Fig. 3.1 using NDT probes (Olympus, Tokyo, Japan), a pulser receiver (JSR DPR300, New York, USA) and an oscilloscope (Agilent Technologies, California, USA). The parameters for each probe and JSR settings are shown in Appendix B.

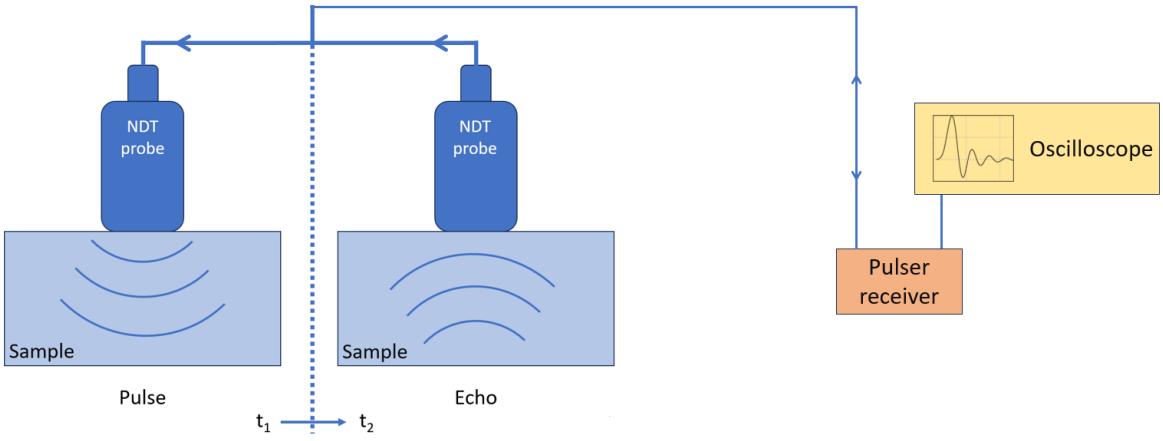

Figure 3.1: Experimental set up of the non-destructive testing for evaluation of acoustic material parameters

A high voltage pulser receiver produces the main pulse as seen in Fig. 3.2 (a). This is the high-voltage component of the device and this signal goes to an NDT piezoelectric probe. This impulse excites a broadband signal. Because the response of the NDT probe is being excited, the resulting pressure wave in the material will have a frequency content centred around the resonance frequency of the probe. Once this pressure wave enters the sample at time t_1, the electronics switches to amplifying the signal that returns to the probe. The

JSR allows the amplification of this return signal to be adjusted via a gain dial. At some time t_2 after the pulse has entered the sample, it reflects from the back of the sample and propagates back to the probe where the amplification occurs and the signal, including the main pulse and amplified return, is displayed on an oscilloscope for monitoring and capture.

Various parameters can be calculated from the resulting signal, such as the sound speed in Eqn. 3.1.

$$c = 2 \cdot t_h / \Delta t \tag{3.1}$$

where t_h is the thickness of the sample and time (Δt) is the flight time measured from the main pulse to the first return. This technique was then repeated for different samples and NDT probes. Once longitudinal sound speed and attenuation were captured in these waveforms, the same experiment was performed for shear waves using shear wave NDT probes.

Samples of different thicknesses were measured for each type of material. This is because measuring acoustic attenuation is not possible without a reference to discard the other possible losses. There are three ways in which the pressure wave gets perturbed when it encounters a sample.

1. Reflection off the first face of the sample
2. Attenuation of wave within the sample
3. Transmission of wave from the secondary face of the sample

Although it is possible to measure each loss and calculate attenuation in the material by subtracting the other losses, in this pulse echo test, where the samples are being 3D printed, a more robust experimental plan was used. By printing six discs of heights; 5, 7.5, 10 and 12.5 mm as seen in Fig. 3.3, it is possible to use the three 5 mm samples as a reference and for averaging. The peak of the echo measured in the 5 mm sample seen in

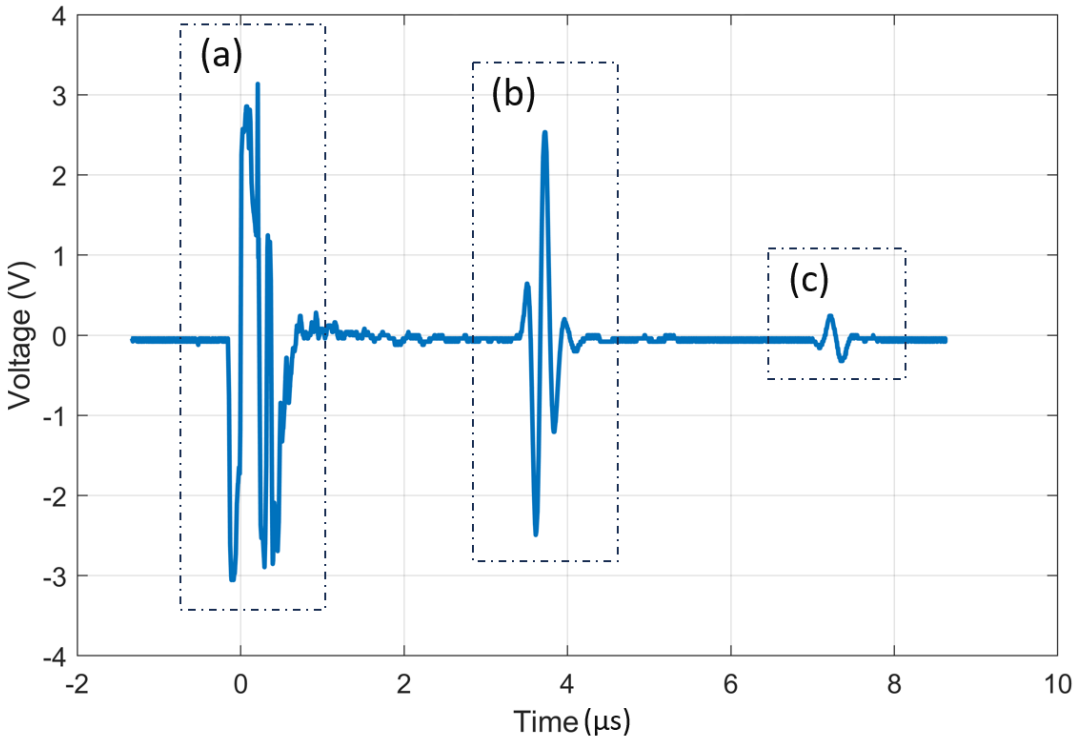

Figure 3.2: The pulse-echo signal of an NDT probe performing a pulse-echo test on a sample. This is enabled by the JSR pulser receiver, (a) is the main transmit/pulse portion of the signal, the JSR electronics amplify the return echo seen from (b) onward, (c) is a multiple of the first return

Fig. 3.2 (b) includes all three sources of loss. This peak compared to the peak found in the 7.5 mm sample includes reflection and transmission losses; hence the difference will be the attenuation in the material. The same can be measured with the 10 mm and 12.5 mm samples giving three estimates to average across.

The FEA model also requires the permittivity of the material, defined as its ability for an electric field to pass through it. Often, the relative permittivity is quoted, which is a ratio to the permittivity of free space / vacuum (ε_0) which is 8.85^{-12} F/m. To calculate the permittivity, the capacitance can be measured across two parallel conducting plates and used in Eqn. 3.2.

$$C = \frac{A\varepsilon_r\varepsilon_0}{th} \tag{3.2}$$

Figure 3.3: A CAD drawing of the six material discs for acoustic characterisation of photopolymer resin

where C is the capacitance, ε_r is the relative permittivity, A is the area of the electrodes and th the thickness of the sample between them. As permittivity is frequency dependent, it is measured at constant stress (ε^T) or constant strain (ε^S) at low or high frequency, respectively. OnScale can accept either value as long as the number and measurement condition are both input. Hence, ε^T was calculated from capacitance measured at low frequency, 1 kHz.

3.1.3 Experimental results

To ensure consistency of material properties in the printed samples, each batch of six was printed simultaneously and the same post-processing treatment was applied. Manufacturers recommend 1.5-3 minutes to fully cure the sample after printing; however, this was found to depend on ambient temperature. To ensure a complete cure, each sample was cured for 3 minutes and then rotated 180 degrees to fully cure the under side. The curing process was performed in a commercial wash-and-cure UV station (Elegoo), which features a rotating plate with UV LED's on one side. Overcuring of the samples presents as yellowing and brittleness after curing. The layer height used for the discs was the same as that used to print the lens (50 µm) to ensure the most accurate representation of the material in the lens. The cure time per layer was determined by calibration prints and

this value varied for each material type. The only exception to the 6 minute post-curing routine was StrongX which requires an elevated temperature of 60 °C and a cure of 120 minutes, which was achieved in a specialised curing station, commercially available by FormLabs (Massachusetts, USA).

Material	Speed of Sound (m/s)	Density (kg/m^3)	Acoustic Impedance (MRayls)
Polystyrene	2400	1050	2.52
Elegoo, ABS-like grey (a)	2336	1194	2.79
Elegoo, Standard grey (b)	2302	1200	2.76
Elegoo, Clear red (c)	2371	1214	2.88
AnyCubic, grey (g)	2305	1230	2.83
AnyCubic, Clear green (d)	2288	1224	2.80
Nova3D, blue (e)	2345	1202	2.82
Low odour (f)	2251	1180	2.65
StrongX (h)	2483	1201	2.98

Table 3.2: The sound speed, density and calculated acoustic impedance of 3D printed photo-polymer resins

Using the pulse-echo technique, the speed of sound results in table 3.2 were obtained. Digital calipers were used to measure the dimensions of the discs and the mass was measured via a set of precision scales (KERN, Balingen, Germany). The speed of sound was calculated using the time between the main pulse and the first reflection for every sample thickness. This was validated against the average time delay measured as the thickness of the samples increased. As can be seen from the results, the sound speed and density are similar to those of the control from the literature for polystyrene. The results in Table 3.2 show that all resins possess a sound speed that would allow focussing in a Fresnel lens. The uncertainty of the sound speeds was $< 1\%$ for all measurements.

An inherent nature of polymers is their compliance because long polymer chains are able to dislocate and move relative to one another. Photopolymers are no exception to this and, as such, can be highly attenuating for pressure waves. As the waves travel through loosely linked polymer chains, the motion causes heating. With higher cross-linking of the bare skeletal elements, the polymer chains become less compliant and the attenuation drops [72, 73]. This results in a harder and more brittle material, which can be seen as lower elongation at break and higher Young's modulus.

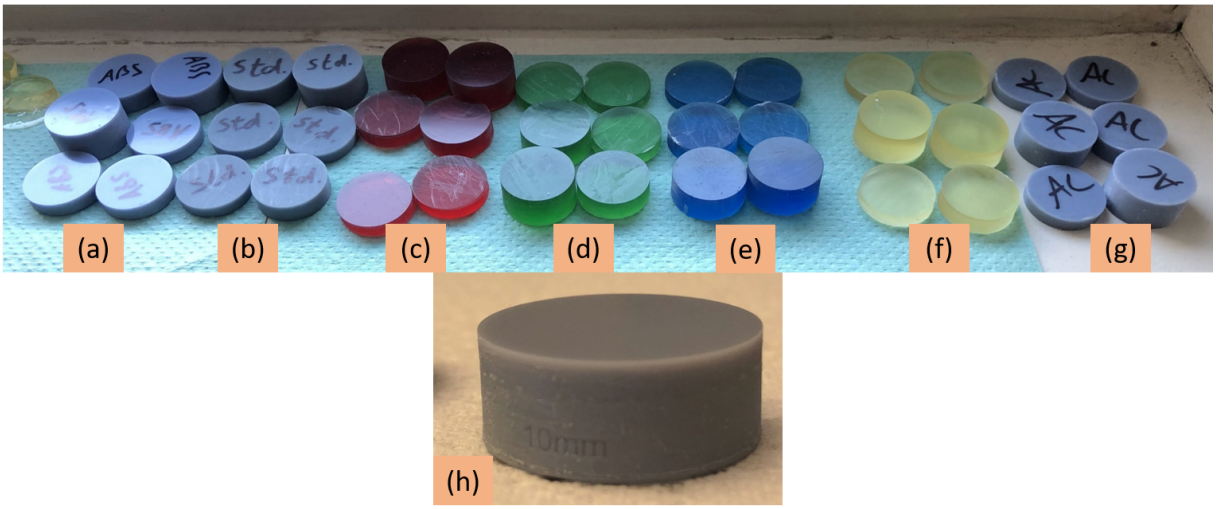

Figure 3.4: The six samples in each material from Table 3.2 and (h) a single up close disc of StrongX showing the resolution of the embossed thickness value. All discs with OD of 25 mm.

By experimentally characterising the samples using the same pulse-echo technique, the attenuation was found for materials with very different elongation at break. The signal decreasing in amplitude and increasing in time of flight is seen for one material in Fig. 3.5. The first return is identified in MATLAB and compared with each subsequent sample. As attenuation is frequency dependent, the test was performed using 0.5 MHz, 2.25 MHz and 5 MHz then linearly interpolated to 1 MHz, from which OnScale can use the dB/MHz/cm value. These attenuation estimates can be seen in Table 3.3 and the characterisation was performed with longitudinal (bulk) waves and shear waves. Shear wave attenuation was so great that in the case of the highest attenuating material, the first return was not a sufficient amplitude for a reading to be above the noise floor on the equipment used. As such, the only shear sound speed that was calculated from the measurements was StrongX at a value of 1078 m/s.

The frequency content of the reflections contains further information. Fig. 3.6 shows this frequency content in the first reflection of a 5 MHz centre frequency transducer. The frequency response of the four different thicknesses of the sample can be clearly distinguished, with the attenuation increasing with respect to the thickness. Another phenomenon that can be seen is the frequency dependent nature of attenuation. In thicker samples, the higher frequencies have higher damping, and so the echo has a lower centre frequency. At the lowest thickness of 5 mm the 5 MHz transducer echo has a centre frequency of 4 MHz and this decreases to a 2.5 MHz centre frequency for the 12.5 mm thick sample.

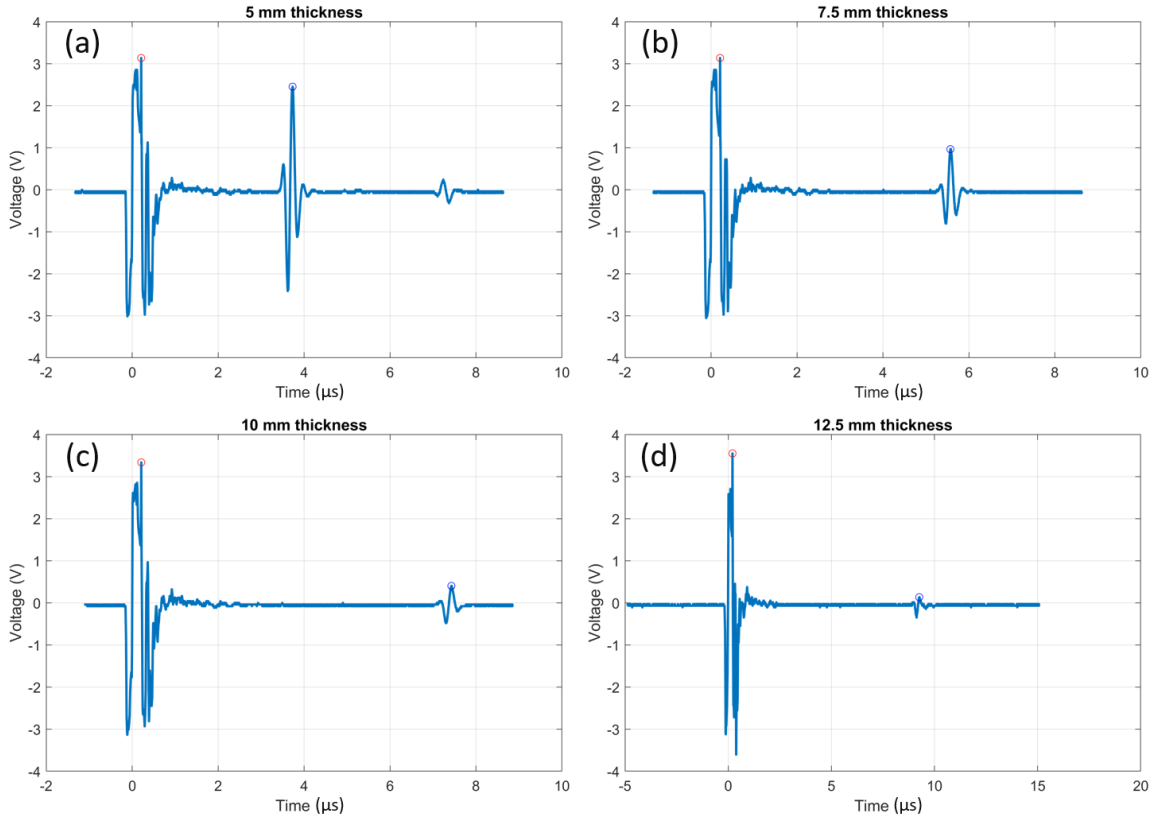

Figure 3.5: The signals obtained from measuring discs of (a) 5 mm, (b) 7.5 mm, (c) 10 mm and (d) 12.5 mm which include the main pulse and reflections

Attenuations were obtained from the FFT data by calculating the loss (in dB) for each sample thickness at many points in frequency. These values were averaged with the time series data to increase the accuracy of the attenuation data.

The amplitude values in the frequency domain were selected at exact frequencies that resulted in values of attenuation at each frequency. This was linearly extrapolated to obtain the attenuation in dB/MHz/cm and averaged. Due to the movement of the peak to lower in frequency (Fig. 3.6), the values in this test vary from 0.2 - 3.4 dB/MHz/cm. However, by averaging multiple samples and centre frequencies of the NDT probes, a value of 3.4 dB/MHz/cm was determined, see Table 3.3.

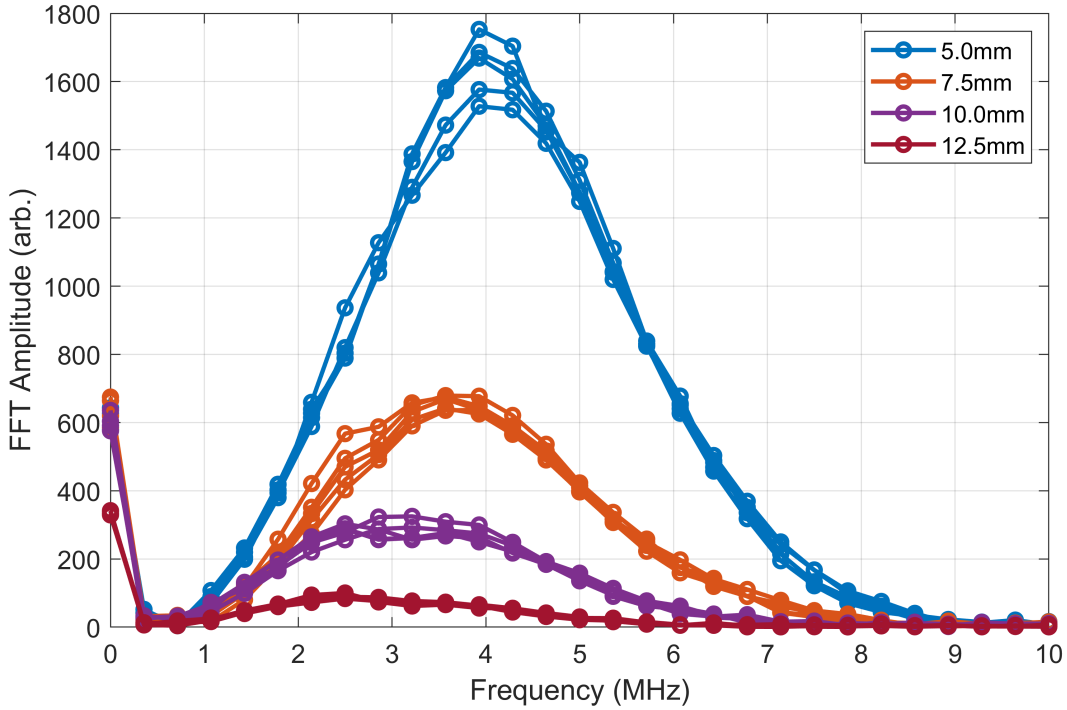

Figure 3.6: The frequency content of StrongX samples in the echo of a pulse-echo test using a 5MHz centre frequency NDT probe

Material	Acoustic Impedance (MRayls)	Bulk attenuation (dB/MHz/cm)	Shear attenuation (dB/MHz/cm)
Polystyrene	2.52	0.2	N/M
Elegoo, ABS-like grey	2.79	12	N/M
Low odour	2.65	8.8	N/M
StrongX	2.98	3.4	11.7

Table 3.3: Experimentally obtained attenuation measurements for photopolymer resins

To determine relative permittivity, the capacitance was measured using the method outlined previously (Eqn. 3.2). Temporary electrodes were applied, which were made from a silver paint (G3691, Agar Scientific, UK), to the top and bottom surfaces of the discs. Using an impedance analyser (E 4990A, Keysight, California, USA) the capacitance was measured at 1 kHz. These values were averaged for each type of material and using equation 3.2 the relative permittivity was calculated, shown in Table 3.4. The dimensions of each sample were measured with digital calipers and averaged.

Material	Relative permittivity (ε_r)
Polystyrene	3.1
Elegoo, ABS-like grey	4.40
Elegoo, Standard grey	4.59
Elegoo, Clear red	4.30
AnyCubic, grey	4.52
AnyCubic, Clear green	4.45
Nova3D, blue	4.28
Low odour	5.11
StrongX	4.61

Table 3.4: The relative permittivity of the photopolymer resins

3.2 Piezoelectric Material Characterisation

From the results of the virtual prototype studies reported in Chapter 2.3 four piezoelectric materials were used (CTS Ferroperm) to explore their material properties and integration into the FUS transducer design. These four materials were;

- PZ29 - A 'soft' piezoceramic
- PZ54 - A HIFU type piezoceramic
- PZ37HD - A porous piezoceramic
- PZ12 - A lead-free piezoceramic

The first two materials were selected on the basis of the results of Chapter 2.3. Both materials performed well in the FEA model. PZ37HD was selected because its sister material, PZ36HD, achieved a high peak pressure in the focal zone. A complete property data matrix was not available for PZ37HD and was therefore not included in the virtual prototype comparisons. However, from the material properties that were available, PZ37HD had higher k_t and d_{33} compared to PZ36HD. Theoretically, these increases relate to higher mechanical displacement for the same electric energy and a higher coupling from the electrical to mechanical energy (Ch 1.3.2). Therefore, PZ37HD was chosen for the development of a prototype. Lastly, a lead-free material was selected due to the EU regulations on hazardous material. The geometry of the piezoelectric sample was consistent for all types of material. This was a simple disc with an outer diameter of 25 mm and a thickness of 2.5 mm.

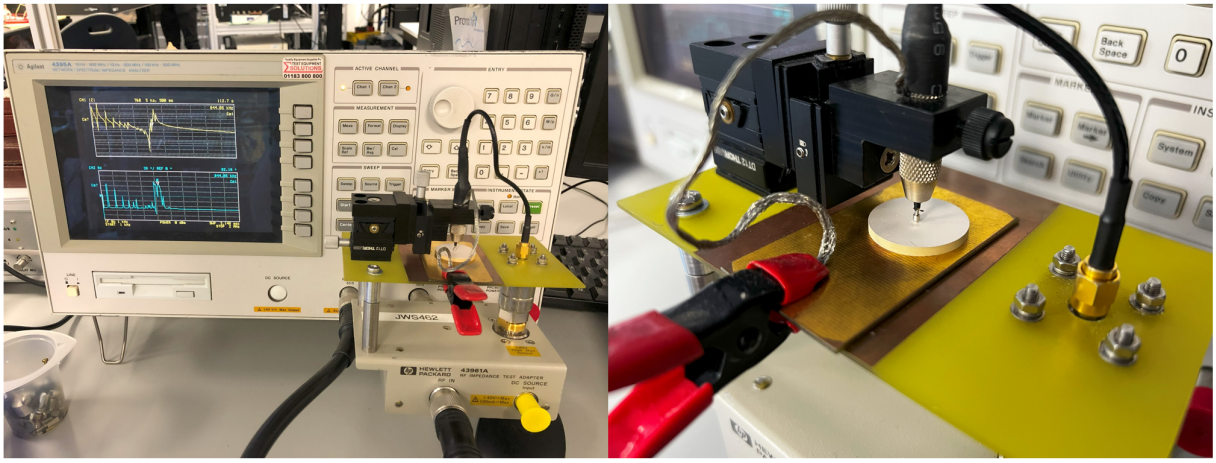

Figure 3.7: (a) Impedance analyser showing (b) a bespoke fixture.

Characterisation of the active materials enabled a database to be assembled from which ageing of the material properties could be investigated. Also, variability within each batch and comparison of the material properties data with those provided by the manufacturer could be explored. The piezoelectric discs were characterised using a 3D laser Doppler vibrometer (LDV) to determine the vibration modes, and scanning electron microscopy (SEM) and X-ray diffractometery (XRD) were used to identify the ceramic and chemical composition, respectively.

3.2.1 Low power impedance spectroscopy

As discussed in Chapter 1.3.2, impedance spectroscopy is a method to characterise the electrical impedance of a piezoelectric material at low excitation voltage. By sweeping the power source over a range of frequencies and exciting the connected sample, an impedance-frequency response can be measured. The impedance analyser used to characterise the materials (Agilent 4395A, CA, USA) has an impedance uncertainty of $\pm 3\%$ [74]. There is a need to minimise the clamping force due to the fixture that is used to hold the piezoelectric disc for impedance analysis. Hence, the connectors at the bottom and top electrodes are a conductive plate and a spring-loaded gold pin, Fig. 3.7 (b). The pin ensures that there is minimal force applied to the sample. This fixture is based on commercially available fixtures for small sample handling.

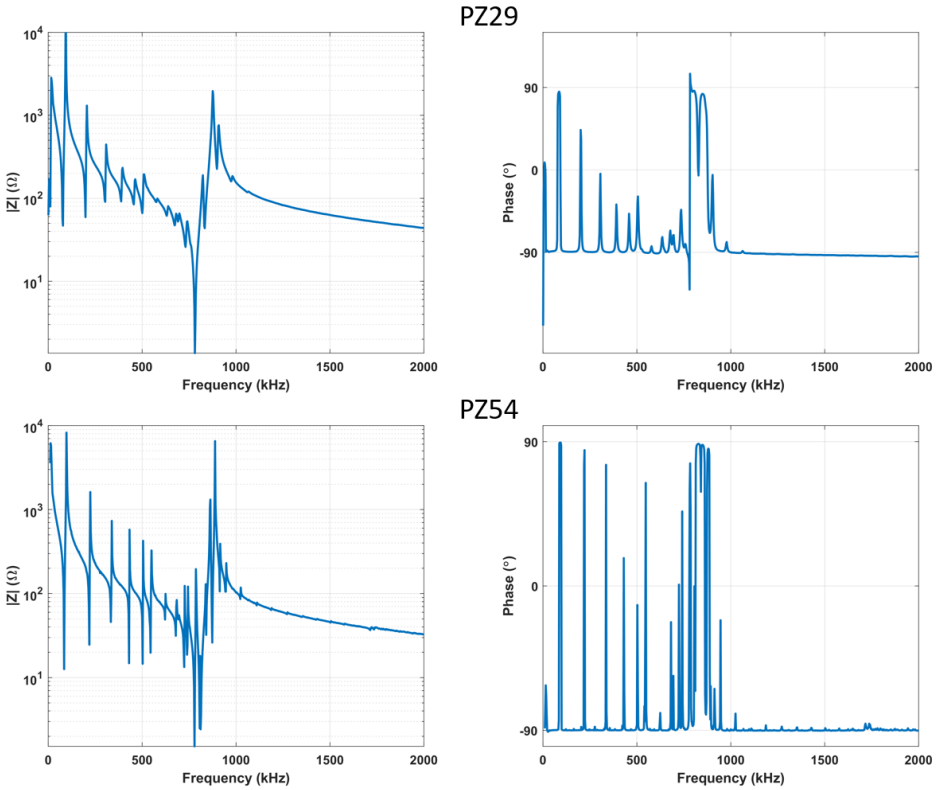

Figure 3.8: The impedance spectra magnitude and phase of the PZ29 and PZ54 discs

The electrical impedance of the PZ29 and PZ54 discs up to 2 MHz is shown in Fig. 3.8. Radial modes start at 50 kHz, with harmonics exhibiting, at decreasing amplitude up to 500 kHz. At 800 kHz the thickness mode is measured. A large amount of energy is present in this mode, and hence radial harmonics are excited between the resonance and anti-resonance frequencies of the thickness mode. The PZ29 measurement is a standard response for a piezoelectric disc. The PZ54 impedance exhibits higher modal density, potentially leading to difficulty in exciting a pure thickness mode. The parasitic radial modes in the vicinity of the thickness resonance frequency can take the energy away from the thickness mode which will effect the performance of the transducer.

The impedance-frequency spectra of PZ37 and PZ12 discs are shown in Fig. 3.9. The porous material, PZ37, has a much lower value of N_t, hence the thickness mode is at 600 kHz for a 2.5 mm thick disc. The mode just below 2 MHz is the second harmonic of the thickness mode. Again, parasitic modes are seen at the thickness resonance. Measurement of the PZ12 disc, Fig. 3.9, shows increased decoupling of the radial and thickness modes,

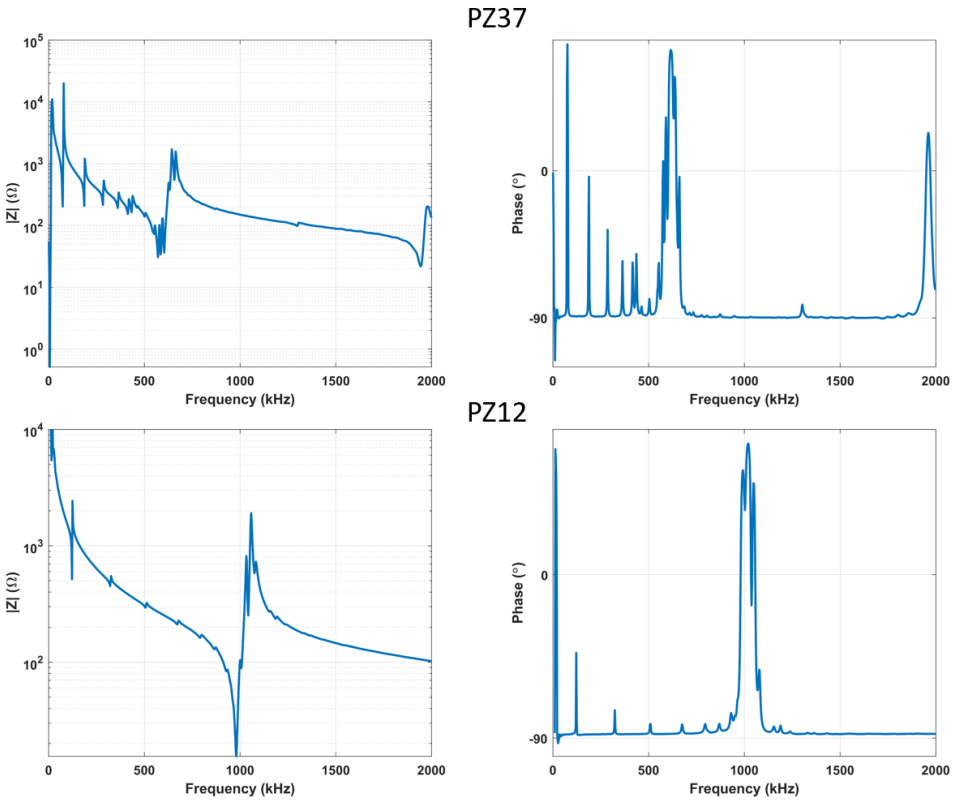

Figure 3.9: The impedance spectra magnitude and phase of the PZ12 and PZ37 discs

which is characteristic of NBT-BT type material. The first radial mode is at 150 kHz; however, the attenuation in the radial harmonics is high compared to the other materials tested. Therefore, at the thickness mode there is much less energy being used to excite unwanted radial harmonics.

Figure 3.10 shows a view of the thickness mode of the discs of each material, plotting every sample to show the variance in each batch. With the exception of one sample of the PZ29 batch (seen as an outlier in purple), each batch is consistent. The variation within the batch is highest for the PZ37 samples and there is strong mode coupling observed at the electrical resonance of the thickness mode, between 575-590 kHz.

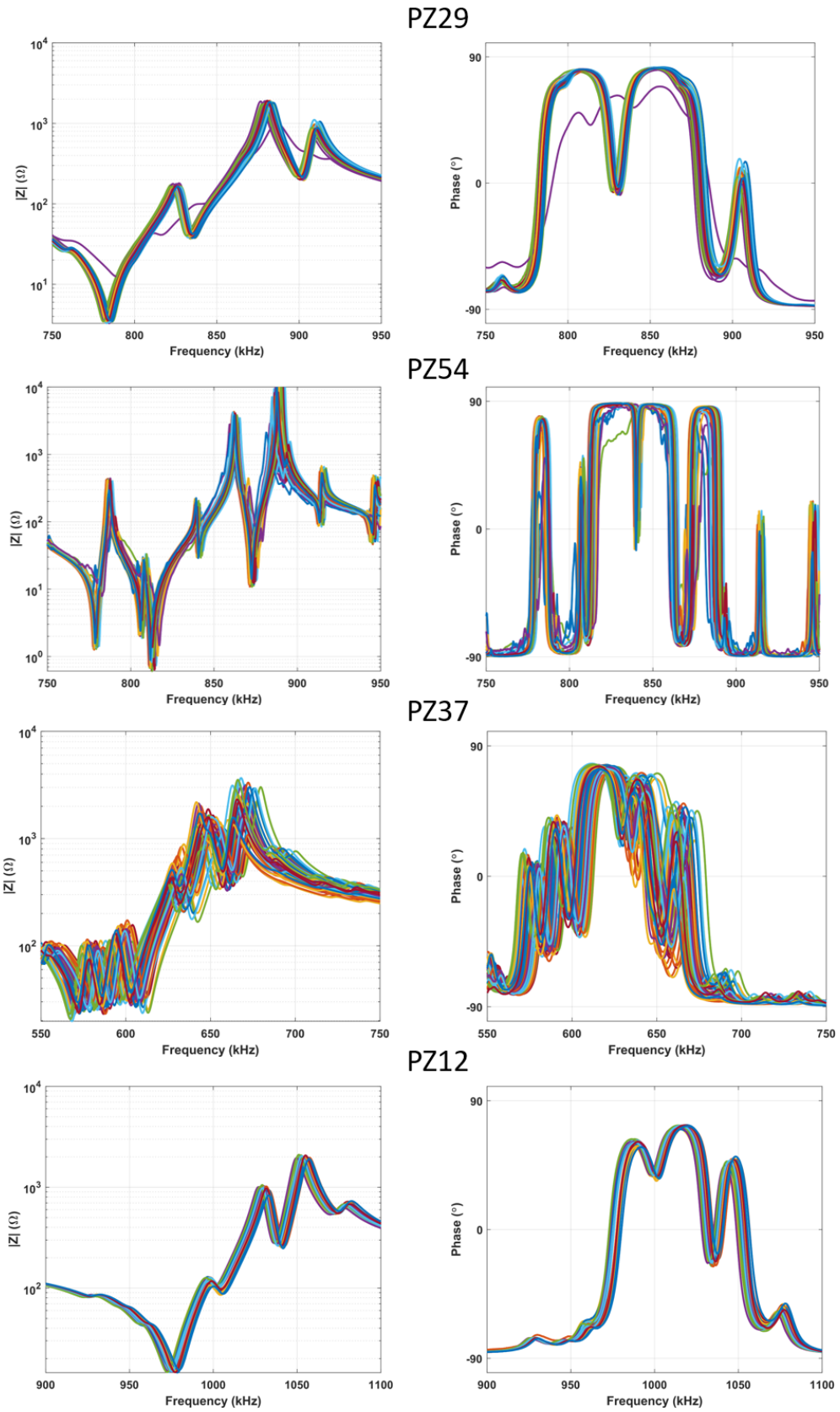

Figure 3.10: Impedance magnitude and phase spectra measured for all samples in each batch of discs, in each impedance magnitude spectrum the thickness mode exhibits at the lowest impedance

3.2.2 Resonance characteristics of the discs

Resonance characteristics and disc batch variance can be derived from the low power impedance spectra. The resonance frequency (f_r), antiresonance (f_a), effective electromechanical coupling coefficient k_{eff} and the effective mechanical quality factor (Q_{eff}), all with respect to the fundamental thickness mode, are shown in Table 3.5.

Material	f_r **(kHz)**	f_a **(kHz)**	k_{eff}	Q_{eff}	d_{33} **(pC/N)**
PZ29	784 ± 1.5	881 ± 1.6	0.4561 ± 0.0016	145 ± 15	589 ± 13
PZ54	813 ± 1.5	887 ± 4.5	0.4011 ± 0.0014	1168 ± 381	440 ± 10
PZ37	580 ± 12.4	663 ± 10.7	0.4829 ± 0.0414	89.5 ± 32	372 ± 15
PZ12	975 ± 2.0	1054 ± 2.0	0.3774 ± 0.0016	110 ± 6	111 ± 5

Table 3.5: Resonance characteristics of the piezoelectric discs, calculated from impedance spectroscopy

The resonance characteristics highlighted in Table 3.5 are often used by transducer designers as a metric of transducer performance. The resonance and antiresonance frequencies of the thickness mode were obtained from impedance spectroscopy shown in Fig. 3.10. The electromechanical coupling factor and the mechanical quality factor (both dimensionless) were calculated as discussed in Chapter 1.3.2. These are denoted as effective parameters because of the excessive mode coupling that renders an isolated dimension, such as the pure thickness coupling (k_t) impossible to distinguish. However, electromechanical coupling is an indication of the efficiency of the transducer in converting the electrical drive signal into mechanical vibrations and is therefore a key parameter for transducers and devices. It is shown in Table 3.5 that variation is much greater for the PZ37 and PZ54 discs. In the case of PZ37, mode coupling in the thickness mode distorts the impedance response so that an accurate measurement off resonance frequency is not possible. The PZ54 samples exhibit a high value of Q_{eff}, but the high modal density affects the accurate identification of the half power points from which Q_{eff} is calculated. Both k_{eff} and Q_{eff} relate to bandwidth of the mode, however, unlike Langevin transducers where a high Q (low bandwidth) is necessary for device performance [75], a higher bandwidth in this case can be an advantage by allowing the FUS device to be operated over a wider frequency range.

All discs have a poling and electrode direction in the 3 axis, through the thickness of the discs. As such, d_{33} is used to determine the mechanical force when an excitation charge is applied to the electrodes (pC/N). The d_{33} was measured using a Berlincourt piezoelectric d_{33} meter (ZJ-6B, Institute of Acoustics of the Chinese Academy of Sciences). This instrument measures the charge from the electrodes of a sample via contact points at the clamp, Fig.3.11 (b). The sample is oscillated by a shaker plate. This configuration enables measurement of the piezoelectric coefficient in the axial direction 3 because the mechanical oscillation is in the same axis. However, d_{31} can also be measured by applying mechanical oscillation in the radial direction. The d_{33} metre has a stated uncertainty of $\pm$ 5% in the (20 - 2000) pC/N range. The metre is calibrated before each measurement with a calibration adjustment using two control samples at 300 pC/N. The measured charge is divided by the force applied via the shaker plate from Eq. 3.11, where q is the charge and F is the applied force [76].

$$d_{33} = \frac{q}{F} \tag{3.3}$$

From Table 3.5, soft PZ29 has the highest d_{33} followed by PZ54, PZ37 and PZ12. Commercially available lead-free materials, including PZ12, generally have low d_{33} and hence have not been a replacement for PZT.

3.3 Laser Doppler Vibrometry

To characterise the vibration modes of the piezoelectric discs, a laser Doppler vibrometer (LDV) (MSA 100, Polytec, Germany) was used.

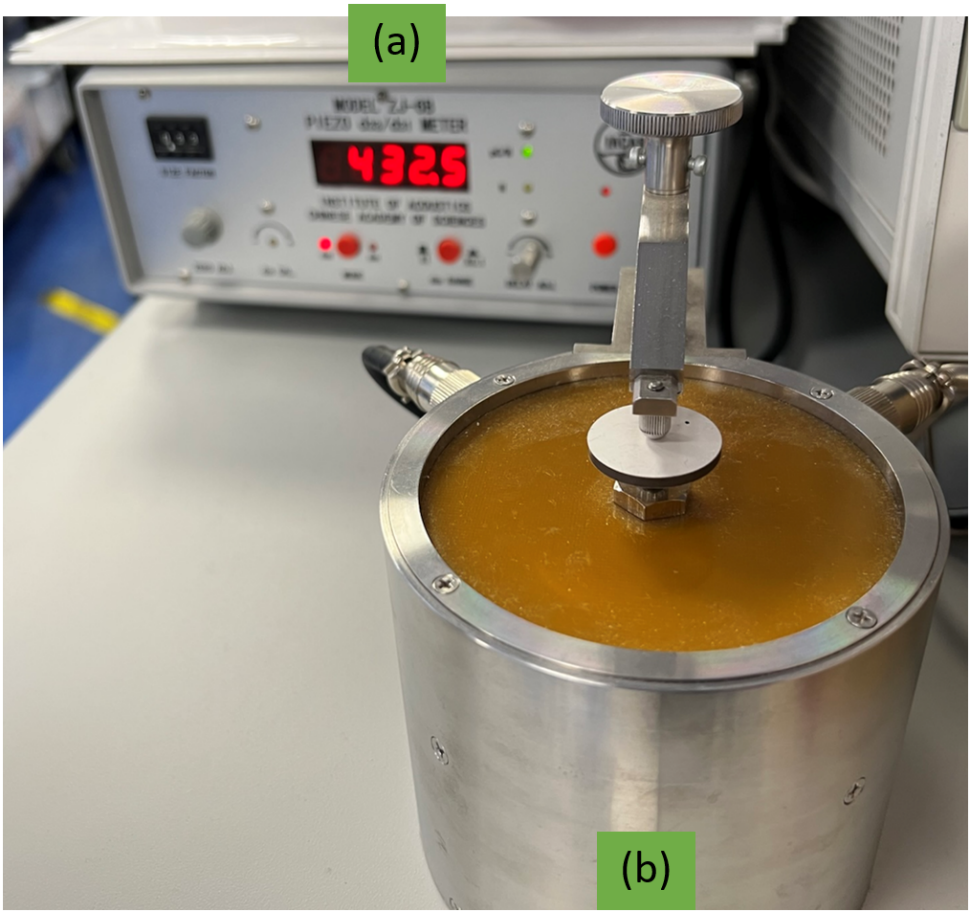

Figure 3.11: (a) d_{33} meter and (b) shaker plate for the characterisation of the piezoelectric coefficient

3.3.1 Introduction

The LDV is an integrated system which comprises of a laser, 2 axis micro positioning stage, waveform generator and control computer. The sample under test is secured on the two axis stage which is mounted on a vibration isolation table. The waveform generator is controlled via the computer which creates the drive signal for the sample under test. The LDV measures the sample surface velocity at a grid of user defined measurement points which are scanned under control of the micro-positioning stage.

The laser system is based on a heterodyne Mach-Zehnder interferometer [77], Fig. 3.12. A laser beam is split into a reference beam and a test beam. The latter is directed to the sample under test while the former is frequency shifted by a Bragg cell. These beams are recombined and, because the source is a coherent light source, the result is an interference pattern and the peaks can be counted by a photo-detector. Because the test beam is

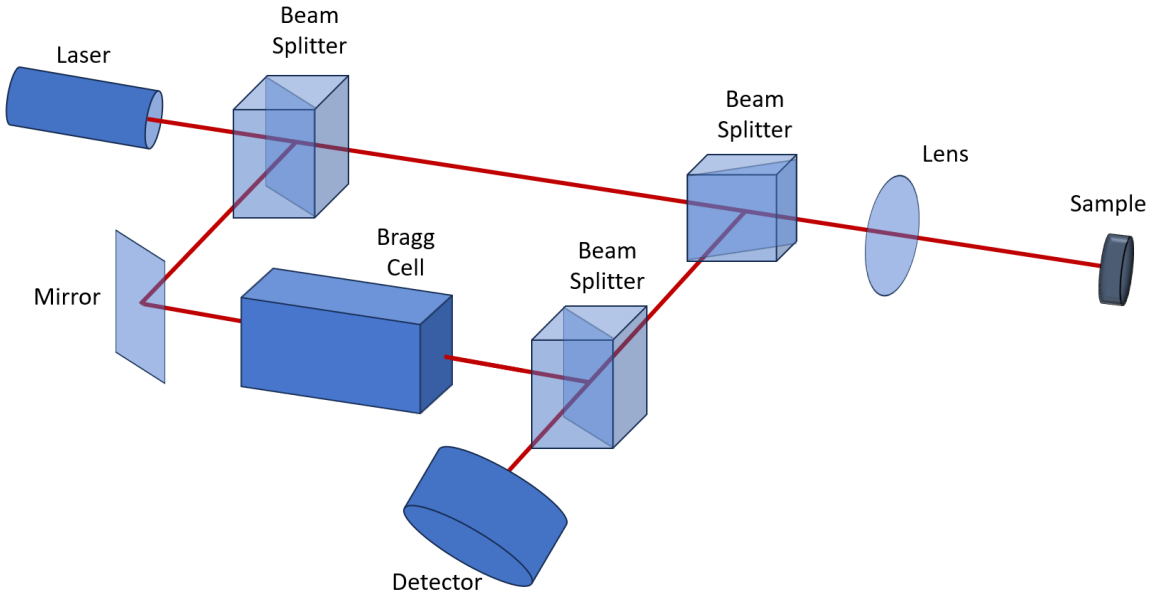

Figure 3.12: Schematic of the basic principles involved with laser doppler vibrometry

frequency shifted due to the Doppler effect of reflection from a vibrating sample surface, the detector can isolate the frequency response of the sample by subtracting both the frequency of the source laser and the Bragg cells frequency modulation. Therefore, the relationship between surface vibration velocity of the sample, v, wavelength of the light source, λ, and the Doppler shift, f_D, is defined by Eq. 3.4;

$$f_D = \frac{2v}{\lambda} \tag{3.4}$$

In the interference pattern the number of interference fringes caused by the surface of the sample moving away from the laser source is equal to that of the surface moving towards the source at the same rate. The Bragg cell results in the reference beam being frequency modulated by 40 MHz with respect to the source laser (which has a frequency of $\approx 5 \times 10^{14}$ Hz). The interference pattern therefore generates a modulation frequency of 40 MHz when the sample is not moving which increases if the surface is coming towards the light source or is less than 40 MHz when moving away. The LDV uses one normal-to-surface and two off-axis detectors to gain 3D vibration response spectra at each grid point. The surface vibration velocity response measured on the grid provides data associated with the vibration of the whole sample by creating a wire mesh of the grid and animating the mesh vibration mode at each of the discs resonance frequencies.

3.3.2 Mode shapes of the material discs as received

One disc of each piezoelectric material was characterised with the LDV. The disc was positioned on a foam backing to approximate a free vibration boundary. The electrodes were connected to the waveform generator via conductive copper tape, which is a temporary solution designed to avoid point masses that could affect the modes of vibration. These fixings were secured to the 2 axis stage to ensure that the sample did not move relative to the stage, shown in Fig. 3.13.

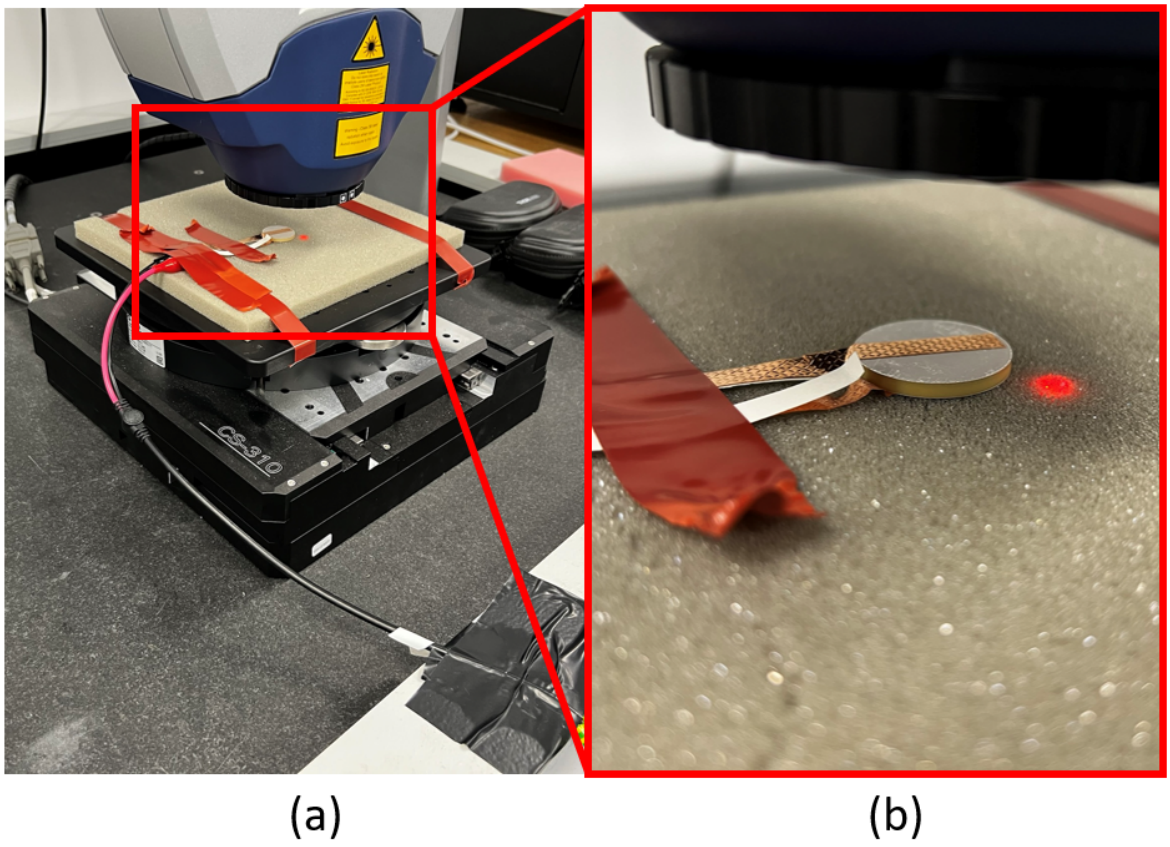

Figure 3.13: (a) the disc secured to a foam backing under the LDV and (b) the temporary electrode connections on the sample.

The excitation signal comprised a 5 V amplitude frequency sweep, ranging from 10 kHz to 2.5 MHz. The tracking and laser settings were 100 averages per grid point in the FFT mode. Lower than 5 V resulted in poor signal-to-noise ratio. Higher than 5 V carries the risk of driving the disc into a nonlinear response regime where the piezoelectric properties are excitation level dependant [78].

Figures 3.14- 3.17 show the LDV measured first radial and thickness modes of the four discs of different materials and the associated velocity-frequency response. The LDV frequency response data is split into X, Y and Z axes where the Z axis corresponds to displacement out plane (Fig. 3.14- 3.17 (c)). The first thickness mode is captured at a peak in the Z axis response at the frequency position that correlates to the resonances found in the impedance data. This is shown in Fig. 3.14- 3.17 (b). Radial modes can be observed with high responses in the X and Y axes, shown in Fig. 3.14- 3.17 (a). PZ29, PZ54 and PZ37 show significant mode coupling that is consistent of the response characterised with impedance spectroscopy. However, PZ12 has a great decoupling of the radial and thickness modes. This leads to the first thickness mode being much more pure than the other PZTs. The purity of this mode will determine if energy will leak into the surrounding parasitic modes. This can result in reduced amplitude at the focus or can result in subfoci in the near field created by the lens responding poorly to the radial mode [79]. The high modal density of PZ54 can be seen in Fig. 3.15 (c). This is the worst response from the piezoelectric discs tested.

A positive correlation between theory, impedance analysis, and modal analysis can be observed in Fig. 3.17. The radial modes quickly attenuate before 800 kHz and this leads to a decoupled thickness mode with a strong Z component of velocity. The modes were validated by observing mode shape via the LDV and cross checked with the resonances found in the impedance analysis. As the LDV measurements were taken at $\sim$ 8 V, the frequency of the modes is lower than that observed in impedance analysis (excited at 1 V) as seen in Table 3.6. This is due to non-linear piezoelectric softening, further discussed in Chapter 6.2.2.

Material	Frequency of mode (kHz)	
	First radial	First thickness
PZ29	76.4	743.3
PZ54	85.5	785.9
PZ37	72.5	608.4
PZ12	121.8	1000.0

Table 3.6: Resonance frequencies of the first radial and first thickness modes for each disc.

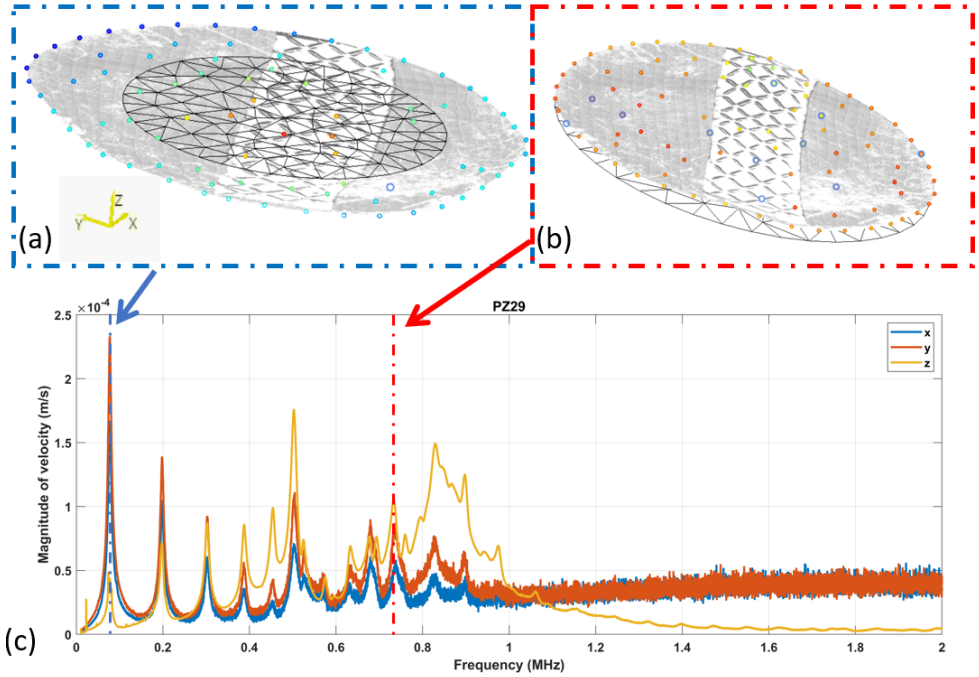

Figure 3.14: The (a) first radial and (b) thickness modes of PZ29 and (c) the average velocity-frequency response in the x, y and z axis from every grid point measured on the disc

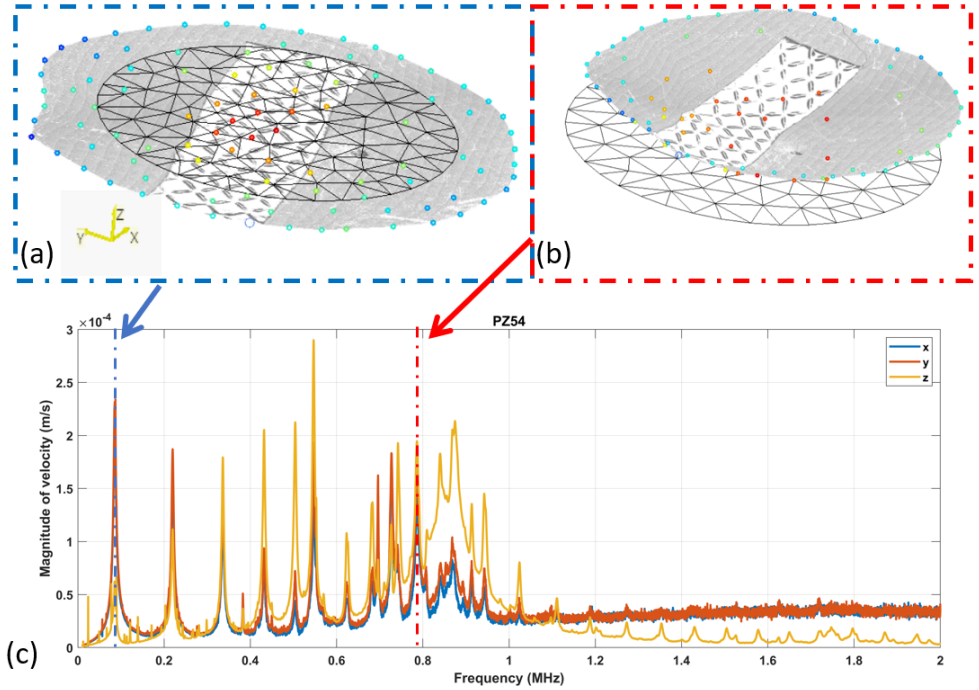

Figure 3.15: The (a) first radial and (b) thickness modes of PZ54 and (c) the average velocity-frequency response in the x, y and z axis from every grid point measured on the disc

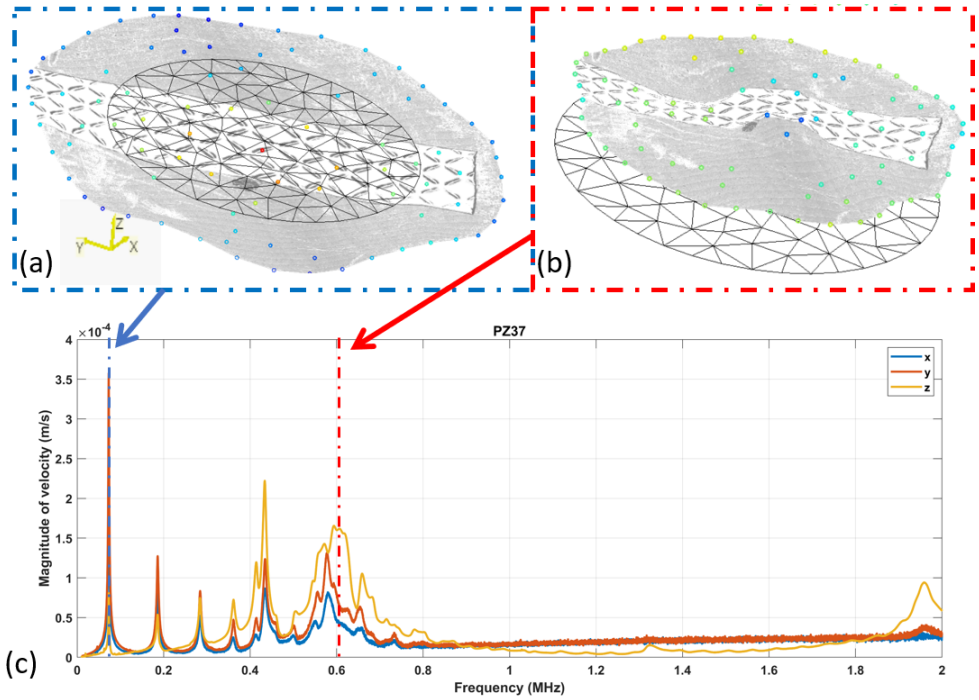

Figure 3.16: The (a) first radial and (b) thickness modes of PZ37 and (c) the average velocity-frequency response in the x, y and z axis from every grid point measured on the disc

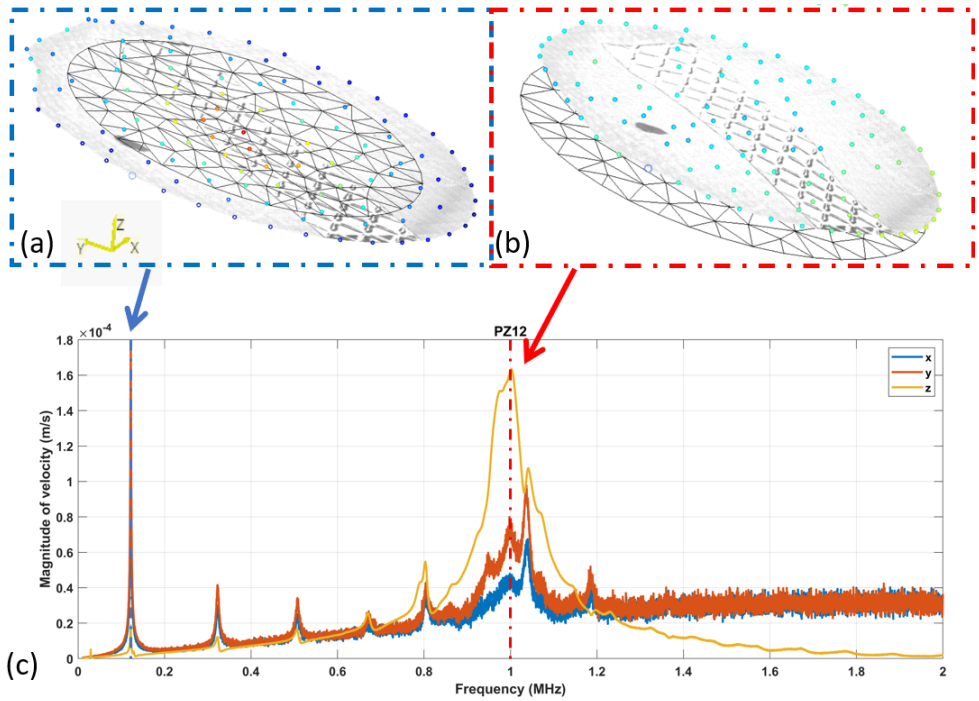

Figure 3.17: The (a) first radial and (b) thickness modes of PZ12 and (c) the average velocity-frequency response in the x, y and z axis from every grid point measured on the disc

3.4 Piezoelectric composition analysis

A scanning electron microscope (SEM) was used to image the surface of the disc samples to identify differences in porosity and structure. Energy-dispersive X-ray spectroscopy (EDX) was also used, utilising the SEM electron source to generate X-rays to identify the elements present in the sample. These processes are complementary and are used in tandem to corroborate the elements found in the SEM data to the crystal structures found in the EDX process. Characterisation of the piezoelectric materials aims to uncover why similar 'PZT-like' materials behave differently when driven in the FUS transducer configuration.

3.4.1 Scanning electron microscope images

The sample preparation for the SEM analysis was carried out by lapping the electrodes to expose the ceramic, cutting the 25 mm OD disc into quarters and coating the remaining quarter with a conductive coating. Due to the small sample mount in the SEM, a reduction in size was necessary; however, the conductive coating was required to guard against the sample becoming charged at the point of electron bombardment. The SEM raster scans a focussed beam of electrons over the sample surface and a detector acquires secondary electrons from the sample. The electrons from the main beam, which have an energy in the order of 1 MeV, go through a number of interactions when colliding with a sample. Secondary electrons are displaced by the primary source of electrons and are unique in this regime because they have an energy in the order of 50 eV. This low energy means that they cannot travel through large thickness of material. Therefore, they are generated in the first few nanometres depth in the sample and characterise the surface topology of the sample [80].

Figures 3.18 - 3.21 show the SEM images of the surface of the four discs. PZ29 exhibits a dense ceramic structure, however, there are still pores left after the sintering process. The individual powder grains can be seen in Fig. 3.18 (b). In contrast, PZ54, Fig. 3.19, is more dense with less pores, this suggests that the sintering process was able to eliminate

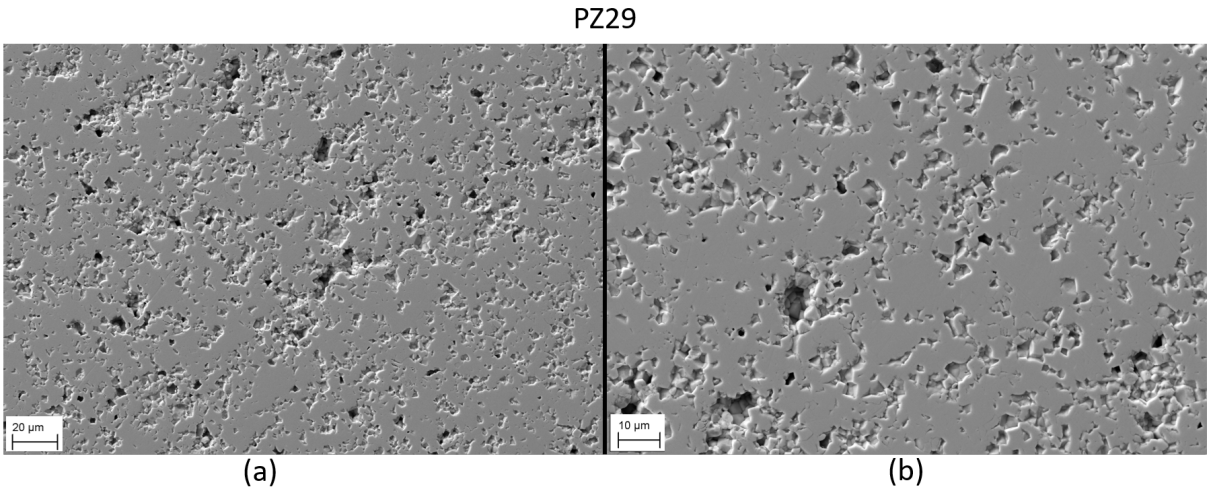

Figure 3.18: SEM images of PZ29 showing (a) at 1.1 K X magnification and (b) an enlarged 2.0 K X magnification

pores. The goal of sintering in the ceramic manufacturing process is to remove the space between the individual particles of ceramic. From this SEM characterisation it can be observed that the material dopant along with the physical manufacturing processes must be developed together to achieve the differences in material properties.

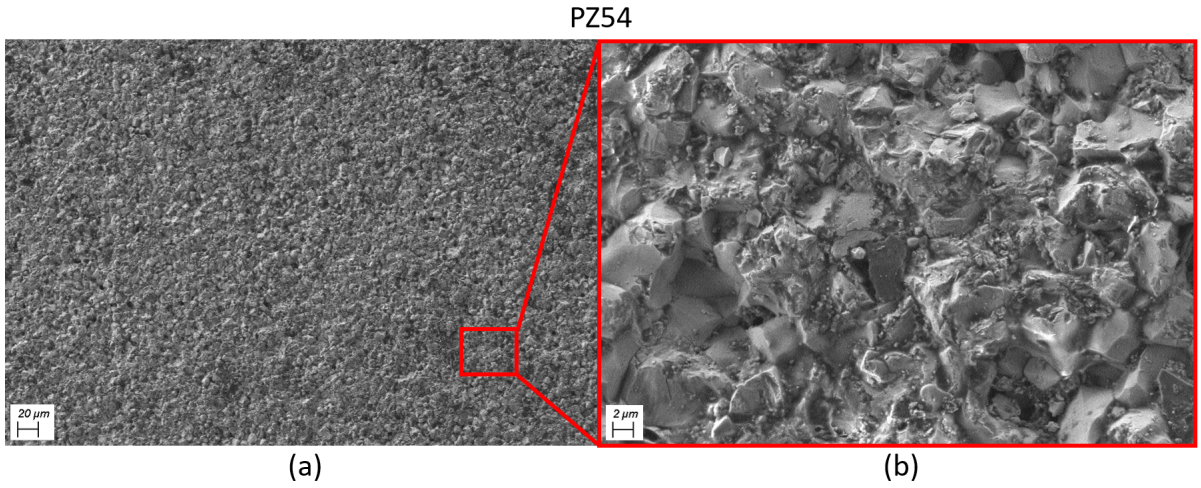

Figure 3.19: SEM images of PZ54 showing (a) at 1.0 K X magnification and (b) an enlarged 5.0 K X magnification

The largest surface artefacts observed were those of PZ37 porous ceramic, as seen in Fig. 3.20. Although the surface roughness and general structure is comparable to PZ29 in Fig. 3.18, the pores are easily identified and larger for PZ37. This is expected for PZ37 because it has lower density from higher porosity; however, it is clear that the pores are not added during the manufacturing process. Rather, they are not removed to the same degree that they are in denser piezoelectric discs such as PZ29 and PZ54. Lastly the PZ12 in Fig.3.21 differs in structure the most with no clear grain sizes or pores.

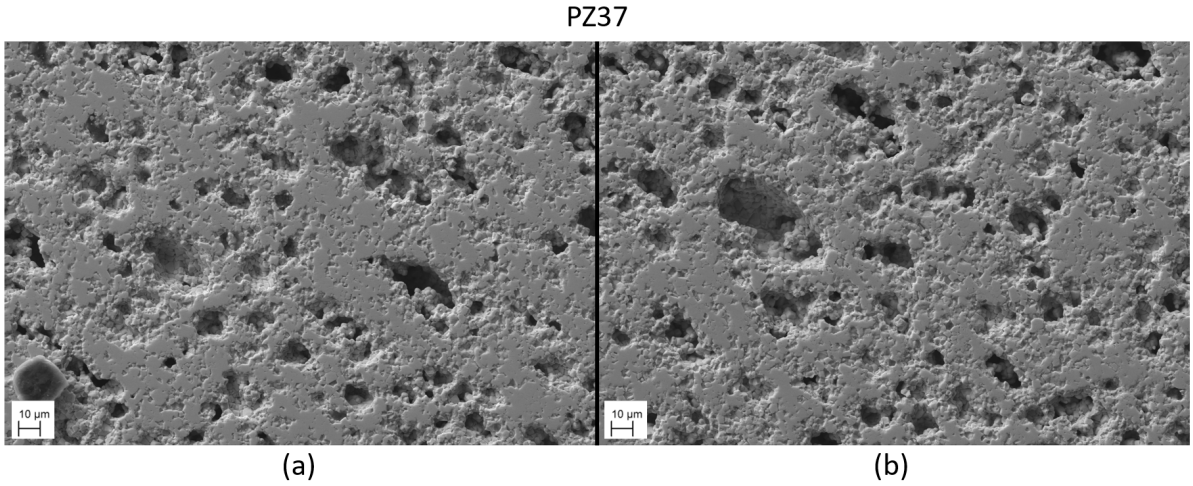

Figure 3.20: SEM images of PZ37 showing (a) a 1.06 K X magnification and (b) another region of a similar 1.15 K X magnification

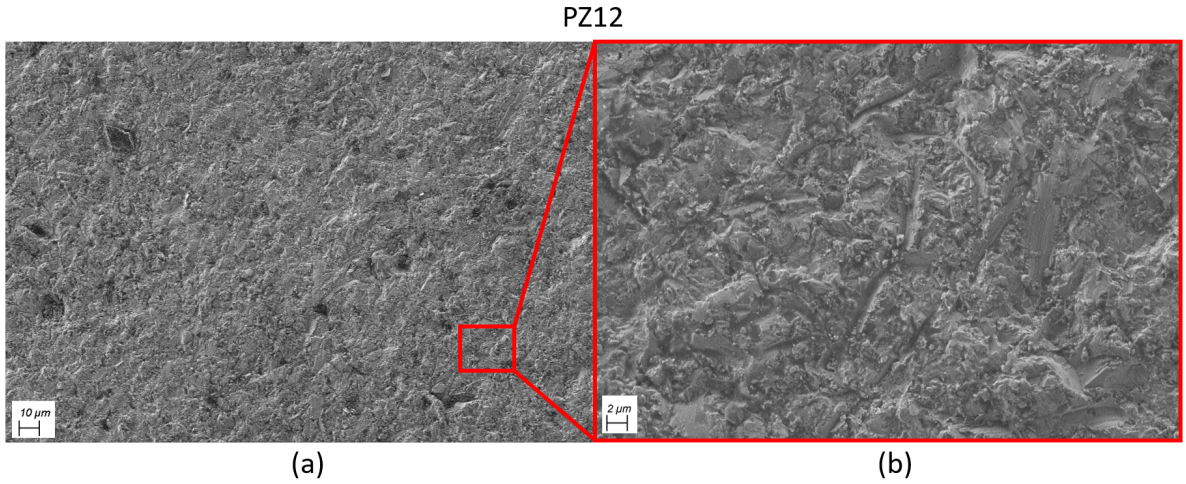

Figure 3.21: SEM images of PZ12 showing (a) at 1.0 K X magnification and (b) an enlarged 5.0 K X magnification

3.4.2 Energy dispersive X-ray spectroscopy

Energy dispersive X-ray spectroscopy (EDX) is used to identify the elements present in the sample. As the sample is bombarded with an electron source, it is possible to displace an inner energy shell electron from the atoms within the sample. An electron from an outer shell then lowers its energy level to replace this, and the difference in energy between the two states is released as an X-ray. The peaks detected in the resulting spectrum can be compared with the unique signature of each element, for example Figure 3.22, which

shows the spectrum for PZ54. There are multiple peaks for each material corresponding to movement from each higher energy level to the lowest. However, ultimately the energy for an element follows Moseley's law in which the square root of the frequency of the emitted X-ray is proportional to the atomic number of the element [81].

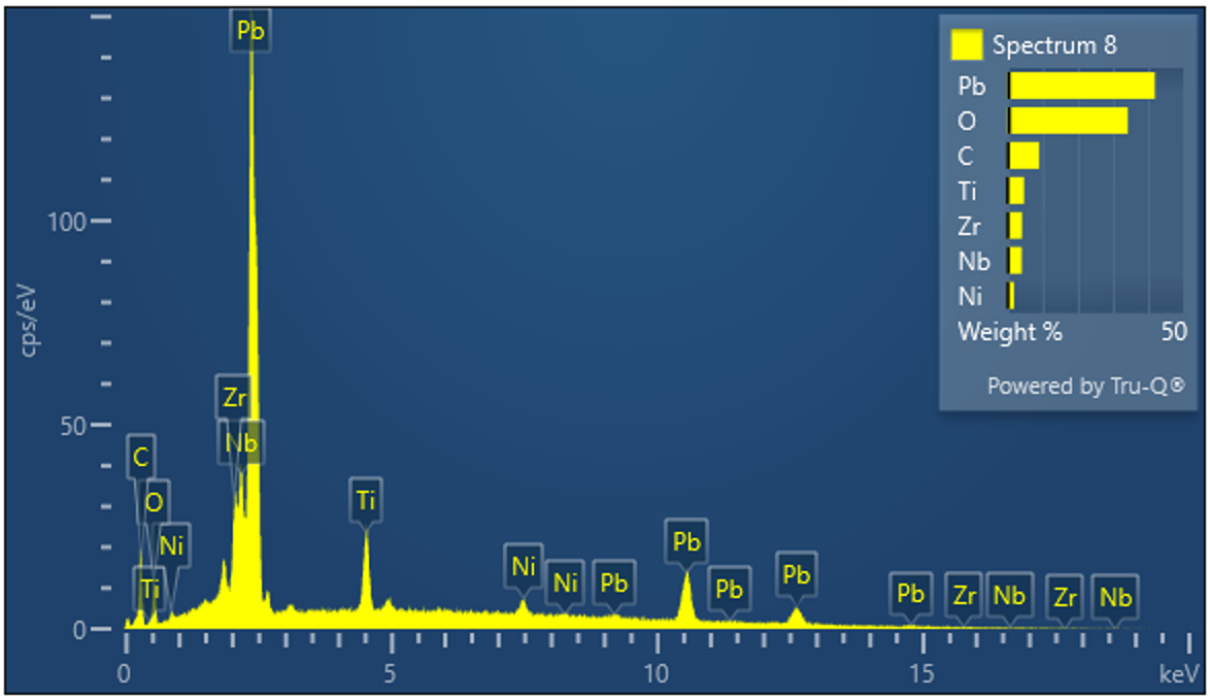

Figure 3.22: An example spectrum obtained via EDX on a sample of PZ54

The results of the characterisation of the piezoelectric material samples are presented in Table 3.7. The addition of strontium in PZ29 has been found to increase density and enhance piezoelectric coefficients by reducing porosity and increasing grain sizes in PZT [82]. PZ54 has more dopants such as Niobium and Nickel than standard PZT (Lead, Zirconium, Titanium, Oxygen). These dopants result in a blend of hard and soft piezoelectric properties. A result of interest is PZ37, which confirms what is observed in the SEM images. The elements are those of a standard PZT ceramic with no additional dopants to structure pore size. This further suggests that the porosity is highly dependant on the sintering stage of manufacturing.

Material	PZ29	PZ54	PZ37	PZ12
Pb	14.84	6.01	15.68	-
O	65.88	84.50	67.59	78.10
Zr	7.96	1.96	6.97	-
Ti	9.69	3.12	9.76	8.77
Sr	1.62	-	-	-
Nb	-	1.69	-	-
Ni	-	0.86	-	-
Na	-	-	-	4.53
Ba	-	-	-	2.12
Bi	-	-	-	4.40

Table 3.7: The elements in each sample as an atomic percentage

3.4.3 X-ray diffraction

X-ray diffraction (XRD) was used to determine the crystal structure and estimate the elemental composition in the samples. An X-ray diffractometer uses an X-ray source and an XRD detector. By manipulating the angle of the sample with respect to the emitter / detector, the intensity of the X-rays can be plotted with respect to 2θ (the angle of incidence and diffraction at the sample). This results in a strong response at specific angles, and this spectrum can be compared against a database of known spectra. The intensity peaks with respect to 2θ relate to Bragg's law [83], Eqn. 3.5:

$$n\lambda = 2d\sin\theta \tag{3.5}$$

where n is the diffraction order, λ the wavelength of X-rays used, θ the angle of incidence to the crystalline plane and d the spacing between them. This technique is most suited to single crystal structures with structural homogeneity. The well defined crystal planes result in clear peaks in the XRD data. The polycrystalline samples in this research do not have identical crystal orientations between crystals and this results in a spreading of adjacent peaks.

Material	XRD composition of best fit
PZ29	$(Pb_{0.94}\ Sr_{0.06})\ ((Zr_{0.6}\ Ti_{0.4})\ O3)$
PZ54	$Pb(Zr_{0.44}\ Ti_{0.44}\ Mn_{0.04}\ Ni_{0.04}\ Nb_{0.04})\ O3$
PZ37	$Pb(Zr_{0.1}\ Ti_{0.9})\ O3$
PZ12	$Bi_{0.5}\ Na_{0.5}\ O3\ Ti$

Table 3.8: The chemical formulae of best fit from XRD analysis of the piezoelectric samples

The calculated best-fit chemical formulae (SmartLab Studio, Rigaku, Tokyo, Japan) are shown in Table 3.8. The formulas are identified from a database of known material spectra in the software and compared to the measured spectra, as shown in Fig. 3.23. The formulas identified as the best fit show an elemental structure similar to the data obtained from the EDX measurements in Table 3.7. The combination of these two data sources raises the level of confidence in the dopant Strontium in PZ29 to decrease pore sizes in the ceramic sintering process. As PZ37 does not have this dopant, the pore sizes are larger. This characteristic was used to give PZ37 a lower density and acoustic impedance. PZ54 has more dopants that have been used to enhance the lower piezoelectric coefficients associated with 'hard' PZTs. The NBT structure of PZ12 lacks Barium, that was detected in the EDX analysis. This can be due to a Barium doped NBT crystal spectra not being included in the XRD software database.

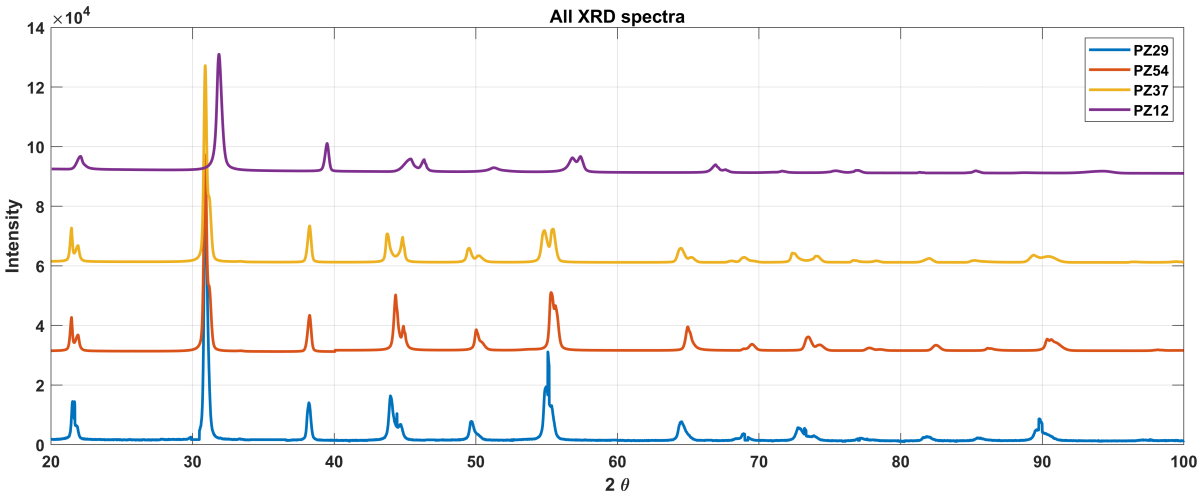

Figure 3.23: All spectra from XRD analysis. Each spectrum is offset by an arbitrary intensity for comparison

In this chapter the active and passive materials involved in the FUS device have been characterised separately. The photopolymer that will be the primary material used in the Fresnel lens and transducer housing was selected after comparison of a range of commercially available resins. The speed of sound and acoustic impedance were considered and had minimal effects on the focal zone. As the speed of sound approached that of water the

Fresnel lens features increased drastically. This was avoided by selecting a sound speed greater than that of water. The problematic characteristic was acoustic attenuation. Polymers have a high acoustic attenuation [84, 73] due to the movement and dislocation of polymer chains and the absorbed pressure waves and the generated heat. A highly cross-linked photopolymer, StrongX, was found to have satisfactory attenuation to incorporate it into the design.

The active piezoelectric material was fully characterised in low power impedance spectroscopy and laser Doppler vibrometry. High modal density was found in PZ54 with parasitic modes very close to the thickness mode. PZ12 showed very low modal coupling between the radial and thickness modes, which limits the energy wasted in driving parasitic modes. PZ29 and PZ37 had ordinary piezoelectric coefficients; however, PZ37 has the added benefit of low acoustic impedance. This was achieved by reducing the density. Using an SEM and analysing the samples with EDX found that Strontium was a dopant in the PZ29 samples. This has been associated with a reduction in porosity during the sintering process and an increase in piezoelectric coefficients. This highlights that the porosity in the PZ37 samples has been tuned by both elemental doping and the ceramic manufacturing process working in tandem to tune the desired structure and characteristics of the piezoelectric materials.

Chapter 4

Device Manufacturing

Three FUS devices for each piezoelectric material (therefore twelve devices in total) were fabricated to investigate the manufacturing variability and the effects on device performance. All the fabrication processes and the challenges they present in terms of variability are described here in detail.

4.1 Active Material Lapping

The first challenge is to reduce the thickness of the piezoceramic disc so that the centre frequency can be tuned. The poled piezoceramic discs were all 25 mm in diameter and 2.5 mm thick. Once discs have been poled, material can be removed by lapping, a method that is commonly used in silicon wafer processing. Material removal by methods such as machining on a CNC (computer numerical control) router or a lathe are not suitable due to the heat generated in these processes. Surpassing the Curie temperature of the material triggers depoling. The ceramics used all have a Curie temperature of around 225 °C, which is easily exceeded at localised tool-sample contacts during the machining process.

To reduce the thickness of the piezoelectric material, lapping machines (Logitech, Scotland) were used with abrasive as a material removal system [85, 86]. The abrasive was a slurry of aluminium oxide of a controlled diameter mixed with water. The aim of the lapping process is to reduce the 2.5 mm thick piezoelectric discs to a thickness that will

correspond to the final device achieving a 1.5 MHz centre frequency. This disc thickness is unique to each piezoelectric material and is defined by its thickness constant N_t (Chapter 3.2.1). In contrast to tuning an isolated piezoceramic element, there are added complications when trying to achieve a device centre frequency due to the addition of wires and the device housing affecting the boundary conditions. To account for this, an initial device was fabricated with a PZ29 disc to explore how the manufacturing steps affected the resonance frequency. This device exhibited a thickness mode resonance of 1.1 MHz. Consequently, a linear relationship was determined between the disc thickness reduction and the ultimate device centre frequency so that lapping of the disc would result in a frequency of 1.5 MHz. The manufacturing procedure is applied to the twelve FUS devices and some subsequently optimised devices.

4.1.1 Lapping Procedure

Lapping is a three body abrasion process in which grinding is performed with loose abrasive particles. The sample is held at a constant force on a lapping plate with abrasive between them. The lapping machine, Fig. 4.1 (a), is an electric motor that turns a lapping plate ((c) and (f) in Fig. 4.1). The jig (b) is held by an arm with rollers so that the jig is free to rotate but is held in position on top of the lapping plate. The abrasive is aluminium oxide and is mixed with water to form a suspension (slurry) and held in a container (e). A valve on the top of the container regulates the flow of slurry to the lapping plate during operation. The lapping machine also has a flatness monitor (d) for the lapping plate as it wears during use.

The sample mounted on a glass slide is held in place with a vacuum on the bottom of the jig (g) that controls the force at which the sample is pressed onto the lapping plate (f). A vacuum is created by a pump, coupled to channels within the jig through a hose and PTFE adapter (i). The use of PTFE creates a low friction fitting that allows the jig to rotate with minimal friction. As the sample decreases in thickness, a micrometre (h) is used to measure material removal. To control the material removal rate, the parameters in Table 4.1 are varied.

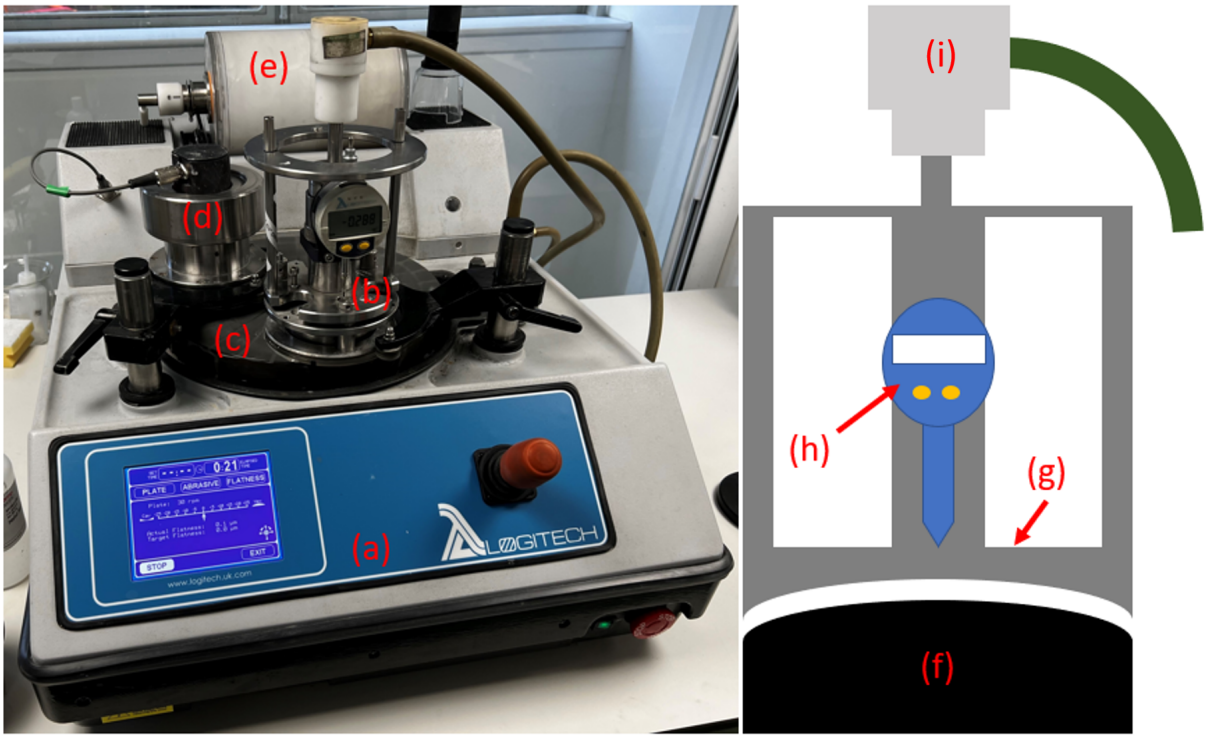

Figure 4.1: (a) Logitech lapping machine in operation of lapping a sample mounted on a (b) lapping jig grinding against a (c) lapping plate. The (d) flatness monitoring sensor is used during operation and the surface of the plate is fed a constant stream of (e) aluminium oxide abrasive. On the right is an exploded cross section of the lapping jig. This sits on the (f) lapping plate which laps the negative of its profile onto the jig (g). The amount of material removed by the process is monitored by a (h) micrometer. The sample is mounted on a glass plate which is held via (i) vacuum.

Parameter	Options
Abrasive slurry	particle diameter concentration drip rate
Lapping plate	material type (Iron, Glass, Polyurethane etc.) rotational speed (RPM)
Jig	force on sample

Table 4.1: The parameters that influence material removal speed in the lapping procedure

During the lapping process of the discs, the first millimetre of material was removed quickly. An iron lapping plate was used with 20 µm aluminium oxide particles. However, during this process, the slurry caused damage to the sample three times deeper than the particle size and this damage determines the surface finish. Therefore, as the sample reaches the target thickness, the particle size was decreased. The smallest particle size (3 µm) was used as a finishing lap. This resulted in 9 µm of surface damage. To further

decrease the roughness of the surface, a polishing procedure is required. The particle size was reduced to the smallest size when the thickness of the sample was just greater than 90 µm more than the target thickness. This allowed the smaller particle size to remove the 90 µm of surface damage left by the larger particles. The remaining surface roughness allows for more surface area for the electrode to bond to in the next manufacturing step.

4.1.2 Mounting Samples

For lapping, the sample was secured to a glass plate, which interfaced with the mounting jig on the lapping machine. To mount the samples to the glass plate in a repeatable way, a wax was used as the adhesive, which could be simply heated once the lapping was complete to release the sample undamaged. The wax setting could be standardised through use of the jig shown in Fig. 4.2, which ensures a thin and flat wax layer.

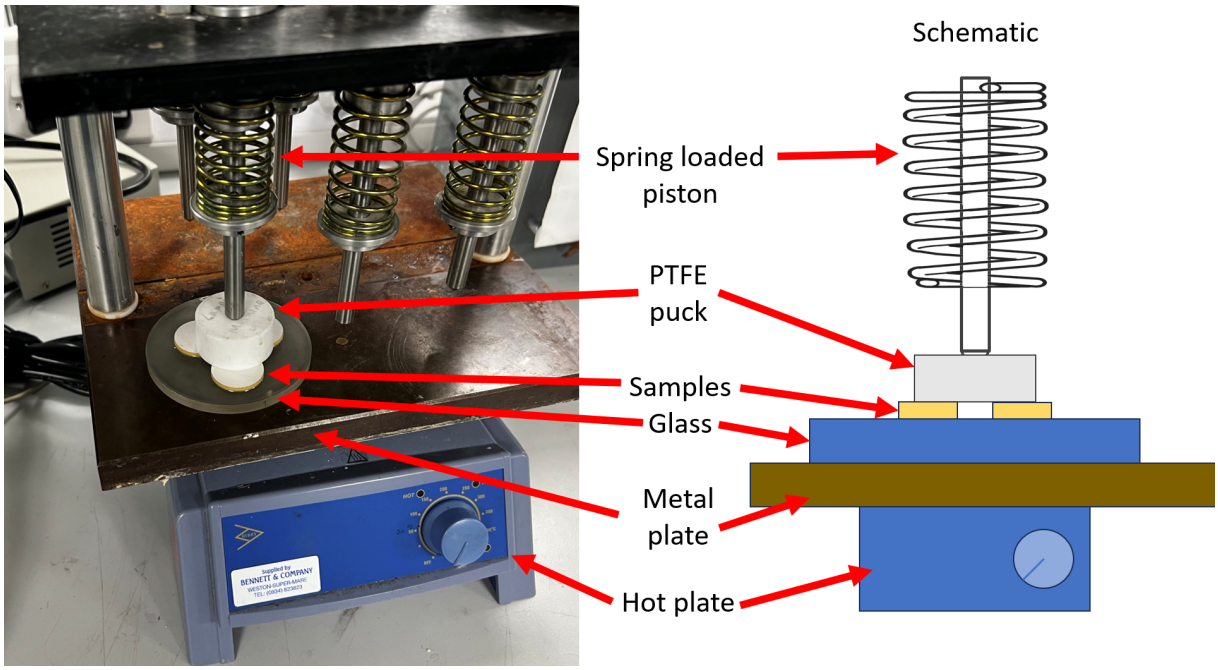

Figure 4.2: The wax mounting jig to standardise the wax setting process.

In this set up the parameters mentioned can be tuned and repeated to produce a wax layer to be sufficiently thin and more crucially, flat. The parameters used in this work were informed by the preprototype stage along with trial and error from previous lapping work [85, 86].

Parameter	Value	Notes
Melt time (mins)	60	
Spring pressure	setting 2/3	spring compression at rest
Puck thickness	setting 3/3	puck thickness increasing spring compression
Melt temperature (°C)	100	
Cooling time (mins)	20 (at 10°C)	metal plate water cooled

Table 4.2: Parameters of wax mounting system tuned for wax layer thickness and flatness

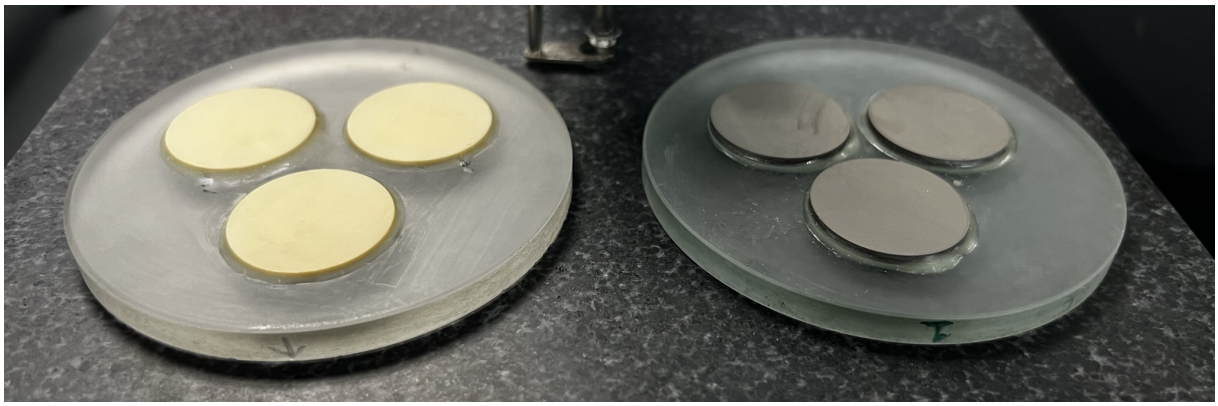

Figure 4.3: Samples mounted on glass plates. On the left is PZ29 and right PZ54.

The twelve devices consist of three of each piezoceramic disc. These batches of three fit on the 80 mm glass plate held by wax, as shown in Fig. 4.3. The discs are indexed with respect to the markings on the outer rim of the glass plate. All surfaces in use must be prepared to ensure they are flat and parallel, the glass plate, lapping plates and jigs.

4.1.3 Calculation and Tracking of Target Thickness

The Fresnel lens for this FUS transducer is designed for a centre frequency of 1.5 MHz. The diffraction efficiency of the lens is reduced when the frequency is changed. In this respect, the piezoelectric disc must generate high acoustic pressure waves at this frequency. However, the thickness constant calculated and discussed in Chapter 2.3.1 was under free boundary conditions. When loaded with the imperfect conditions of being in a housing, the thickness resonance changes. This was characterised with a pre-prototype made from PZ29 where the 1.5 MHz centre frequency of the unloaded disc dropped to 1.1 MHz when integrated into the device. To account for this drop, the piezoelectric discs target thickness

Disc material	f_r (kHz)	N_t (Hz·m)	Target Thickness (µm)
PZ29	784	1960	980
PZ54	813	2033	1016
PZ37	580	1450	725
PZ12	975	2438	1219

Table 4.3: The target disc thickness for a 2 MHz thickness resonance frequencies as calculated from the thickness resonance measured on an impedance analyser.

resonance was increased to 2 MHz. Table 4.3 shows the thickness resonance frequency of the original 2.5 mm discs as measured on an impedance analyser. The thickness constant for the discs was confirmed and a target thickness was calculated for a resonance frequency of 2 MHz.

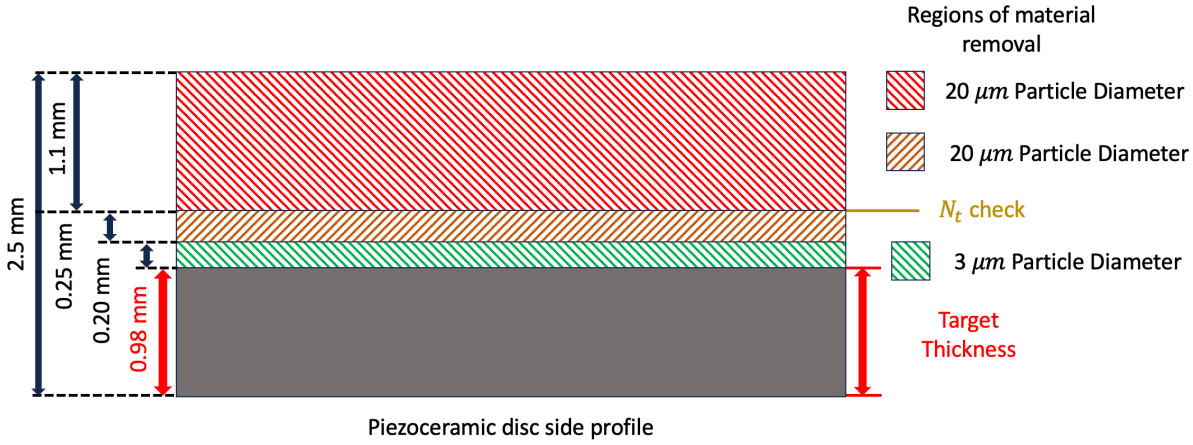

Figure 4.4: The lapping plan for PZ29 disc reducing the thickness of the disc gradually with marked regions of testing. The list on the right indicates the size of particles used in the slurry.

Figure 4.4 shows the lapping plan for a disc of PZ29 as the material is removed from the thickness. The side profile shows the initial 2.5 mm thickness and the target thickness taken from Table 4.3. An initial lap of 1.1 mm was performed with a course particle diameter of 20 µm. During this process, the material removed from the disc was measured using the micrometre on the lapping jig. The micrometer is not as accurate as the fixed linear micrometre with a granite reference flat, so a check was performed to recalculate N_t. The discs were unmounted from the wax and measured with a fixed micrometre over a granite reference flat. Five points were measured spread throughout the surface of the disc, north, east, south, west, and middle. This was done to gauge how flat the lapping plate had become during the process and would show if any plane had been lapped into the surface or if a convex/concave shape appeared. Temporary electrodes were added to the disc with silver paint (G3691, Agar Scientific, UK), and the electrical impedance was

measured with an impedance analyser. The target thickness was then recalculated with the new value of N_t. Using the size of 20 µm abrasive slurry particles, there is 60 µm damage on the surface. Therefore, at a point 200 µm before the target thickness, the particle size of 3 µm was used.

Before reducing the size of the abrasive particles, all contamination of 20 µm abrasive must be removed from the lapping machine, or the sample will have surface scarring because large particles score the surface. The lapping plate was lapped by the test block with the 3 µm particles. This not only destroys larger contaminants, but also allows the test block and lapping plate to become the same shape again. Once the surface of the test block is mated to the lapping plate, the test block is measured again. If the lapping plate is more than 2 µm away from flat, it must be corrected before the final lap of the discs.

Material	Target Thickness (µm)	Final Thickness (µm)	Thickness Resonance Frequency (kHz)
PZ29	1026	1020.6 ± 3.0	2000.0 ± 50.1
PZ54	975	969.2 ± 6.4	2203.3 ± 107.9
PZ37	725	758.9 ± 7.9	1983.7 ± 35.4
PZ12	1218	1222.1 ± 9.2	2010.6 ± 9.4

Table 4.4: The resonance frequency of the piezoelectric discs after lapping, including the measured thickness and the target thickness. The target thickness was determined from the initial N_t value calculated from the data measured from the full thickness samples. The final thickness and resonance were measured.

The final thicknesses of the discs can be seen in Table 4.4. The thicknesses were within 5 µm of the target thickness, with the exception of the PZ37 disc. Due to the lower target thickness and the resonance frequency checking stage indicating a thickness resonance frequency within 1% of the target, this thickness was deemed satisfactory. Each disc was measured in five places with the measured thickness consistently within 5 µm. A temporary electrode was then applied to each disc to allow measurement of the resonance frequency on an impedance analyser. The resulting thickness mode resonance frequencies are shown in Table 4.4. The final thickness of the PZ54 disc is close to the calculated target thickness. However, the resulting resonance frequency is significantly higher than expected along with the variation within the batch, leading to a higher standard deviation than the other batches. Considering all of the other materials are correct in their estimations and the PZ54 discs went through the lapping process at the same time as the PZ29 discs, the material itself may be the reason for this offset. During the lapping process the material

removal time (in µm/minute) was estimated for each material. The PZ54 discs had a low material removal rate, which meant that the material was much harder than the others. This hardness could have influenced the estimation of N_t in the interim steps leading to an overestimation in the target thickness.

4.2 Electroding and Wire Bonding

Silver paint (Agar Scientific, UK) provided a fast and repeatable temporary electrode with high conductivity and low volume of electrode. However, the adhesion to piezoceramic materials is poor. Permanent electrodes consisted of a two-part silver ink (118-09A / B119-44, with a thinner, CMI 113-21) (Creative Materials, Ayer, MA, USA) [87]. The silver ink was applied with a spin coater (Ossila, Sheffield, UK) using jigs to interface the fixing to the piezoelectric samples and the microscope glass slides. The jigs were additively manufactured in an mSLA printer.

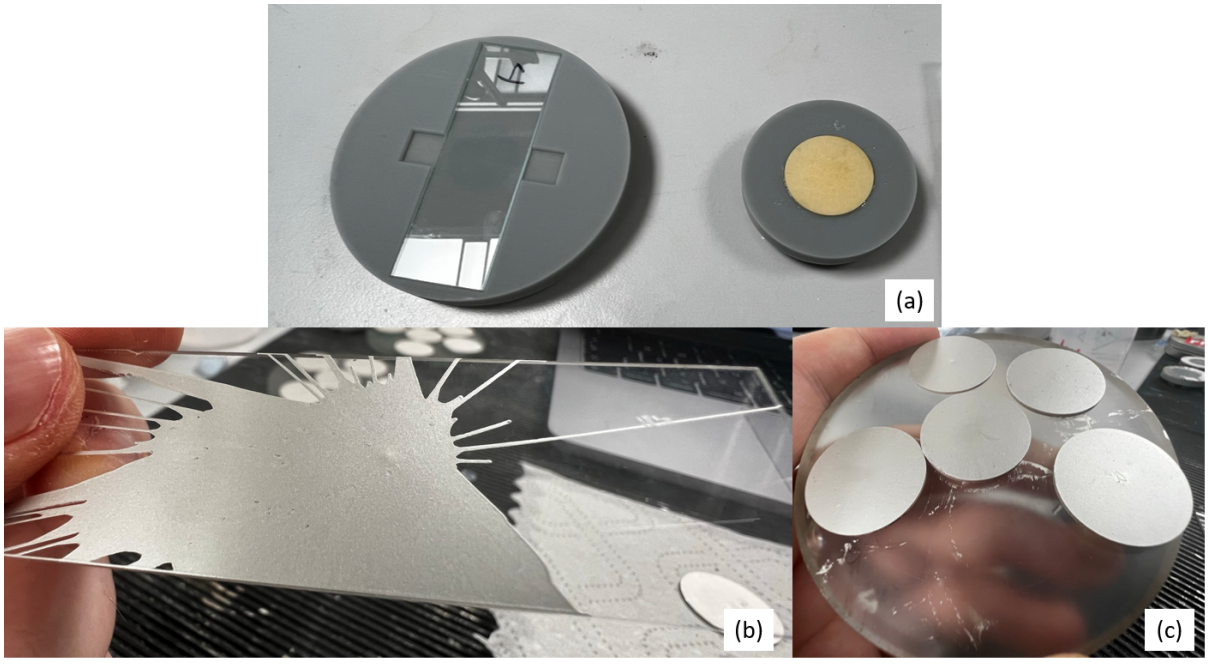

Figure 4.5: (a) a microscope glass slide and piezoelectric disc positioned in an additively manufactured spin coating jig. (b) a glass slide and (c) five piezoelectric discs after spin coating and curing.

Figure 4.5 shows the spin coater jigs used to mount a microscope glass slide and each piezoelectric disc and the electroded disc surfaces after curing. The ink has a low curing temperature of 80°C (for 4 hours), which is much lower than the Curie temperature of all the piezoelectric materials used. An electrode thickness of < 5 µm was achieved with a spin speed of 3000 RPM for a duration of 20 seconds.

Impedance analysis of the piezoelectric discs exhibited minimal change in comparison to those with temporary electrodes applied. A wire was adhered to each electrode (two per disc) with a two-part conductive epoxy (8330S. MG Chemicals, Ontario, Canada) which was cured at room temperature for 24 hours.

4.3 Additive Manufacturing of the Fresnel lens and housing

Additive manufacturing (AM) is fast and cost-effective, which aligns well with the aims of manufacturing bespoke FUS transducers. For AM of an ultrasonic transducer a homogeneous material with low acoustic attenuation is required. The resolution of the 3D printer must be capable of the feature sizes required for the Fresnel lens (<100 µm). This rules out conventional fused deposition modelling (FDM) printers which use materials such as PLA, ABS and PETG. For 3D printing of the components of the FUS transducer, mSLA printing was selected (Elegoo Mars 2 Pro, Shenzhen, China) an XY resolution (related to LCD pixel density) of 47 µm and Z resolution (related to stepper motor rotational accuracy) of 10 µm.

4.3.1 Calibrating Layer Cure Times

Crucial for optimising mSLA printing is the layer cure time, the amount of time the build plate will stay above the FEP (at a distance of the layer height) while the photopolymer is exposed to UV radiation. This time is dependent on the material properties. Each photopolymer resin data sheet contains a recommended exposure time, however validation

is crucial. The exposure time is sensitive to temperature, UV diode output power (which varies between printers), and layer height. Properties such as concentration of resin and photoblockers have not been investigated as a result of the resins being commercially available, and hence those material properties are not known or published due to commercial sensitivity. This optimisation is particularly important when the size of the features on the printed parts approaches the resolution of the printer. Open source calibration parts were used to optimise the exposure time for resins.

The exposure settings were monitored periodically as ambient temperature varied and the photopolymer resin aged, each time a new combination of resin and layer height was needed. An example of the calibration process is shown in Fig.4.6 with failed features in red circles. In Figure 4.6 (a) the exposure is closest to optimal, there is a good definition in the negative spaces. However, the features highlighted have failed; there is evidence that the thin bars were printed and destroyed in the wash and cure process. At 3 seconds (Fig. 4.6 (b)) exposure there is less definition in negative spaces; however, the point in the middle is defined; this is overexposed in Fig. 4.6 (c) and highlighted.

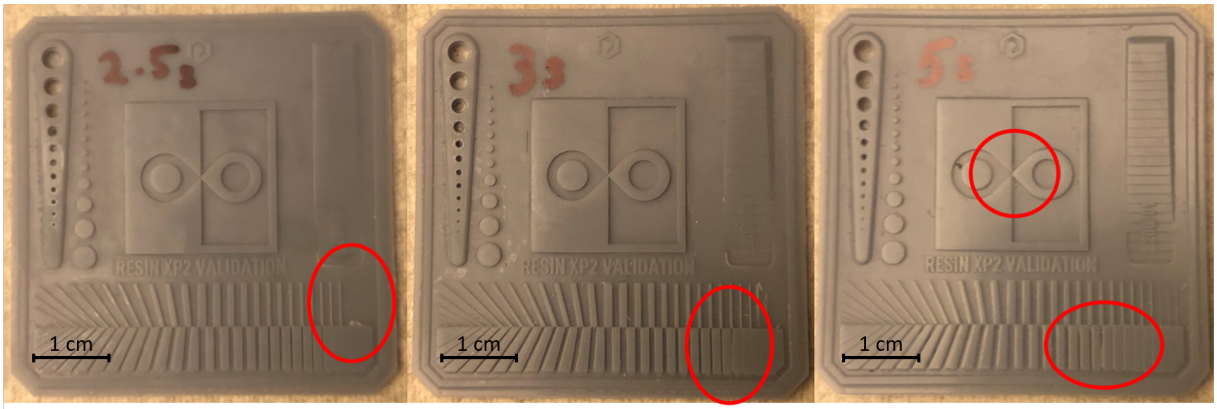

Figure 4.6: Standard Elegoo photopolymer resin XP2 results with exposure settings of (a) 2.5 s, (b) 3 s and (c) 5 s.

For long exposure times, an additional open source cones of calibration (TableFlipFoundry) was used as an additional assessment [88]. On the success side the cones are connected by a pinch point and the cross-section diameter decreases from 450 to 350 µm. The failure side has cross-section diameters decreasing from 280 to 200 µm. The exposure time was tuned to result in only one cone succeeding, so the exposure was on the boundary between

underexposure and acceptable. Figure 4.7 shows the optimised exposure time for StrongX photopolymer resin. On the success side, only one cone was successful. The optimal exposure setting for StrongX in a lab temperature of 29.5 °C and a layer height of 10 µm was 17 seconds.

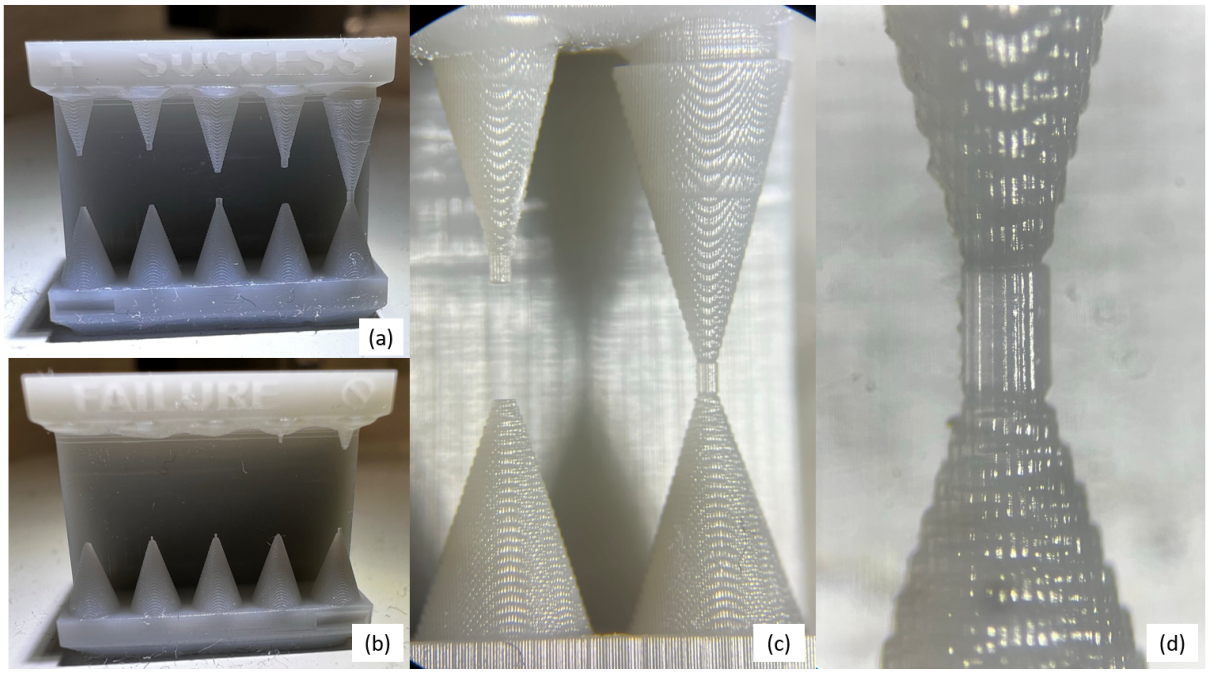

Figure 4.7: (a) the success side of the cones of calibration, (b) the failure side, (c) a magnified view of one failed cone and one successful one and (d) a magnified view of the successful cone.

4.3.2 Post-processing

The final step in the process is a post-processing cure that improves cross-linking of any remaining bare skeletal structures of the polymers that did not bond during the printing process. In this cure, the tensile strength and Young's modulus of the material increase [89]. StrongX requires a 120-minute UV cure at an elevated temperature of 60 °C. This was achieved in a cure station (FormLabs, MA, USA).

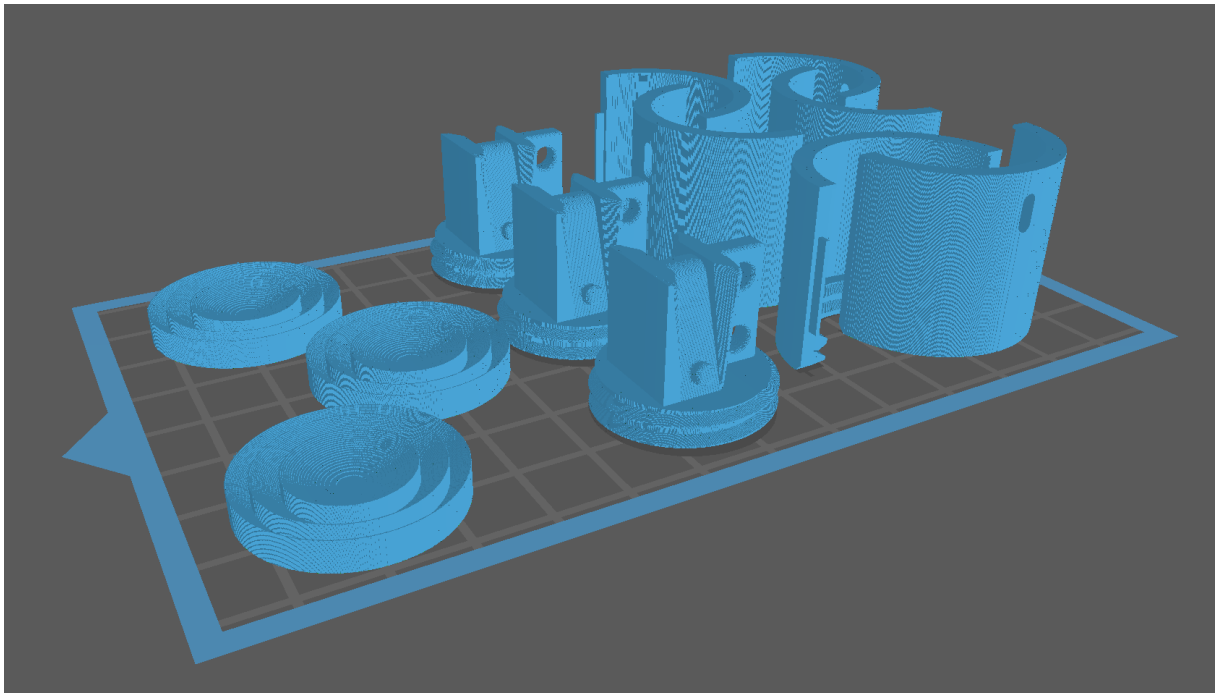

Figure 4.8: The final arrangement of the parts for three FUS transducers on the 3D printer build plate.

4.3.3 Manufacturing Lens and Housing

To ensure reproducible FUS transducer parts, the quantity and location of parts on the build plate were kept consistent. The parts were placed as seen in Fig. 4.8. On the left are the three Fresnel lenses, in the middle are the robotic attachment pieces and on the right are three housings split into semi-cylinders.

4.3.4 Validating Print Repeatability

To validate the accuracy achieved by the 3D printer, an optical profilometer was used (Alicona Infinite Focus, Graz, Austria). A surface scan was performed from the central plateau of the lens to the outer edge to ensure that all steps were captured, as seen in Fig. 4.9 (a). As the 3D printing method used is inherently more accurate in the XY plane, the first 19 steps were measured and compared to the CAD file provided to the printer. The lenses were measured once the manufacturing process was completed. There was some variation in the global tilt of the lens, observed as a gradient in Fig. 4.9 (b). The gradient was calculated in the first step of a post-processing algorithm which measures the best-fit

gradient of the central plateau of the lens. The gradient was then subtracted from all data points. The adjusted data was then aligned with the first step of the original model data as seen in Fig. 4.9 (c). This allows for a direct comparison of the height of each printed step with the model. The difference between the radius of the model and the measured radius was 26.5 ± 10 µm, which is within the accuracy of the printer (XY resolution, 50 µm). This difference was averaged over all lenses and was very consistent, indicating that accurate exposure times had been selected for the StrongX resin.

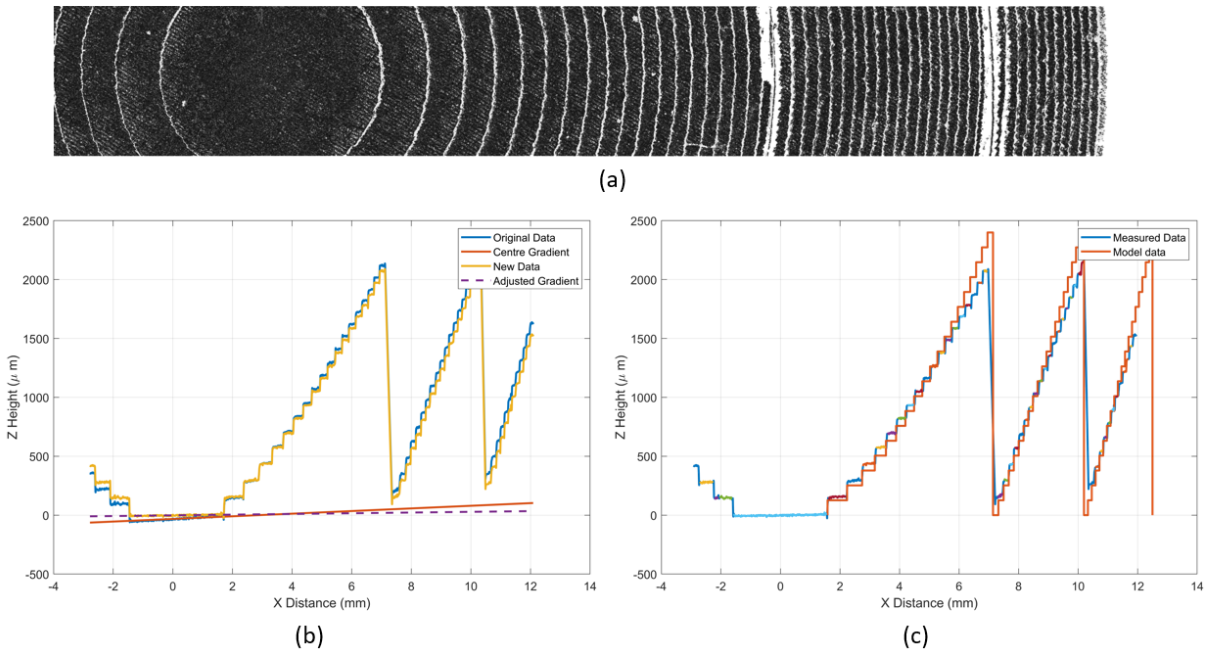

Figure 4.9: Optical profilometry scan of (a) the surface of a Fresnel lens, with the central plateau seen on the left, (b) a line across the surface of the lens and adjusted for any global gradient, (c) the adjusted data compared to the original model data of the lens.

The height offsets of the steps were inconsistent in the Z direction due to the variation in layer height. The profile can be seen in Fig. 4.10, caused by the build plate setting to a lower height than requested by the CAD model, seen as a negative offset of up to 200 ± 4 µm. The offset for all lenses is shown in Fig. 4.11. The lenses all have a phase number of 20, so should have 20 steps in the innermost set (or 'ladder'). As the first of the steps is the plateau, the remaining 19 are compared to the model. However, in eight of the examples there are only 18 measured steps. The correct model was printed, as the radial dimensions for all other steps are accurate. This is the top ring of the lens and is not supported, therefore the step was destroyed by the wash and cure post-processing.

The combination of the top steps being destroyed and the printing inaccuracy affect the efficacy of the lens including the focal intensity and spot size.

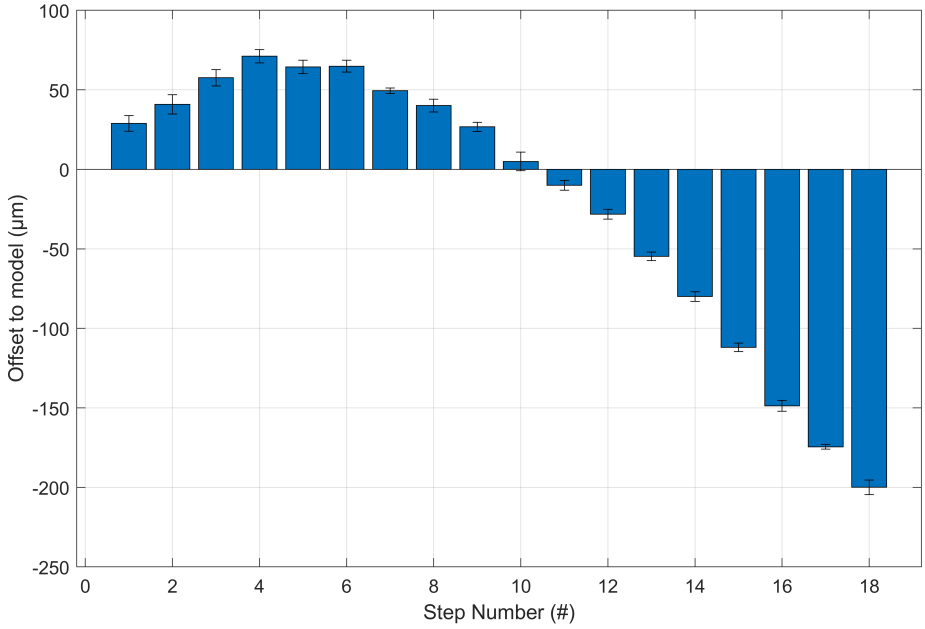

Figure 4.10: The height offset of each step in one Fresnel lens ($D_{PZ12(1)}$) from that of the modelled lens

4.4 Device Assembly

To assemble the miniaturised FUS devices in a repeatable way jigs were made to aid alignment of the lens and housing components.

4.4.1 Adhesion of Lens to Piezoelectric Disc

A crucial interaction in the FUS device is the coupling of the piezoelectric disc to the base of the 3D printed Fresnel lens. This adhesion must be strong and stiff. The adhesive layer must be thin to minimise attenuation losses. Cyanoacrylate adhesive (RS Components Ltd., Corby, UK) was therefore chosen. A jig was modelled, as shown in Fig. 4.12 (a) and (b), to contain the piezoelectric disc at the base. A trench was included to accommodate the wires attached to the electrodes. Figure 4.12 (c) shows the piezoelectric disc in the jig. Cyanoacrylate adhesive was applied to its top surface and the Fresnel lens was quickly lowered onto the disc, Fig. 4.12 (d), the adhesive having a subsequent cure time of 10

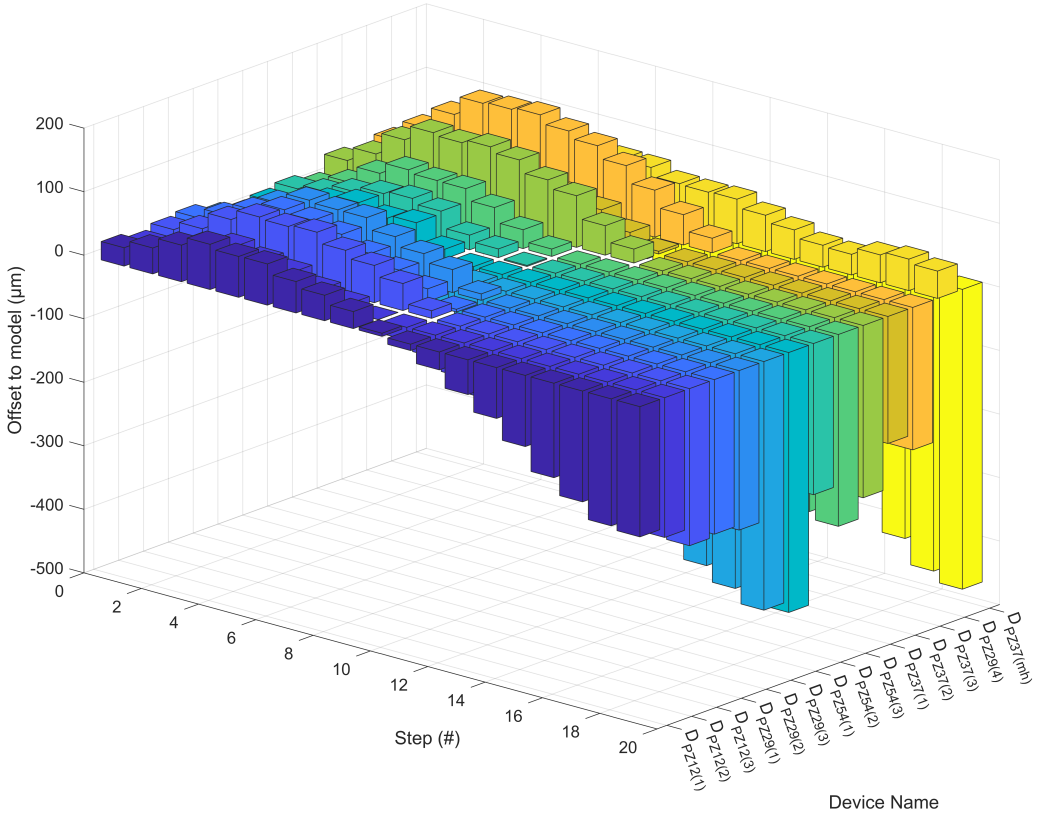

Figure 4.11: The offset from the model of the printed lenses measured with an optical profilometer.

seconds. The three tall pillars of the jig fit so that the lens is centred on the disc, but there is clearance to allow the whole assembly to be removed aided by a PTFE coating. This produced a repeatable alignment and the final assembly is shown in Fig. 4.12 (e) with the lens and disc aligned.

4.4.2 Setting of Housing

To fix the Fresnel lens and piezoelectric disc assembly to the housing elements, an epoxy (Ablestik 45 clear, Loctite, CT, USA) was used. This epoxy has an adjustable compliance by varying the mixing ratio. For this application, the stiffest configuration was selected, which requires a mixing ratio of 1:1. As seen in Fig. 4.13 (a), epoxy was applied in the sockets on the female half of the semi-cylinder housing and under the support ring. More

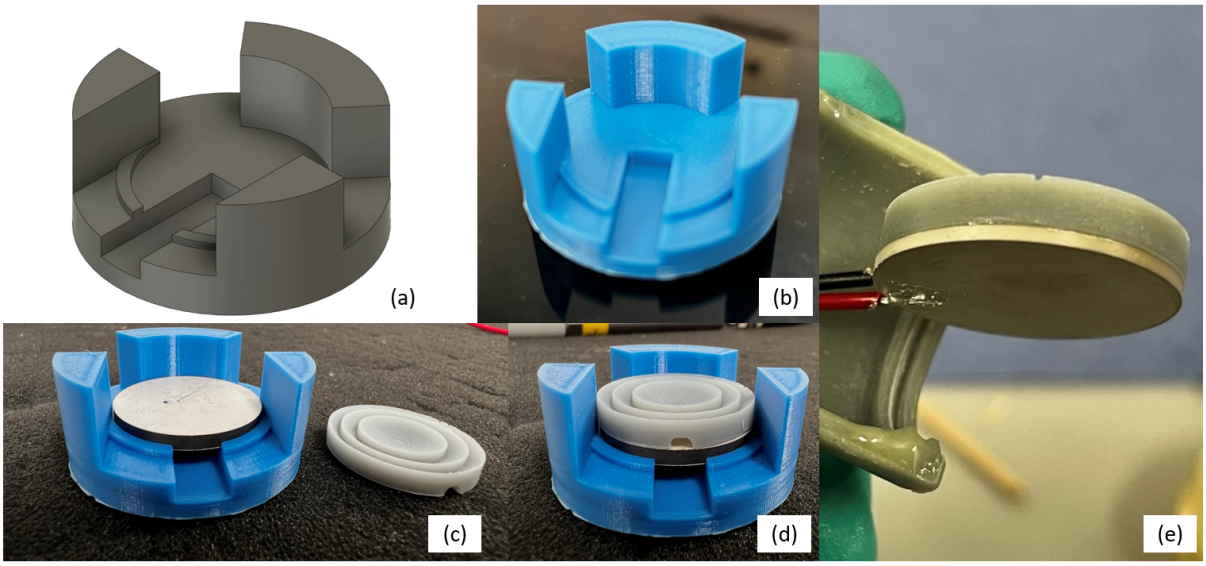

Figure 4.12: (a) The modelled jig for attaching the Fresnel lens to the piezoelectric disc, (b) the printed jig, (c) the piezoelectric disc within the jig, (d) the Fresnel lens centred on top of the disc and (e), the aligned and adhered lens and disc.

epoxy was used around the lens assembly. The wires were pulled through the wire hole and the lens was pushed flush against the support ring for alignment. Excess epoxy was removed and an elastic support band (Fig. 4.13 (b)) was included for the epoxy curing cycle, which was 24 hours at room temperature.

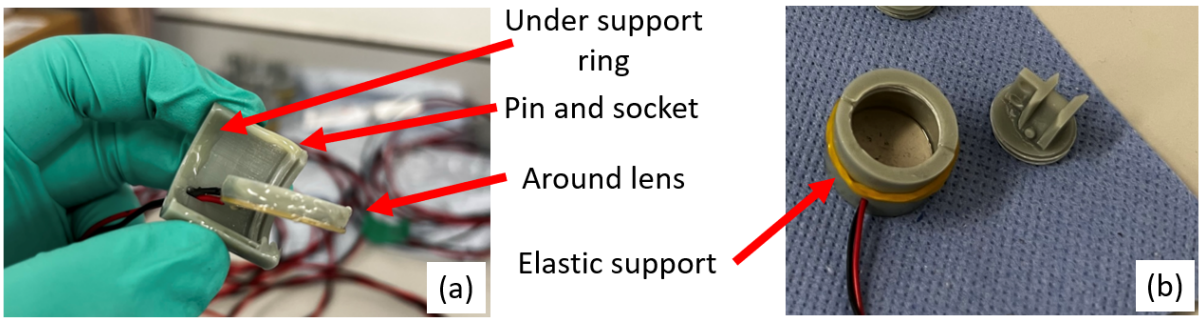

Figure 4.13: (a) The female semi-cylinder and lens assembly coated in epoxy in key areas and (b) the housing curing with the aligned lens assembly, supported with an elastic support band.

4.4.3 Backing Layer Fabrication

The backing layer was chosen to provide a large acoustic impedance mismatch behind the piezoelectric disc to limit the energy transmitted from the back of the transducer. Air is a good candidate for this task, but a more robust backing layer encapsulates the gas. To achieve this, glass microspheres (K1 type, 3M, MN, USA) were mixed into clear epoxy

(Ablestik 45). The microspheres were mixed with the two parts of the epoxy separately, while the epoxy is in its least viscous form. The microspheres had a typical density of 0.125 g/cc and the epoxy, 1.1 g/cc. The microspheres were mixed into the epoxy parts and saturation occurred at 0.73 g to 7 g respectively. When mixed, the viscosity of the epoxy rapidly increases. The final volume fraction was 47% glass microspheres to epoxy and this was poured into the housing assembly cleaning any spillage into the housing thread, Figure 4.14.

Figure 4.14: Assembly of Fresnel lens, piezoelectric disc and housing face down with freshly poured backing layer.

4.4.4 Impedance Measurements during Manufacturing

The impedance response was measured to track the effects of each manufacturing step as follows:

1. The disc as received (2.5 mm thickness)
2. The disc after lapping
3. The addition of wires and electrodes
4. Adhesion of the Fresnel lens to the disc
5. Setting of lens assembly in housing

6. Inclusion of backing layer

Since there was a consistent change in the impedance magnitude-frequency response for all devices, the FUS transducer PZ29 device 1 ($D_{PZ29(1)}$) is shown here for discussion, Fig. 4.15.

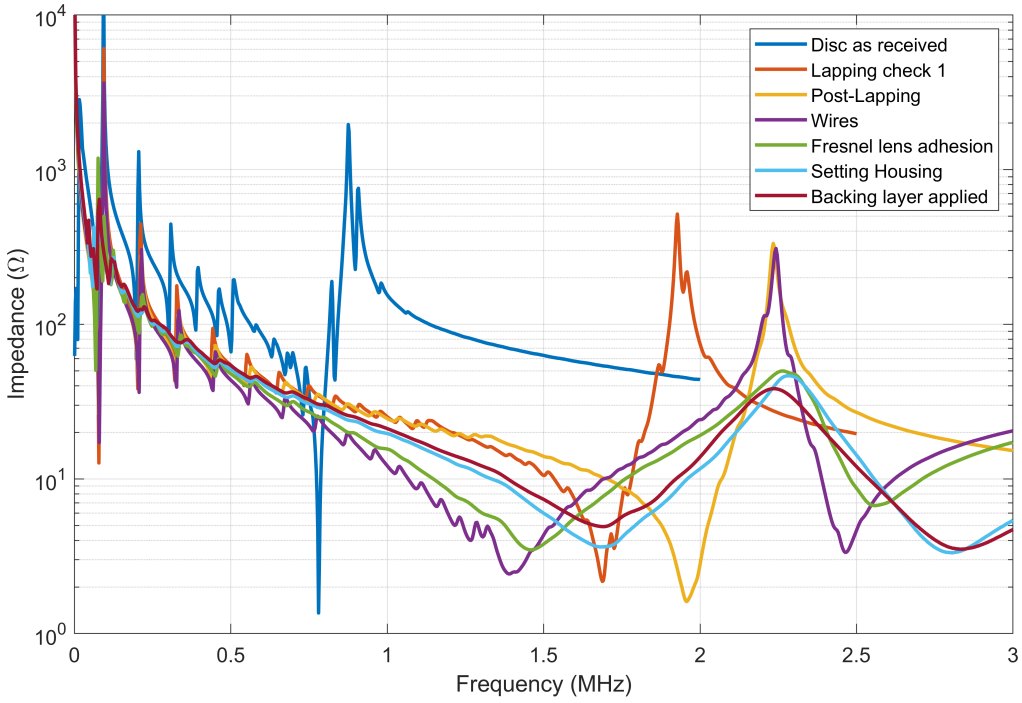

Figure 4.15: FUS device PZ29 device 1 ($D_{PZ29(1)}$) impedance magnitude-frequency response at each step in the manufacturing process.

The progress of lapping can be seen from the received disc through lapping check 1 to the post-lapping check. This increased the thickness mode resonance from 800 kHz to the required 2 MHz. With the attachment of wires to the disc, the frequency drops to less than 1.5 MHz. This is due in part to the added mass of silver epoxy. A more predominant factor is the resistance of the wire, which has a total resistance of 400 mΩ. This is not significant in large impedance devices; however, the impedance magnitude is < 5 Ω in the miniaturised FUS devices leading to the wires being a comparatively significant load. The adhesive layers add stiffness to the device, leading to increased resonance frequency and higher damping. The addition of the backing layer further increases the damping, and the resonance frequency remains at 1.7 MHz.

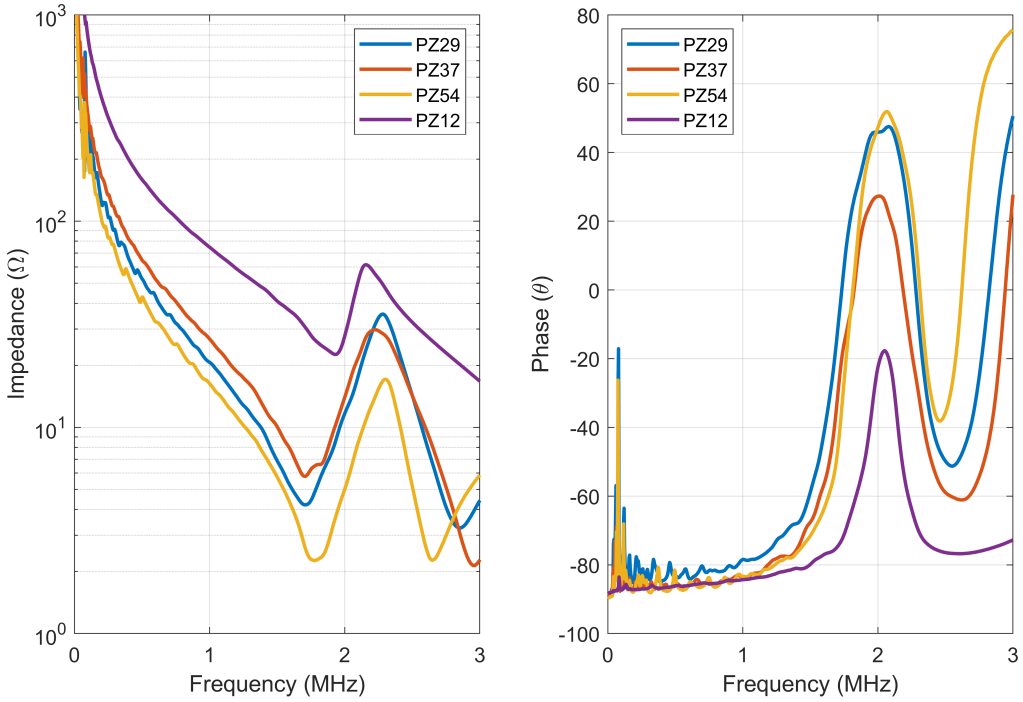

Figure 4.16: The impedance magnitude and phase of all miniaturised FUS devices that have been averaged within the batch, at the final stage of manufacturing.

Figure 4.16 shows the average impedance within the material batches of the miniaturised FUS devices after manufacturing. The batch-to-batch variation exhibited as a mean thickness resonance of (1.74 ± 0.2) MHz. The PZ12 devices are distinguished by the higher impedance at resonance and the smaller variation between the 3 transducers. The impedance phase of PZ12 devices only reaches -20° whereas all the others are positive phase at resonance. When driven at this resonance frequency, the further the phase drifts from zero the more reactive power will be given to the device which does not contribute to the real power of the device.

4.5 Robotic Integration Devices

The FUS transducers are to be coupled to soft tissue by the actuation of a DaVinci surgical robot. Therefore, a prototype sleeve was developed as an attachment mechanism to fit over a device containing a PZ29 disc, Fig. 4.17.

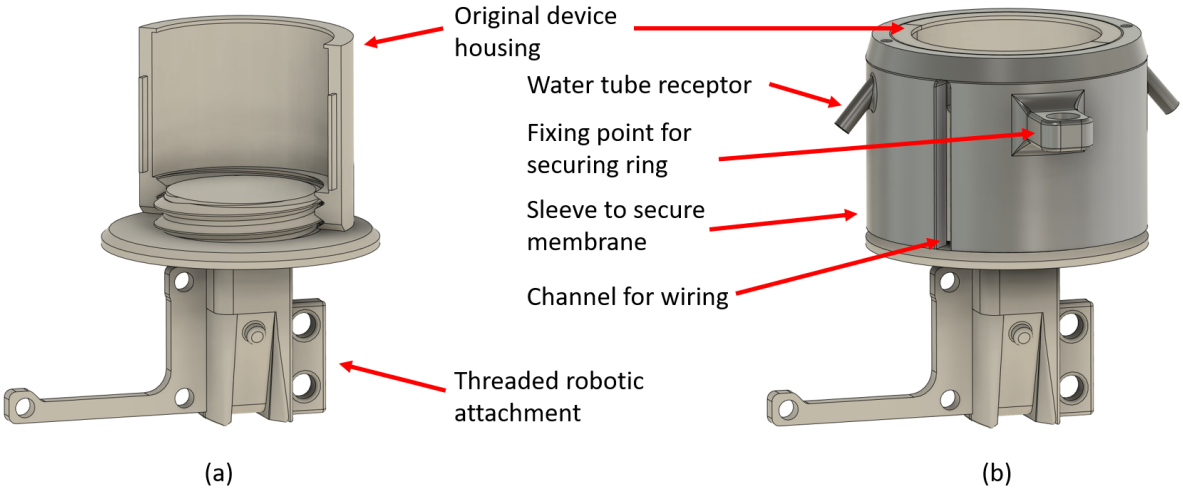

Figure 4.17: (a) An adapted robotic integration attachment fitted to an original housing, (b) with a sleeve fitted over the device.

The attachment interfaces with the threads at the base of the original device, as seen in Fig. 4.17. The left of the daVinci attachment is an L-shaped mount to carry an inertial measurement unit (IMU) and, on the right, two holes enable connection to IR reflectors for camera tracking of the device. Immediately below the threads of the robotic attachment is a ridge that protrudes the diameter of the device by 2.3 mm. The sleeve is fitted to the device from the top and epoxy secures it to the protruding ridge. The wires of the device are aligned with the channel cut in the sleeve, as seen in Fig. 4.17 (b). Two tube receptors are incorporated into the top of the sleeve, which exit on the top rim, and were used to fill a latex membrane on the front of the device with water. Water acts as a coupling mechanism for the ultrasonic energy to propagate into the target soft tissue and latex is a suitable membrane because its thickness is much smaller than the wavelength of pressure waves that propagate through it.

The sleeve was 3D printed and secured to the device, Fig. 4.18. A latex membrane was then fixed with a securing ring to cover the front of the device. On one of the water tube receptors, a syringe full of water was attached, and on the other a tube was connected to a pressure sensor. The syringe was depressed to fill the latex membrane in a convex shape, and the syringe tip valve was sealed to preserve a constant volume of water in the latex membrane. Fresh chicken breast was used as the soft tissue. The increase in pressure as the device was pushed onto the chicken breast (Fig. 4.18 (c)) was used as force feedback for the robotic control system. This force was measured by a pressure sensor exposed to the water within the membrane/housing which was a closed system. This force was tuned

to result in a flat and constant interface between the transducer and tissue. To couple the latex to the chicken breast, a generous layer of ultrasound coupling gel was used, which also decreased the friction between the robot and tissue, maintaining constant force on the tissue surface.

This series of tests was used to develop an autonomous robotic control system to maintain a constant contact force of the FUS transducer on the tissue and move the transducer through a path that could result in ablation of a tumour within the tissue [90]. Ablation experiments were not performed at this stage.

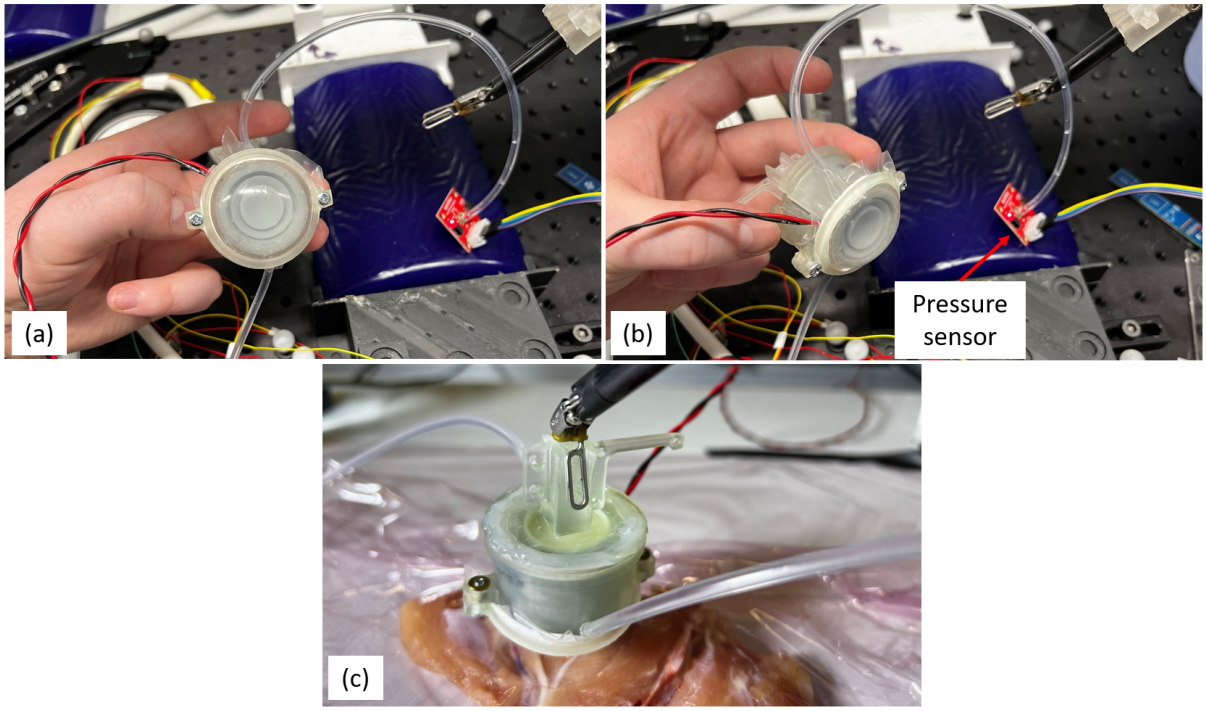

Figure 4.18: (a) The FUS device with latex membrane, (b) the membrane and securing ring seen and pressure sensor. (c) the device actuated with the DaVinvi surgical robot.

The tissue coupling mechanism was incorporated into the housing of the next batch of devices, rather than as a separate attachment. This reduced the diameter of the device. The device housing is shown in Fig. 4.19. The input of the water tube on the inside of the latex membrane was moved to further reduce the outer diameter of the device.

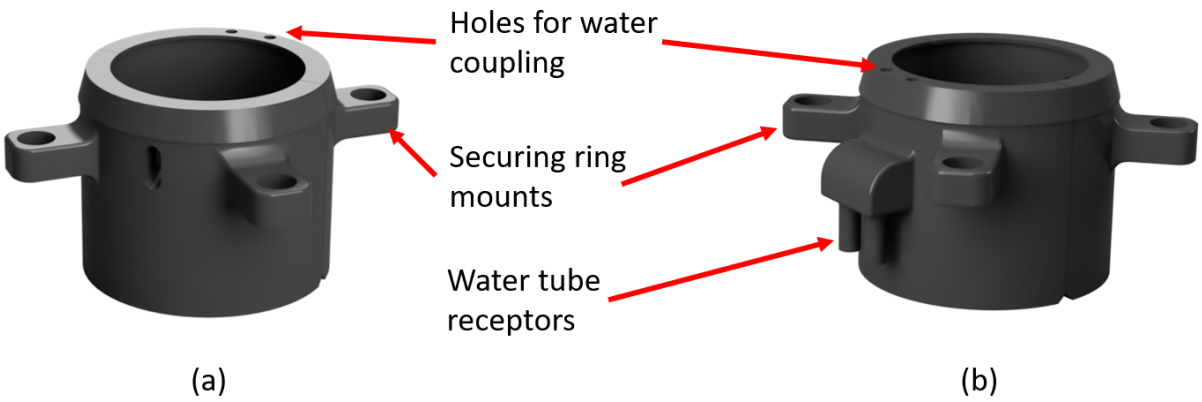

Figure 4.19: The robot coupling mechanism integrated into the housing of the FUS device as seen from the (a) front and (b) back of the housing.

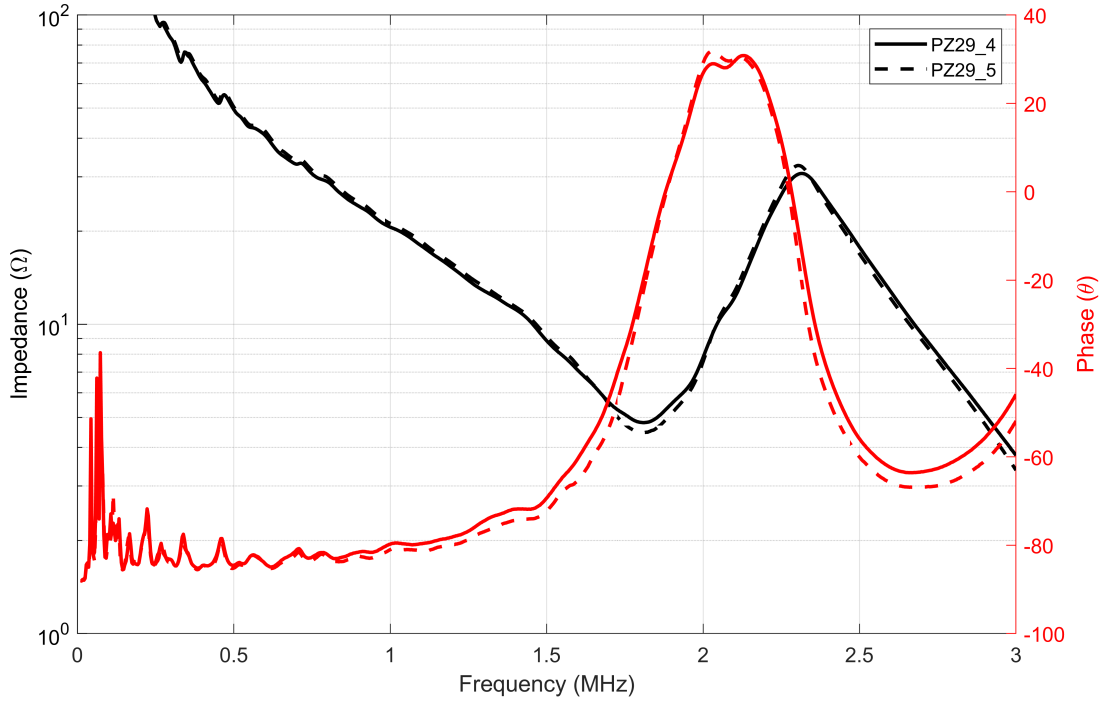

Figure 4.20: Impedance of two FUS devices incorporating PZ29 discs with an integrated tissue coupling mechanism.

The two devices with the tissue coupling integrated into the housing are denoted $D_{PZ29(4)}$ and $D_{PZ29(5)}$ and the impedance is shown in Fig. 4.20. The fundamental thickness resonance was comparable to the other FUS devices with a frequency of 1.8 MHz and phase of -18 °. The small variation between devices verifies good repeatability in the manufacturing process. The final devices are shown in Fig. 4.21.

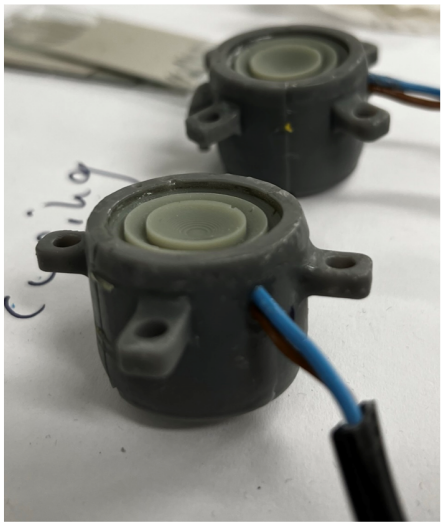

Figure 4.21: Devices $D_{PZ29(4)}$ and $D_{PZ29(5)}$.

4.6 Thermal management integration

Two further modifications were made to the housing design to aid in the dissipation of heat when devices are under load. The housing of one device was manufactured with the same internal components as the original batch of transducers but with a metal outer housing, and one device incorporating internal cooling channels in the housing through which coolant can be pumped. The former was manufactured in a one inch optical lens tube (SM1L10E, ThorLabs, NJ, USA), adding a securing ring to align the Fresnel lens to the front of the lens tube, Figure 4.22. A hole drilled in the side of the metal housing allowed the wires to exit. Shielded RG58 cabling was used and the shielding was soldered to the housing to prevent transmission of electromagnetic frequencies. The shielding was then insulated and reinforced with epoxy and heat shrink. A gap, which was filled with epoxy, between the housing and the piezoelectric disc prevented shorting.

The second design modification to dissipate heat from the piezoelectric element was to integrate channels within the housing for coolant to flow. As discussed in chapter 2.1.3, the cooling channels were designed to cover a large surface area within the walls of the housing. The channels were square holes of 1.4 mm thickness within the 1.8 mm housing

Figure 4.22: FUS transducer with lens tube housing.

walls. This results in a 200 µm wall thickness for heat to transfer through to the coolant. As the housing was manufactured in two halves, two tubes were connected to each half as seen in Fig. 4.23. A Y-splitter allowed for two coolant inputs. This was attached to a 5V DC pump to supply the cooling channel with water.

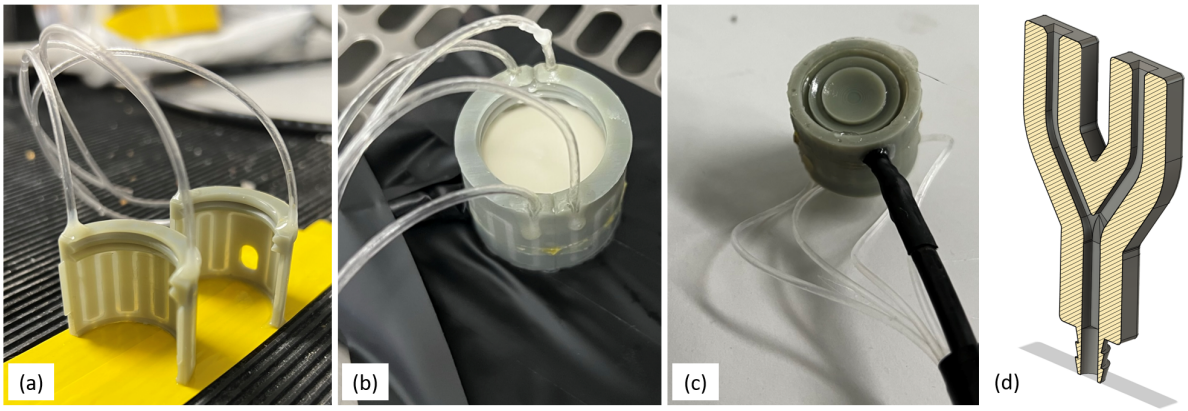

Figure 4.23: (a) Cooling integrated housing with water tubes connected to the cooling channels, (b) the backing layer, (c) a view of the front face of the transducer and (d) the cooling tube splitter.

In this case the piezoelectric disc material in both devices was PZ37 because of its performance when driven at high power. Fig. 4.24 shows the impedance of these two FUS transducers. The impedance magnitudes and phases are a close match, but the impedance is higher than previous devices and the phase is now -40 °. It is expected that the phase is a result of the cabling used, leading to higher capacitance in the system, significantly lowering the phase. As power transfer in AC systems is scaled by $cos(\theta)$, increasing this phase value to zero is important for the device output power. Impedance matching can be used to tune the phase and impedance magnitude to suit the output requirements of the power source.

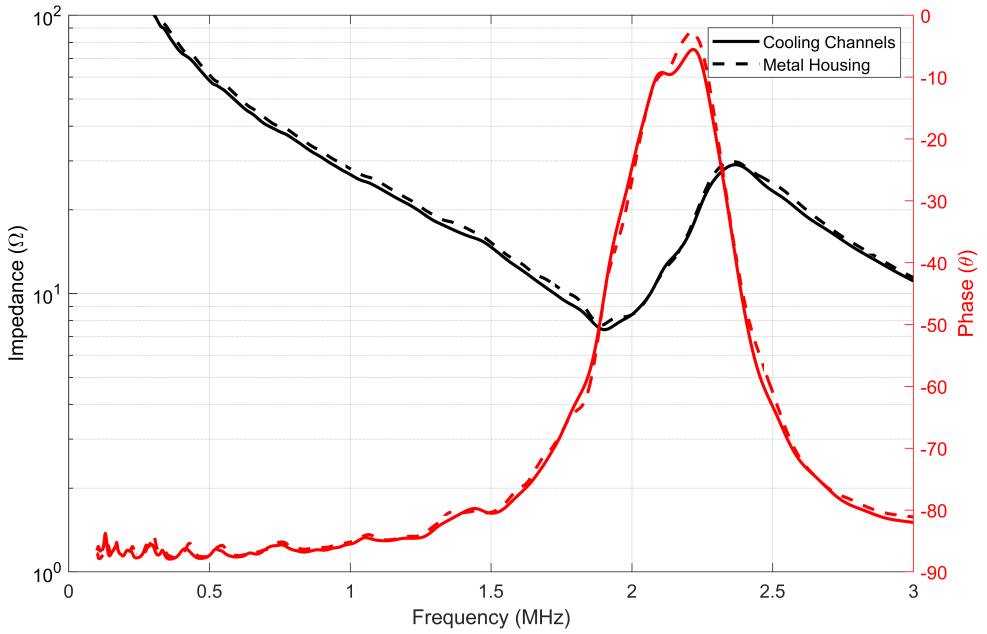

Figure 4.24: The impedance magnitude and phase of the metal and cooling channel housings.

The device manufacturing processes outlined in this chapter resulted in the fifteen waterproof FUS transducers ready for testing in the acoustic scanning tank and radiation force balance. The piezoceramic discs were machined down to a thickness that would produce a thickness mode resonance frequency of 2 MHz. This was achieved by lapping the discs in stages. The electrode that was removed from the disc in this process was reapplied with a spin coated silver ink. A photopolymer was cured in an mSLA 3D printer to form the Fresnel lens and the housing for the FUS transducer. The feature sizes of the Fresnel lens were validated with an optical profilometer to determine the accuracy of the additive manufacturing process. These components were integrated into the batch of FUS transducers with epoxy to secure and align the Fresnel lens and piezoceramic disc to the housing. A backing layer was manufactured and the device was back filled to help with waterproofing. Further devices were manufactured to integrate a force feedback system for robotic control and to manage the heat of the piezoceramic disc when driven at high excitation.

Chapter 5

Electrical Driving

Piezoelectric materials are used in the transduction of electrical energy to mechanical energy (and vice versa). This means that they exhibit both mechanical and electrical characteristics and mechanical parameters have electrical counterparts, which enable a complete representation of a piezoelectric device connected to a power amplifier circuit. Table 5.1 links the mechanical to electrical parameters in Mason's equivalent circuit, which is shown in graphical form in Fig. 5.1.

Electrical Parameter	Mechanical Parameter
Voltage (V)	Force (F)
Current (I)	Velocity (u)
Electrical Resistance (R)	Damping (R_D)
Capacitance (C)	Compliance (inverse of spring stiffness (k))
Inductance (L)	Mass (m)

Table 5.1: Mechanical parameters and the electrical counterparts in an equivalent circuit model.

The mechanical model is the damped harmonic oscillator. This is intuitive as the oscillator has resonance determined by the mass, m, and the spring constant, k, and the damping, R_D. An LCR circuit also has resonance that leads to the electrical equivalence described in Table 5.1. Figure 5.1 (a) shows Mason's equivalent circuit for an ultrasonic transducer where C_0 is the clamped capacitance of the device [91].

The impedance frequency response provides a full characterisation of the dynamics of the device. A typical electrical impedance curve is shown in Fig. 5.2.

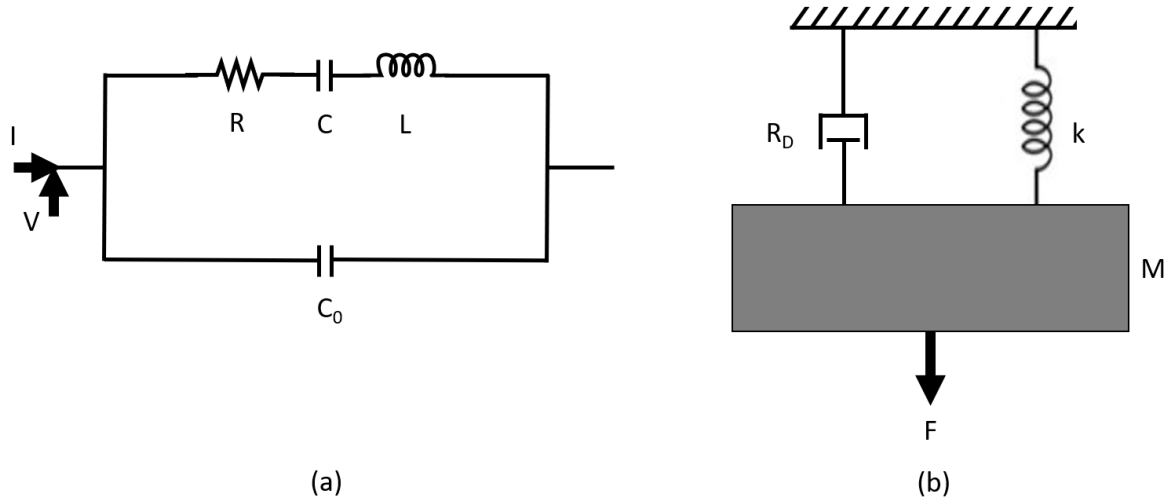

Figure 5.1: (a) Mason's equivalent circuit and (b) the mechanical counterpart, the damped harmonic oscillator

Impedance, Z, and its reciprocal, admittance, Y, are defined in Equations 5.1 and 5.2.

$$Z = R + iX \tag{5.1}$$

$$Y = G + iB \tag{5.2}$$

where R is resistance, X is reactance, G is conductance, B is the susceptance and i is the imaginary unit vector.

The minimum impedance is at the resonance frequency (f_r) and the maximum impedance is at the antiresonance frequency (f_a). At these frequencies the phase is zero degrees, so the impedance is real and has no imaginary component. Therefore, the resonance frequency can be identified as the maximum conductance, and the antiresonance frequency is the maximum resistance. The impedance of an LCR circuit can be described by Eq. 5.3.

$$Z = \frac{1}{i\omega_0 C_0} \frac{(\omega^2 - \frac{1}{LC}) - \frac{\omega R}{L}}{(\omega^2 - \frac{C_0 + C}{LC_0 C}) - i\omega\frac{R}{L}} \tag{5.3}$$

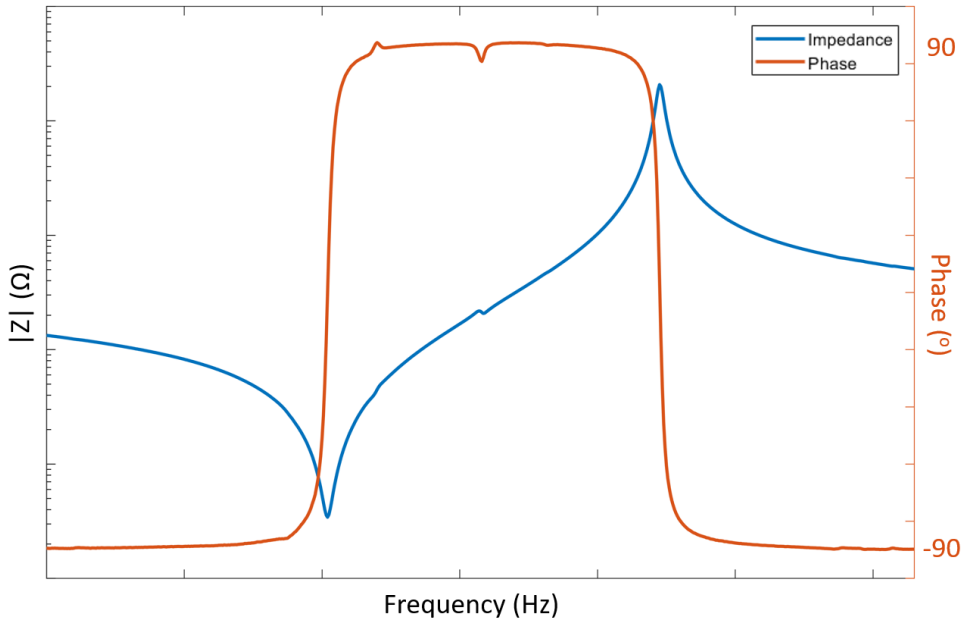

Figure 5.2: A typical electrical impedance frequency response

where ω is the driving frequency ω_0 is the circuit resonance frequency and i is the imaginary unit vector. By omitting the contribution of resistance in Eq. 5.3 the resonance and antiresonance frequencies, ω_r and ω_a can be obtained from Eqn. 5.4 and Eqn. 5.5, respectively.

$$Z \to 0, \omega = \sqrt{\frac{1}{LC}} = \omega_r \tag{5.4}$$

$$Z \to \infty, \omega = \sqrt{\frac{(C_0 + C)}{LC_0C}} = \omega_a \tag{5.5}$$

Therefore, the resonance frequency corresponds to a short-circuit condition in the LCR circuit, and the antiresonance corresponds to an open circuit.

The impedance characteristics at resonance are dependent on the piezoelectric device and are sensitive to factors such as input power and temperature. Therefore, a method of electrically driving the device at the correct impedance must be realised. A typical power amplifier has a standard electrical output impedance of 50 Ω. Piezoelectric devices can have an impedance at resonance lower than this (such as the devices in this work), or larger, such as Langevin transducers [92]. An impedance mismatch between the load and source leads to reflection of the electrical power and decreased efficiency of the device being powered.

5.1 Electrical Impedance Matching

Adjusting the load impedance to maximise power transfer from a source is known as impedance matching. There are two methods useful in impedance matching of ultrasonic devices, complex conjugate matching and complex impedance matching. The former is applied when the source and load impedances are fixed (or too far apart to be adjusted appropriately). In this case, the aim is to negate the difference in reactance such that $Z_{load} = Z^*_{source}$ (where * denotes the complex conjugate). Which can be achieved if the load impedance can be reduced to equal the source impedance [93].

The efficiency of an amplifier, with a source impedance of 50 Ω, for increasing load impedance is shown in Fig. 5.3. The relationship is given in Eq. 5.6 [94].

$$r_{12} = \frac{Z_2 - Z_1}{Z_2 + Z_1} \tag{5.6}$$

where Z_2 is the load impedance, Z_1 is the source impedance, and r_{12} is the power reflection from impedance one to two. This reflection is normalised and shown as efficiency in Fig. 5.3. At 50 Ω a zero reflections perfect match and the 100% efficiency is achieved in an idealised device. The efficiency of power transfer to the load is less than 10% if the load impedance is <2.5 Ω or >1 kΩ. Impedance matching is therefore critical to resolve these losses.

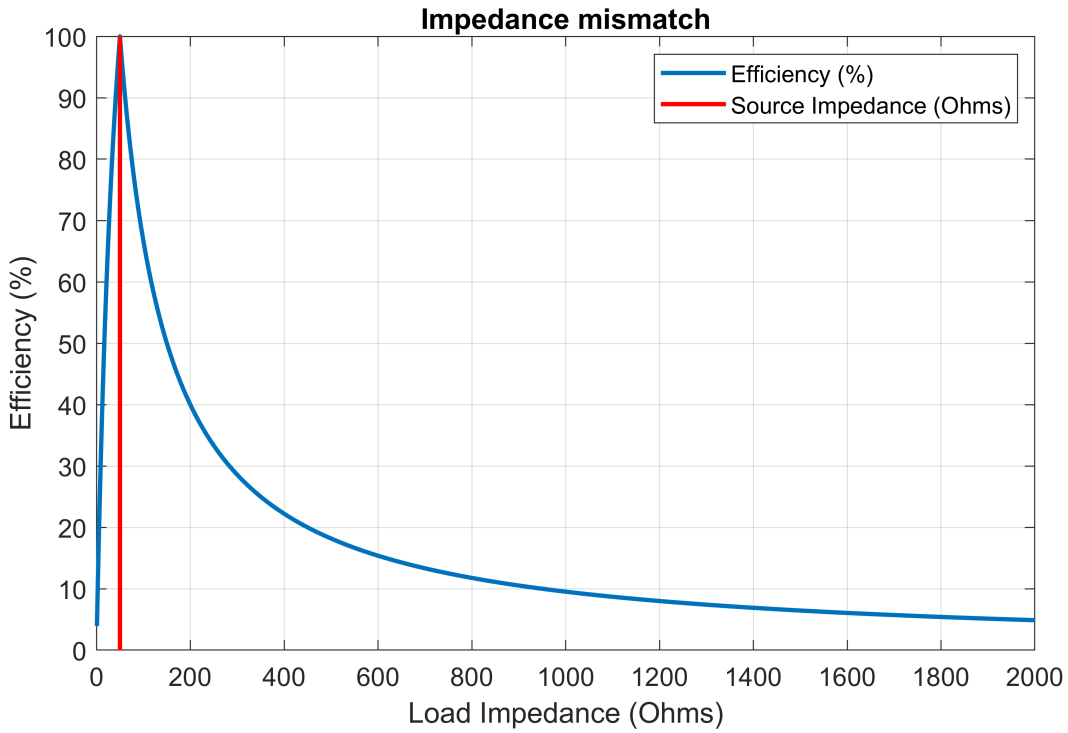

Figure 5.3: Efficiency of power transfer from a 50 Ω source to a load for increasing impedance of the load.

5.1.1 LC Matching Systems

Complex conjugate matching focusses on negating the imaginary component of impedance, reactance. Reactance in a circuit can be influenced by two components, a capacitor and an inductor. Capacitive reactance is an opposition to the change in voltage and is expressed in Eq. 5.7.

$$X_C = -\frac{1}{\omega C} = -\frac{1}{2\pi f C} \tag{5.7}$$

where f is the frequency and C the capacitance.

The capacitor at DC creates a large difference in charge across two conductive plates and hence acts as an open circuit and inhibits the flow of current. The reactance in this case is infinite. As the frequency of the signal across the capacitor increases to infinity the opposite occurs where a short circuit condition is realised and the reactance goes to zero.

For a positive reactance an inductor is utilised. The inductor consists of wire wound around a ferrous core. The excitation of an electric field in the wire produces a perpendicular magnetic field. With alternating current in the wire, the magnetic field is constantly changing, which leads to a corresponding electric field in the ferrous core. The magnetic field in the core is in a direction that opposes the current which initiated the process. Hence, inductive reactance is the opposition to the change in current, Eq. 5.8.

$$X_L = \omega L = 2\pi f L \tag{5.8}$$

where L is the inductance.

The inductance is positive reactance and therefore influences the phase of voltage to current. In a purely inductive circuit the voltage leads current by $\frac{\pi}{2}$ whereas for a capacitive reactance, the voltage lags current by $\frac{\pi}{2}$. For an idealised piezoelectric transducer this results in a pure mode seen in Fig. 5.2. Below resonance and above antiresonance the phase is -90 degrees, capacitive, while between resonance and antiresonance phase is +90 degrees, inductive.

An impedance matching circuit can be calculated in multiple ways. The equivalent LCR circuit can be simulated on an impedance anlyser. The matching network values are calculated and the circuit is placed between the device and impedance analyser to check the new apparent impedance. A graphical representation of a Smith chart is shown in Fig. 5.4 [95].

If the impedance is represented a graph, where resistance, R, is the x-axis and the reactance, X, the y-axis, the negative portion of the x-axis is not used, because the resistance is always positive. This indicates that all negative values on the y-axis are capacitive and positive values are inductive. The smith chart bends the y axis around to form circles of equal resistance.

The right hand side of the Smith chart is the impedance side (red) and on the left side is the admittance side (blue). The chart can be normalised to the source impedance; however, in this example all values are with respect to a 50 Ω source impedance. The value of 50 Ω can be observed in the centre of the chart and lies on the only straight line; this line is purely resistive. A purely resistive 50 Ω source impedance is the point at the centre of the Smith chart and the load impedance is measured and plotted elsewhere. The closer the measured point is to the middle of the chart, the closer the impedance matching is. The top half of the chart represents the inductive reactance and the lower half is the capacitive.

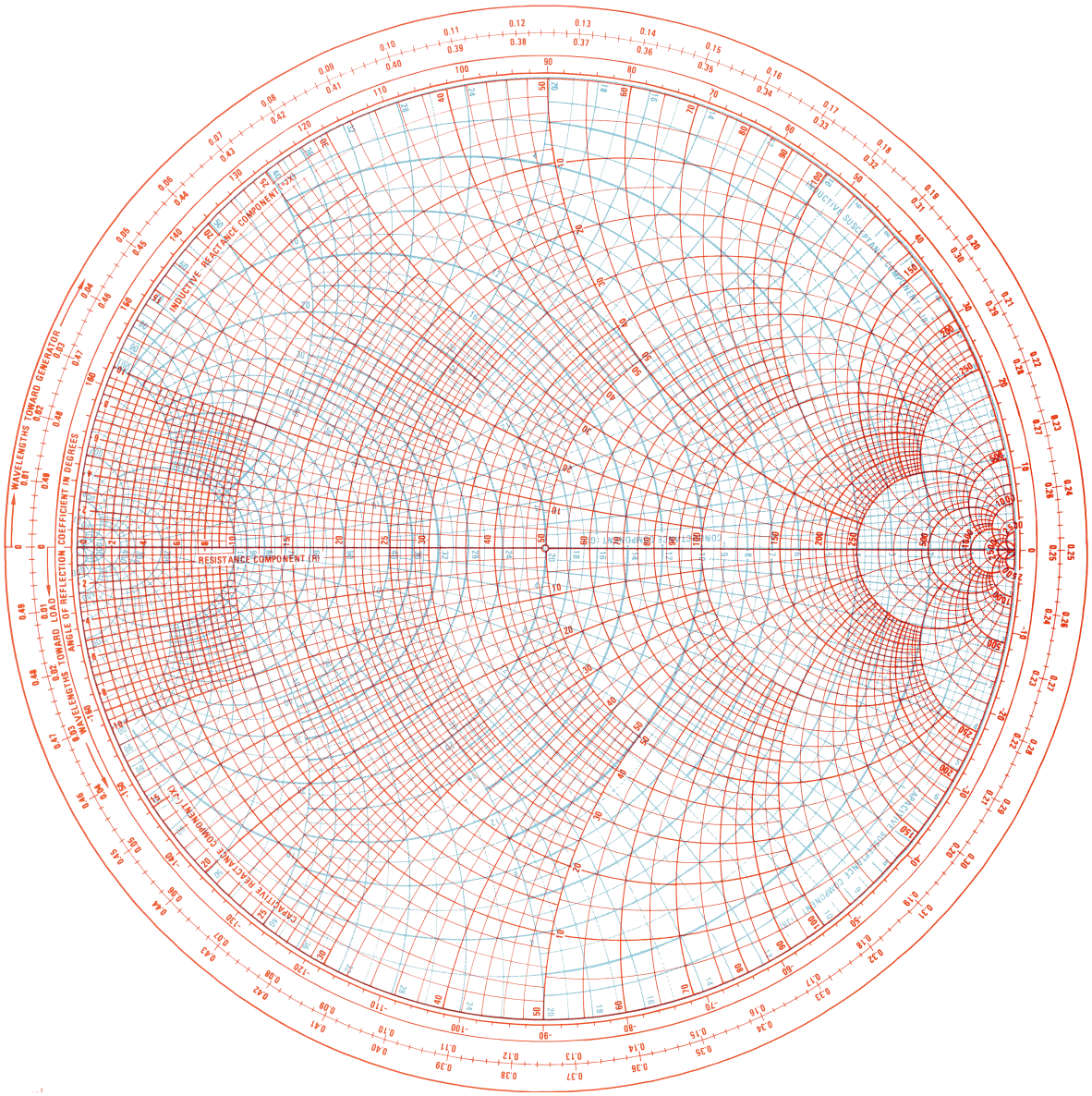

Figure 5.4: The combined admittance (blue) and impedance (red) Smith chart for impedance matching (also known as a immittance chart).

An example of using the Smith chart is shown in Fig. 5.5. The measured impedance of the device is shown as a green dot that has an impedance of $Z_L = 100 + j80$. This is found by tracing the red impedance line back to the resistance axis for the real part and tracing the red impedance line to the outer edge of the Smith chart to read the imaginary part. The reciprocal can also be read from the admittance side of the graph to obtain $Y_L = 0.0061 - j0.0049$. The path for the point to traverse to move towards the middle of the chart for perfect matching is indicated. The first step (green arrow) moves along the admittance circle (blue) to where it intersects the 50 + jX circle. As this is moving in the direction of negative reactance, this is realised by adding a capacitor. The difference in the susceptance from the starting point to the end point is the value of susceptance that will be added via the capacitor. The complex reciprocal of this value provides a reactance to be converted to capacitance. Similarly, because the movement of the point is along the admittance circle, this is realised by adding the reactive capacitance in parallel. After the intermediate step, the orange arrow moves along the impedance circle. This is achieved by a series component and in the positive direction of reactance is realised by an inductor. The value of reactance to be provided by the inductor is the difference in reactance from the intermediate step coordinates to the final matched coordinates on the Smith chart.

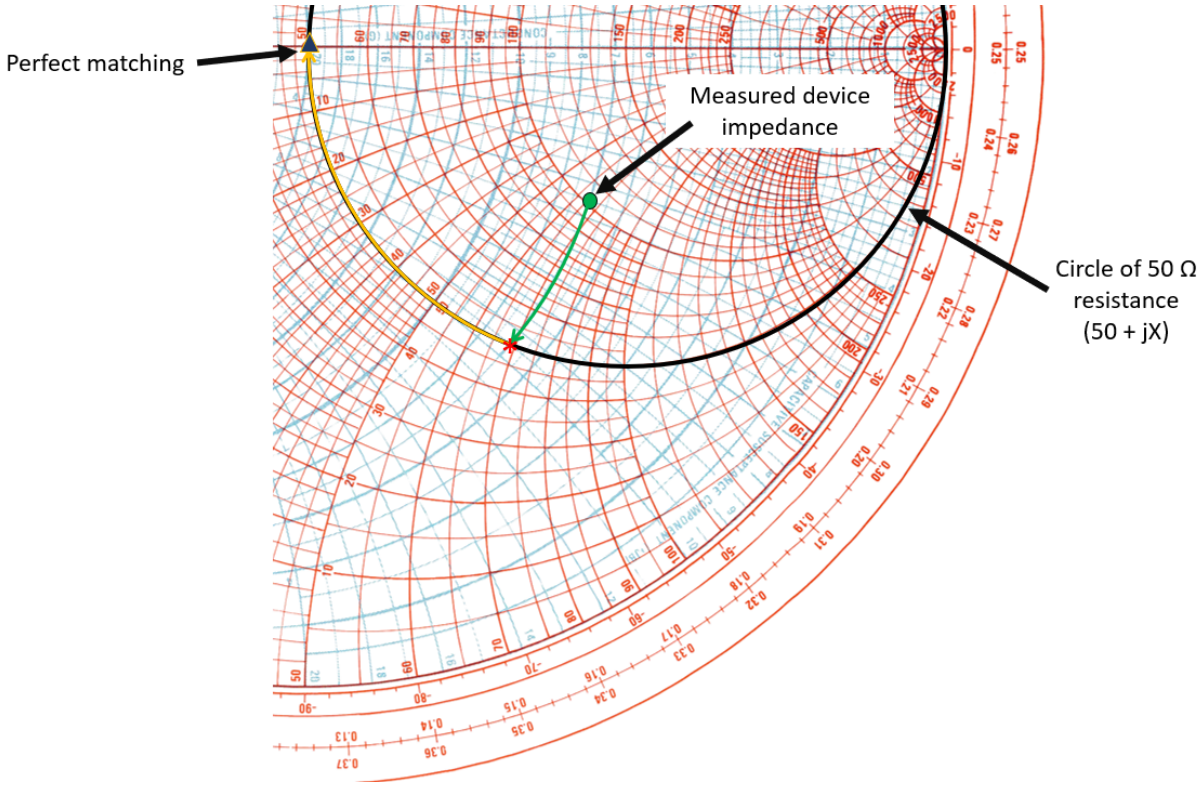

Figure 5.5: A cropped view of a Smith chart showing the path taken for a measured impedance to be impedance matched with an LC circuit.

As the impedance of the arbitrary load is within the circle of 50 Ω resistance (a real component of the impedance greater than 50), the LC circuit follows the design of Fig. 5.6 (a). This information leads to a solution of a series inductor followed by a parallel capacitor. The values can be calculated following the equations in Table. 5.2.

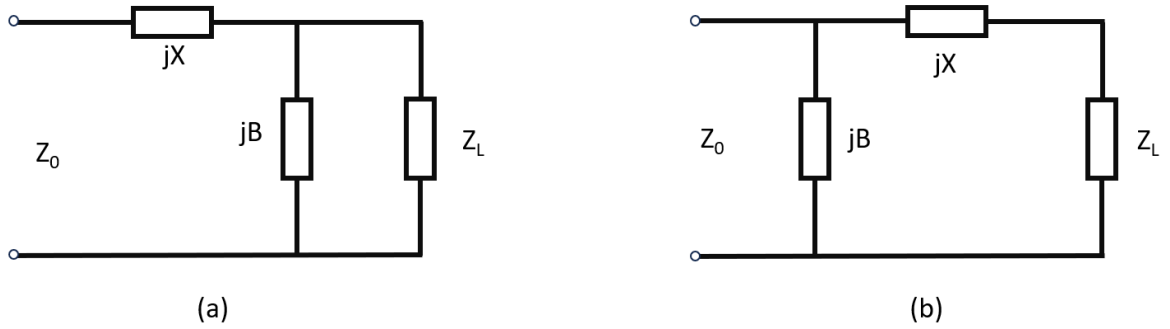

Figure 5.6: The two options of LC matching circuit where (a) is chosen if the load impedance is within the 50 + jX circle and (b) where the load impedance is outside the 50 + jX circle. X is reactance and B is susceptance.

Value	Required L or C	Relationship
-ve b	L	$L = \frac{Z_0}{2\pi f b}$
+ve b	C	$C = \frac{b}{2\pi f Z_0}$
-ve x	C	$C = \frac{1}{2\pi f x Z_0}$
+ve x	L	$L = \frac{x Z_0}{2\pi f}$

Table 5.2: Calculation of inductance and capacitive values for elements in Fig. 5.6, where b and x are normalised values of susceptance and reactance.

Normalised susceptance, b, and reactance, x, in Table 5.2 are calculated from Eqns. 5.9 - 5.11:

$$b = \frac{B}{Y_0} = BZ_0 \tag{5.9}$$

$$x = \frac{X}{Z_0} \tag{5.10}$$

$$Z_0 = \sqrt{\frac{L}{C}} \tag{5.11}$$

where Z_0 and Y_0 are the characteristic impedance and admittance, respectively.

The FUS transducers all have an impedance outside the 50 + jX circle, so the LC circuit must conform to Fig. 5.6 (b). This is confirmed by transducers with similar characteristics being matched with a series inductor and parallel capacitor in literature [96]. However, due to the equivalent circuit described in Fig. 5.1, adding inductance can decrease the resonance frequency (due to increasing the mass in the equivalent spring mass damper). The FUS transducer must operate at 1.5 MHz and thererfore an alternative matching solution is required.

5.1.2 Transformer Matching

In electronics, transformers are used to manage impedance in audio equipment, isolate circuits from floating ground (DC offset) [97] and for power distribution in high-voltage power lines [98]. Transformers are often called coupled inductors because of their use of an oscillating electric current in a wire that excites magnetic fields around the wire, as shown in Fig. 5.7. This is coupled into a ferrous core by inducing an electric field within it, leading to a second induced magnetic field generated by the core. This magnetic field opposes the direction of the initial magnetic field. Therefore, a single-wound coil is a pure inductor. Pure inductance can be thought of as electrical inertia, that resists the change in field polarity. However, a transformer has another coil of wire around the core, leading to a transformation of the magnetic field generated by the first coil into the second. The relationship between the oscillating electric field in each set of wires is related to the number of turns in each.

In Fig. 5.7 (b), the red wire represents the primary winding, with the higher voltage, V, and a higher number of turns, N. The impedance of the primary winding circuit, Z, is also higher, however current is lower on this side. This is due to the conservation of power across the transformer. As the voltage is decreased to the secondary windings (green), the current increases to maintain constant power. The relationship is described in Eq. 5.12.

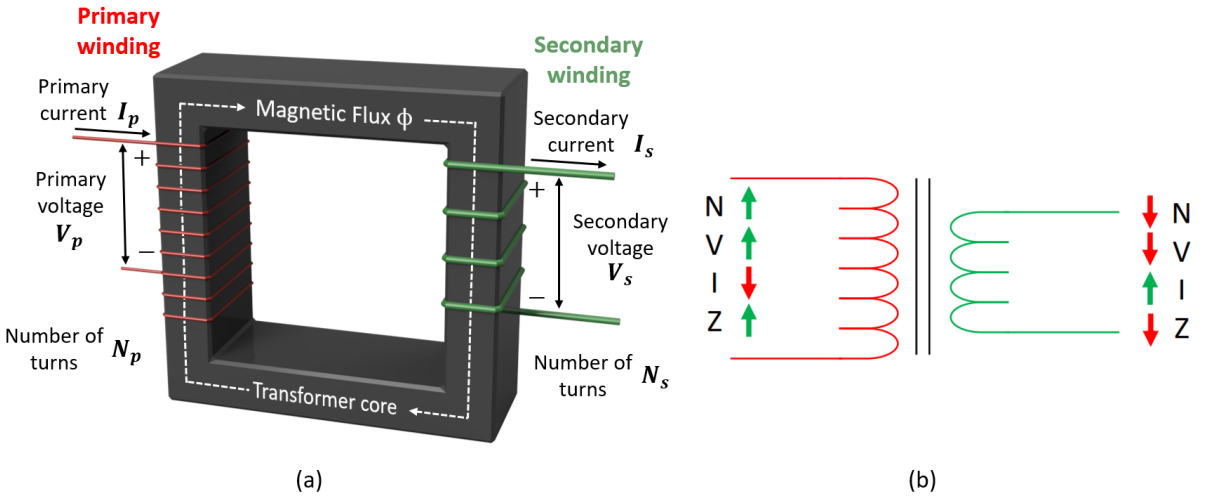

Figure 5.7: (a) A transformer schematic and (b) circuit diagram showing the transformation of the electric field in each winding.

$$\frac{V_p}{V_s} = \frac{I_s}{I_p} = \frac{N_p}{N_s} = a \tag{5.12}$$

where V is voltage, I is current, N is the number of turns, and a is the turns ratio. The primary coil is indicated by subscript p and the secondary coil is indicated by subscript s. The impedance transformation is given in Eq. 5.13.

$$Z_p = a^2 Z_s \tag{5.13}$$

where Z is the impedance of the circuit on the primary and secondary side of the transformer. Therefore, tuning the turns ratio to allow for the transformation of impedance from one side of the transformer to the other cannot be decoupled from the change in voltage and current dictated by the turns ratio. Transformers also have inherent losses and additional reactance which can be managed but not negated.

The losses and reactance of a transformer can be explained using a cross-sectional view, Fig. 5.8. The magnetic field generated by the primary winding extends out to the ferrous core and, in a standard set-up (Fig. 5.7 (a)) it does not influence the secondary windings. In an E core (Fig. 5.8 (a)), the two windings are wrapped much closer so that the field lines

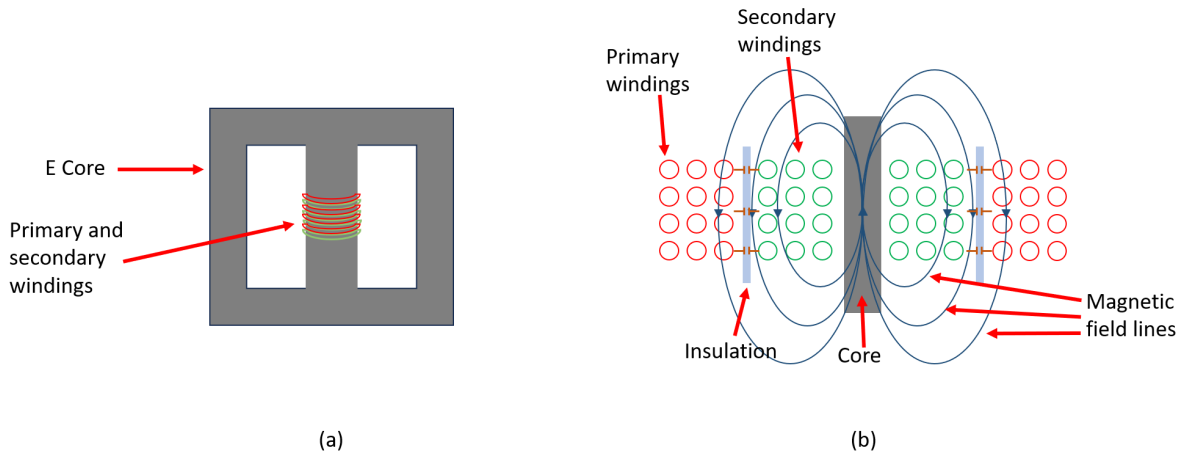

Figure 5.8: Schematic of a transformer (a) showing an E-core and winding overlap and (b) a cross sectional view of the magnetic fields induced.

are coupled directly to the other side and the coupling is increased. The cross section of this transformer in Fig. 5.8 (b) shows the magnetic field in the core. This is the strongest coupling route and is preferred, to enable the characteristics of an inductor mentioned previously. However, there is also leakage reactance which is the magnetic field generated by the windings locally in the space immediately surrounding them. The magnetic flux of these fields is in-phase with the currents that create them. If the secondary side is connected to a purely inductive load, the load current and the circulating magnetic flux will lag the primary voltage by $\frac{\pi}{2}$. As induced voltages are proportional to the rate of change of flux, any flux pointing upwards in this space around the windings will induce voltages in phase with the applied voltage. However, any flux pointing downward induces a voltage out of phase (π) with the applied voltage. This leads to a decrease in the voltage which is otherwise induced in the secondary winding, equivlant to a leakage impedance applied in series with the ideal transformer output. In practice, leakage reactance is useful because it limits short-circuit currents, but it also reduces the secondary voltage under load, known as regulation, which consumes reactive power. To manage these losses, the windings can be placed close together. This leaves less free space between them, reducing the leakage reactance and increasing apparent coupling. This is shown in Fig. 5.8 (b) as a capacitance between windings and the distance is controlled by the thickness of insulation applied.

Losses within the conducting wires are known as winding resistance. For DC, the resistance of the wire is simply a function of its length divided by the cross-sectional area. For AC, there are additional losses. When an alternating magnetic field is applied to a conductor, eddy currents are induced around the magnetic field lines. These currents generate local losses even when the conductor is not carrying a current. Therefore, any conductor that is placed within the magnetic field lines, but is electrically isolated from the windings of the transformer, also generates eddy currents and adds to the losses of the transformer.

The skin effect is also a source of resistance in a conductor. The magnetic field created by the flow of current in the conductor can be shown as concentric circles following the current. The flux density at any point is proportional to the total current enclosed by the magnetic path over the length of the circular path. The total current enclosed by the magnetic path increases at a greater rate than the circular path length, towards the outer edge of the conductor. This leads to a higher flux density towards the edge and a decrease near the centre, forcing more current to flow on the edge of the conductor. This is known as the skin effect.

The total AC resistance is given in Eq. 5.14.

$$R_{AC} = R_{DC} + R_e + R_s \tag{5.14}$$

where R_{DC} is the total conductive loss at DC (I^2R), R_e is the total eddy loss and R_s is the loss due to skin effect. These are known as load losses and increase with respect to load current.

The FUS devices that require impedance matching operate at a frequency of 1.5 MHz. At this frequency, the transformer core must be ferrite. Ferrite is a ceramic created by pressing an oxide powder and binding it by sintering. This reduces the electrical inertia created by inductance by limiting the eddy currents generated within the core to each small grain size. Nickel-zinc and manganese-zinc are ‘soft’ ferrites, known to have higher resistivity caused by smaller eddy currents that reduce opposition to higher frequencies

and allow for operation in the MHz range. The manufacturer data sheet for the transformer cores quotes a value of inductance per turn of wire which can be used to calculate the additional reactance. A matching transformer can be realised by considering these laws and designing around the losses outlined.

5.2 Manufacturing Transformers for Impedance Matching

For a transformer for the FUS device operating at a frequency of 1.5 MHz there is one option for core material, a ferrite core. The thickness and type of wire was then selected to minimise winding resistance and was sized to support the current required on the transducer side of the transformer. An enammel coated single core copper wire with a diameter of 0.7 mm was selected with a current rating of 1.6 Amps [99]. The wire is wrapped around a coilformer so the ferrite core can be moved indipendantly of previously wound cores. A coilformer was selected that allows for approximately 32 winds per layer. The E-core size is also called E42 with a material rating of N87. The rating of the core determines the purity of the material, where a higher value indicates lower losses within the core [100]. With no air gap, the core generates an inductance of 3950 nH per turn of wire added. However, the inductance per turn can be dropped to 201 nH with a 1.5 mm air gap between the core halves. The inductance can also be optimised by changing core type.

The turns ratio required for a matching transformer was calculated for all devices. If the variation in impedance magnitude was minimal between devices then one transformer could match multiple devices. A list of manufactured transformers can be found in Table 5.3. The devices made are named after the material in them. This leads to the first three devices made from PZ29 are named $D_{PZ29(1)}$, $D_{PZ29(2)}$ and $D_{PZ29(3)}$. The specially made devices with cooling channels incorporated into the housing design is named D_{PZ37cc} and the metal housing device is D_{PZ37mh}.

Transformer	Matched device	Turns ratio (a)	Impedance magnitude (Ω)	Phase (°)	Resonance frequency (MHz)
1	$D_{PZ29(1)}$	3.13	52.54	-6.5	1.58
	$D_{PZ29(3)}$		53.61	-13.5	1.55
2	$D_{PZ29(2)}$	3.19	58.42	-12.5	1.58
3	$D_{PZ29(4)}$	3.54*	50.08	-7.4	1.52
	$D_{PZ29(5)}$		45.91	-17.0	1.58
4	$D_{PZ54(1)}$	4.70*	51.30	-3.5	1.48
5	$D_{PZ54(2)}$	4.60	48.00	-2.6	1.44
	$D_{PZ54(3)}$		45.21	-2.0	1.44
6	$D_{PZ37(1)}$	3.16	40.23	-14.1	1.53
	$D_{PZ37(2)}$		42.35	-8.4	1.58
	$D_{PZ37(3)}$		44.89	-14.4	1.59
7	$D_{PZ12(1)}$	1.5	N/A	N/A	N/A
	$D_{PZ12(2)}$		22.10	-29	1.81
	$D_{PZ12(3)}$		30.01	-4.5	1.93
8	D_{PZ37cc}	2.5	44.74	-12.5	1.62
	D_{PZ37mh}		45.41	-13.0	1.60

Table 5.3: Transformers used to match the FUS devices (* required more windings to decrease resonance frequency than other devices)

Devices with small variations in the resonance magnitude and frequency were grouped and driven with the same transformer, Table 5.3. In the case of $D_{PZ29(4)}$ and $D_{PZ54(1)}$, the impedance magnitude was similar to other devices within the batch, however the resonance frequency was different enough to justify a separate matching transformer. More internal winds were added while keeping the turns ratio similar to the other devices of the same piezoelectric material.

The turns ratio is fixed to achieve the target magnitude of impedance, therefore the number of primary turns depends on the inductance generated by the total number of turns in the transformer. Too much inductance is equivalent to adding mass to the spring-mass system, which will decrease the resonance frequency. This positive reactance (inductance) also increases the phase at resonance, which will decrease the real power transferred if the phase increases away from zero degrees. For these reasons, the total turns in the transformer were minimised. However, too few turns in the primary coil can lead to saturation of the ferrite core. As saturation is dependant on the magnetic flux density, a low number

of turns on the primary coil means that the magnetic field is concentrated around a few turns rather than spread over many. Therefore, transformers were tuned at low power to minimise inductance for the total turns such that the resonance frequency stays above 1.5-1.6 MHz. This allows the number of turns on the primary side to be maximal without compromising the resonance frequency.

To manufacture the transformers, the low impedance side was wound first, often 8-15 turns (Fig. 5.9 (a)). A layer of electrical insulation tape was added to isolate the inner windings from the outer winding (Fig. 5.9 (b)). The high impedance windings were then added (Fig. 5.9 (c)). The core was added to the wound transformer and the ends were connected to BNC connectors and placed in an electrical isolation box to mitigate the chance of contact with a high power transformer (Fig 5.9 (d) and (e)).

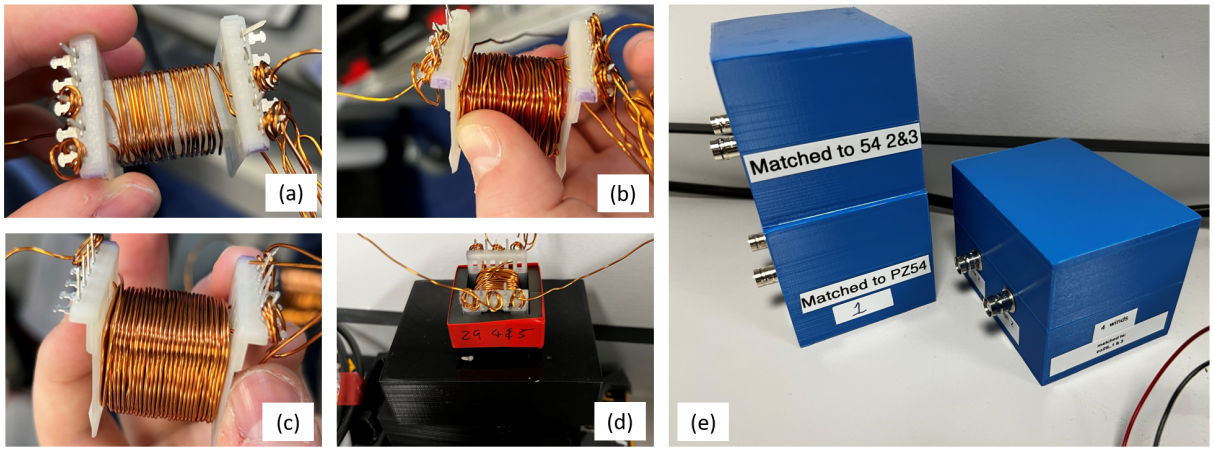

Figure 5.9: The process of manufacturing a transformer with (a) the low impedance coils, (b) a layer of isolation tape and first turns of high impedance coil, (c) the completed high impedance coil, (d) labelled transformer with core added and, (e) transformers in electrical isolation boxes with BNC connections.

5.2.1 Transformer testing

A coupling test was performed on the transformers to ensure that there was no air gap. The equation for coupling is given in Eq. 5.15.

$$k = \sqrt{1 - \frac{L_{short}}{L_{open}}} \tag{5.15}$$

where L_{short} is the inductance of the primary coil when the secondary is electrically shorted and L_{open} is the inductance of the primary coil when the secondary coil is open. The coupling was measured for both an air core (no core) and a ferrite core. With an air core the transformer coupling was on average 59% efficient whereas with a ferrite core this value rises to >99%. Air gaps were easily detectable with the ferrite core coupling value decreasing rapidly. This led to further cleaning and resetting to ensure the coupling was higher than 99%.

Device $D_{PZ29(4)}$ was used in an experiment to determine the effect of transformer inductance on the impedance. Figure. 5.10 shows an impedance measurement of a transformer with an increasing number of primary winding turns. With the maximum number of turns on the first layer of the coilformer (29 winds), the transformer moves the device resonance frequency to 1.05 MHz. The number of turns of the primary coil was then reduced, while keeping the turns ratio consistent. With a primary coil of 14 turns the resonance is closer to the target of 1.5 MHz, however at 12 turns the resonance frequency is at 1.6 MHz. The number of turns on the secondary coil was therefore overestimated and were therefore decreased, hence decreasing the turns ratio and therefore the magnitude of impedance at resonance. At 12 internal winds and an in situ adjustment of - 12 winds from the secondary coil, the resonance frequency was 1.5 MHz with a magnitude of 50 Ω.

The in situ tuning of each transformer was necessary to mitigate any fluctuations in resistivity from the transformer fabrication and installation into the isolation boxes. The isolation box includes two BNC adapters to allow for a quick change of transformers/devices in experiments. The adhesion to the BNC terminations with solder changed the characteristics of the transformers enough for additional adjustment to be necessary. This was caused by the FUS devices having an impedance of less than 10 Ω, meaning the resistance in the cabling and connections was proportionally significant.

The results of impedance matching of the FUS devices of each piezoelectric material are shown in Fig. 5.11. The target driving frequency and source impedance are shown as two red lines. The unmatched devices (in dashed lines) are between 2 and 10 Ω with the exception of PZ12. With impedance matching, the magnitude and resonance frequency can be tuned to suit the application.

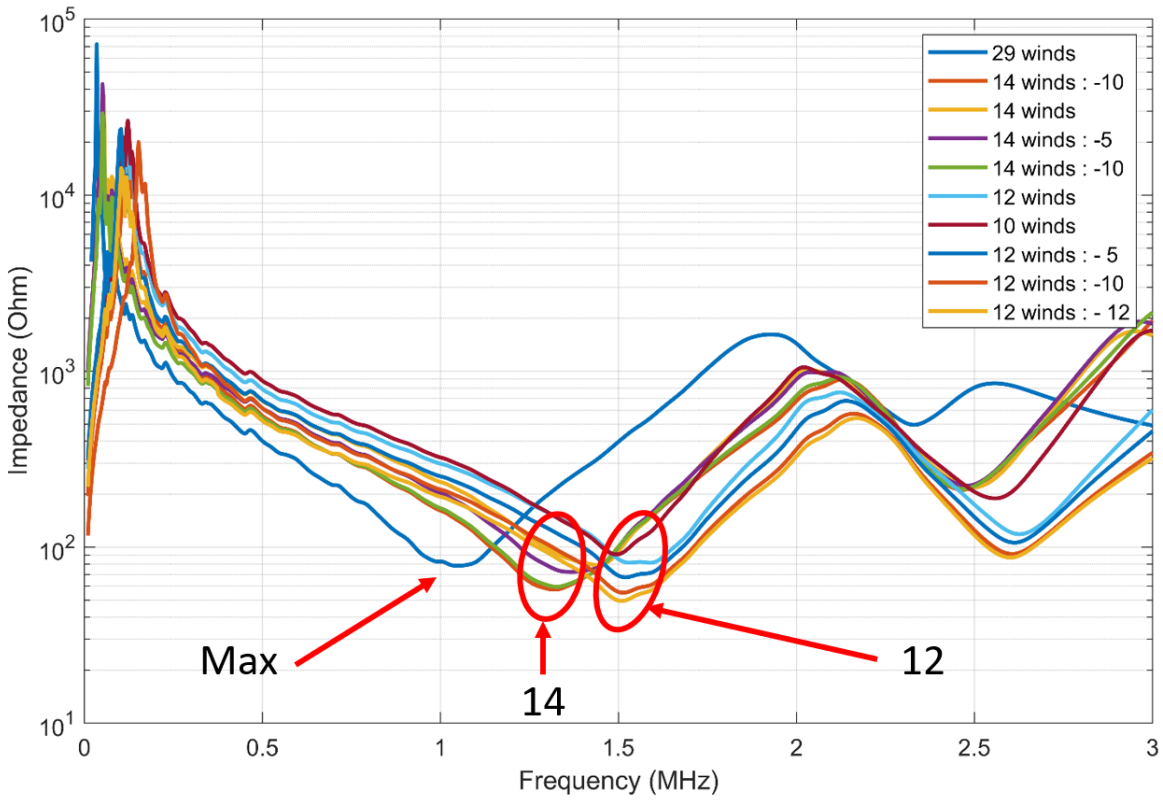

Figure 5.10: The impedance magnitude of $D_{PZ29(4)}$ during the process of tuning a matching transformer.

The FUS devices incorporating PZ12 did not respond to transformer matching in the same way as the others. The impedance magnitude was 17 Ω and therefore the turns ratio was less than that of other devices that started at much lower impedance. This led to a smaller number of total turns, which did not reduce the resonance frequency significantly. Lead-free PZ12 has lower piezoelectric coefficients and low permitivity. It is more capacitive at resonance and does not reach +90 degrees impedance phase at resonance. These characteristics mostly affect the reactance of the device, which the transformer does not change significantly.

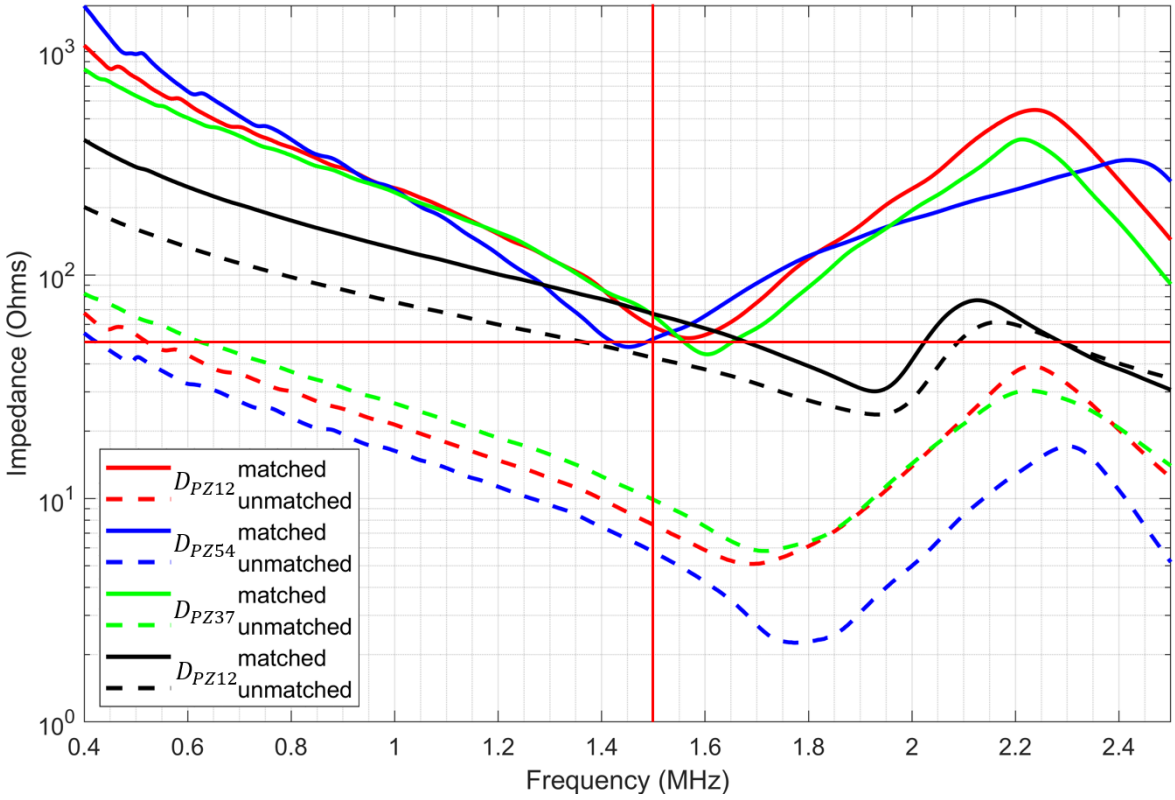

Figure 5.11: Impedance of unmatched (dashed line) and matched (solid line) FUS devices, with the source impedance and target frequency indicated by solid red crosshairs

5.3 High Power Driving and Electrical Efficiency Validation

The impedance measurements previously shown of the matched devices show the apparent impedance as seen by the source. However, an RF amplifier (E&I, NY, USA) displays the power output with forward and reflected powers. This is a real indication of matching in the system. The reflected power caused by an impedance mismatch of FUS device $D_{PZ37(1)}$ at 1.5 MHz is shown in Fig. 5.12 (a). $D_{PZ37(1)}$ has an unmatched impedance magnitude of 10Ω. As the drive signal supplied to the amplifier is increased, the power output by the amplifier increases in a linear trend up to 600mVpp. After this, the impedance mismatch has reflected back enough power to the amplifier that the amplifier overheats. Although the amplifier is actively cooled, the motherboard decreases power output if heated beyond 70°C. The losses at higher driving voltages are masked by other non-linearities due to the heating of the piezoelectric element. However, at low drive voltages the reflected power is 66%, which is consistant with Eq. 5.6.

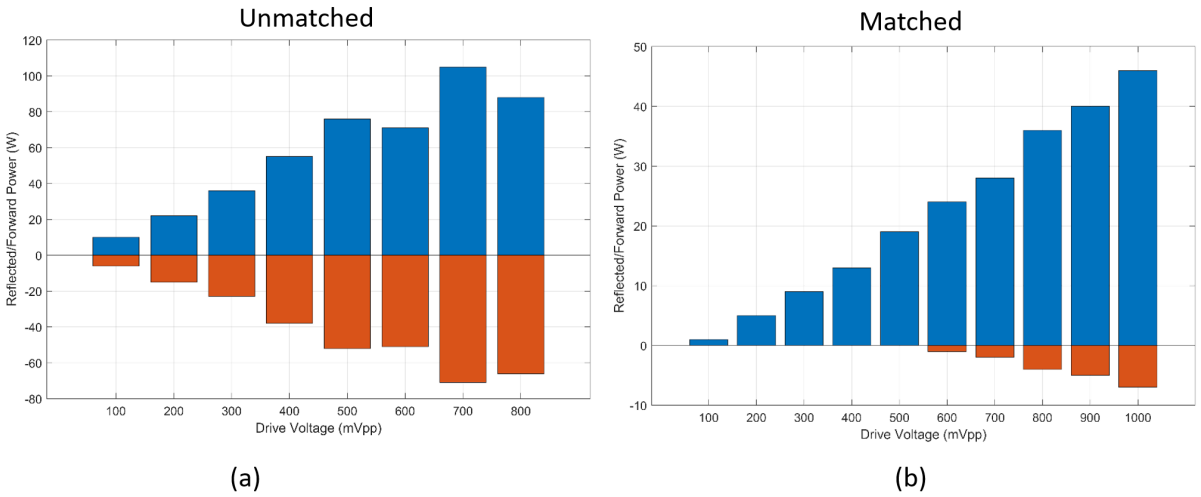

Figure 5.12: The forward and reflected power from a source to (a) an unmatched load and (b) matched load. Blue indicates forward power and orange, reflected power.

With the matching transformer in place, there is a significant decrease in the reflected power, as seen in Fig. 5.12 (b). The reflected power at low drive voltage is zero and power reflection only occurs above 600mVpp.

To drive the FUS devices at high power an electrical impedance matching transformer was used. Due to the high impedance mismatch between the devices and the source, a matching circuit was a necessary step to take. Initially, the reflected power was 66% as the average impedance of the devices was 10 **Ω** while the amplifier was 50 **Ω**. An LC matching circuit was investigated however the large inductance value led to a drastic decrease in the resonant frequency of the FUS devices. By using a matching transformer there was more precise control of the inductance while using the turns ratio as an almost decoupled parameter to match the impedances. Eight impedance matching transformers were manufactured to cover the range of impedance magnitudes, phases and resonance frequencies. When the devices were driven at high power the input signals discussed throughout this chapter were ran through a 52 dB RF amplifier. Hence, a 1 Vpp input signal was seen as a 400 Vpp input to the matching transformer.

Chapter 6

FUS Device Characterisation

The acoustic output of the manufactured FUS devices was characterised in two ways. First, the acoustic field was measured at low acoustic power. This acoustic field was compared with the FEA results to validate the predicted focal zone dimensions. In this experimental procedure carried out in a water tank, a needle hydrophone is used to achieve the necessary resolution. The needle hydrophone is a fragile sensor that cannot be exposed to cavitation and therefore the FUS devices could only be tested at low power to protect the needle hydrophones. Hence, a second experimental technique is to use a radiation force balance (RFB) to measure the total acoustic power output of the FUS devices. RFB data, in conjunction with the acoustic field pressure data, can be used to fully characterise the focal zone size and intensity under high power driving conditions, more indicative of a device in operation.

6.1 Acoustic Field Measurements

To measure the axisymmetric acoustic field of the FUS transducer, the 3D pressure field is characterised from three 2D measurement plane scans. This is done to decrease the number of measurement points with respect to a full 3D volumetric scan while maintaining an accurate profile of the acoustic field. Fig. 6.1 (a) shows the 3D pressure field obtained from FEA. At the focal zone, the amplitude of pressure decreases rapidly in the XY plane, and data points that are not in the focus provide minimal data. However, before and after the focus in the Z plane, the interference pattern can be used to identify asymmetry.

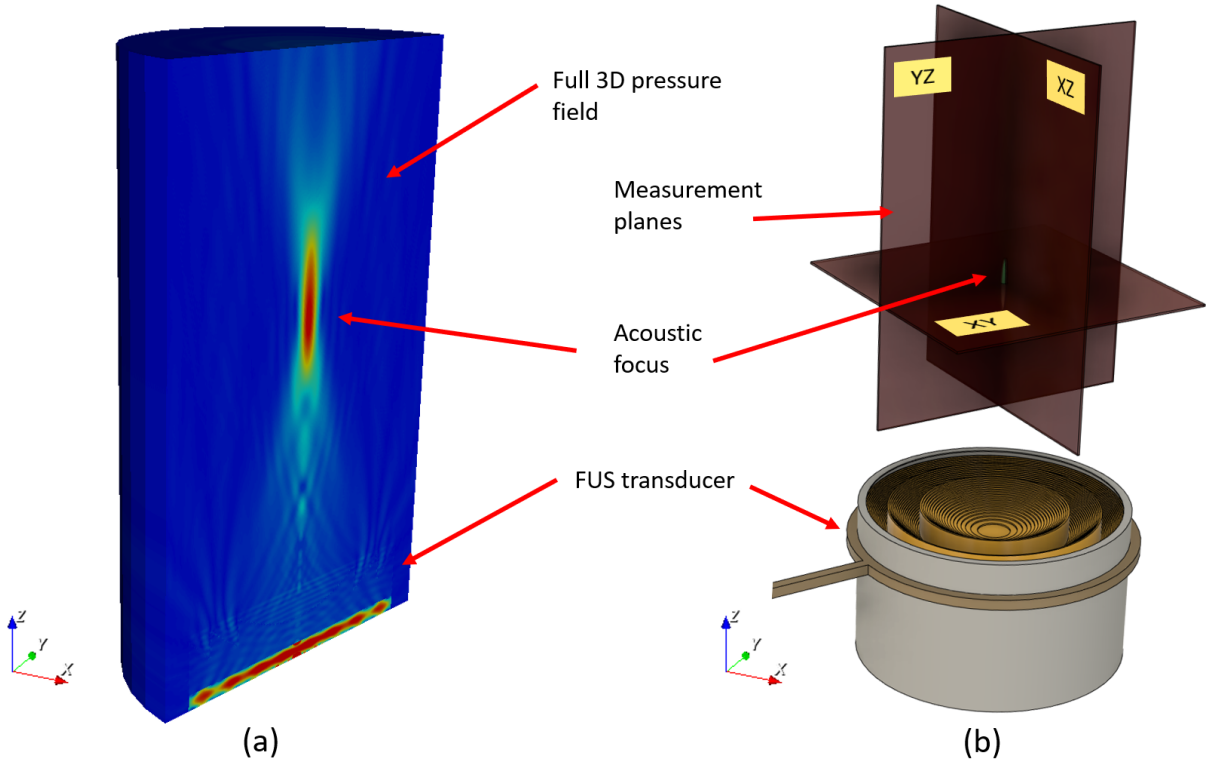

Figure 6.1: (a) The acoustic field of a FUS transducer as predicted by FEA showing the full 3D pressure field and (b) the three 2D planes which fully capture the axi-symmetric field

As the pressure field is axisymmetric, the XZ and YZ scans ideally are identical and so measurement scans in these planes can also capture any asymmetry

6.1.1 Acoustic scanning tank experimental procedure

A scanning tank was used to characterise all FUS devices manufactured. The tank, of dimensions 86 x 56 x 41 cm^3, is filled with type III clean water (via reverse osmosis) from an RO water purification system (Barnstead Pacific, ThermoFisher Scientific, USA). The water is degassed by running a water pump which draws the water through numerous small aperture holes drilled in a PVC pipe. The pipe creates a low pressure zone that pulls dissolved gases out of the water. The pump is operated for 8 hours when the tank is initially filled with gassed RO water. This has been empirically demonstrated in our lab to provide sufficient removal of gases in the scanning tank to prevent cavitation over the

mechanical indices employed. To maintain the de-gassed water, the pump is operated 2 hours per day until a water change. The use of degassed water is to increase the cavitation threshold, reducing the likelihood of the needle hydrophone being damaged by cavitation exposure.

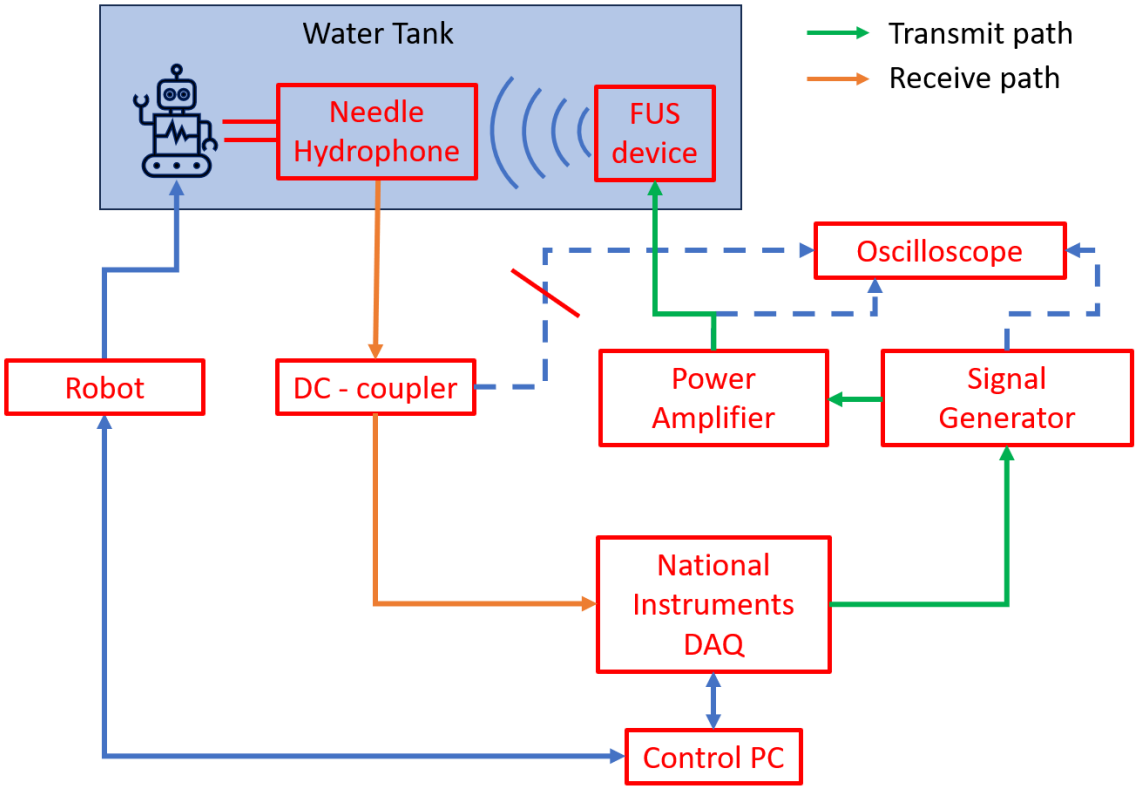

Figure 6.2: A schematic diagram of the acoustic scanning tank

Figure 6.2 shows a schematic of the acoustic scanning tank and the equipment used. The control PC hosts software (LabVIEW, National Instruments (NI), TX, USA) written to control and synchronise the scanning tank robot to the device under test. The control PC uses a data acquisition card (DAQ card, NI) to send a trigger signal to a signal generator. The signal generator (33500B waveform generator, Agilent, CA, USA) is programmed to transmit an 8 cycle, to reach the steady-state of the FUS transducer, 1.5 MHz sinusoidal signal with an arbitrary amplitude of 50 mVpp when triggered. This signal was amplified by an RF amplifier with 50 dB gain (2100L, E&I, NY, USA). The power amplifier was directly connected to the FUS device being tested. The FUS device transmits pressure waves in the degassed water, and the needle hydrophone (PA, Dorchester, UK) is positioned within the field to measure this pressure. The needle hydrophone has a pre-amplifier that is powered by a DC coupler. The coupler also provides a 50 Ω impedance output channel used to connect the signal measured by the needle hydrophone to the DAQ card which is read by the control PC. The signal generator, power amplifier, and

DC coupler were connected to an oscilloscope to measure the signals in a much longer time window than can be managed by the control PC. However, the 50 Ω termination of the DC coupler to the oscilloscope must be severed before the measurement begins, to limit additional noise.

The control PC uses the trigger signal to start a measurement and record the signal received from the needle hydrophone after a calibrated delay time (due to time of flight in water). Once the measurement is complete, the PC commands the robot to move the needle hydrophone to the next scanning measurement position in the tank and then repeats the process.

The needle hydrophone controls the resolution of the final scan, as each measurement point is always one needle diameter away from the last. The maximum diameter of the needle must be $\lambda/4$ or less [101], however the smaller the diameter of the needle tip, the lower the sensitivity. The compromise for a 1.5 MHz signal in water was a needle tip of 200 µm diameter.

Before measuring the acoustic field, the needle hydrophone must be aligned with the FUS device. Due to the axisymmetric nature of the device, if unaligned, the focal zone will not be accurately measured, or will be missed altogether. To align the system, the FUS device is first visually aligned with the needle hydrophone. The needle hydrophone mount is designed so that it is always horizontal and aligned rotationally; therefore, the only remaining alignment is translational.

First the needle hydrophone and signal generator are connected to the oscilloscope to estimate the distance. The time of flight between the sent and received pulses is inserted into LabVIEW which correctly centres the signal in the time window. The alignment is then performed by sweeping the robotic stage in each axis to find where the signal is at a maximum. The intersection of maximum pressure amplitude in each axis is the location of the focus. The needle hydrophone is then moved 50% farther away from the FUS device

and a sweep is performed on the X and Y axes. If the maximum pressure is at the centre, the device is aligned. If the device is unaligned, the maximum pressure amplitude in one or both of the axes will be offset, and the FUS device should be remounted. The process is repeated until both checks on the Z-axis are confirmed.

Once alignment is complete, a raster scan of the acoustic field is started. A settling time is used to delay the trigger signal. This allows any vibration in the robot arms to settle before a measurement is taken.

6.1.2 Post-processing data

At each scan measurement point, a waveform was captured. The signal read by the DC coupler is the signal produced by the FUS device but is also shaped by the response of the needle hydrophone. The needle hydrophone was calibrated at the National Physical Laboratory (NPL, Teddington, UK) with calibration data provided at 1 MHz intervals from 1 to 30 MHz. This data was interpolated, and the phase was inferred via a Hilbert transform to convert the data to a complex calibration spectrum.

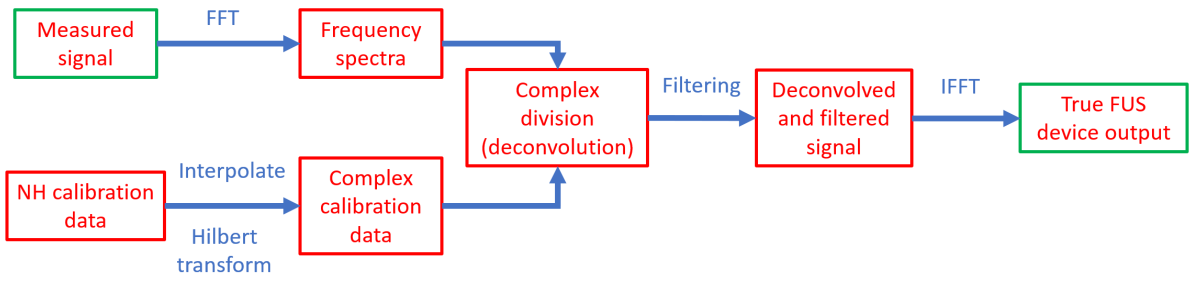

Figure 6.3: The post processing procedure for all measured waveforms captured in the acoustic scanning tank

The postprocessor work flow is described in Fig. 6.3. The time series signals are marked in green boxes, and the frequency spectra are shown in red boxes. The complex calibration data is interpolated with respect to the length of the measured frequency signal. The complex division of these two spectra is the end of the deconvolution process which converts the data from a voltage to a pressure, Eq. 6.1.

$$\psi = \frac{\text{FFT(Measured Signal)}}{\text{FFT(Calibration data)}} \tag{6.1}$$

where ψ is the measured signal that is deconvolved with the response of the needle hydrophone.

After deconvolution filters were applied, a high-pass filter far below the centre frequency of the FUS device removed any DC offset and low-frequency noise. A low pass filter was applied at 30 MHz as there is no calibration data above this frequency. Infinite impulse response (IIR) Butterworth filters were used to limit FFT artefacts. The aggression of the filters was adjusted to ensure that noise was omitted while maintaining filter stability. A filter order of 7 was never exceeded.

The deconvolved and filtered signal was passed through an inverse fast Fourier transform (IFFT) to reconstruct the time series data in pressure (MPa). The peak negative pressure (PNP) for each measurement point was recorded, and displayed as a heat map of the acoustic pressure field.

6.1.3 Pressure field results

Peak negative pressures are often quoted rather than peak pressure in an experimental setting. This is because cavitation is initiated when the gas is ripped from the solution in pockets of negative pressure; hence this is more important to measure than peak pressures. In FEA simulations, the low power, linear characteristics of the FUS transducers produce equal low and high pressure regions. When dispersive and non-linear effects occur in experiments, the negative pressure increases at a slower rate than positive pressure and are a higher priority to measure. Therefore, the PNP is plotted for each device in the XY, XZ and YZ planes.

Figure 6.4 shows the acoustic pressure field of device $D_{PZ29(1)}$ in the XZ plane. The pressure field shows good agreement with the FEA results at the focal zone with similar -6dB beam widths, as seen in Table 6.1. The contour plot of each measurement plane was used for an accurate and repeatable -6 dB contour, as seen in Fig. 6.4 (b). The full pressure field also contains information of the symmetry of the Fresnel lens. The green saddle feature in the near field, between 1 and 4 mm in the Z axis, shows close agreement to the expected interference pattern from FEA.

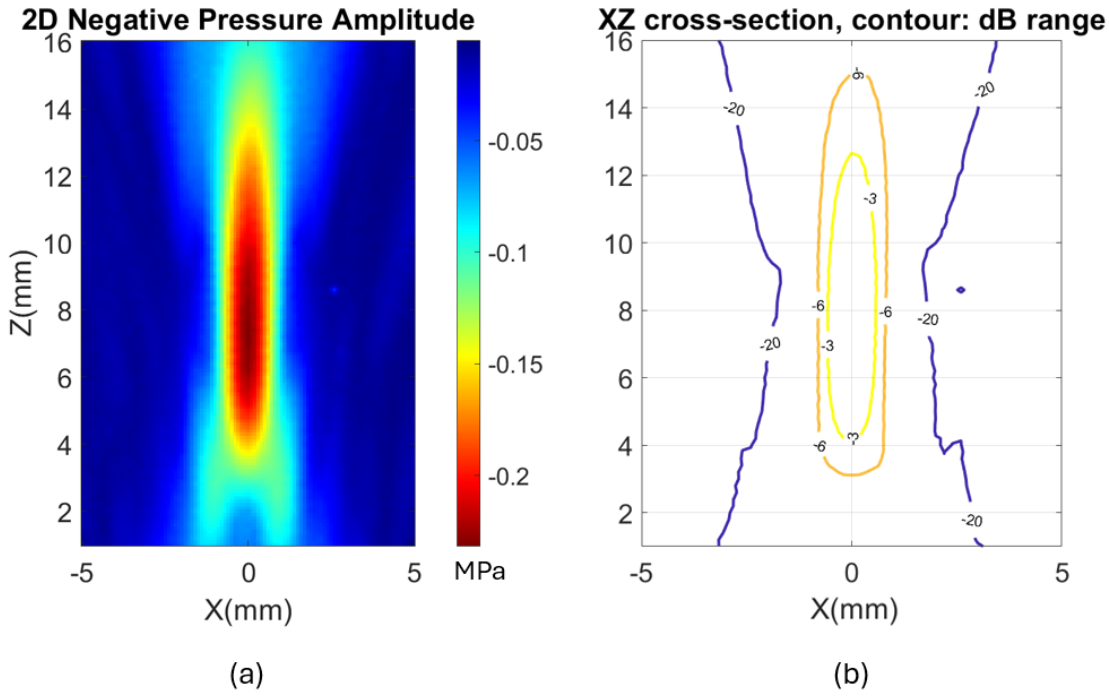

Figure 6.4: (a) Pressure field of FUS device $D_{PZ29(1)}$ in the XZ plane and (b) the corresponding -3, -6 and -20 dB contours.

The acoustic focal zone was found to be consistently 22 mm from the housing face on the FUS devices. This equates to a 25 mm focal length, as numerically modelled, from the plateau in the centre of the lens, which is 3 mm below the tallest Fresnel lens feature.

An XY scan was performed at the pressure maximum in the Z dimension, Fig. 6.5. The XY scan shows the cross-section of the focal zone as a test of symmetry and a confirmation of the radial dimension from the XZ and YZ scans.

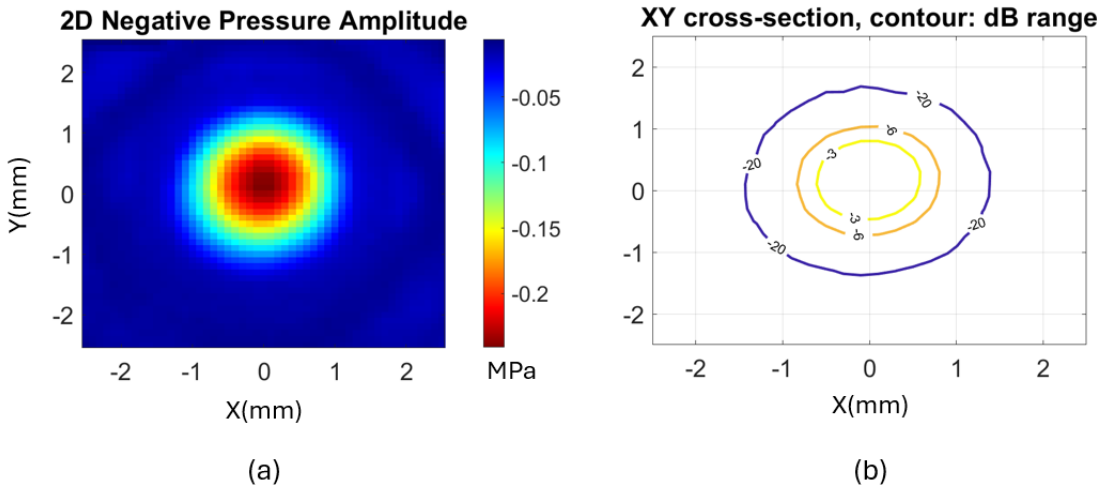

Figure 6.5: (a) Pressure field of FUS device $D_{PZ29(1)}$ in the XY plane and (b) the corresponding -3, -6 and -20 dB contours.

As the acoustic field measurements were to characterise the field shape and focal zone parameters at low power, an arbitrary drive voltage of 50 mVpp was set for the signal generator. This was amplified by 50 dB in the power amplifier with the FUS device connected without any additional electrical matching circuit. The dimensions of the focal zone at the -6 dB contour and the peak negative pressures of each device are shown in Table 6.1.

The field shape measured in the acoustic scanning tank agrees well with the analytical and FEA predictions in Table 6.1. The PNP measured at the spatial peak of each acoustic field show characteristics of the devices electrically and mechanically. The lowest PNP is output from the D_{PZ54} devices at 0.18 MPa and the highest from the D_{PZ37} devices at 0.38 MPa. The electrical impedance mismatch of these devices contributes to a lower electrical power received. D_{PZ54}, having the lowest impedance, consequently exhibits the greatest impedance mismatch to the source, leading to a low output. Meanwhile, D_{PZ29} achieves a higher PNP with better electrical matching and higher d_{33}. The D_{PZ37} devices with the porous piezoceramic material performed much better than their electrical impedance matching can explain. Instead, the better acoustic matching of the porous ceramic to the Fresnel lens leads to a higher pressure at the focal zone. Although D_{PZ12} devices have better electrical matching than all other devices, the lower piezoelectric coefficients, such as d_{33}, limit the pressure amplitude. The D_{PZ37cc} device contains PZ37 and has a lower PNP at the focal zone than the D_{PZ37} devices. This final device was flawed in a few key

FUS device	Radial length (mm)	Axial length (mm)	Peak negative pressure (PNP) (-ve MPa)	Normalised PNP (dB)
Analytical	1.4	9.7	N/A	N/A
FEA	1.6	11.5	N/A	N/A
$D_{PZ29(1)}$	1.8	11.0	0.21	-2.6
$D_{PZ29(2)}$	1.8	10.6	0.30	-1.0
$D_{PZ29(3)}$	1.6	10.6	0.26	-1.6
$D_{PZ29(4)}$	1.8	12.0	0.26	-1.6
$D_{PZ29(5)}$	1.8	11.8	0.29	-1.2
$D_{PZ54(1)}$	1.6	9.8	0.19	-3.0
$D_{PZ54(2)}$	1.8	11.8	0.14	-4.3
$D_{PZ54(3)}$	1.8	10.8	0.15	-4.0
$D_{PZ37(1)}$	1.6	11.2	0.35	-0.4
$D_{PZ37(2)}$	1.8	11.0	0.35	-0.4
$D_{PZ37(3)}$	1.6	9.8	0.38	0.0
$D_{PZ12(1)}$	1.6	11.0	0.20	-2.8
$D_{PZ12(2)}$	1.6	10.0	0.20	-2.8
$D_{PZ12(3)}$	1.6	10.4	0.17	-3.4
D_{PZ37cc}	1.8	10.6	0.25	-1.8
D_{PZ37mh}	2.0	15.2	0.23	-2.2

Table 6.1: Measured focal zone dimensions at the -6dB contour and PNP of all manufactured FUS devices.

areas. The full beam pattern, Fig. 6.7 shows misalignment even on the best scans. This is due to the Fresnel lens being mounted at an angle within the housing, caused by a flawed manufacturing of the housing. The resulting misalignment reduces the confidence that the peak of the focal zone has been accurately captured.

The pressure field of device D_{PZ37mh} can be seen in Fig. 6.6. The securing ring at the top of the 1 inch lens tube used as the housing was used in place of the 3D printed securing lip used in the other devices. The securing ring reduced the effective aperture of the Fresnel lens to 22.9 mm, while the 3D printed equivalent was 24.3 mm aperture. The reduced aperture greatly affected the size of the focal zone seen in Figs. 6.6 (b) and (c), increasing the axial length by 25% on average.

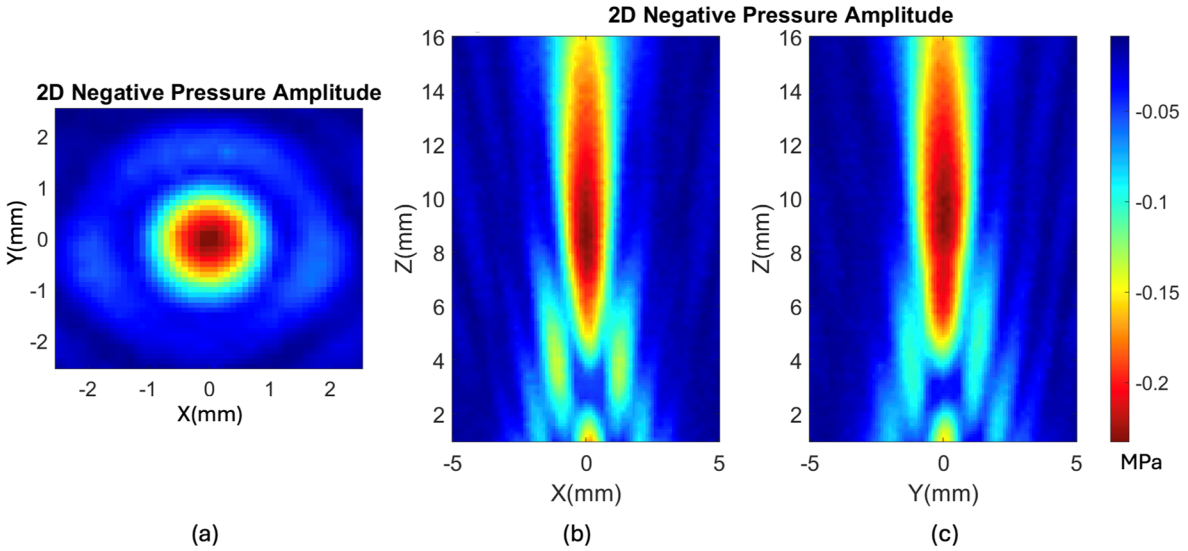

Figure 6.6: The pressure fields of FUS device D_{PZ37mh}, including measurements in the XY plane (a), XZ plane (b) and the YZ plane (c)

6.1.4 Frequency Steering

The Fresnel lens in the miniaturised FUS transducer is designed with a centre frequency of 1.5 MHz. If the frequency of the pressure waves are different from this, the position of the focal zone will change. With a conventional lens, the acoustic focus moves closer to the device as the frequency is increased. However, with the acoustic Fresnel lens the focus moves away from the device with increasing frequency. This opposes literature on which direction the focal zone will move if the frequency is changed. A patented design [102] states increasing the frequency of the signal can be utilised to ablate the skin close to the transducer, whereas the operational frequency of the transducer is stated to ablate deeper into the tissue. The phenomenon being utilised in this application is increasing the frequency until the attenuation is large enough that all energy is absorbed in a short length from the transducer itself. This phenomenon is therefore the opposite steering direction and a separate application than the frequency steering presented in this work. The Fresnel lens frequency steering was first modelled in FEA to confirm the theory and subsequently measured in the acoustic scanning tank. The diffraction effect of the Fresnel lens can be seen clearly in the acoustic field of D_{PZ37cc} which was captured in the YZ plane for driving frequencies from 1 MHz to 2 MHz, Fig. 6.7.

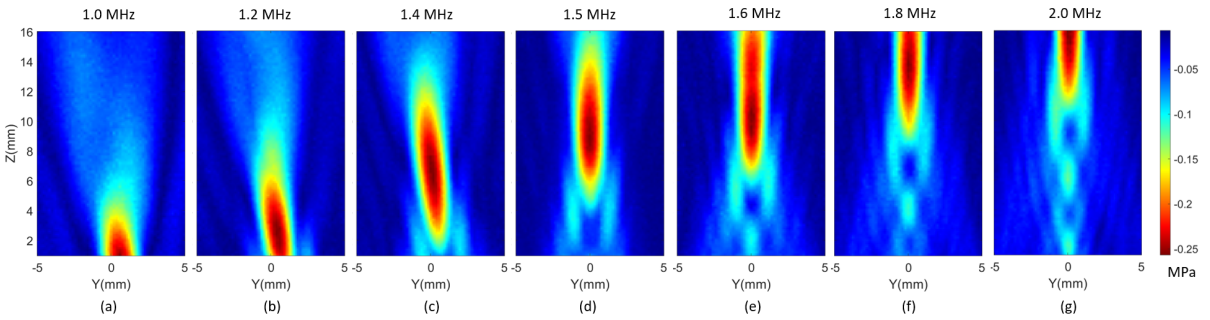

Figure 6.7: The focal zone of D_{PZ37cc} as a the frequency of the drive signal is increased from 1 MHz to 2 MHz, showing the frequency steering technique.

Figure 6.8 shows the position of the focal zone as the frequency of the drive signal increases. Manipulation of the focal zone position via frequency control is typically reserved for large piezoelectric arrays with complex amplifiers and driving electronics. Being able to manipulate the focal zone position with a single element transducer could be a benefit for applications in laparoscopic robotic surgery, enabling fine tuning of the ablation of tumours within the body.

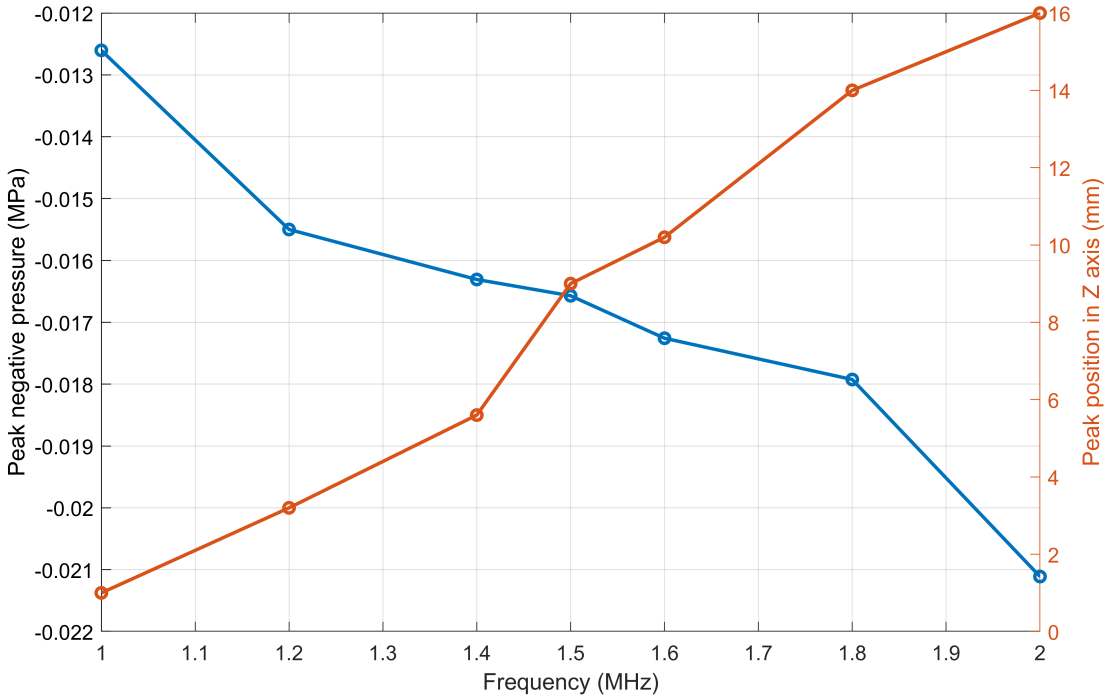

Figure 6.8: The PNP at the focus at each drive frequency and the position of the peak with respect to the FUS device, D_{PZ37cc}

The relationship between the peak negative pressure and frequency is complex with the following overlapping phenomena, ranked here in terms of their least to most significant influence on the PNP in the focus:

- Frequency dependant attenuation
- Resonance of the piezoelectric element
- Electrical matching
- Diffraction efficiency of the Fresnel lens
- Dispersion

Attenuation in water increases with respect to frequency; however, in water this is minimal. The piezoelectric element in device D_{PZ37cc} has a resonance frequency of 1.8 MHz. If this was the dominant factor, the PNP would reach a turning point at this frequency and increase because the device went through peak performance at resonance. The electrical matching of the device to a 50 Ω source results in a decrease in electrical matching with respect to frequency that minimises the power transfer. This is the opposite to what can be seen in Fig. 6.8. The efficiency of the Fresnel lens is highest at the designed centre frequency of 1.5 MHz, and a turning point is not seen at this frequency. This infers that the most significant impact on focal zone characteristics is dispersion. As frequency increases, the pressure waves become more focussed. This reduces the size of the focal zone and therefore decreases the PNP. This can also be seen in the radial and axial lengths at the -1 dB contour of the pressure field, which decrease from 0.8 mm to 0.6 mm and 4.4 mm to 4 mm, respectively.

The interactions that lead to the linearly decreasing PNP do not need to be decoupled and individually characterised, but the totality of the resulting effects adjust the relative strength of the signal at each frequency, controling both position and amplitude. Therefore, the signals used can, for example, contain one frequency to target a certain focal zone depth. However, the signals with a larger frequency content can elongate the focal zone. Also, the relative strength of each frequency bin can be controlled to mitigate the decrease in PNP and carefully control the dose of acoustic energy deposited.

6.2 Radiation Force Balance (RFB)

A radiation force balance (RFB) (Precision Acoustics, Dorchester, UK) is used to measure the total acoustic output of the FUS devices at high drive voltages, Fig. 6.9. The RFB uses an acoustic absorbing baffle to fully absorb the energy emitted from the FUS device. The baffle is suspended in a water tank and attached to calibrated scales with an accuracy of 0.1 mg.

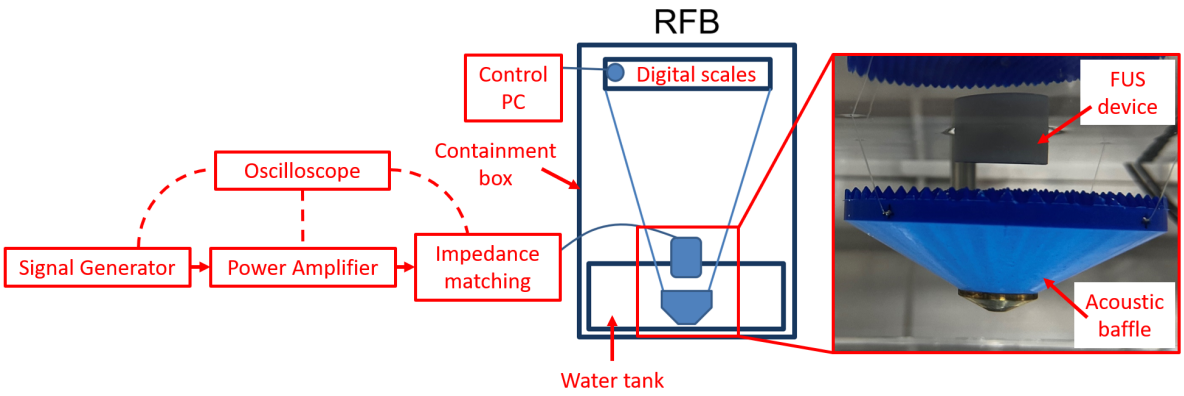

Figure 6.9: A schematic of the radiation force test set up.

To drive the FUS devices at high power, a signal generator supplied the required voltage signal to an RF amplifier with 50 dB gain. The impedance matching transformer was connected to the amplifier that was connected to the FUS device. An oscilloscope was used to measure the signal generator output, the power amplifier output (via a 20dB attenuator) and the transducer side of the transformer. The FUS device was then clamped facing towards the acoustic baffle that was suspended from precision scales. The scales were connected to a control PC for data collection. The Fresnel lens and acoustic baffle were thoroughly soaked, and any trapped air bubbles were agitated with a water pump. The water was room temperature, 20°C, reverse osmosis (RO) type III clean water that had been de-gassed. To ensure minimal damage to the baffle the FUS devices were positioned 10 mm away. This positioning was to ensure the acoustic field was absorbed before the energy converged at the focal point, to avoid any damage to the baffle. The water tank and digital scales were placed in a containment box to limit the effects of air currents and temperature changes on the scales.

The mass reading from the scales is converted to an acoustic power (P_{RFB}) in the data acquisition software. The conversion from mass to power is found in Eq. 6.2.

$$P_{RFB} = c \cdot m_{rad} \cdot g \cdot F_{CAL} \cdot F_{IEC_{Corr}} \tag{6.2}$$

where c is the temperature dependant sound speed (taken to be 1482.36 at 20 °C), m_{rad} is the mass corresponding to the vertical component of radiation force, g is the acceleration due to gravity, F_{CAL} is the calibration correction factor and $F_{IEC_{Corr}}$ is the correction factor to account for non-ideal behaviour as specified by IEC 61161 [103] [104]. Substituting all corrections and constants results in a multiplier constant of 14.5 mW mg^{-1}. The measured mass from the scale consists of the components described in Eq. 6.3.

$$m_{total} = m_{baffle} + m_{rad} \tag{6.3}$$

where m_{total} is the total mass displayed on the scales and m_{baffle} is the apparent mass of the baffle suspended in water. The radiation force component was isolated simply by periodically zeroing the scales to account for m_{baffle} and drift caused by air currents and temperature changes.

During measurements, the FUS device was turned on for a period of 5 seconds followed by 5 seconds off. This was repeated 5 times for averaging. An example of this operation is shown in Fig. 6.10. The radiation force was calculated by monitoring the difference in acoustic power when the device was on versus off. This is necessary due to the drift of the precision scales resulting in a non-zero number when in the off cycle. However, instabilities at the transitions required the measurement to be taken at steady state, indicated in Fig. 6.10 as asterisks.

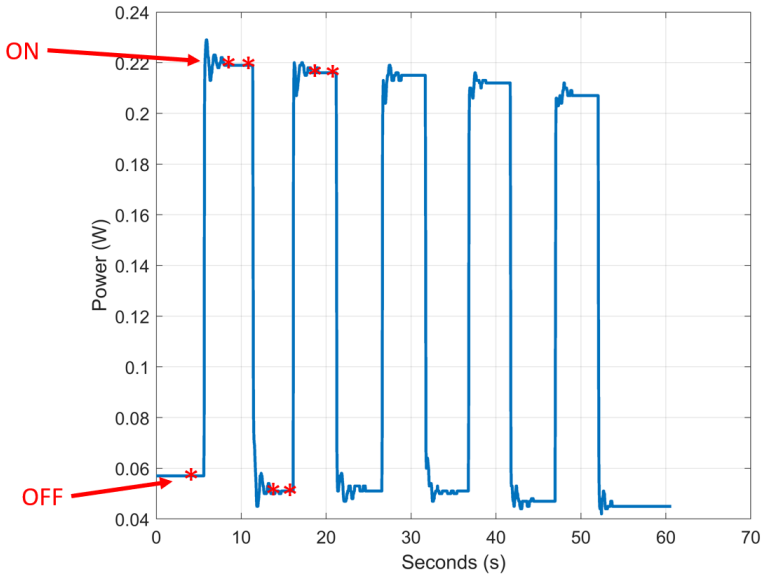

Figure 6.10: Acoustic radiation power of device $D_{PZ37(3)}$ at a drive voltage of 100mVpp from the signal generator with a duty cycle of 50%.

6.2.1 RFB results

The build-up and transfer of heat at the focal zone of a FUS transducer occur in vastly different time periods than the ultrasonic waves. A wave consisting of eight periods at 1.5 MHz lasts only 5.6 µs, whereas thermal effects occur in seconds to minutes. To spread the acoustic energy over a time period more suitable to thermal effects, a duty cycle (DC) is introduced. By turning the ultrasonic signal on and off, energy can build in the target steadily, and this also reduces the stress on the FUS device. The DC of high-power FUS devices can be as low as 5%. However, the prototype devices in this study have comparatively low power, and a higher duty cycle of 50% was used in the RFB experiment. In return, this means that the measured power from the FUS device is temporally averaged.

The current and voltage were recorded and are shown in Fig. 6.11. During the high-power excitation of the FUS devices, the current supplied to the device was observed to drop over the course of the 5 second on cycle of the RFB test, Fig. 6.11 (c), indicating that the impedance is increasing, which the passive impedance matching transformer cannot track or account for. The increasing impedance led the RF amplifier to increase the output voltage in response to the change in the impedance phase of the FUS device, Fig. 6.11 (b). The voltage input to the signal generator was a more repeatable method to measure

the driving amplitudes at high powers, as seen in Fig. 6.11 (a). The signals were 100mVpp to 1000mVpp at intervals of 100mVpp. However, it can be seen that the signal generator overshoots the requested voltage by up to 14.5%, as measured in Fig. 6.11 (a). The signals in the experiment were captured by a PicoScope (Pico Technology, St Neots, UK) that triggered when the FUS device was in the on-cycle. The triggering was tuned to capture a minimum of five buffers per on-cycle (1 per second) with each buffer consisting of ten signals which were averaged to mitigate noise. Therefore, the increases in the current trace seen in Fig. 6.11 (c) is the recovery of the FUS device after a 5 second off-cycle, which is more prominent in the 1000mVpp trace.

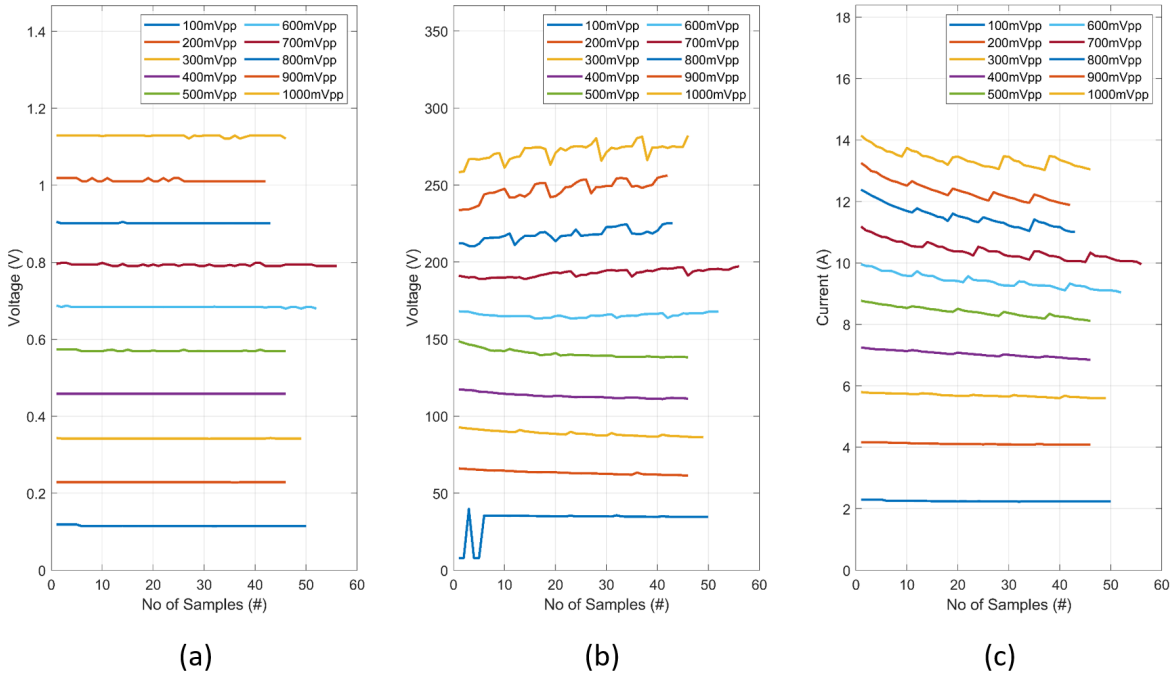

Figure 6.11: The signal supplied to $D_{PZ37(3)}$, at (a) the signal generator output, (b) the RF amplifier output and (c) the current in the FUS transducer. As no data is triggered when the device is in an off cycle, there are no 'off' gaps in the data. Hence the captured data is shown with respect to number of captures (samples).

The acoustic power output of the FUS device measured by the precision scales at high drive signals can be seen in Fig. 6.12 (a). The power of the device is highest at the start of each five-second on-cycle with a 37% drop throughout the first on-cycle. The power output then decreases throughout the experiment. Figure 6.12 (b) shows an average total power for each on-cycle showing that, the decrease in power is proportional to the input voltage. However, the loss of power is not permanent and is recovered with sufficient off time between experiments.

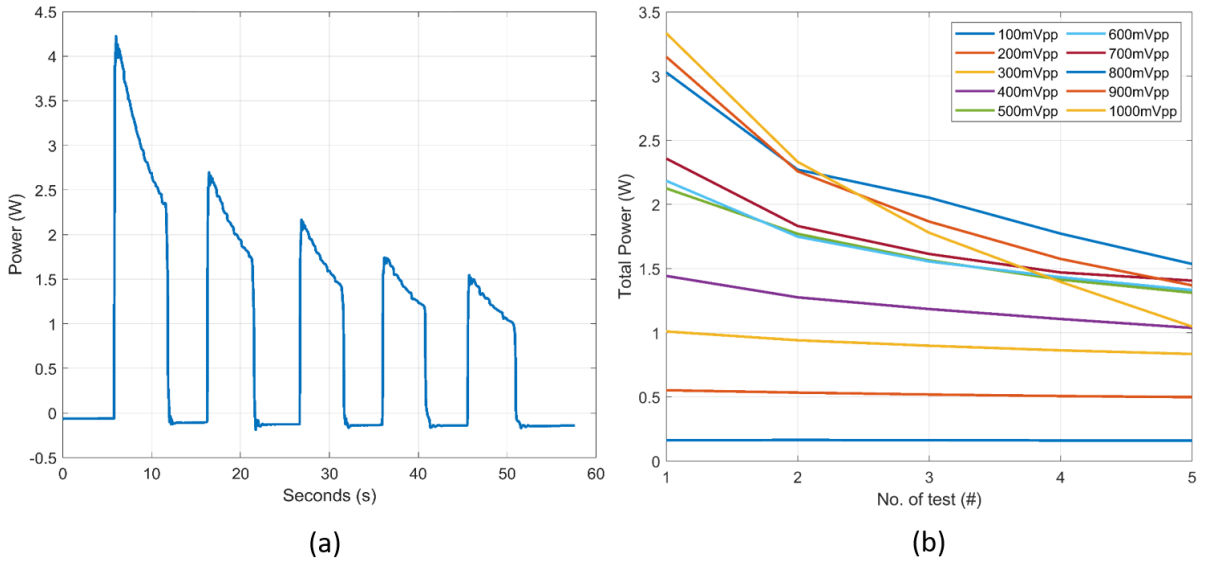

Figure 6.12: (a) Acoustic power output of $D_{PZ37(3)}$ at 900 mVpp drive signal and (b) the average acoustic power at each voltage input.

The acoustic power was measured for all FUS devices with the average for the devices of each type of piezoelectric material up to their failure voltage level is shown in Fig. 6.13. The low power output of D_{PZ29} is confirmed by all these devices, which achieve a maximum acoustic power of 0.22 W at 167V, above which they all failed. The D_{PZ54} devices achieved a higher acoustic output and a higher drive voltage before failure. The high power outputs achieved by D_{PZ37} and D_{PZ12} show promise; D_{PZ37} achieved 3.4 W at 272 V. The D_{PZ12} FUS devices achieved the highest acoustic power with 3.9 W at 378 V. D_{PZ12} produced the equivalent acoustic power to D_{PZ37}, while requiring a 100V higher drive voltage. The higher efficiency of the D_{PZ37} devices is due to the better acoustic impedance matching that results from having a porous, low density ceramic. D_{PZ37mh} followed the trend of the D_{PZ37} devices but failed at a lower drive voltage of < 2.5 W. Device D_{PZ37cc} did not perform well in comparison to other D_{PZ37} devices and experienced instability at the on/off transitions in the experiment.

The RFB acoustic power was combined with the acoustic field measurements from the scanning tank using Eqn. 2.6. The approximation of the field to a spatial peak intensity at the focus for each set of devices is shown in Table 6.2. As the baffle of the RFB was much larger than the 6dB beamwidth of the FUS devices, the side lobes are included in the value I_{SP}. This approximation also assumes that the beamwidth was measured in linear acoustic propagation conditions and that the acoustic field is a plane wave [66]. The acoustic power measured by the RFB is temporally averaged because of the scale's slow

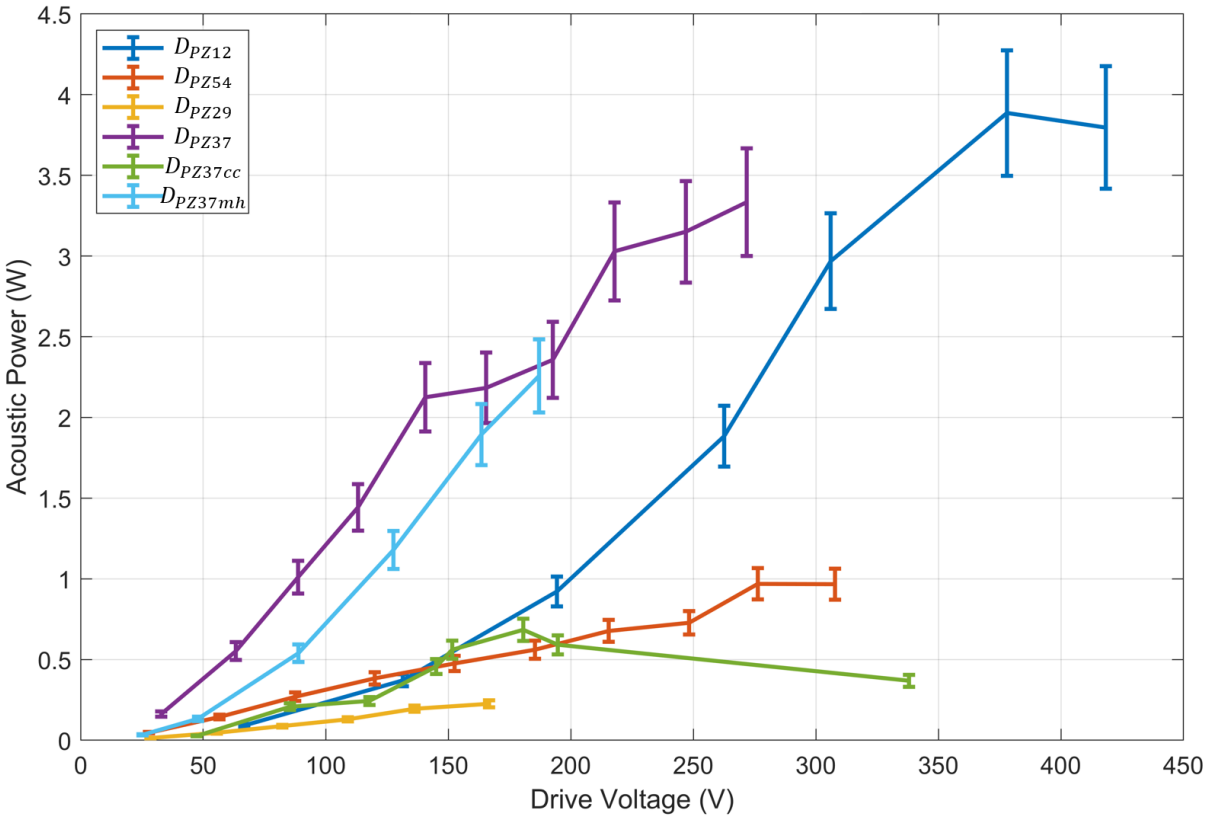

Figure 6.13: The acoustic power output of all manufactured FUS devices vs RF amplifier output

sampling frequency (with respect to pulse repetition rate) and baffle's relaxation time. Consequently, the intensity calculated from this acoustic power is as the 50% duty cycle is incorporated into the acoustic power output. Continuous wave (CW) driving conditions could not be maintained by the devices due to significant heat build-up.

The relatively low acoustic power output of the FUS devices was offset by the small focal zone to achieve substantial intensities at the focus. The main hindrance to ablating tissue in a procedure is maintaining a high and constant pressure amplitude at the focus. The values in Table. 6.2 can be compared to the I_{SPTA} of 1.0 kW/cm^2 in literature that is the minimum threshold for ablation [31]

FUS Devices	Intensity I_{SPTA} (W/cm^2)
D_{PZ29}	190 ± 57
D_{PZ54}	832 ± 250
D_{PZ37}	2886 ± 866
D_{PZ12}	3363 ± 1009
D_{PZ37cc}	319 ± 96
D_{PZ37mh}	1763 ± 529

Table 6.2: The spatial peak temporal average intensity of each device type, calculated from the combination of RFB and acoustic field measurements. The uncertainties of the NH calibration (20%) and the RFB uncertainty (10%) were combined for the intensity uncertainty.

The characteristics of the power loss during the RFB experiment is indicative of heat building up in the transducer and limiting the output of the piezoelectric disc. The loss of power occurs in a time period of the order of seconds, is proportional to the drive voltage and exhibits as decreasing power asymptotically to equilibrium. This led to the devices with cooling channels and metal housing that will reach thermal equilibrium faster and limit this effect. However, results for device D_{PZ37cc} indicate that the device failed due to manufacturing inconsistencies of the complex geometry housing.

6.2.2 High power impedance analysis

The impedance of device D_{PZ37cc} was characterised at high power to understand the thermal effects within the transducer. At high power, dielectric losses scale proportionally [78]. This causes the resonance frequency of the piezoelectric to decrease in frequency at a different rate from the anti-resonance. For the static electrical matching transformer, this change in impedance at high power caused the device to lose matching. To characterise this drift, a MATLAB-generated swept sinusoidal voltage signal was used to drive the FUS device. The frequency content of the signal is shown in Fig. 6.14 (a). The distortions in the FFT are due to the lack of windowing used on the sinusoid. This leads to FFT aberrations caused by the abrupt cut off at the beginning and end of the signal. The signal was a pure sine sweep, Eqn. 6.4.

$$y = A \cdot \sin(2\pi f_0 t + \frac{f_1 - f_0}{2T} t^2) \tag{6.4}$$

where A is the wave amplitude, f_0 and f_1 are the start and stop frequencies, T is the total sweep time and t is the time step. The start and stop frequencies were chosen to be 1.25 and 1.75 MHz respectively. This was to capture the resonance at 1.5 MHz as the energy is concentrated within this frequency band; all frequencies outside this band will not have sufficient energy to measure the impedance.

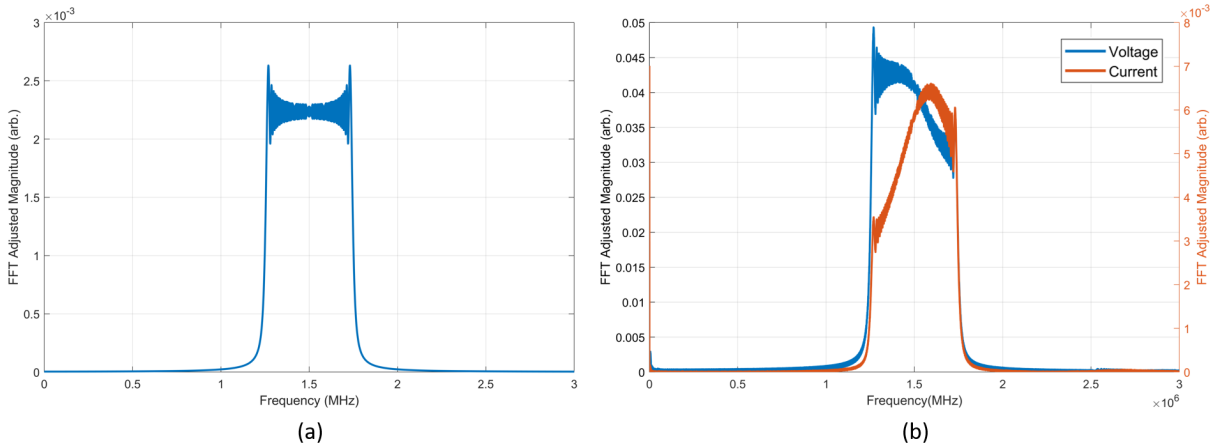

Figure 6.14: Frequency content of (a) the generated voltage signal and (b) the voltage signal from the RF amplifier output

The measured frequency content of the voltage and current on the FUS device are shown in Fig. 6.14 (b) after being excited by the signal. The current is a maximum at the resonance frequency. The complex division of the voltage and current frequency spectra is used to calculate the impedance at each voltage level, as seen in Fig. 6.15

A resonance frequency drop from 1.75 MHz to 1.6 MHz is measured through the voltage range of 100 mVpp to 1 Vpp as the signal generator output into a 52 dB RF amplifier. The impedance magnitude increases with the drive voltage from 45 Ω to 55 Ω. To optimise the electrical impedance matching the device must be fully characterised to observe the drop to thermal equilibrium and match at that frequency. However, the experimental procedure decoupled thermal effects from the piezoelectric response. Thermal effects effected the acoustic power output and decreased the resonance frequency, based on previous impedance matching analysis. The thermal effects are coupled to the dielectric losses that are characterised in Fig. 6.15 however more experiments must be employed to fully characterise the effect of both non-linearities.

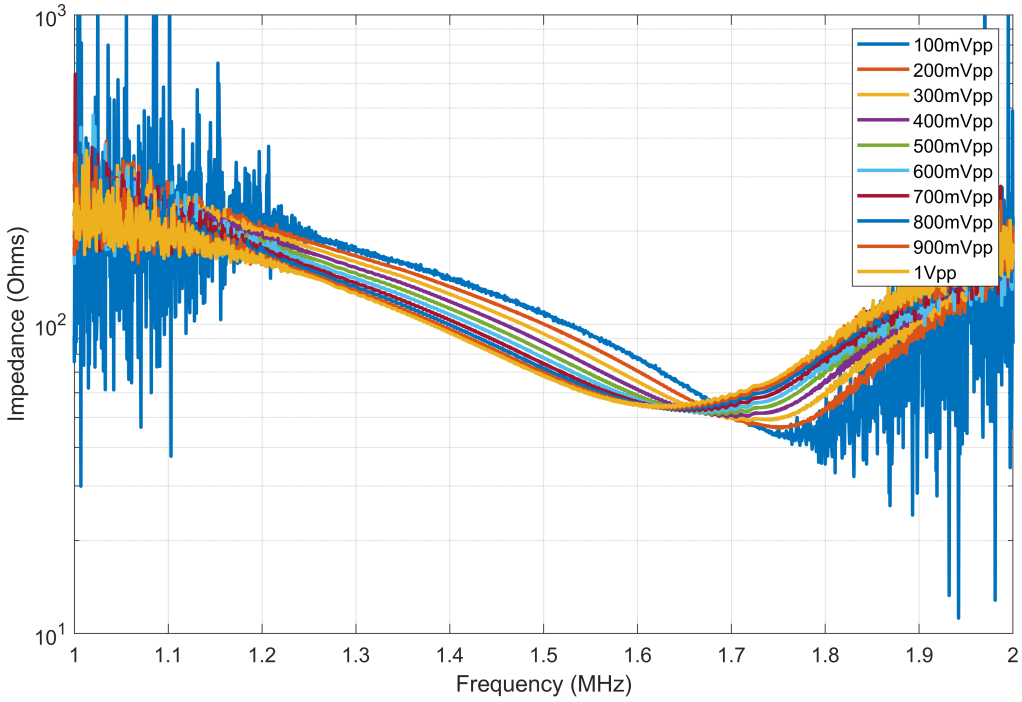

Figure 6.15: Impedance magnitude of the FUS transducer, D_{PZ37cc} at increasing drive voltages

The photopolymer resin used to print the Fresnel lens and housing is highly insulating. This insulation made thermocouples impractical for probing the temperature of the piezoelectric disc in the devices. The insulation leads to heat build-up under driving conditions that is difficult to characterise because the piezoelectric disc itself is not visible. Therefore, potential experimental methods such as using thermal cameras are also not practical.

All FUS devices manufactured were characterised fully in an acoustic scanning tank to determine the acoustic field maps. This was compared to the -6 dB contour dimensions of the FEA model in Table. 6.1. The 3D volumetric scan is not feasible in an experimental setting therefore the devices were characterised via a set of three 2D plane scans, YZ, XZ and XY. There is a strict alignment protocol that is followed for these measurements however the alignment of the Fresnel lens in the housing of D_{PZ37cc} made the alignment of this device challenging. By sweeping the drive signal up in frequency with a bandwidth of 1 MHz centred on the device resonance of 1.5 MHz, the position of the focal zone was moved 15 mm, centred on the focal length of 25 mm. This is possible due to the inherent properties of a Fresnel lens that focus pressure waves from constructive interference of a specific wavelength.

The total acoustic power output of the devices was measured on an RFB and the focal zone was approximated to an intensity, I_{SPTA}, by combining the acoustic power at high driving voltages with the acoustic field map from the scanning tank. This characterisation showed devices made from lead-free material, D_{PZ12} achieved a high intensity at the focal zone. However, this was much less efficient than D_{PZ37}. The same acoustic power output was achieved with up to 100 V less drive voltage. During the high power driving, piezoelectric softening was reducing the power output significantly. Characterisation of the dielectric losses via a high power impedance analyser on one device (D_{PZ37cc}) showed the extent of resonance frequency and impedance magnitude change that lead to loss of impedance match. Two devices with cooling solutions were made to combat this, D_{PZ37cc} and D_{PZ37mh}. The former did not achieve the expected acoustic power output due to manufacturing inconsistencies while the latter did not focus as strongly. This led to a larger -6 dB beam width that limited the intensity at the focal zone.

Chapter 7

Conclusion and Further Work

7.1 Conclusions

This thesis developed a miniaturized focused ultrasound (FUS) transducer integrated into a robotic platform, addressing the limitations of conventional extracorporeal large-diameter FUS devices. Unlike complex phased arrays that require extensive electronics, this design employs an acoustic Fresnel lens coupled with a planar piezoelectric element to achieve high focal zone pressures. Several FUS devices were modelled in FEA, each with a different piezoelectric material, including PZ29, PZ54, and PZ36HD with PZ29 and PZ54 achieving the highest acoustic pressures (16.4 MPa), demonstrating their suitability for therapeutic applications. To counteract the generation of heat from the losses of the piezoceramic, two thermal management systems were implemented and proved the necessity to cool the device during operation.

Manufacturing was optimised using an mSLA 3D printing technique, which offered low attenuation, high material homogeneity, and significantly reduced costs compared to metal-based alternatives. Commercial photopolymer resins were characterised and a database of acoustic properties for each was established. StrongX (Liqcreate, NL) was identified as the most suitable material for the lens due to its low acoustic attenuation and favourable mechanical properties. A batch of twelve transducers was produced to test manufacturing repeatability, and each material achieved the target resonance frequency within ±1%, confirming the reliability of the process. Three transducers were made with a lead-free

piezoelectric element, PZ12, and performed well in comparison to the traditional PZT-like materials. A force feedback system was integrated into the ultrasonic coupling mechanism at the front of the FUS device using a closed system of water being monitored with a pressure sensor. A control loop was developed to maintain a nominal pressure of the device to the target tissue for autonomous procedures.

Electrical impedance matching was successfully achieved using a transformer, minimising power reflection and enhancing efficiency at high driving voltages. Comprehensive 3D acoustic field mapping was conducted to characterise focal zone properties, and a novel frequency-steering technique was developed to enable positional adjustment of the focal point in the Z-axis, achieving 64% translation of the focal length. This technique provides the benefits of annular arrays at a fraction of the complexity.

High-power testing revealed significant heat buildup, reducing acoustic power output by up to 40% within 20 seconds due to thermal losses in the resin and piezoelectric elements. To mitigate this, various housing designs incorporating cooling channels and metal integration were explored. Future optimisation of both electrical driving and thermal management will enable higher acoustic intensities, making the device suitable for a broader range of therapeutic applications.

Overall, the miniaturised FUS transducer, integrated with robotic actuation, offers a promising alternative to conventional large-scale systems by enabling precise, low-cost, and adaptable ultrasound therapy for minimally invasive procedures. The ability to steer the focal zone and achieve high acoustic pressures establishes this platform as an ideal candidate for robotic-assisted laparoscopic surgery and other clinical applications requiring compact FUS devices.

7.2 Recommendations for further work

There are a number of steps that can be taken to optimise the miniaturised FUS devices in this thesis. The following is a list of areas to target;

Optimisation of the materials used

The photopolymer material used was targeted as a result of its strength and high cross-linking characteristics. This market is growing rapidly, and there are already alternatives on the market that seek to increase this strength by incorporating additives such as glass. A more suitable material for the Fresnel lens of this device would be one that has similar acoustic impedance, higher sound speed, and much lower attenuation.

The interaction between the lens and the piezoelectric material is also vital. The porous piezoceramic proved that acoustic coupling of the two materials can improve the overall acoustic output. The incorporation of a piezoelectric 1-3 composite material instead of the PZT disc could increase this coupling.

Characterisation of heat build up

In addition to the initial work to characterise the dielectric losses within the piezoelectric ceramic of the FUS transducer, a study could be carried out on the effect of heat. The electric impedance can be characterised while the device is at a steady-state temperature in an oven. The same study of high-power swept sinusoids can be incorporated. This would inform the design of the electrical matching transformer such that the device would be perfectly matched when the piezoelectric element has undergone softening at the operational drive powers.

Impedance matching optimisation

Once the non-linear piezoelectric softening has been characterised in this device, an optimised matching transformer can be built. The matching transformer would instead be statically matched to the device's impedance at high power. A more robust solution can be found in a resonance tracking device, however, this is more difficult to achieve at the frequency of these devices.

Clinical studies

To finalise the device effectiveness, progress should be made towards clinical trials. Trials on phantom material will be involved in the immediate development of the FUS devices. However, this work must also be achieved in *ex vivo* tissue in animal models and subsequently *ex vivo* cadaveric tissue. The final tests would be performed in large animal trials *in vivo* for either soft tissue ablation or other hyperthermia treatments.

Appendices

A Acoustic scanning tank data

Each of the sixteen FUS devices that were manufactured have been characterised in a 3D acoustic scanning tank. A needle hydrophone measured acoustic pressure in the XY, XZ and YZ planes. Each device was aligned with respect to the acoustic focus and a scan of 10 mm x 15 mm was taken in the YZ and XZ planes. A smaller scan to capture the focal zone in the XY plane was captured in a window of 5 mm x 5 mm. The amplitude of the pressure measurements is shown in the heat map on the right, in MPa. Each device was driven with an arbitrary input voltage of 50 mVpp and passed through a 50 dB RF amplifier. This was to ensure the pressures generated by the devices were small enough to not permanently damage the needle hydrophone.

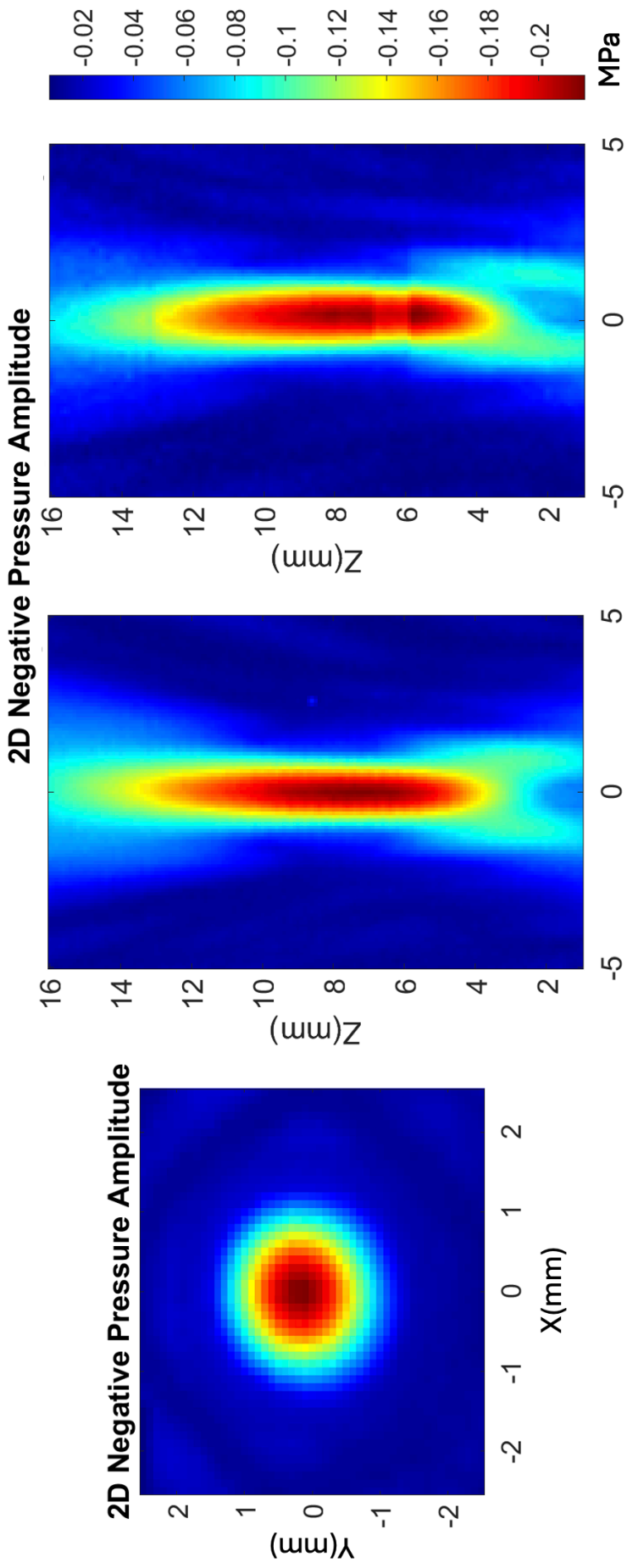

Figure A.1: Acoustic scanning tank scans of the FUS device $D_{PZ29(1)}$. Including (a) the XY plane, (b) XZ plane and (c) YZ plane.

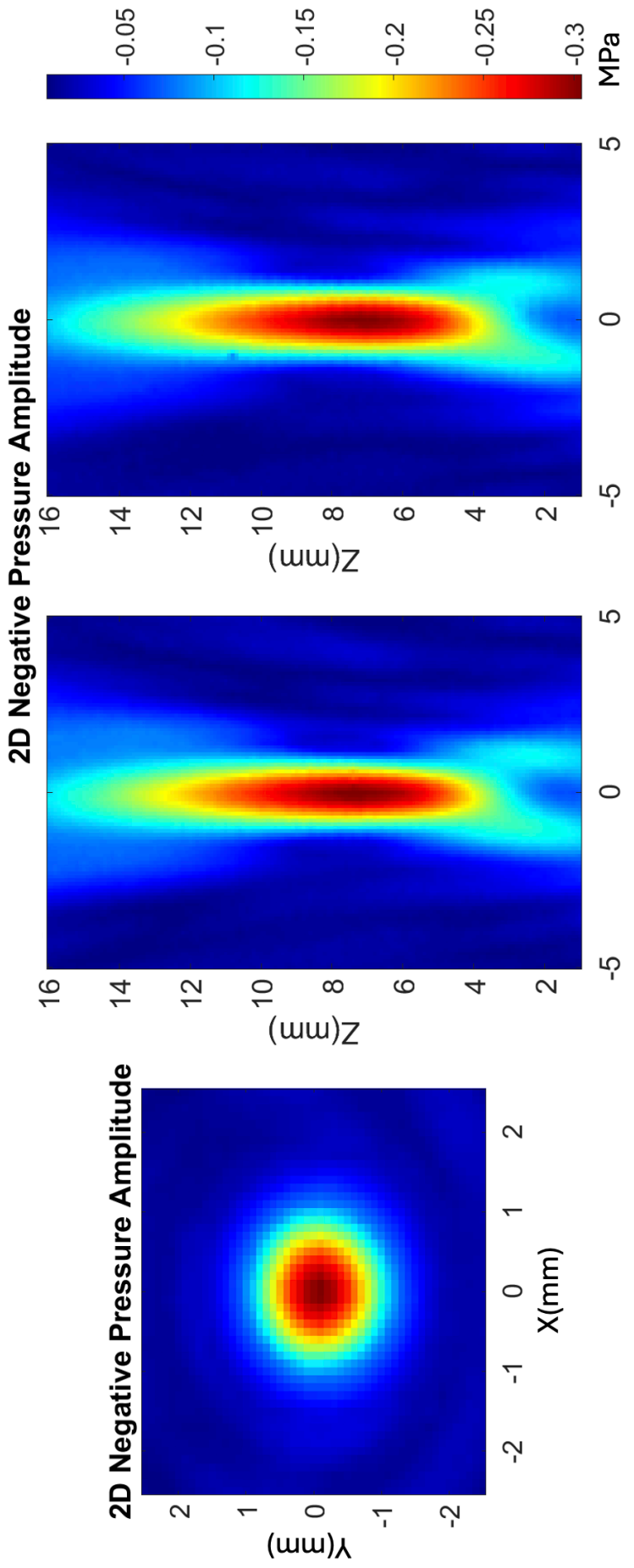

Figure A.2: Acoustic scanning tank scans of the FUS device $D_{PZ29(2)}$. Including (a) the XY plane, (b) XZ plane and (c) YZ plane.

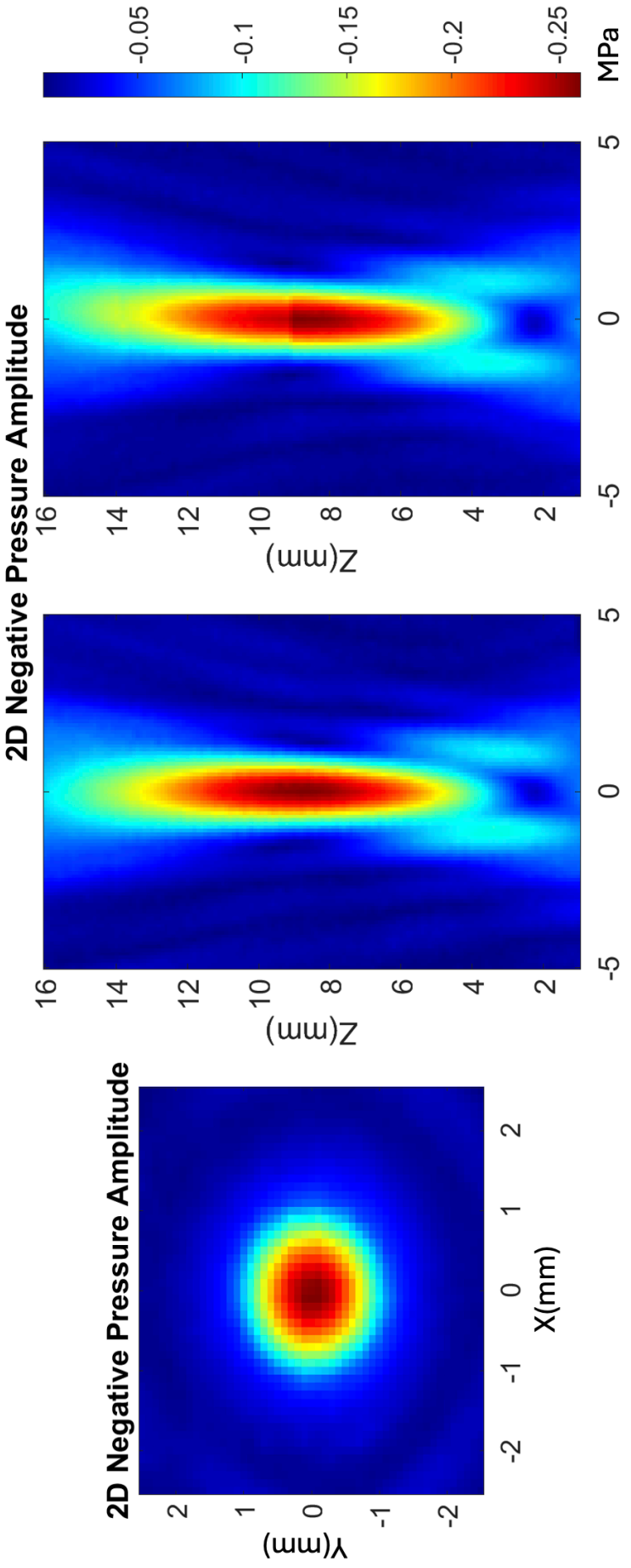

Figure A.3: Acoustic scanning tank scans of the FUS device $D_{PZ29(3)}$. Including (a) the XY plane, (b) XZ plane and (c) YZ plane.

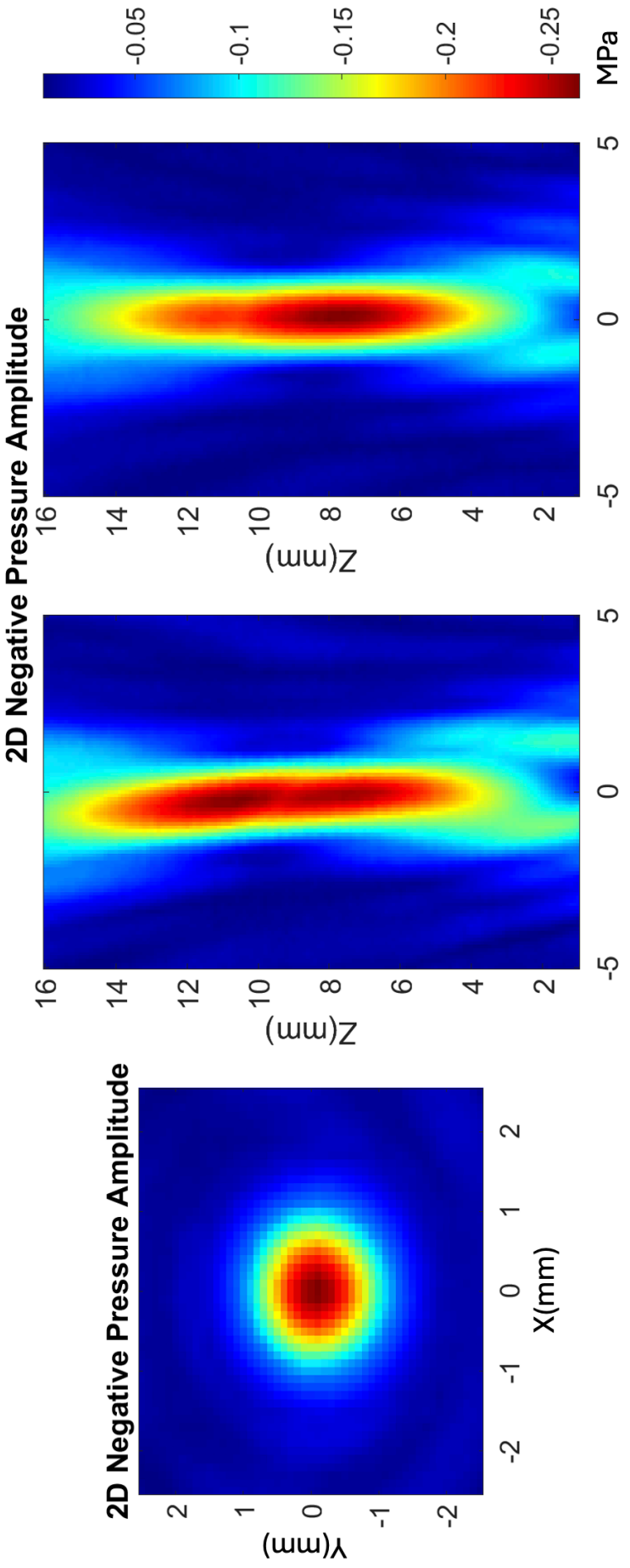

Figure A.4: Acoustic scanning tank scans of the FUS device $D_{PZ29(4)}$. Including (a) the XY plane, (b) XZ plane and (c) YZ plane.

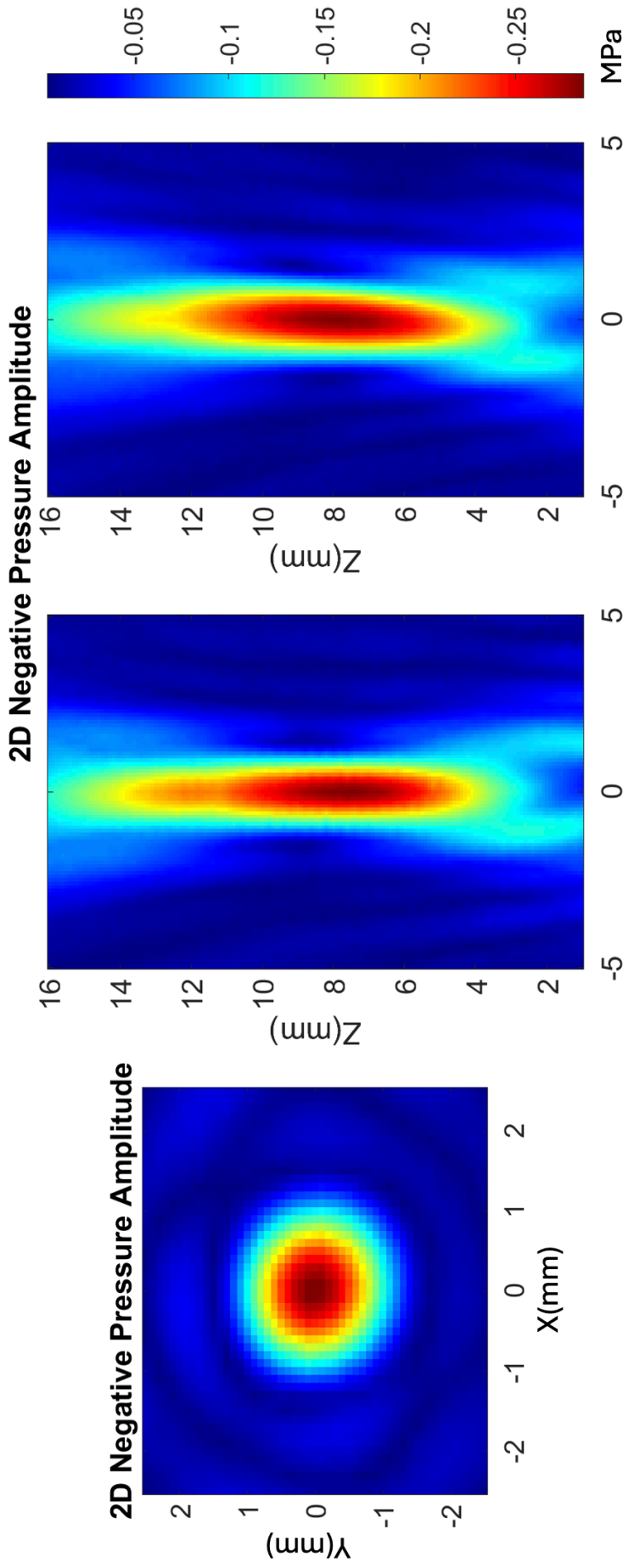

Figure A.5: Acoustic scanning tank scans of the FUS device $D_{PZ29(5)}$. Including (a) the XY plane, (b) XZ plane and (c) YZ plane.

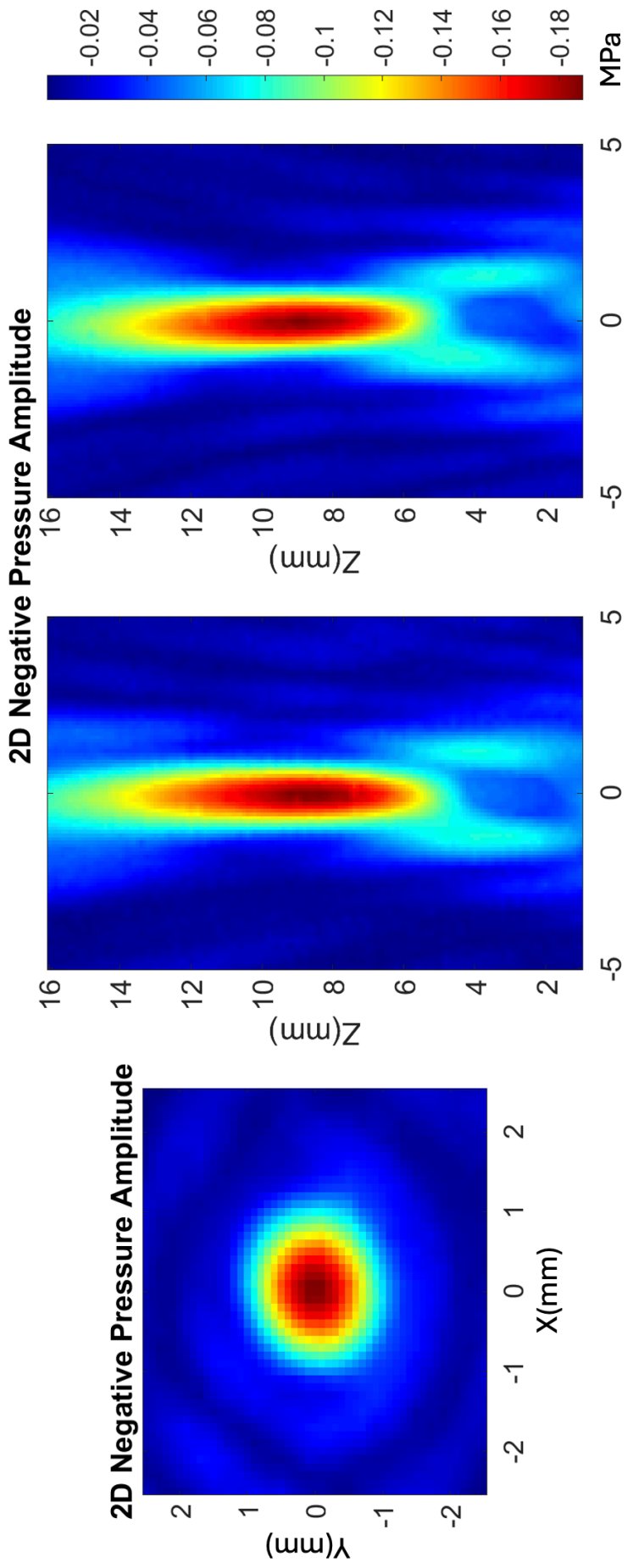

Figure A.6: Acoustic scanning tank scans of the FUS device $D_{PZ54(1)}$. Including (a) the XY plane, (b) XZ plane and (c) YZ plane.

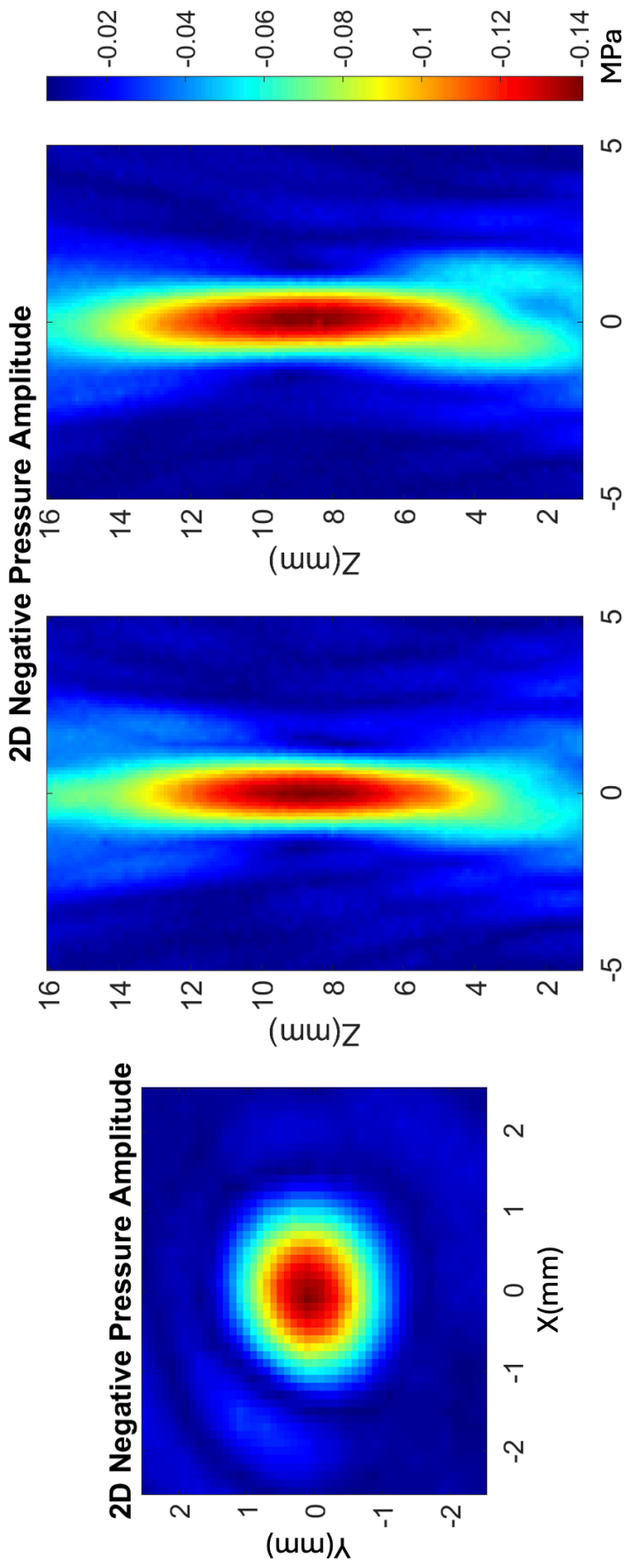

Figure A.7: Acoustic scanning tank scans of the FUS device $D_{PZ54(2)}$. Including (a) the XY plane, (b) XZ plane and (c) YZ plane.

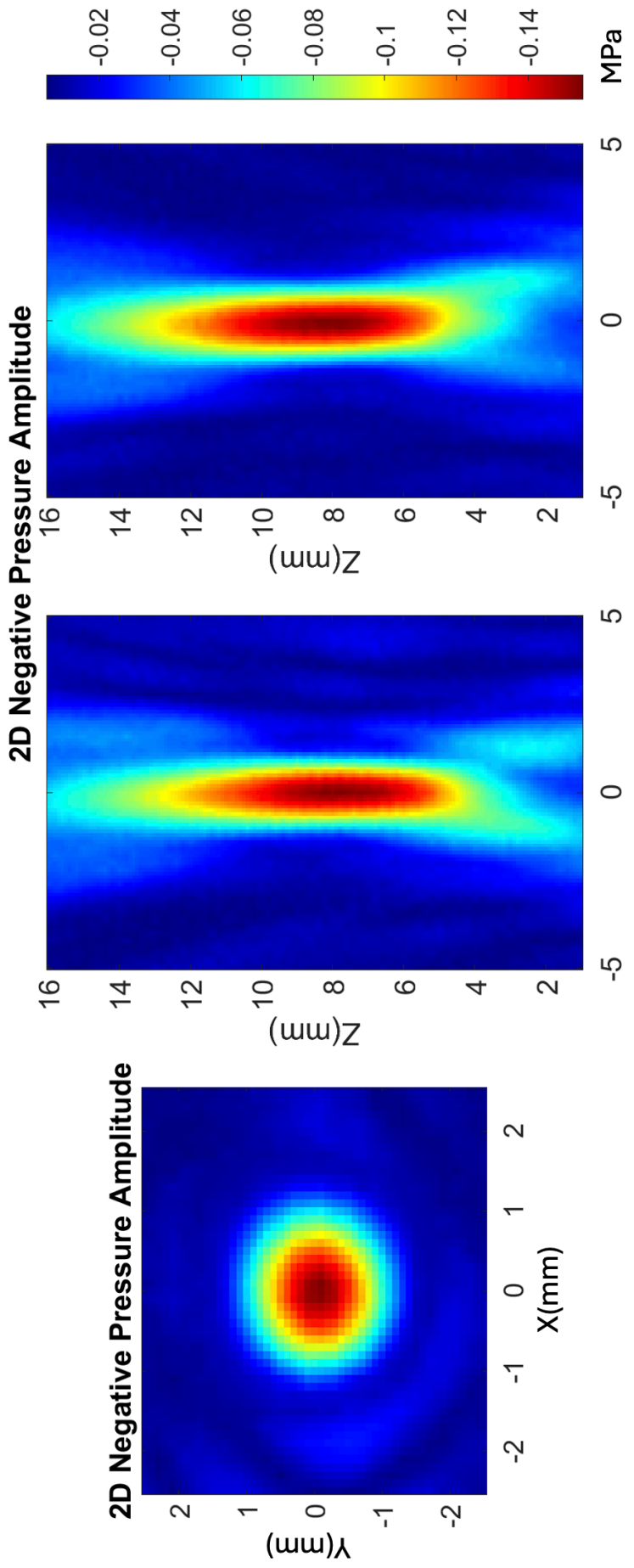

Figure A.8: Acoustic scanning tank scans of the FUS device $D_{PZ54(3)}$. Including (a) the XY plane, (b) XZ plane and (c) YZ plane.

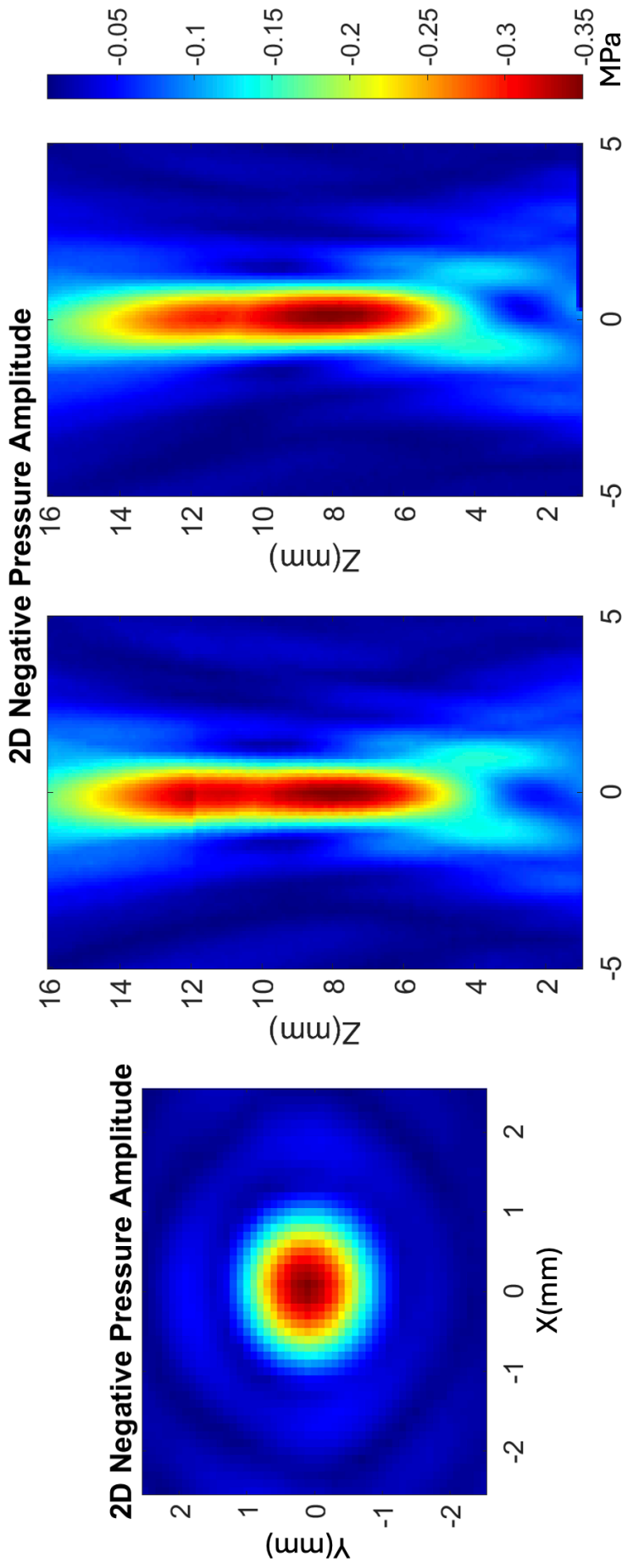

Figure A.9: Acoustic scanning tank scans of the FUS device $D_{PZ37(1)}$. Including (a) the XY plane, (b) XZ plane and (c) YZ plane.

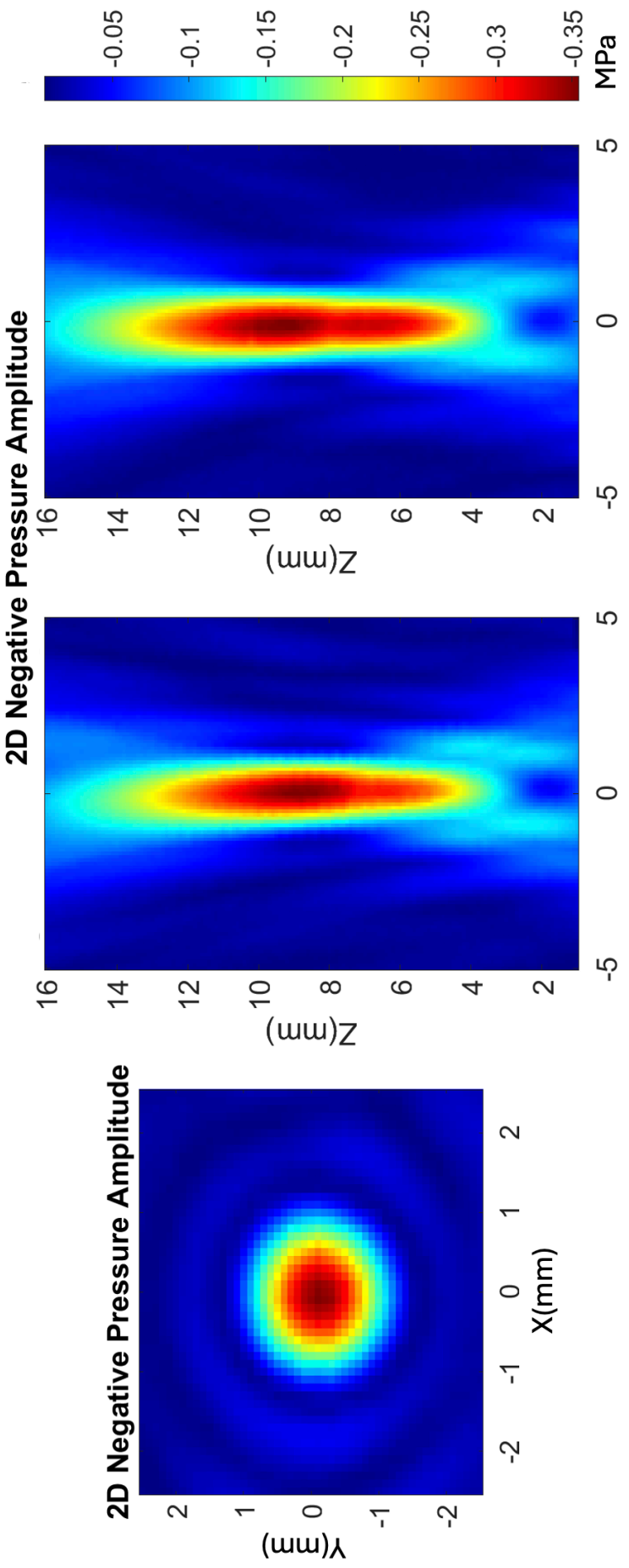

Figure A.10: Acoustic scanning tank scans of the FUS device $D_{PZ37(2)}$. Including (a) the XY plane, (b) XZ plane and (c) YZ plane.

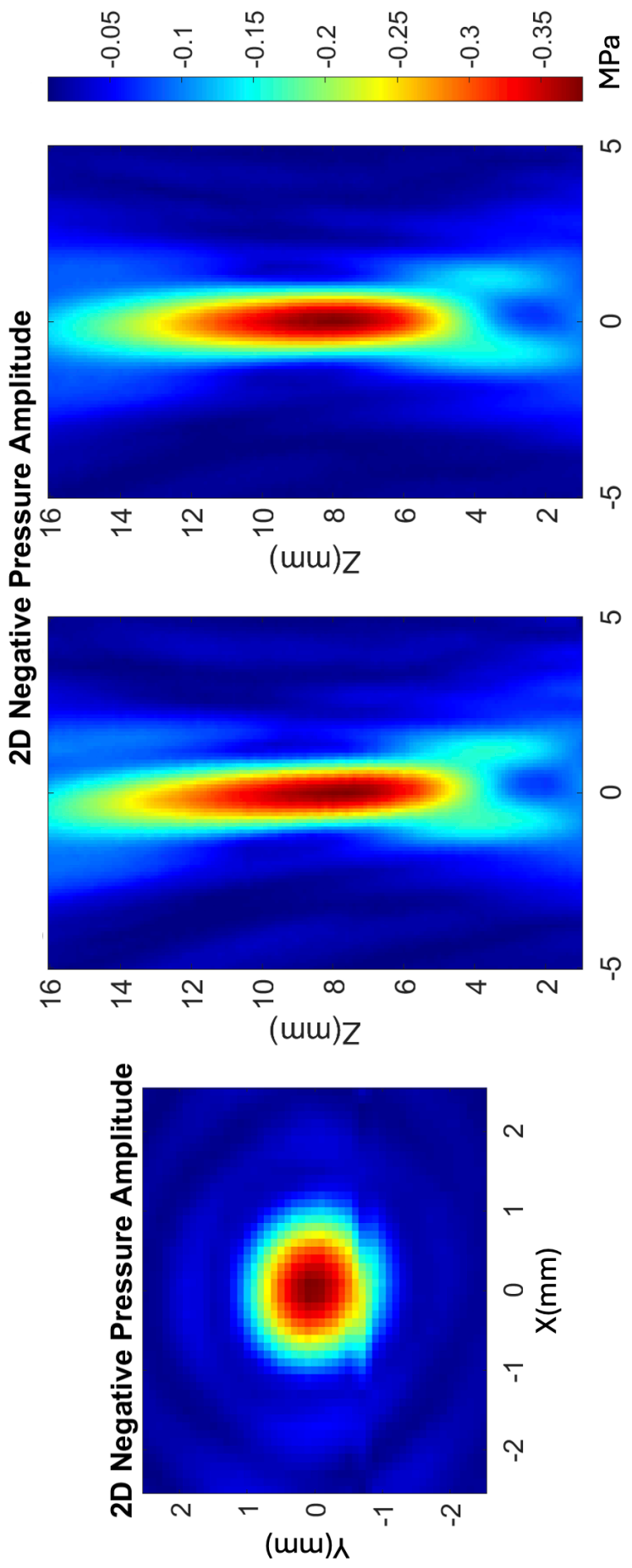

Figure A.11: Acoustic scanning tank scans of the FUS device $D_{PZ37(3)}$. Including (a) the XY plane, (b) XZ plane and (c) YZ plane.

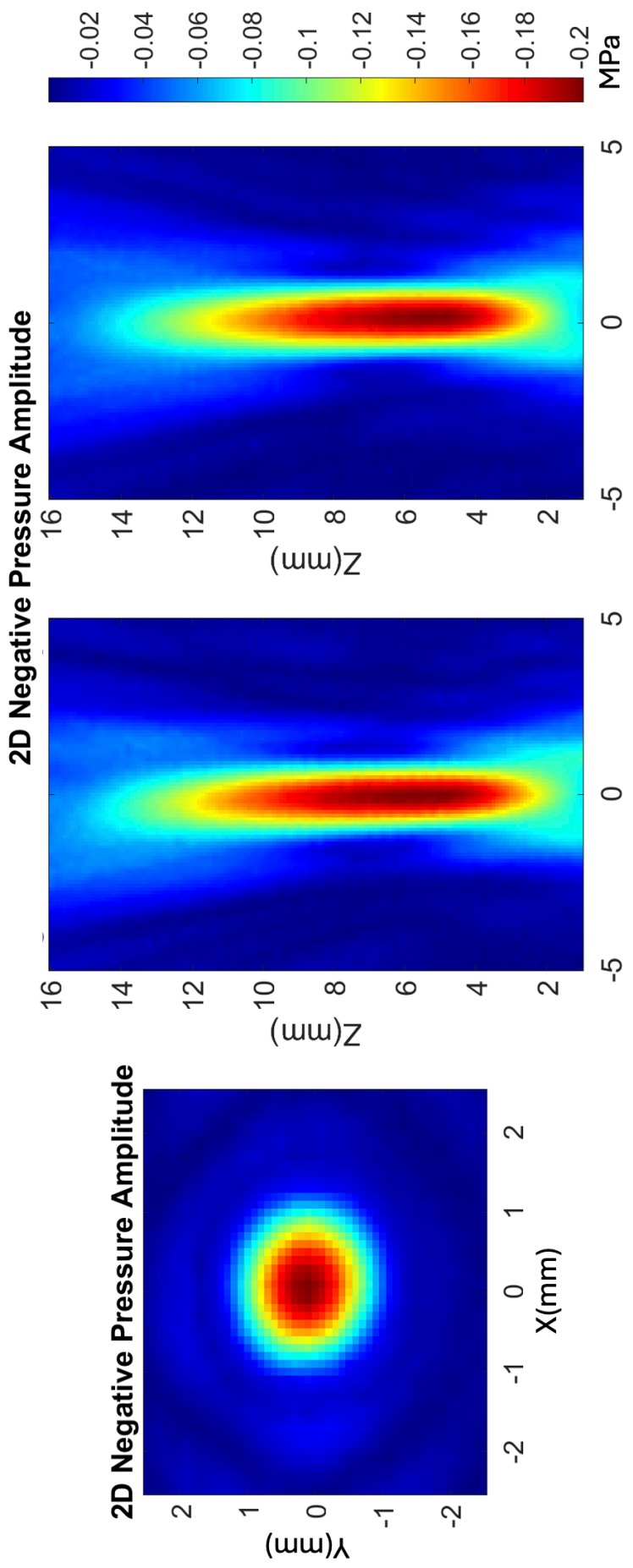

Figure A.12: Acoustic scanning tank scans of the FUS device $D_{PZ12(1)}$. Including (a) the XY plane, (b) XZ plane and (c) YZ plane.

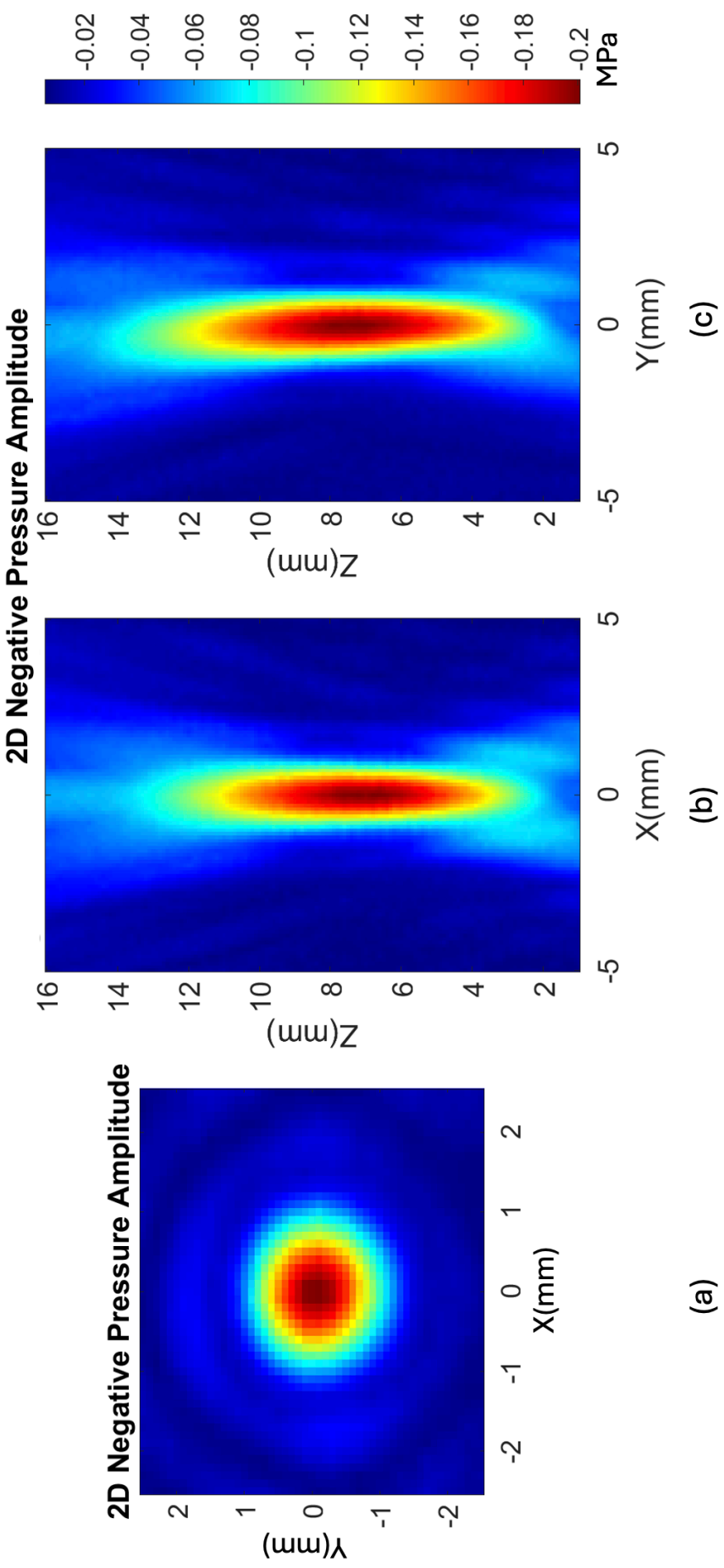

Figure A.13: Acoustic scanning tank scans of the FUS device $D_{PZ12(2)}$. Including (a) the XY plane, (b) XZ plane and (c) YZ plane.

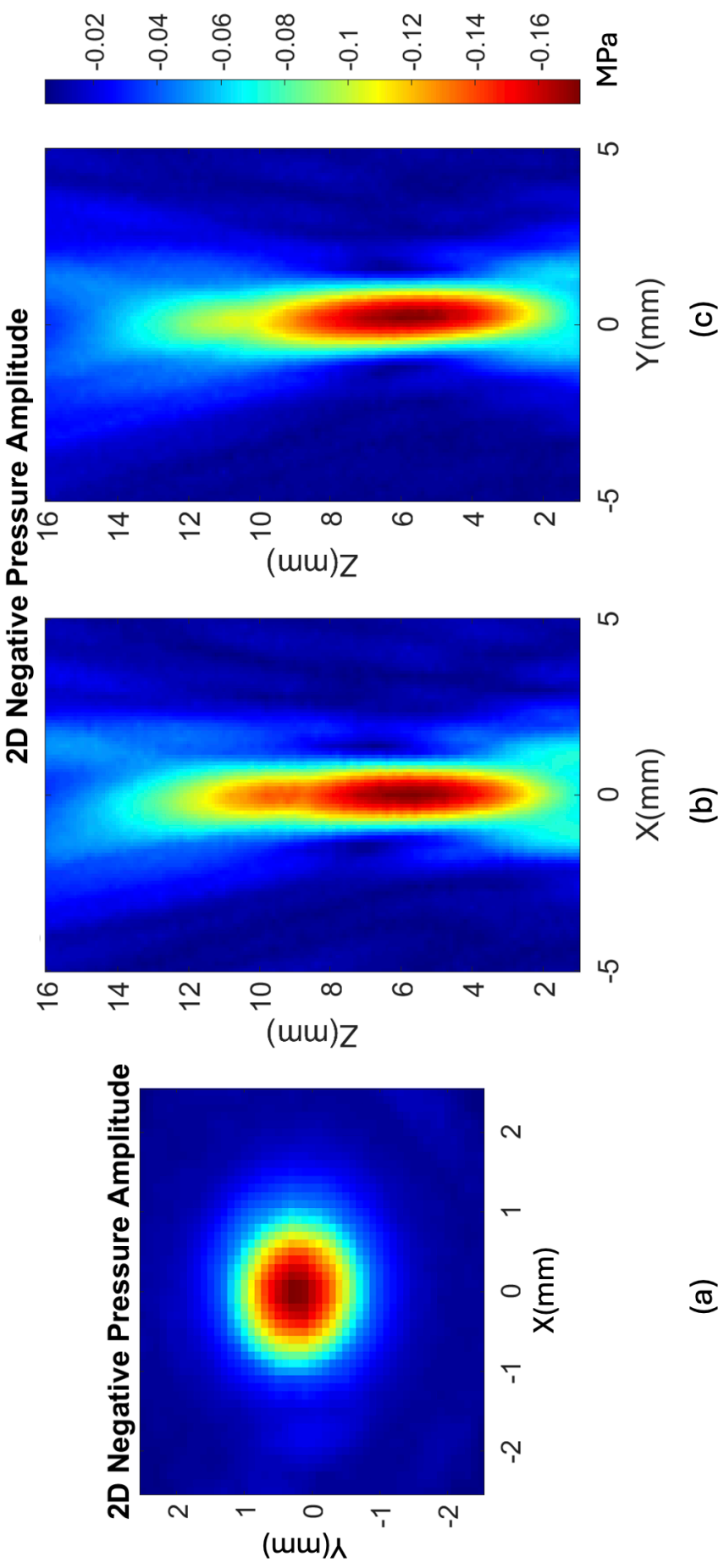

Figure A.14: Acoustic scanning tank scans of the FUS device $D_{PZ12(3)}$. Including (a) the XY plane, (b) XZ plane and (c) YZ plane.

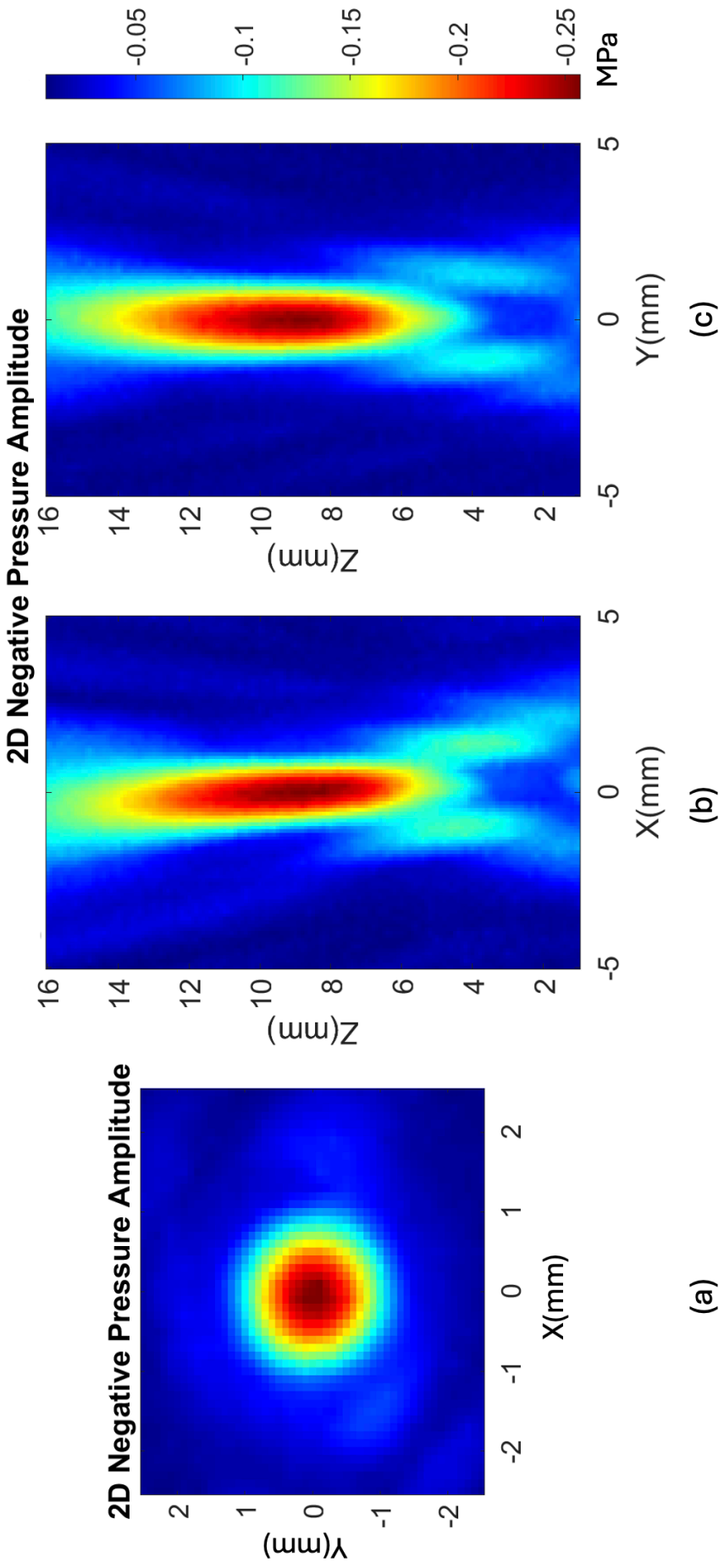

Figure A.15: Acoustic scanning tank scans of the FUS device D_{PZ37cc}. Including (a) the XY plane, (b) XZ plane and (c) YZ plane.

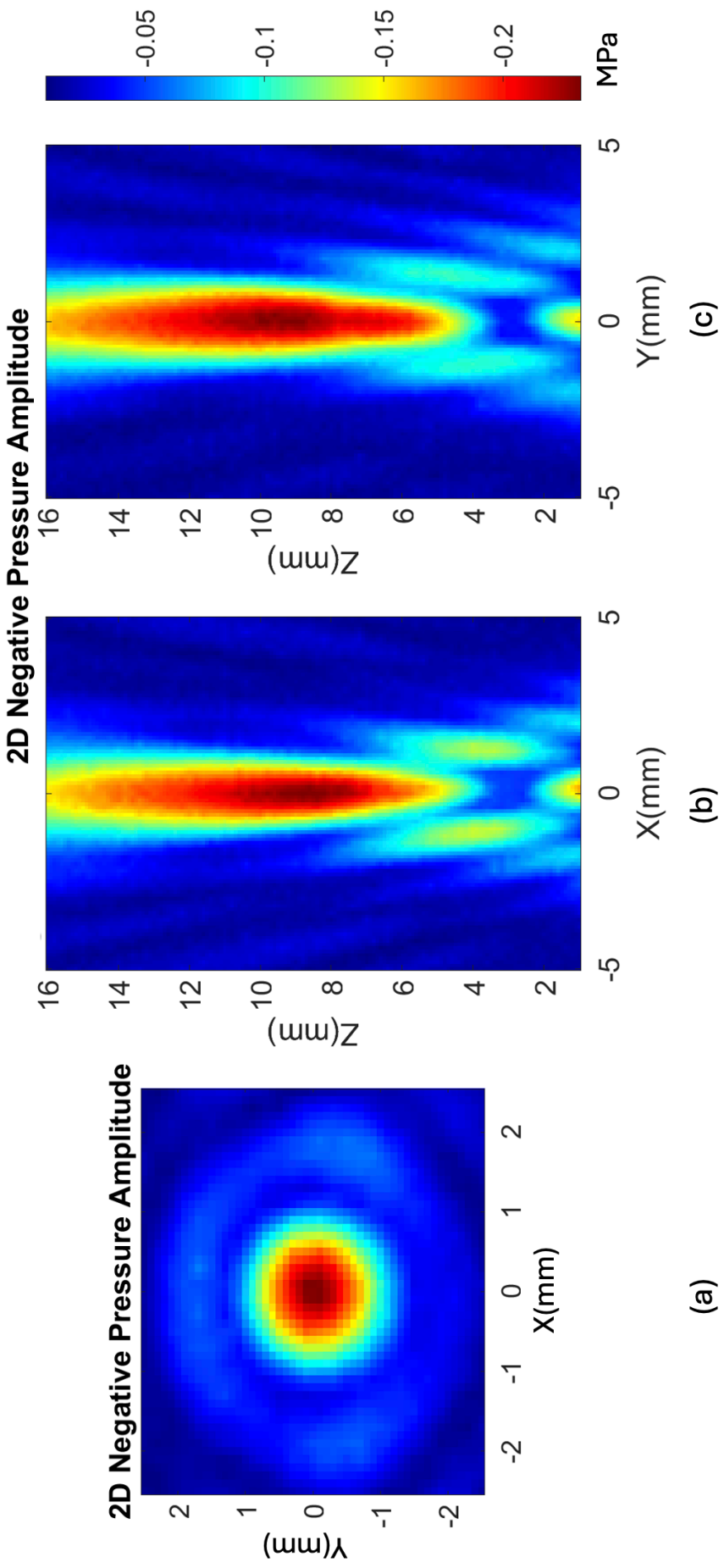

Figure A.16: Acoustic scanning tank scans of the FUS device D_{PZ37mh}. Including (a) the XY plane, (b) XZ plane and (c) YZ plane.

B NDT measurement parameters

Parameter	NDT probe		
	0.5 MHz	2.25 MHz	5 MHz
Probe S/N			
Longitudinal	V101-RB	V104-RB	V107-RB
Shear	V151-RM	V152-RM	V154-RM
Gain	25 dB	38 dB	50 dB
HP filter	OUT	OUT	1 MHz
LP filter	5 MHz	10 MHz	15 MHz
RPF rate	5	5	5
Pulse amplitude	10	10	10
Pulse energy	HIGH 3	HIGH 3	HIGH 3
Damping	5	5	5

Table 6: The parameters used in the JSR pulser receiver (DPR 300) with longitudinal contact probes from Olympus at various frequencies. Gain is tuned while observing an oscilloscope and kept constant for all measurements on each material. This is accounted for in post-processing. For shear wave measurements, gain was maximum (60-70 dB) and amplitude was maximum (15).

References

[1] G. Reese. *Music in the middle ages*. W.W. Norton, 1942.

[2] R.J. Urick. *Principles of Underwater Sound for Engineers*. Peninsula Publishing, 1983.

[3] R.T. Beyer. *Sounds of Our Times*. Springer New York, 1999.

[4] J.W. Strutt. *The Theory of Sound*. Vol. 1 and 2. Dover Publications, 1877.

[5] J. Curie and P. Curie. "Sur l'electricite polaire dan les cristaux hemiedres a faces inclinees". In: *Bulletin de Minéralogie* 3.4 (1880), pp. 90–93. DOI: 10.3406/bulmi.1880.1564.

[6] G. Lippmann. "Principe de la conservation de l'electricite". In: *Annales de chimie et de physique* 1 (1881), pp. 381–394. DOI: 10.1051/jphystap:0188100100038100.

[7] L. Spallanzani. "Lettere sopra il sospetto di un nuovo senso nei pipistrelli". In: *Nella Stamperia Reale* 1 (1794).

[8] R. Kenneth. "The Fessenden Oscillator: History, electroacoustic model, and performance estimate." In: *The Journal of Acoustical Society of America* 1 (1994). DOI: https://doi.org/10.1121/1.409629.

[9] P. Langevin. "Piezoelectric Signaling Apparatus". In: *US Patent 2,248,870* (1941).

[10] A. von Hippel et al. "High dielectric constant ceramics". In: *Industrial & Engineering Chemistry* 38.11 (1946), pp. 1097–1109. DOI: 10.1021/ie50443a009.

[11] B. Jaffe, R. S. Roth, and S. Marzullo. "Properties of Piezoelectric ceramics". In: *Journal of research of the National Bureau of Standards* 55.5 (1955), pp. 239–254.

[12] R.W. Wood and A.L. Loomis. "The physical and biological effects of high-frequency sound-waves of great intensity". In: *The London, Edinburgh, and Dublin Philosophical Magazine and Journal of Science* 4.22 (1927), pp. 417–436. DOI: 10.1080/14786440908564348.

[13] H. Gohr and Th. Wedekind. "Der Utraschall in der Medizin". In: *Klinische Wochenschrift* 19.2 (1940), pp. 25–29. DOI: https://doi.org/10.1007/BF01772492.

[14] G.D. Ludwig. “Device with radar principle detects foreign objects in body tissue”. In: *Department of defence office of public information* (1949).

[15] U. Nixdorff. “The inaugurator of transmitted echocardiography: Prof. Dr Wolf-Dieter Keidel”. In: *European Journal of Echocardiography* 10.1 (2009), pp. 48–49. DOI: 10.1093/ejechocard/jen233.

[16] G.D. Ludwig. “The velocity of Sound through Tissues and the Acoustic Impedance of Tissues”. In: *The Journal of the Acoustical Society of America* 22.6 (1950), pp. 862–866. DOI: https://doi.org/10.1121/1.1906706.

[17] T.F. Hueter, R.H. Bolt, and H.T. Ballantine Jr. “On the Detection of Brain Tumors by Ultrasonics”. In: *The Journal of the Acoustical Society of America* 22.5 (1950), pp. 686–687.

[18] M.B. McNay and J.E. Fleming. “Forty years of obstetric ultrasound 1957-1997: from A-scope to three dimensions.” In: *Ultrasound in medicine & biology* 25.1 (1999), pp. 3–56. DOI: 10.1016/s0301-5629(98)00129-x.

[19] J. Gruetzmacher. “Piezoelektrischer Kristall mit Ultraschallkonvergenz ”. In: *Zeitschrift fur Physik* 96.5-6 (1935), pp. 342–349.

[20] J.G. Lynn et al. “A new method for the generation and use of focused ultrasound in experimental biology”. In: *Journal of General Physiology* 26.2 (1942), pp. 179–193. DOI: 10.1085/jgp.26.2.179.

[21] P.D. Wall et al. “The Use of High Intensity Ultrasound in Experimental Neurology”. In: *Journal of the Acoustical Society of America* 25.2 (1953), pp. 281–285. DOI: 10.1121/1.1907032.

[22] W.J. Fry et al. “Physical Factors Involved in Ultrasonically Induced Changes in Living Systems: II. Amplitude Duration Relations and the Effect of Hydrostatic Pressure for Nerve Tissue”. In: *Journal of the Acoustical Society of America* 23.3 (1951), pp. 364–368. DOI: 10.1121/1.1906774.

[23] W.J. Fry et al. “Production of focal destructive lesions in the central nervous system with ultrasound”. In: *Journal of Neurosurgery* 11 (5 1954), pp. 471–478. DOI: 10.3171/jns.1954.11.5.0471.

[24] P.D. Wall et al. “Changes produced in the central nervous system by ultrasound”. In: *Science* 114.2974 (1951), pp. 686–687. DOI: 10.1126/science.114.2974.686.

[25] W.J. Fry et al. *The Use of Ultrasound in Neurosugery.* 1960.

[26] J. C. Bamber. “Attenuation and Absorption”. In: *Physical Principles of Medical Ultrasonics*. John Wiley & Sons, Ltd, 2004. Chap. 4, pp. 93–166. DOI: https://doi.org/10.1002/0470093978.ch4.

[27] G. Ter Haar. "Ultrasound focal beam surgery". In: *Ultrasound in Med. & Biol* 21.9 (1995), pp. 1089–1100. DOI: 10.1016/0301-5629(95)02010-1.

[28] L. Chen et al. "Treatment of implanted liver tumors with focused ultrasound". In: *Ultrasound in Medicine and Biology* 24.9 (1998), pp. 1475–1488. DOI: 10.1016/S0301-5629(98)00134-3.

[29] N.A. Watkin et al. "High Intensity focussed ultrasound ablation of the kidney in a large animal model". In: *Journal of Endourology* 11.3 (1997), pp. 191–196. DOI: https://doi.org/10.1089/end.1997.11.191.

[30] G. Vallancien et al. "Focused extracorporeal pyrotherapy". In: *European Urology* 23 (1993), pp. 48–52. DOI: 10.1159/000474680.

[31] A. Gelet et al. "Prostatic Tissue Destruction by High-Intensity Focused Ultrasound: Experimentation on Canine Prostate1". In: *Journal of Endourology* 7.3 (1993). DOI: doi:10.1089/end.1993.7.249.

[32] N. A. Watkin, G.R. Ter Haar, and I. Rivens. "The intensity dependence of the site of maximal energy deposition in focused ultrasound surgery". In: *Ultrasound in Medicine in Biology* 22.4 (1996), pp. 483–491.

[33] Z. Neeman and B.J. Wood. "Radiofrequency ablation beyond the liver". In: *Techniques in Vascular and Interventional Radiology* 5.3 (2002), pp. 156–163. DOI: 10.1053/tvir.2002.36419.

[34] O. Seror. "Ablative therapies: Advantages and disadvantages of radiofrequency, cryotherapy, microwave and electroporation methods, or how to choose the right method for an individual patient?" In: *Diagnostic and Interventional Imaging* 96.6 (2015), pp. 617–624. DOI: 10.1016/j.diii.2015.04.007.

[35] G. Tsoumakidou et al. "Image-Guided Spinal Ablation: A Review". In: *Cardio-Vascular and Interventional Radiology* 39.9 (2016), pp. 1229–1238. DOI: 10.1007/s00270-016-1402-6.

[36] A. Worthington et al. "Image-Guided High Intensity Focused Ultrasound System for Large Animal Nerve Ablation Studies". In: *IEEE Journal of Translational Engineering in Health and Medicine* 4 (2016), pp. 1–6. DOI: 10.1109/JTEHM.2016.2581811.

[37] D. Sinden and G. ter Haar. "Dosimetry implications for correct ultrasound dose deposition: Uncertainties in descriptors, planning and treatment delivery". In: *Translational Cancer Research* 3.5 (2014), pp. 459–471. DOI: 10.3978/j.issn.2218-676X.2014.10.02.

[38] J. E. Soneson. “A user-friendly software package for HIFU simulation”. In: *AIP Conference Proceedings* 1113 (2009), pp. 165–169. DOI: 10.1063/1.3131405.

[39] G. ter Haar. “Therapeutic ultrasound”. In: *European Journal of Ultrasound* 9 (1 1999), pp. 3–9. DOI: 10.1016/s0929-8266(99)00013-0.

[40] S. Mitragotori. “Healing sound: the use of ultrasound in drug delivery and other therapeutic applications”. In: *Nature reviews. Drug discovery* 4 (2005), pp. 255–260.

[41] G. ter Haar and C. Coussios. “High intensity focused ultrasound: Physical principles and devices”. In: *International Journal of Hyperthermia* 23.2 (2007), pp. 89–104. DOI: 10.1080/02656730601186138.

[42] Sonic concepts. *Hifuplex system family*. 2019. URL: https://sonicconcepts.com/hifuplex/.

[43] R. F. Paterson et al. “Laparoscopic Partial Kidney Ablation with High Intensity Focused Ultrasound”. In: *Journal of Urology* (2003). DOI: 10.1016/S0022-5347(05)64124-9.

[44] J.B. adams et al. “High-intensity focused ultrasound ablation of rabbit kidney tumors”. In: *Journal of Endourology* 10.1 (1996), pp. 71–75.

[45] I.R.S. Makin et al. “Miniaturized ultrasound arrays for interstitial ablation and imaging”. In: *Ultrasound in Medicine and Biology* 31.11 (2005), pp. 1539–1550. DOI: 10.1016/j.ultrasmedbio.2005.07.008.

[46] R. Seip et al. *High-Intensity Focused Ultrasound (HIFU) Phased Arrays : Recent Developments in Transrectal Transducers and Driving Electronics Design*. 2003.

[47] S.C. Chan et al. “Finite Element Modeling of Binary Acoustic Fresnel Lenses”. In: *Review of Progress in Quantitative Nondestructive Evaluation* 14 (1995), pp. 923–930. DOI: 10.1007/978-1-4615-1987-4_116.

[48] D. Melodelima et al. “Thermal Ablation by High-Intensity-Focused Ultrasound Using a Toroid Transducer Increases the Coagulated Volume. Results of Animal Experiments”. In: *Ultrasound in Medicine and Biology* 35.3 (2009), pp. 425–435. DOI: 10.1016/j.ultrasmedbio.2008.09.020.

[49] T. Fjield et al. “Design and experimental verification of thin acoustic lenses for the coagulation of large tissue volumes”. In: *Physics in Medicine and Biology* 42.12 (1997), pp. 2341–2354. DOI: 10.1088/0031-9155/42/12/003.

[50] M. Ferri et al. “Enhanced Numerical Method for the Design of 3-D-Printed Holographic Acoustic Lenses for Aberration Correction of Single-Element Transcranial Focused Ultrasound”. In: *Ultrasound in Medicine and Biology* 45.3 (2019), pp. 867–884. DOI: 10.1016/j.ultrasmedbio.2018.10.022.

[51] J.F. Nye. *Physical Properties of Crystals: Their Representation by Tensors and Matrices*. Oxford science publications. Clarendon Press, 1985. ISBN: 9780198511656. URL: https://books.google.co.uk/books?id=ugwql-uVB44C.

[52] Y. Wang et al. “The fundamentals and applications of piezoelectric materials for tumor therapy: recent advances and outlook”. In: *Materials Horizons* 10.4 (2023), pp. 1140–1184. DOI: 10.1039/d2mh01221a.

[53] Philips electronics and materials Division. *Piezoelectric ceramics*. Vol. 2. Philips, 1968, pp. 4–17.

[54] K. Uchino. *Manufacturing Methods for Piezoelectric Ceramic Materials*. January. Woodhead Publishing, 2017, pp. 385–421. DOI: 10.1016/b978-0-08-102135-4.00010-2.

[55] S. Sherrit and B.K. Mukherjee. “Characterization of Piezoelectric Materials for Transducers”. In: *JPL* (2007).

[56] D. B. A.H. Meitzler, H.F. Tiersten, and A.W. Warner. “An American National Standard IEEE Standard on Piezoelectricity”. In: *Std 176-1987* (1988), pp. 1–74. DOI: 10.1109/IEEESTD.1988.79638.

[57] T. Ikeda. *Fundamentals of Piezoelectricity*. Oxford science publications. Oxford University Press, 1996.

[58] W.P. Mason. “Physical Acoustics and the Properties of Solids”. In: *The Journal of the Acoustical Society of America* 28.6 (1956), pp. 1197–1206. DOI: 10.1121/1.1908593.

[59] D. Damjanovic. “Ferroelectric, dielectric and piezoelectric properties of ferroelectric thin films and ceramics”. In: *Reports on Progress in Physics* 61 (1998), pp. 1267–1324.

[60] K.V. Wong and A. Hernandez. “A Review of Additive Manufacturing”. In: *ISRN Mechanical Engineering* 2012 (2012), pp. 1–10. DOI: 10.5402/2012/208760.

[61] B. Hadimioglu et al. “High-efficiency Fresnel acoustic lenses”. In: *IEEE Ultrasonics symposium*. 1993, pp. 579–582.

[62] M. Redwood. “Transient Performance of a Piezoelectric Transducer”. In: *The Journal of the Acoustical Society of America* 33.4 (1961), pp. 527–536. DOI: 10.1121/1.1908709.

[63] G.R. Liu and S.S. Quek. *Finite Element Method, a practicle course*. Elsevier Science, 2003, pp. 1–11.

[64] OnScale. *The Basics*. 2020. URL: https://support.onscale.com/hc/en-us/articles/360015653612.

[65] N.Y. Gnedin, V.A. Semenov, and A.V. Kravtsov. "Enforcing the Courant–Friedrichs–Lewy condition in explicitly conservative local time stepping schemes". In: *Journal of Computational Physics* 359 (2018), pp. 93–105. DOI: 10.1016/j.jcp.2018.01.008.

[66] C.R. Hill et al. "Lesion development in focused ultrasound surgery: A general model". In: *Ultrasound in Medicine and Biology* 20.3 (1994), pp. 259–269. DOI: 10.1016/0301-5629(94)90066-3.

[67] Hossein J. Gohari. "Focusing of ultrasound beams". In: *Masters Thesis, University of Oslo* (1997), pp. 1–102.

[68] Shin Chuen Chan et al. "Finite element analysis of multilevel acoustic Fresnel lenses". In: *IEEE Transactions on Ultrasonics, Ferroelectrics, and Frequency Control* 43.4 (1996), pp. 670–677. DOI: 10.1109/58.503729.

[69] OnScale. *OnScale Documentation*. 2019.

[70] V.T. Rathod. "A review of acoustic impedance matching techniques for piezoelectric sensors and transducers". In: *Sensors* 20.14 (2020), pp. 1–65. DOI: 10.3390/s20144051.

[71] CTS Ferroperm. *CTS Ferroperm materials data sheet*. 2020.

[72] M. Sinha and D. J. Buckley. "Acoustic Properties of Polymers". In: *Physical Properties of Polymers Handbook*. Springer New York, 2007, pp. 1021–1031. DOI: 10.1007/978-0-387-69002-5_60.

[73] T. Yu et al. "Acoustic insulation and absorption mechanism of metallic hollow spheres composites with different polymer matrix". In: *Composite Structures* 248 (2020). DOI: 10.1016/j.compstruct.2020.112566.

[74] Agilent. *Agilent 4395A datasheet*. 2000. URL: https://www.testequipmenthq.com/datasheets/Keysight-4395A-Datasheet.pdf.

[75] D. A. Deangelis and G. W. Schulze. "Performance of PZT8 Versus PZT4 Piezoceramic Materials in Ultrasonic Transducers". In: *Physics Procedia*. Vol. 87. Elsevier B.V., 2016, pp. 85–92. DOI: 10.1016/j.phpro.2016.12.014.

[76] M. Steward, W. Battrick, and M. Cain. "Measuring Piezoelectric d33 coefficients using the Direct Method". In: *Measurement Good Practice Guide No. 44* 44 (2001), pp. 1–30.

[77] Polytec. *Polytec MSA 100 3D micro system analyser*. 2023. URL: https://www.polytec.com/uk/vibrometry/products/microscope-based-vibrometers/msa-100-3d-micro-system-analyzer.

[78] J Stevenson et al. "Characterisation of PZTs Non-Linear Behaviour for High-Power Systems". In: *IEEE International Ultrasonics Symposium, IUS*. 2021. DOI: 10.1109/IUS52206.2021.9593358.

[79] H.J. Lee et al. *High temperature, high power piezoelectric composite transducers*. 2014. DOI: 10.3390/s140814526.

[80] K. C.A. Smith and C. W. Oatley. "The scanning electron microscope and its fields of application". In: *British Journal of Applied Physics* 6.11 (1955), pp. 391–399. DOI: 10.1088/0508-3443/6/11/304.

[81] H. G. J. Moseley. "The High-Frequency Spectra of the Elements". In: *The London, Edinburgh, and Dublin Philosophical Magazine and Journal of Science* 26 (156 1913), pp. 1024–1034.

[82] M. Khalid, M. Shoaib, and A. A. Khan. "Strontium doped Lead Zirconate Titanate ceramics: Study of calcination and sintering process to improve piezo effect". In: *Journal of Nanoscience and Nanotechnology* 11.6 (2011), pp. 5440–5445. DOI: 10.1166/jnn.2011.3791.

[83] C.F. Holder and R.E. Schaak. "Tutorial on Powder X-ray Diffraction for Characterizing Nanoscale Materials". In: *ACS Nano* 13.7 (2019), pp. 7359–7365. DOI: 10.1021/acsnano.9b05157.

[84] M. Sinha and D. J. Buckley. *Chapter 60, Acoustic Properties of Polymers*. General Electric Global Research Centre, 2007. DOI: 10.1007/978-0-387-69002-5.

[85] I.D. Marinescu, E. Uhlmann, and T.K. Doi. *The handbook of lapping and polishing*. Vol. 1. CRC Press, 2006. ISBN: 9781420017632.

[86] A.W. Stähli. *The Technique of Lapping*. 2013.

[87] Creative Materials Inc. *118-09A, Conductive Ink, Data Sheet*. https://server.creativematerials.com/datasheets/DS_118_09.pdf. [Online; accessed 14/02/2024]. 2018.

[88] TableFlipFoundry. *TableFlipFoundry cones of callibration* . https://www.tableflipfoundry.com/. [Online; accessed 16/02/2024]. 2022.

[89] Liqreate. *StrongX data sheet*. https://www.liqcreate.com/downloads. [Online; accessed 19/02/2024]. 2022.

[90] N. Marahrens et al. "Enabling Autonomous Ultrasound-Guided Tumour Ablation during Robotic Surgery". In: *IEEE Proceedings, BIOROB* (2024), p. 6.

[91] V.P.Mason. *Electromechanical Transducers and Wave Filters*. D. Van Nostrand Company, 1942, pp. 201–209.

[92] X. Li et al. "Can Mn:PIN-PMN-PT piezocrystal replace hard piezoceramic in power ultrasonic devices?" In: *Ultrasonics* 138 (2024). DOI: 10.1016/j.ultras.2024.107257.

[93] R. Lee. *Electronic Transformers and Circuits*. Wiley, 1947.

[94] D. K. Kraus and K. R Carver. *Electromagnetics*. McGraw-Hill, 1984.

[95] Douglas Aircraft Company. *A Practical Introduction To Impedance Matching*. 1980.

[96] M.G. Kim et al. "Impedance matching network for high frequency ultrasonic transducer for cellular applications". In: *Ultrasonics* 65 (2016), pp. 258–267. DOI: 10.1016/j.ultras.2015.09.016.

[97] muRata Power Solutions. *Quad data bus isolators - Data sheet*. https://www.murata-ps.com/pub/data/magnetics/kmp_1600.pdf. [Online; accessed 29/03/2024]. 2018.

[98] K. L. Gebert and K. R. Edwards. *Transformers principles and applications*. American Technical Society, 1974. ISBN: 9780826916020.

[99] Block-trafo. *Wire current rating - Data sheet*. https://docs.rs-online.com/e937/0900766b8129257e.pdf. [Online; accessed 31/03/2024]. 2018.

[100] TDK. *Transformer core E42 - Data sheet*. https://www.farnell.com/datasheets/3974231.pdf. [Online; accessed 31/03/2024]. 2022.

[101] International Electrotechnical Comission. *Ultrasonics - Field characterization - Specification and measurement of field parameters for high intensity therapeutic ultrasound (HITU) transducers and systems*. https://webstore.iec.ch/publication/7197. [Online; accessed 22/04/2024]. 2014.

[102] J. Sliwa. "High intensity focused ultrasound transducer with acoustic lens (Patent No. US20080195003A1)". In: *United States Patent and Trademark Office* (2007).

[103] IEC. *Ultrasonics - Power Measurement - Radiation force balances and performance requirements*. 2006.

[104] Precision Acoustics. *Radiation Force Balance - Product Insructions V 4.13*. 2020.